DGK Veröffentlichungen der DGK

Ausschuss Geodäsie der Bayerischen Akademie der Wissenschaften

Reihe C | Dissertationen | Heft Nr. 936

**Kristin Vielberg**

# Thermosphere and radiation effects in forward and inverse non-gravitational force modelling

**München 2024**

**Bayerische Akademie der Wissenschaften**

ISSN 0065-5325 ISBN 978-3-7696-5348-9

**Diese Arbeit ist gleichzeitig veröffentlicht in:**
**bonndoc – Publikationsserver der Rheinischen Friedrich-Wilhelms-Universität Bonn**
**https://hdl.handle.net/20.500.11811/11288 oder https://nbn-resolving.org/urn:nbn:de:hbz:5-74145, Bonn 2024**

DGK Veröffentlichungen der DGK

Ausschuss Geodäsie der Bayerischen Akademie der Wissenschaften

Reihe C | Dissertationen | Heft Nr. 936

# Thermosphere and radiation effects in forward and inverse non-gravitational force modelling

An der Landwirtschaftlichen Fakultät
der Rheinischen Friedrich-Wilhelms-Universität Bonn
zur Erlangung des akademischen Grades
Doktorin der Ingenieurwissenschaften (Dr.-Ing.)
vorgelegte Dissertation

von

Kristin Vielberg

München 2024

Bayerische Akademie der Wissenschaften

ISSN 0065-5325 ISBN 978-3-7696-5348-9

Diese Arbeit ist gleichzeitig veröffentlicht in:
bonndoc – Publikationsserver der Rheinischen Friedrich-Wilhelms-Universität Bonn
https://hdl.handle.net/20.500.11811/11288 oder https://nbn-resolving.org/urn:nbn:de:hbz:5-74145, Bonn 2024

Adresse der DGK:



Ausschuss Geodäsie der Bayerischen Akademie der Wissenschaften (DGK)

Alfons-Goppel-Straße 11 ● D – 80 539 München

Telefon +49 - 331 - 6264 1685 ● E-Mail post@dgk.badw.de

http://www.dgk.badw.de

Referent: Prof. Dr.-Ing. Jürgen Kusche

Korreferenten: Prof. Dr.-Ing. Susanne Glaser
Prof. Dr.-Ing. Torsten Mayer-Gürr (TU Graz, Österreich)

Tag der mündlichen Prüfung: 12. Januar 2024

© 2024 Bayerische Akademie der Wissenschaften, München

Alle Rechte vorbehalten. Ohne Genehmigung der Herausgeber ist es auch nicht gestattet,
die Veröffentlichung oder Teile daraus auf photomechanischem Wege (Photokopie, Mikrokopie) zu vervielfältigen

ISSN 0065-5325 ISBN 978-3-7696-5348-9

## Abstract

Precise non-gravitational satellite force models are crucial for various space-based applications, such as satellite gravimetry, thermospheric neutral density estimation and precise orbit determination, thus contributing to a better understanding of the Earth system.

Satellite orbits are perturbed by gravitational and non-gravitational forces. For satellites in low-Earth orbits, in addition to the dominant force due to atmospheric drag, the most important non-gravitational forces are related to the radiation of the Sun and the Earth. The electromagnetic solar radiation as well as the Earth's outgoing radiation, consisting of emitted thermal radiation and the reflected sunlight, are either absorbed or reflected at the satellite's surface. The resulting forces are known as Solar and Earth radiation pressure, respectively. The re-emission of the absorbed heat causes the thermal re-radiation pressure force.

Over the last years, significant progress has been made in the modelling of aerodynamic forces. However, only few publications focused on the improvement of radiation pressure force models. The modelling of the radiation pressure forces depends on measured fluxes as well as on the satellite's mass, surface area and plate materials, of which especially the fluxes and material properties are known to introduce errors.

The aim of this thesis is to extend the existing radiation pressure force models, first, by detecting and overcoming systematic errors in the analytical formulations. In a second step, the extended model is applied in an inverse estimation approach to further improve remaining inconsistencies.

From the inspection of existing analytical radiation pressure force models, several extensions are suggested. These include the consideration of temporal variations in the solar flux and the solar spectrum as well as the impact of the atmosphere on the ray of sunlight. Additionally, the use of albedo and emission data introduces errors that can be avoided nowadays due to the availability of observed fluxes at the top of atmosphere and the consideration of the angular dependence of Earth's radiation. The transient re-emission of the satellite's absorbed radiation is often omitted, but is considered here as transient heat-conductive.

The extended radiation pressure force models are applied on satellites with simple shape, i.e., the Gravity Recovery And Climate Experiment (GRACE) satellites consisting of flat surfaces and on spherical Satellite Laser Ranging (SLR) satellites. The extensions of the forward force modelling are validated carefully (1) by comparing the modelled forces to accelerometer measurements (for GRACE), and (2) by evaluating their impact on the satellite orbit based on residuals to SLR measurements (for GRACE and spherical satellites). To reduce the effect of aerodynamic mismodelling, the year 2008 with low solar activity is selected. The validation revealed that a fine discretization (1°) of the Earth's footprint leads to the largest improvements in the Earth radiation pressure force modelling, i.e., for GRACE the SLR residual root mean square (RMS) decreases by 38 %. Choosing hourly radiation data together with angular dependency models additionally reduces the residual RMS by 2 %. Furthermore, considering fitted heat-conductive thermal re-radiation for GRACE decreases the SLR residual RMS by 36 % compared to using instantaneous re-radiation. The impact of the force model extensions on spherical SLR satellites is found to be generally smaller, which is related to their orbital altitude of more than 700 km.

The extended non-gravitational force models can be applied in an inverse approach, where an adjustment to measured forces allows for the estimation of selected parameters in the model to improve on the remaining inconsistencies. In the estimation of thermospheric neutral densities, this study found that extensions of the radiation pressure force modelling impact the neutral density by up to 5 % depending on the solar activity. It is therefore likely that omissions caused by application of the standard models contribute to the differences between existing estimates. In a second example, first experiments to solve for radiation-related parameters based on extended radiation pressure force models are carried out. Here, the quality of the accelerometer calibration still limits the inverse estimations from GRACE data and finding a stable parametrization remains challenging. Estimating radiation pressure scale factors from SLR data reveals that Ajisai is a promising candidate to further the research on the adjustment of radiation-related parameters. All in all, the results are encouraging to determine physical radiation pressure model parameters from

satellite accelerometry and SLR data in the future in order to enable the retrieval of a geodetic Earth's energy imbalance estimate.

## Zusammenfassung

Hochgenaue nicht-gravitative Kräftemodelle für Satelliten sind für eine Vielzahl weltraumgestützter Anwendungen wie die Satellitengravimetrie, die Schätzung der thermosphärischen Neutraldichte und die präzise Orbitbestimmung von entscheidender Bedeutung und tragen somit zu einem besseren Verständnis des Systems Erde bei.

Der Orbit eines jeden Satelliten wird durch gravitative sowie durch nicht-gravitative Kräfte gestört. Bei Satelliten in erdnahen Umlaufbahnen stehen neben der dominierenden Kraft, die auf den atmosphärischen Luftwiderstand zurückzuführen ist, die wichtigsten nicht-gravitativen Kräfte in Zusammenhang mit der Strahlung der Sonne und der Erde. Die elektromagnetische Sonnenstrahlung sowie die ausgehende Strahlung der Erde, welche sich aus der emittierten Infrarotstrahlung und dem reflektierten Sonnenlicht zusammensetzt, werden an der Satellitenoberfläche absorbiert oder reflektiert. Die daraus resultiernden Kräfte pro Flächeneinheit werden als Strahlungsdruck von Sonne bzw. Erde bezeichnet. Zusätzlich verursacht die Abstrahlung der absorbierten Strahlung am Satellit die sogenannte thermische Rückstrahlungkraft.

In den letzten Jahren hat sich die Modellierung der aerodynamischen Kräfte erheblich weiterentwickelt. Allerdings erschienen bisher nur wenige Veröffentlichungen zur Verbesserung der Kräftemodelle des Strahlungsdrucks. Die Modellierung des Strahlungsdrucks hängt sowohl von den gemessenen Strahlungsflüssen als auch von Masse, Oberfläche und Material des Satelliten ab, wobei insbesondere die Strahlungsflüsse und die Materialeigenschaften bekanntermaßen zu Fehlern führen.

Das Ziel dieser Arbeit ist die Erweiterung der Strahlungsdruckmodelle. Zunächst werden systematische Effekte in den analytischen Gleichungen aufgedeckt und beseitigt. In einem zweiten Schritt wird das erweiterte Kräftemodell in einem inversen Schätzungsansatz angewandt, um übrige Inkonsistenzen zu verbessern.

Nach der Untersuchung existierender analytischer Strahlungsdruckmodelle werden verschiedene Erweiterungen vorgeschlagen. Dazu gehören die Berücksichtigung zeitlicher Variationen der Sonnenstrahlung und ihres Spektrums sowie der Effekt der Atmosphäre auf die Ausbreitung dieser Strahlung. Darüber hinaus führt die Verwendung von Albedo- und Emissionsdaten zu Fehlern, die heutzutage durch die Verfügbarkeit von beobachteten Strahlungsflüssen an der Obergrenze der Atmosphäre und die Berücksichtigung der Winkelabhängigkeit der Erdstrahlung vermieden werden können. Außerdem wird die zeitverzögerte Emission der absorbierten Strahlung am Satelliten oftmals vernachlässigt, wohingegen sie hier berücksichtigt wird.

Die erweiterten Strahlungsdruckmodelle werden an Satelliten mit einfacher Geometrie getestet: an einem der Gravity Recovery And Climate Experiment (GRACE) Satelliten bestehend aus flachen Paneelen sowie an kugelförmigen Satellite Laser Ranging (SLR) Satelliten. Die Erweiterungen der Vorwärtsmodellierung des Strahlungsdrucks werden validiert, indem (1) die modellierten Kräfte mit GRACE Akzelerometermessungen verglichen werden sowie (2) ihre Auswirkungen auf den Satellitenorbit anhand von Residuen zu SLR-Beobachtungen bewertet weren (für GRACE und Kugelsatelliten). Um den Effekt der aerodynamischen Fehlmodellierung zu minimieren, wird das Jahr 2008 mit niedriger solarer Aktivität ausgewählt. Die Validierung zeigt, dass eine verfeinerte Diskretisierung (1°) des Footprints der Erde zu den größten Verbesserungen bei der Modellierung des Erdstrahlungsdrucks führt, d.h. für GRACE verringern sich die SLR-Residuen um 38 %. Die Wahl von stündlichen Strahlungsdaten mit Modellen für die Winkelabhängigkeit reduziert die Residuen um weitere 2 %. Außerdem verringert die Berücksichtigung der angepassten thermischen Rückstrahlung für GRACE die SLR-Residuen um 36 % im Vergleich zur Verwendung einer sofortigen Abstrahlung. Die Auswirkungen der erweitereten Kräftemodelle auf Kugelsatelliten ist generell geringer, was insbesondere auf die größere Bahnhöhe von mehr als 700 km zurückzuführen ist.

Die erweiterten nicht-gravitativen Kräftemodelle können in einem inversen Ansatz angewandt werden, wobei die Anpassung an gemessene Kräfte eine Schätzung ausgewählter Parameter im Modell ermöglicht, um verbleibenden Inkonsistenzen zu verbessern. In dieser Arbeit wird gezeigt, dass die Erweiterungen des Strahlungsdruckmodells die Bestimmung der Neutraldichte der Thermosphäre um bis zu 5 % je nach Sonnenaktivität beeinflussen und ihre Nichtbeachtung in vorherigen

Studien möglicherweise zu den Unterschieden zwischen existierenden Schätzungen beitragen. In einem weiteren Beispiel werden erste Versuche zur Schätzung von strahlungsbezogenen Parametern basierend auf den erweiterten nicht-gravitativen Kräftemodellen ausgeführt. Dabei limitiert die Qualität der kalibrierten Akzelerometerbeobachtungen zur Zeit noch die inverse Schätzung aus GRACE-Beobachtungen und die Suche einer stabilen Parametrisierung bleibt eine Herausforderung. Die Schätzung von Skalierungsfaktoren für den Strahlungsdruck aus SLR-Daten zeigt, dass Ajisai ein vielversprechender Kandidat für weitere Forschungen zur Bestimmung strahlungsbezogener Parameter darstellt. Insgesamt sind die Ergebnisse ermutigend, zukünftig physikalische Strahlungsdruckparameter aus Satellitenakzelerometrie und SLR-Beobachtungen zu bestimmen, um die Schätzung einer geodätischen Energiebilanz der Erde voranzubringen.

## Ein Gedicht über die Dichte

Es war einmal eine Mission,
die sollte sich für die Erdschweremessung besonders lohnen.
Die Mission hieß GRACE -
ihr Nachfolger ist schon in Space.
GRACE bestand aus zwei Satelliten. Und die flogen
um die Erde
durch die Thermosphäre
als ob nichts wäre...

Fast nichts.
Denn da war noch Reibung
wenig wäre eine Übertreibung
und doch war es genug,
um die Satelliten zu bremsen in ihrem Flug.

Für die Vorhersage der Position
wird sich eine präzise Dichte lohnen.
Die Erforschung der neutralen Dichte
ist also ganz schön wichtig.

Die Neutraldichte ist nicht konstant, sie verändert sich
mit Sonnenzyklus, Jahrzeiten, und Tageslicht,
und kommt es zu 'nem Sonnensturm,
führt die Interaktion
des Lichts mit dem Magnetfeld
zu Polarlichtern an den Polen der Welt.

Würde die Dichte gleich bleiben,
könnte sich der Satellite immer identisch an der Atmosphäre reiben,
doch dann würd ich kein Gedicht über die Bestimmung der Neutraldichte schreiben.

Durch diese sich verändernden Reibungen
entsteht eine Kraft,
die es schafft,
den Satelliten zu entschleunigen.

Diese Beschleunigung wird am Satelliten gemessen,
doch unterdessen
stören andere Kräfte
die Messprozesse.

Ihr wisst - die Neutraldichte (und somit die Reibung) verändert sich
hinzukommen Strahlungsdruck durch Sonnenlicht,
und der Strahlungsdruck der Erde,
hat alles nichts zu tun mit der Schwere.
Denn das sind die nicht-gravitativen Kräfte,
also schreibt in eure Hefte:
Akzelerometer messen nicht-gravitative Kräfte.

Akzelerometer -
was ist das denn jetzt schon wieder?

Das ist ein kleiner Käfig,
im Massenzentrum - versteht sich -
mit einer Testmasse, die dort schwebt,
und in ihrer Position gehalten wird
durch einen Elektromagnet.
Mit jeder Kraft, die hierauf wirkt,
ändert sich die Stärke des Magnets
und stets
wird sie verwandelt
in Beschleunigungen, die wir hier behandeln.

Also die Messung haben wir jetzt schon:
das ist die Beschleunigung an jeder Position.
Brauchen wir noch ein Modell
und dann geht die Bestimmung der Dichte ganz schnell.
Doch die Modelle sind kompliziert
ich hab sie jetzt schon einige Zeit studiert
und arbeite daran sie zu verbessern,
damit wir eine bessere Schätzung haben als gestern.

Kommen wir also zu den Modellen.
Gehen wir aus von elektromagnetischen Wellen.
Diese können den Satellit erhellen,
und ruck zuck
entsteht durch die Interaktion mit der Oberfläche ein Druck.

Direkt wirkt der Strahlungsdruck der Sonne
und bevor ich bald zum Ende komme,
gibt's noch den Strahlungsdruck der Erde.
den ich euch jetzt erkläre.

Das Sonnenlicht wird
an der Erdoberfläche reflektiert
und man glaub es fast nicht,
dass diese Strahlung den Satelliten tifft!

Jetzt kommt's drauf an:
wird das Licht,
das den Satelliten trifft,
reflektiert
oder absorbiert?
Das wird anhand des Materials studiert.
Ist es glatt wie ein Spiegel
oder matt wie ein Ziegel?
Ich hoffe, ihr seid noch nicht verwirrt,
denn davon hängt es ab, wie der Satellit beschleunigt wird.

Doch es gibt auch Epochen,
da wird die sichtbare Strahlung nicht gebrochen.
Denn da fliegt der Satellit
im Dunkeln, wo folgendes geschieht:
Also was passiert hier?
Nur die Infrarotstrahlung der Erde erreicht ihr Ziel.

Die Strahlung von Sonne und Erd'
sorgt auch dafür, dass der Satellit sich erwärmt.
Seine veränderliche Temperatur
sorgt für eine Abstrahlung in Abhängigkeit der Struktur
und der Geometrie
doch alle Details kennst du nie.

Und so modellieren wir die Strahlungsdruckbeschleunigungen,
und nicht zu vergessen die durch Reibungen.
Damit haben wir jetzt Messungen und Modelle,
die man gleichsetzt und dann,
mit ein bisschen umgestelle,
nach der Dichte auflösen kann.
Mit einer *resolution*
von 10 Sekunden
können wir nun Phänomene der Thermosphäre erkunden.

Das war die Geschichte
über die Bestimmung der Dichte.
Mit einer Mission,
die sollte sich lohnen:
nicht nur für die Bestimmung der Schwere,
sondern auch für die Erforschung der Atmosphäre.
Und so flog GRACE,
durch den Space
und wenn sie nicht verglüht sind,
dann schweben sie noch heute.

Kristin Vielberg, September 2022.
Gewinnerbeitrag beim Space Science Slam der ersten nationalen Wissenschaftskonferenz der Raumfahrt 2022 in Bonn. Deutschlandfunk berichtet: `https://www.deutschlandfunk.de/sternzeit-100.html?drsearch:date=2022-12-04`

# Acknowledgments

I started working on this thesis almost six years ago with the aim of learning how to do research. Coming to the end of this instructive and intense process, I am honestly proud of my journey and I acknowledge that writing a thesis is not possible without the continuous and great support from a lot of people. I am very grateful to all of them.

First of all, I would like to thank my supervisor Prof. Dr.-Ing. Jürgen Kusche. I find myself very lucky for the opportunity to work on my thesis within the group of Astronomical, Mathematical and Physical Geodesy (APMG). The subject has fascinated me since my Bachelor studies and I am grateful to have learned a lot about space geodesy. While working on this thesis, I had the chance to deepen my knowledge also in neighbouring topics, visit various conferences and follow my scientific interests, which I appreciate very much. Thanks a lot for always being open for new ideas, for the interesting discussions that motivated me a lot, and for supporting me all along the way.

I would like to thank my referees Dr.-Ing. Susanne Glaser and Prof. Dr.-Ing. Torsten Mayer-Gürr. It has always been a pleasure to meet you at various conferences. Your expertise, kindness and the interesting discussions have inspired me a lot.

I am also grateful for the funding that has allowed me to spend my time on different scientific projects and to work with many national and international people. My first PhD project was the TIK project "Entwicklung eines operationellen Prototyps zur Bestimmung der thermosphärischen Dichte auf Basis eines Thermosphären-Ionosphären Kopplungsmodells" funded by Deutsches Zentrum für Luft- und Raumfahrt (DLR). Within this project, I am thankful for the chance to collaborate with colleagues from Deutsches Geodätisches Forschungsinstitut (DGFI-TUM) in Munich, and from Weltraumlagezentrum in Uedem. This project was the follow-up project of the D-SAT project "Bestimmung von thermosphärischen Dichteparametern mit Hilfe von Akzelerometermessungen an Bord verschiedener Satellitenmissionen sowie mit Hilfe von GPS-bestimmten Satellitenorbits", where I gained first scientific experiences as a student assistant. Afterwards, I had the chance to work on the EEI-geodetic project "Direct Measurement of Earth's Energy Imbalance with Geodetic Satellites – Feasibility Study" funded by the German Research Foundation (DFG). In addition, I am grateful for the opportunity to be part of the TOLEOS project "Thermosphere Observations from Low-Earth Orbiting Satellites" funded by the European Space Agency (ESA), where I enjoyed working with international experts involved in the thermospheric neutral density estimation. Special thanks to Christian Siemes for the great collaboration, for sharing the calibrated accelerations, and for the fruitful discussions not only within TOLEOS, but also within the Joint Working Group 2 "Improvement of thermosphere models" within the GGOS Focus Area "Geodetic Space Weather Research", where I had the opportunity to be Vice Chair between 2019 and 2023. Many thanks also to SPP 1788 for the chance to attend interesting colloquia and summer schools and to meet many international scientists. Without all this funding, it would not have been possible to make the most of my time as a PhD student.

Furthermore, I am grateful for the pleasant working environment in the APMG group and the kind collaboration with the GESS and TG groups. I am very lucky working with all of my past and present colleagues, learning from you and having a good time at work and in between. Special thanks goes to my colleagues Anno, Armin, Bernd, Christina and Kerstin for proof-reading parts of this thesis and for your valuable suggestions. Thanks to Anno for guiding me patiently through GROOPS. Sophie and Hana, thanks for being such nice office mates. I am also grateful to Ehsan for introducing me to the world of scientific research.

Finishing this work would not have been possible without the support of many people outside the science community. Thanks to Stephan Rothes for the strong support. I have learned a lot.

I am very lucky to be greatly supported by my family and friends, who believed in me all along the way. It is a pleasure to have each of you in my life. Special thanks to my mum Bärbel Hagedorn for your patience, kindness and for always standing behind me no matter what, and to my dad Richard Vielberg for your motivating support and for inspiring me early with building satellites from building bricks together. Last but not least, I am very grateful for having my partner Bernd

in my life. Thank you for your love and support, for your patience and for always believing in me.

# Contents

**1 Introduction** **1**
1.1 The importance of non-gravitational force modelling . . . 1
1.2 Forward modelling . . . 3
1.3 Inverse modelling . . . 5
1.4 Research objectives . . . 8
1.5 Thesis outline . . . 10

**2 Physical background** **13**
2.1 Satellite dynamics . . . 13
2.2 The thermosphere and thermospheric neutral density . . . 15
2.2.1 Vertical structure of the atmosphere . . . 15
2.2.2 Variation of the thermospheric neutral density . . . 15
2.2.3 Overview of thermospheric neutral density models . . . 17
2.3 Earth's radiation budget . . . 18
2.3.1 Concept of radiation . . . 18
2.3.2 Radiation of the Sun . . . 19
2.3.3 Outgoing radiation of the Earth . . . 21
2.3.4 Earth's energy imbalance . . . 23

**3 Satellite observations** **29**
3.1 The GRACE(-FO) mission . . . 29
3.1.1 Mission overview . . . 29
3.1.2 Measurement principle and instruments . . . 29
3.1.3 Data . . . 30
3.1.4 Macro-model . . . 32
3.1.5 Space-borne accelerometry . . . 33
3.1.5.1 Measurement principle . . . 33
3.1.5.2 Challenges . . . 34
3.1.5.3 Accelerometer calibration . . . 36
3.2 Satellite laser ranging (SLR) . . . 39
3.2.1 Measurement principle . . . 39
3.2.2 Overview of SLR missions . . . 40

**4 Non-gravitational satellite force modelling** **41**
4.1 Aerodynamics . . . 41
4.1.1 Aerodynamic coefficient . . . 42
4.1.2 Relative Velocity . . . 44
4.2 Radiation pressure . . . 44
4.2.1 Solar radiation pressure . . . 45
4.2.2 Earth radiation pressure . . . 57
4.2.3 Lunar radiation pressure . . . 66
4.2.4 Thermal re-radiation pressure . . . 67
4.3 Satellite-induced forces . . . 71

4.3.1 Temperature sensitivity . . . 71
4.3.2 Twanks . . . 71
4.3.3 Magnetic torquers . . . 71
4.3.4 Thruster firings . . . 71
4.3.5 Antenna thrust . . . 72
4.3.6 Electromagnetics . . . 72
4.4 Definition of standard and extended models . . . 73
4.4.1 Standard model . . . 74
4.4.2 Extended model according to Vielberg and Kusche (2020) . . . 74
4.4.3 Extended model as used in thesis . . . 75

**5 Results of forward non-gravitational force modelling 77**
5.1 Results for the satellite mission GRACE . . . 77
5.1.1 SRP . . . 80
5.1.2 ERP . . . 82
5.1.3 TRP . . . 84
5.1.4 Validation using accelerometer data . . . 87
5.1.5 Validation using SLR data . . . 93
5.2 Results for spherical SLR satellites . . . 99
5.2.1 Challenges for spherical satellites . . . 100
5.2.2 SRP . . . 101
5.2.3 ERP . . . 101
5.2.4 Validation with POD . . . 102

**6 Inverse estimation: Thermospheric neutral density 107**
6.1 Inverse estimation based on accelerometer data . . . 107
6.1.1 Parametrization . . . 108
6.1.2 Algorithm . . . 109
6.1.3 Results . . . 113
6.2 Inverse estimation based on POD . . . 120
6.2.1 Parametrization . . . 120
6.2.2 Algorithm . . . 121
6.2.3 Comparability to accelerometer-based results in terms of scale factors . . . 122
6.2.4 Comparison of scale factors . . . 122

**7 Inverse estimation: Earth's energy imbalance 125**
7.1 Inverse estimation based on accelerometer data . . . 125
7.1.1 Parametrization . . . 126
7.1.2 Algorithm . . . 127
7.1.3 Results . . . 128
7.2 Inverse estimation based on SLR data . . . 132
7.2.1 Parametrization . . . 132
7.2.2 Algorithm . . . 133
7.2.3 Results . . . 133
7.3 Comparability of the results from GRACE and SLR . . . 136

**8 Conclusion 137**
8.1 Conclusions . . . 137
8.2 Recommendations . . . 140

**A Coordinate transformation: ECEF to CRF 143**

**B Simulation of star camera data 145**

**C Derivatives of analytical radiation pressure equations 147**

**List of Figures** **149**

**List of Tables** **151**

**Bibliography** **153**

# Chapter 1

# Introduction

Nowadays, thousands of satellites orbit the Earth and accurate information of their motion is required for operational and scientific applications. The orbit of a satellite is not only affected by gravitational forces, but also by non-gravitational ones. Whereas gravitational forces acting on a satellite result from the gravitational attraction of Earth, Sun, Moon and other celestial objects, the non-gravitational forces result from the interaction of photons and gas molecules with the satellite's surface. For low-Earth Orbit (LEO) satellites, the largest non-gravitational force is attributed to the atmospheric drag directed opposite to the satellite's velocity. With increasing altitude, the drag acceleration decreases (Fig. 1.1) due to the less dense atmosphere. Besides the atmospheric drag, the most important non-gravitational forces acting on a satellite are related to the radiation of the Sun and the Earth. The electromagnetic solar radiation reaches the surface of the satellite directly, where the photons are either reflected or absorbed, which causes the Solar Radiation Pressure (SRP) acceleration. Similarly, the Earth Radiation Pressure (ERP) acceleration results from the Earth's outgoing radiations reaching the satellite consisting of the emitted thermal radiation and the reflected sunlight. With increasing distance from the Earth's surface, the acceleration due to ERP becomes less relevant, whereas the effect of SRP becomes prevalent (Fig. 1.1). In addition, the radiation of Sun and Earth, which is absorbed at the satellite's surface, heats up the satellite and leads to temperature variations. The emission of this thermal energy causes the Thermal Re-radiation Pressure (TRP) acceleration.

The magnitude of theses non-gravitational accelerations is rather small, however large enough to cause orbit perturbations. For one of the Gravity Recovery And Climate Experiment (GRACE) satellites, the average acceleration is about $3.0 \times 10^{-8}\,\mathrm{ms}^{-2}$ for SRP, $1.2 \times 10^{-8}\,\mathrm{ms}^{-2}$ for ERP, and $0.7 \times 10^{-8}\,\mathrm{ms}^{-2}$ for TRP during April 2011. In comparison, the average acceleration due to aerodynamics during the same month is largest with $1.1 \times 10^{-7}\,\mathrm{ms}^{-2}$.

## 1.1 The importance of non-gravitational force modelling

Accurate models of these forces are required for a variety of satellite-related applications, e.g., within the Precise Orbit Determination (POD) of Global Navigation Satellite System (GNSS) satellites (Fliegel et al., 1992; Arnold et al., 2015; Steigenberger et al., 2015; Darugna et al., 2018; Bury et al., 2019), Satellite Laser Ranging (SLR) satellites (Sośnica et al., 2014; Panzetta et al., 2018), and several Earth observation satellites such as Swarm (Montenbruck et al., 2018b), radar altimetry and radar imaging satellites (Zelensky et al., 2010; Peter et al., 2017; Hackel et al., 2017; Rudenko et al., 2023). Not only POD, but also orbit predictions to assess the mission lifetime including reentry in the Earth's atmosphere benefit from precise non-gravitational force models. As an example, during increased solar activity, which leads to a denser atmosphere, the Gravity Recovery And Climate Experiment Follow On (GRACE-FO) mission decayed up to 20 m daily (Landerer et al., 2022), while the lifetime of the GRACE mission exceeded the planned five years by additional ten years due to an unexpectedly low solar activity within solar cycle 24.

In addition, non-gravitational forces need to be separated from gravitational measurements within gravity field recovery. Therefore, several LEO gravity field missions, e.g., GRACE (Tap-

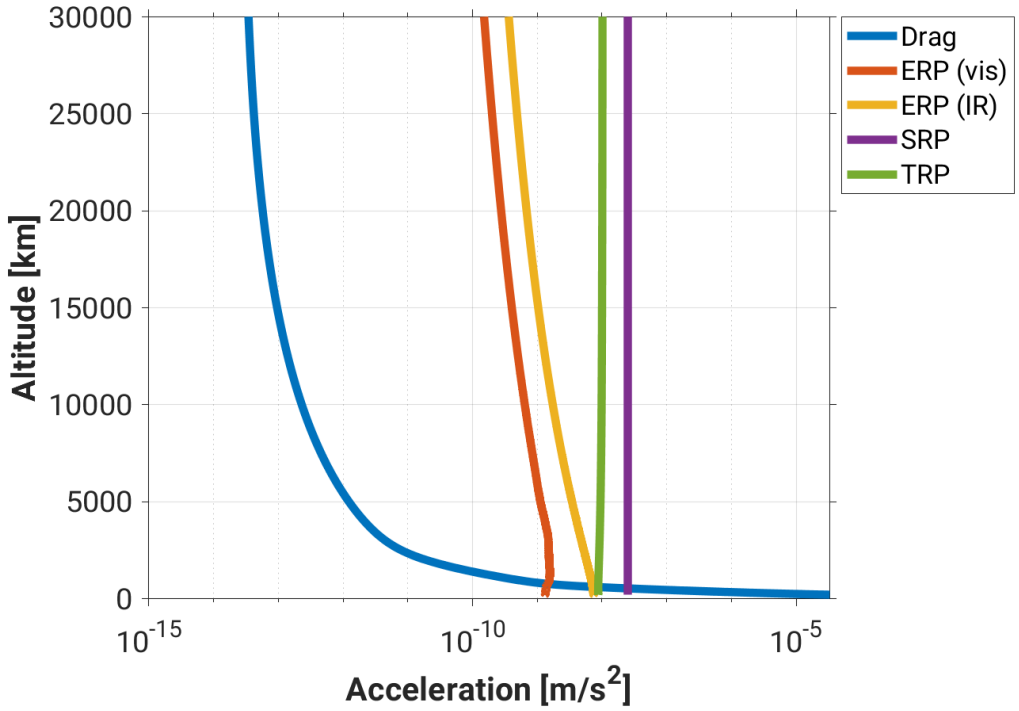



Figure 1.1: Variation of modelled non-gravitational accelerations with altitude. The computations are based on the position and orientation of the GRACE-A satellite on April 1, 2011, at midnight: -92° longitude, -52° latitude, 490 km altitude. Then, the individual forces were computed for simulated positions above and below before calculating the norm.

ley et al., 2004), CHAllenging Minisatellite Payload (CHAMP) (Reigber et al., 2002), or Gravity Field and Steady-State Ocean Circulation Explorer (GOCE) (Floberghagen et al., 2011), carry space-borne accelerometers, which measure the sum of the non-gravitational accelerations (and not the individual components). However, in case accelerometer data are missing as at the end of the GRACE mission or are of insufficient quality as for the Swarm mission (Siemes et al., 2016; Lück, 2022), accurate force models are required to simulate the total non-gravitational accelerations for further processing. The accelerometer measurements onboard GRACE-D, which is the trailing satellite of the GRACE-FO mission launched in May 2018, showed a higher noise level than expected, and thus, a transplant of accelerometer data from the leading satellite GRACE-C is required (McCullough et al., 2019). Using modelled non-gravitational accelerations in the transplant has led to an improvement of the so-called Accelerometer Transplant L1B (ACT1B) product (Bandikova et al., 2019; Behzadpour et al., 2021). Furthermore, the ongoing development of space-borne accelerometers in combination with novel cold atom interferometer (e.g., Christophe et al., 2018; Abrykosov et al., 2019; Siemes et al., 2022) will likely lead to lower noise levels of measured non-gravitational accelerations in the near future, which necessitates also the improvement of non-gravitational force models.

Accurate non-gravitational force models are also required to derive the thermospheric neutral density and wind velocity from measured accelerometer data (Sutton et al., 2007; Doornbos et al., 2010; Doornbos, 2012; March, 2020). This application requires the separation of drag and radiation pressure accelerations, where a good along-track modelling of the radiation pressure component is required for density estimates especially during low solar activity when the drag signal is relatively small and an error of 5% in the modelled radiation pressure leads to an error of 5% in the density estimate. The wind estimation also benefits from accurately modelled cross-track radiation pressure accelerations.

Another topic, where non-gravitational force models are essential, is the POD of radar altime-

try missions, which are designed to monitor sea level (Chelton et al., 2001). Systematics in the estimated orbit directly impact the measured sea surface height. Since non-gravitational forces are required in the POD, the demand for precise non-gravitational force models increased with the launch of the first radar altimetry mission Topex/Poseidon in 1992 to reach the desired (and still not reached) orbit accuracy of 1 cm. In this context, high fidelity satellite models to represent the satellite's complex shape have been tested in the non-gravitational force modelling, however, the computational effort required approximations. Furthermore, first models of the thermal re-radiation pressure have been developed and validated using surface temperature measurements (Antreasian and Rosborough, 1992; Marshall et al., 1992). These efforts contributed to an accuracy of 2 cm for 10-day orbit arcs (Chelton et al., 2001). The Jason missions continued the successful radar altimetry measurements with launches of three satellites between 2001 and 2016, of which Jason-3 reached an orbit accuracy of 1.5 cm (Picot et al., 2018). Additionally, several Sentinel satellites guaranteed continuity of sea level measurements. The recent mission is Sentinel-6A launched in 2020. Reaching the desired orbit accuracy of 1 cm for current Jason and Sentinel missions is still ongoing research (Peter et al., 2017; Montenbruck et al., 2018a; Hauschild et al., 2022; Rudenko et al., 2023). Improvements in different measurement techniques as well as in the non-gravitational force modelling will aid reaching this goal in the future.

Furthermore, the non-gravitational force modelling of SLR satellites is important for POD including validations of GNSS orbits. Measurements to spherical SLR satellites are currently used to realize the geocentre origin of the global Terrestrial Reference Frame (TRF) (Meindl et al., 2013; Glaser et al., 2015; Glaser et al., 2020). The simple shape together with a large area-to-mass ratio of SLR satellites such as LAser GEOynamics Satellite or Laser Geometric Environmental Observation Survey (LAGEOS) is beneficial to reduce the impact and complexity of the non-gravitational forces compared to GNSS satellites. The improvement of precise solar radiation pressure force models for GNSS satellites is expected to reduce biases in the geocentre estimation from GNSS only (Glaser et al., 2020).

Improved force models might also be used to further studies on the Earth's energy imbalance. First results in this direction had been achieved by Boudon (1986) from the evaluation of the CACTUS accelerometer on-board the nearly spherical CASTOR satellite during the 1970s. In their study, an annual mean Earth radiation budget for the period July 1975 to July 1976 had been successfully obtained from the conversion of accelerations to fluxes. This procedure was resumed by Hakuba et al. (2018), who proposed a future satellite mission with improved accelerometry on-board a highly reflective or perfectly absorbing spherical satellite to complement recent estimates of Earth's energy imbalance.

## 1.2 Forward modelling

Non-gravitational force modelling is the main topic of this thesis. In a forward model, non-gravitational forces can be simulated analytically for satellites with available geometry and surface-material data. In case a macro-model containing these information is not available, such as for GNSS satellites, analytical models cannot be applied and instead empirical models are used in the radiation pressure force modelling (Montenbruck et al., 2015; Montenbruck et al., 2017; Arnold et al., 2015). However, analytical force modelling will become more relevant for Galileo satellites, since optical properties have been published recently (Bury et al., 2019). In the following, the current status of the drag and radiation pressure force models is presented with a focus on analytical radiation pressure force modelling with aspects from Vielberg and Kusche (2020).

Aerodynamic accelerations can be separated into the drag acceleration with lift and side effects. Aerodynamic models require information about the atmosphere including its composition, temperature and winds at the position of the satellite, which is commonly obtained from empirical density models. Then, the interaction of the gas molecules with the satellite's surface is accounted for in the aerodynamic coefficient, which improved a lot during the last decade (e.g., Pilinski et al., 2010; March et al., 2019b; Bernstein and Pilinski, 2022) and is still an active area of research. From free molecule flow theory (Sentman, 1961), the mean path of the molecules w.r.t. the satellite dimen-

sions can be derived. In this context, more collisions are assumed to occur between the molecules and the satellite's surface than between the incident molecules themselves. Below 400 km the assumption of diffuse molecule reflections seems valid, however, at higher altitudes, the reflection is more specular and models in this regard are still under development. Aerodynamic models have been widely studied in the context of thermospheric neutral density and wind estimation (e.g., Sutton et al., 2005; Doornbos, 2012; March, 2020).

In contrast, only few and mostly early studies on SRP (e.g., Marshall et al., 1992; Montenbruck and Gill, 2012) and even less on ERP accelerations are available (e.g., Knocke et al., 1988; Montenbruck and Gill, 2012). The interaction of incoming fluxes with the satellite's surface commonly considers specular and diffuse reflection as well as absorption using the satellite's thermo-optical material properties. This is still a reasonable assumption, however, anisotropic reflection and thermal re-radition are often omitted. Additionally, in the flux modelling of Sun and Earth, there is a lot of room for improvement and consistency. The magnitude of SRP in terms of the solar flux is about $1360\,\mathrm{W/m^2}$ at an altitude of 400 km, whereas the Earth's outgoing flux is about $340\,\mathrm{W/m^2}$ (Wild et al., 2013), to which the longwave flux contributes about twice as much as the shortwave flux. All fluxes vary with the constellation of Sun, Earth and satellite, including the satellite's altitude above the Earth's surface. The solar flux mainly depends on the solar cycle and the solar rotation with periods of about 11 years and 27 days, respectively. The Earth's outgoing fluxes correspond to the incoming solar flux and thus depend on the solar cycle as well as on the diurnal cycle.

Analytical SRP force models are based on the visible solar flux at the position of the satellite, which is commonly approximated by the solar constant and is not able to capture temporal variations. Moreover, the solar spectrum is not considered appropriately, since the flux and its interaction with the satellite's surface material are frequency-dependent. Within the Earth's shadow, only the Earth's infrared radiation reaches the satellite. The Earth's shadow is often modelled geometrically with a spherical Earth (Montenbruck and Gill, 2012), but omitting the Earth's flattening and the impact of the atmosphere on the ray of sunlight causes errors in semi-shadowed regions (Robertson, 2015).

In comparison to SRP, analytical ERP force models are based on modelled albedo and emission data (Knocke et al., 1988). Errors introduced by this approximation can be avoided nowadays due to the availability of observed fluxes at the top of atmosphere, which are already used in recent ERP models (e.g., Wöske et al., 2019) and within the consideration of angular dependence of Earth's radiation (Vielberg and Kusche, 2020). The observed fluxes of Earth's outgoing radiation are provided by the Clouds and the Earth's Radiant Energy System (CERES) project. The CERES instrument consists of a radiometer sensor measuring the radiation at the top of atmosphere, commonly assumed to 20 km, at three spectral channels in slant direction (Wielicki et al., 1996). In the CERES data processing, measured radiation is converted to radiative flux by applying empirical Angular Distribution Models (ADMs) (Su et al., 2015a; Su et al., 2015b). To obtain hourly sampling, which is currently the highest temporal resolution available, the CERES synoptic 1° (CERES SYN1deg) hourly product combines measurements from CERES instruments on-board the Terra and Aqua spacecrafts with hourly optical data from geostationary satellites (Doelling et al., 2016). In comparison with the monthly available Energy Balanced And Filled (EBAF) data, the CERES SYN1deg products are not constrained to a prescribed land, atmosphere and ocean heat content rate (Loeb et al., 2018). Thus, the CERES SYN1deg data contain biases, which are expected to introduce systematic errors in the ERP modelling. On the other hand, EBAF data rely on a given heat content rate that may not reflect current reality sufficiently.

Furthermore, the satellite's thermo-optical material properties and their variation over time due the exposure to ultraviolet radiation from the Sun and atomic oxygen erosion (Silverman, 1995b) are not well known and introduce additional modelling errors. Recently, first high fidelity models have been developed for different satellites and allow for the consideration of more complex shapes, e.g., antennas, in the non-gravitational force modelling (Ziebart, 2004; Kenneally, 2016; March et al., 2019a; Wöske et al., 2019). The advantage of these complex models is that they allow for including shadowing effects and thermal re-radiation in more detail, however, the computational

effort can be very large and additional information on the thermo-optical material properties is not included, so their uncertainty remains problematic.

In addition to the aerodynamics and radiation pressure forces, several satellite-induced non-gravitational forces are known to act on a satellite (Flury et al., 2008; Peterseim et al., 2012). Thruster firings or antenna thrusts introduce additional non-gravitational accelerations. Their consideration is of importance to obtain realistic force models. Additionally, the measurements can be disturbed by internal temperature variations or mechanical oscillations of a thin foil on-board the bottom of the GRACE satellite (Flury et al., 2008). The order of magnitude of these artificial satellite-induced forces can be quite large as they can occur in terms of spikes, however, their period is relatively small in the order of seconds.

## 1.3 Inverse modelling

Early analytical radiation pressure force models have been developed to improve the orbit determination of SLR satellites (Rubincam and Weiss, 1986). Since the thermo-optical material properties of these spherical satellites represent the largest uncertainty in analytical force modelling for SLR satellites, a radiation pressure coefficient, i.e., a scaling factor of the radiation pressure, is commonly estimated within a POD (Bloßfeld et al., 2018; Panzetta et al., 2018; Hattori and Otsubo, 2019; Zeitler et al., 2021). This leads to the second topic of this thesis, which focuses on the inverse modelling in the context of non-gravitational forces.

As outlined above, there is a need for precise non-gravitational force models. There are several aspects that can lead to improved forward modelling of these forces. Nevertheless, the possibilities to overcome all inconsistencies is limited, e.g., due to incomplete information about the satellite's thermo-optical material properties. This is where inverse models are expected to be helpful. Inverse models allow for the estimation of specific parameters in the model by adjusting the force model to observations. The relation between observed and modelled non-gravitational accelerations has already been used for different applications such as the calibration of accelerometer data (e.g., Klinger and Mayer-Gürr, 2016; Vielberg et al., 2018), which is not only required for gravity field recovery, but also for the estimation of the thermospheric neutral density (e.g., Sutton et al., 2007; Doornbos et al., 2010; Siemes et al., 2023). Within a POD, e.g., based on SLR measurements, scale factors for the thermospheric neutral density have been estimated together with measurement biases (e.g., Zeitler et al., 2021). Thus, choosing a careful parametrization of potential systematic errors in the forward model may lead to updated force models, which could not only aid in improving POD, gravity and thermosphere recovery, but also provide clues on systematic errors in radiation data products used in the radiation pressure force modelling.

The inverse estimation is based on the relation between the observed $\boldsymbol{a}_{\text{obs}}$ and modelled non-gravitational accelerations including aerodynamics $\boldsymbol{a}_{\text{aero}}$, radiation pressure $\boldsymbol{a}_{\text{RP}}$ and satellite-induced $\boldsymbol{a}_{\text{sat}}$ effects under consideration of an error $\epsilon$

$$\boldsymbol{a}_{\text{obs}} = \boldsymbol{a}_{\text{aero}} + \boldsymbol{a}_{\text{RP}} + \boldsymbol{a}_{\text{sat}} + \epsilon. \tag{1.3.1}$$

The most obvious observed non-gravitational accelerations are accelerometer measurements, which are available for several dedicated gravity field missions at altitudes around or below 500 km. On the other hand, such observations can be obtained from observed satellite dynamics after removing the gravitational signal. Suitable precise tracking-techniques are GNSS, SLR, and Doppler Orbitography and Radio-positioning Integrated by Satellite (DORIS). In addition, Two-Line Element (TLE) files contain information about an object's average motion from radar observations.

The right hand-side of Eq. (1.3.1), i.e., modelled non-gravitational accelerations, can be obtained analytically for satellites with available macro-models. These are commonly accessible for the gravity field missions such as GRACE, and for spherical SLR satellites. To allow for realistic results in the inverse estimation, the forward model needs to be as precise and consistent as possible beforehand.

Then, a careful parametrization of systematic errors of both measurements and models is required, i.e., rank-deficiencies in the parametrization need to be avoided, before performing the

inverse estimation in a least squares sense. Therefore, I provide an overview on possible systematics before presenting possibilities of how to perform an inverse estimation aiming to improve such parameters.

Beginning with the accelerometer measurements, a calibration is required before further use. Calibration parameters are usually biases and scale factors for each axis, e.g., on a daily basis, which are neither error-free nor uncorrelated with respect to each other, which then introduces further errors in the calibrated observations. Using other observation types such as range measurements between SLR stations and the satellite, the measured range is corrected by applying estimated range biases and other related parameters such as station coordinates.

Within the aerodynamic model, information about the atmosphere at the satellite's position is required including the mass and amount of individual gases, which sum up to the thermospheric neutral density. This density, which varies on time scales between seconds to several years, is usually taken from models, since in-situ data are not only sparse but also not available after the mid 1980s (e.g. Sarris et al., 2020). Consequently, the model development also lacks current measurements. An overview of the thermospheric neutral density from selected empirical and physical models in

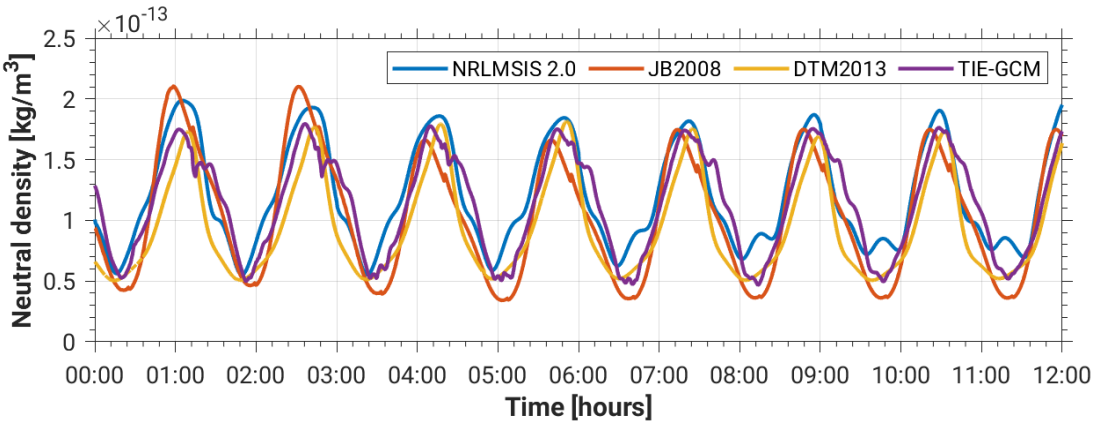



Figure 1.2: Thermospheric neutral density from three empirical models (Naval Research Laboratory Mass Spectrometer Incoherent Scatter radar version 2.0 (NRLMSIS 2.0), Jacchia-Bowman 2008 (JB2008), Drag Temperature Model (DTM)2013 and one physical model (Thermosphere–ionosphere–electrodynamics general circulation model (TIE-GCM)) evaluated along the orbit of the GRACE-A satellite on June 1, 2008.

Fig. 1.2 shows that there are significant differences between the models. Density variations are directly reflected in the aerodynamic acceleration, whereas temperature and wind data that can also be obtained from these models and horizontal wind models, respectively, have a minor impact. In addition, models are not able to predict the fast response of the thermosphere to geomagnetic storms. Thus, obtaining in-situ densities from an inverse approach is not only essential for improving the non-gravitational force model, but also for extending the data base used to improve existing empirical models (Forootan et al., 2022), or to assimilate these observations into physical models to achieve a higher temporal resolution in the future (Corbin and Kusche, 2022). An extended data base of in-situ thermospheric neutral densities would also benefit climate studies of atmospheric processes such as the cooling of the upper atmosphere due to the anthropogenic increase of $C0_2$ (e.g., Roble and Dickinson, 1989; Laštovička et al., 2012; Sarris et al., 2020). There exist already several studies on obtaining the thermospheric neutral density from accelerometer measurements (e.g., Sutton et al., 2007; Doornbos et al., 2010; Vielberg et al., 2018; Krauss et al., 2020; Siemes et al., 2023) and density estimates, e.g., in terms of scale factors, integrated over several orbital revolutions from observed orbit dynamics (e.g., Emmert et al., 2004; Picone et al., 2005; Doornbos et al., 2007; Doornbos et al., 2008; Panzetta et al., 2018; van den IJssel et al., 2020; Emmert et al., 2021; Zeitler et al., 2021). The thermospheric neutral density has been selected as an Essential Geodetic Variable by the Global Geodetic Observing System (GGOS) in 2018.

Additionally, several groups are working towards improved gas-surface interaction models (Moe and Moe, 2005; Sutton, 2009; Doornbos, 2012; Pilinski et al., 2010; Walker et al., 2014; March et al., 2017; Mehta and Linares, 2018; Bernstein and Pilinski, 2022). As it is still difficult to model the gas interaction with the satellite's material depending on the orbital height, estimating an altitude-dependent accommodation coefficient in an inverse approach seems reasonable.

Within the radiation pressure modelling, systematic errors in the thermo-optical material properties, which are provided by the manufacturers in the macro-model and are assumed to be incorrect (personal correspondence with Srinivas Bettadpur, 10/2021), have a direct impact on the modelled forces. Furthermore, the material properties change during the mission lifetime due to the exposure to ultraviolet radiation (e.g., Silverman, 1995a), resulting in a systematic time dependency.

Furthermore, the fluxes incident on the satellite's surface are required. Especially the Earth's outgoing longwave and shortwave fluxes, which are ideally taken from CERES SYN data with a temporal resolution of one hour, are known to have systematic errors. These errors also impact the estimate of the Earth's Energy Imbalance (EEI), which is basically the difference between the Earth's incoming and outgoing radiation and known to be out of balance due to anthropogenic emissions leading to global warming (von Schuckmann et al., 2023). The consequent imbalance is recently estimated to be $0.76 \pm 0.2\,\mathrm{W/m^2}$ for the period 2006 to 2020 and is known to accelerate (von Schuckmann et al., 2023). This value is in good agreement with the imbalance from CERES EBAF data for the period 2005 to 2015 of $0.71 \pm 0.1\,\mathrm{W/m^2}$, whereas the imbalance obtained from the CERES SYN1deg product amounts to $4.3\,\mathrm{W/m^2}$ (Loeb et al., 2018). The imbalance from EBAF provides the better estimate from CERES products since the data are constrained to (ocean) heat content estimates. Due to the importance of quantifying global warming, there is the necessity for independent estimates of EEI. To underline this importance, the Earth's radiation budget has been assigned as one of the Essential Climate Variables by the Global Climate Observation System. Therefore, parametrizing errors in the radiation data within an inverse model would not only benefit the improvement of radiation pressure force models but may also lead to an attempt to design a geodetic EEI. However, within such estimation it is expected that these errors are hardly separable from the systematics in the material properties.

To conclude from the challenges and expected systematics in the forward modelling and in the observations, the parametrization of an inverse model should ideally consider the following aspects:

- measurement correction: bias and scale factor in case of accelerometer measurements; range biases and station coordinates in case of SLR measurements
- aerodynamic correction: thermospheric neutral density, cross-wind speed, accommodation coefficient
- radiation pressure correction: Earth's outgoing longwave and shortwave fluxes, solar flux
- macro-model correction: thermo-optical material properties, geometry

Fig. 1.3 presents an overview of the possibilities to estimate these parameters in a least squares estimation. For that purpose, precisely modelled non-gravitational accelerations are fitted to accelerometer measurements. Solving for the parameters listed above within a joint estimation is theoretically possible and would combine the measurement calibration with the correction of modelled non-gravitational forces. However, this one-step procedure, which is certainly innovative, would require very extensive numerical testing, e.g., due to rank defects, and a consideration of carefully selected constraints. Additionally, the interpretation of the resulting estimates is expected to be complicated due to high correlations between the parameters (Vielberg and Kusche, 2020).

To simplify the joint estimation, one could think of applying an elimination of parameters. For example, the thermospheric neutral density from accelerometer data has a resolution of 10 s and the changes during one orbit of high solar activity are about one order of magnitude larger than during low solar activity. During storm times, the density can rapidly increase at short time scales (minutes). In comparison, the Earth's outgoing radiation is not sensitive to such solar events, so there is no need to solve for corrections of radiation data sets at short time scales. In addition, the

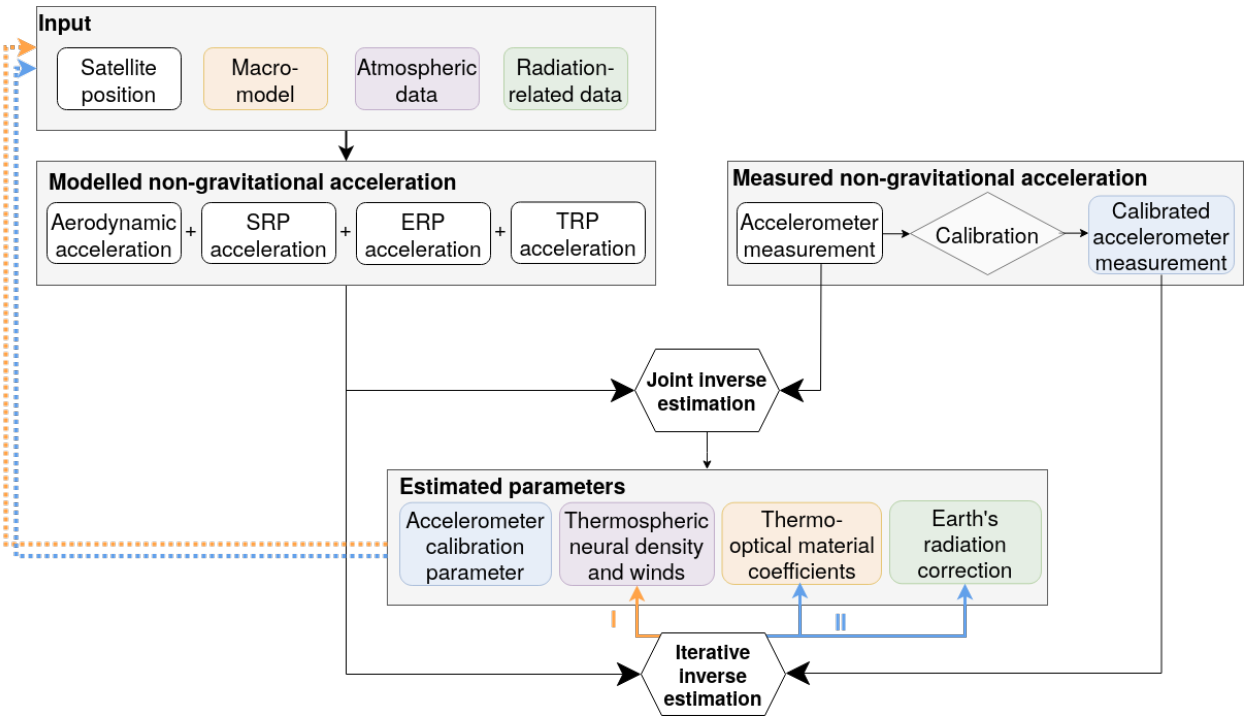



Figure 1.3: Flow chart of inverse estimations. Related parameters are marked in similar colours. Cases I and II are the selected examples of the iterative inverse estimation.

satellite experiences the radiation of a whole footprint, i.e., local changes are not resolvable. Thus, focussing on global or alternatively latitude-dependent corrections instead seems more reasonable, which would require a good global coverage. For GRACE, a suitable global coverage as it is used in the context of gravity field recovery (Kvas et al., 2019a) is reached after 30 days. Nevertheless, this procedure is expected to be challenging and would still require extensive numerical testing and constraints.

Thus, performing an estimation of selected parameters in an iterative stepwise procedure seems more appropriate as illustrated at the bottom of Fig. 1.3. In this case, calibration parameters for the measured accelerations are estimated first. Then, solving for selected parameters in an inverse estimation is possible. Here, the thermospheric neutral density and cross-wind speeds are selected as the first example, since this procedure has already turned out to be very successful (Doornbos et al., 2010; Siemes et al., 2023). As a second example, the estimation of radiation-related parameters is selected, since the quality of thermo-optical properties as well as systematics in the radiation data limits the accuracy of the radiation pressure force modelling. First attempts of this approach have been performed in Vielberg and Kusche (2020), however, it turned out that finding a suitable parametrization is still challenging and further effort is needed to obtain a stable parametrization.

The results from these inverse estimations can be used again to improve the force modelling. This iteration might be repeated until convergence. Nevertheless, updating the inverse model with a new density estimate requires the separation of the individual gases in the aerodynamic model, which would require additional assumptions. Since such assumptions would introduce another uncertainty, this suggested iterative procure is limited, however, it is worth to pave the way into that direction.

## 1.4 Research objectives

From the sections above, the following research questions can be formulated:

- How can we improve non-gravitational force models compared to existing standard approaches?

- How can we overcome inconsistencies between currently available concepts and measurements, and the parametrization of existing forward radiation pressure force models?
- What is the impact of improved radiation pressure force models for the thermospheric neutral density estimation?
- Is it possible to estimate remaining systematics of the forward force modelling in an inverse model?
- What can we learn about EEI from using improved radiation pressure force models in an inverse estimation?

Based on these questions, this thesis aims at extending radiation pressure force models to allow for the improvement of the thermospheric neutral density and existing radiation data sets. Consequently, the first part of this thesis focusses on the improvement of the forward modelling of radiation pressure forces and the second part concentrates on the inverse modelling. To guide through these goals, I formulate the following objectives.

**1. Detect and overcome inconsistencies in analytical radiation pressure force models**
Aerodynamic and radiation pressure forces amount to the non-gravitational forces acting on a satellite, of which the aerodynamic force models have been well investigated during the past years, whereas only few studies focussed on SRP (Marshall et al., 1992; Montenbruck and Gill, 2012), ERP (Knocke et al., 1988; Marshall et al., 1992), and TRP (Antreasian and Rosborough, 1992; Marshall et al., 1992; Wöske et al., 2019) modelling. Thus, the focus of this thesis is on the improvement of analytical radiation pressure force models. This requires at first a detailed understanding of existing solar, Earth, and thermal re-radiation pressure models. In this context, inconsistencies will be detected and suggestions for improvements and extensions will be made. The focus will be on a GRACE-like satellite, i.e., a LEO satellite with flat surfaces, but many of the suggestions can also be applied to other LEO, altimetry or GNSS satellites.

**2. Formulation of an extended radiation pressure force model**
Based on the findings from the first objective, an extended radiation pressure force model will be formulated. This model is expected to yield the most realistic results as it includes the suggested extensions. In Vielberg and Kusche, 2020, a suggestion for an extended radiation pressure force model has already been made. This suggestion will be updated here, if necessary.

**3. Validation of the extended radiation pressure force model**
The force model extensions from the second objective need to be validated carefully. However, validating radiation pressure force models is known to be challenging, since direct measurements are not available. Therefore, first the impact of the extensions on the modelled radiation pressure will be outlined for GRACE. Second, the radiation pressure extensions will be compared to GRACE accelerometer data, where the accelerometer calibration as well as the aerodynamic model will be kept fixed. To keep the errors of the aerodynamic model to a minimum, a period with low solar activity will be selected. In order to validate the modelled radiation pressure accelerations with independent data, the force model extensions will be applied within a POD. A comparison of the estimated positions to SLR measurements is expected to reveal the benefit of the extended model. To test the adaptation of the force model extensions also for satellites with different shapes, the extended radiation pressure force models will also be applied on selected spherical satellites and validated within a POD using SLR measurements as input.

**4. Assess the impact of extending the radiation pressure force model on the estimation of the thermospheric neutral density**
A common application, where radiation pressure force models are required, is the estimation the of thermospheric neutral density. The thermospheric neutral density estimation is selected as a first example for an inverse estimation. Such density can be derived from measured accelerometer data at a high temporal resolution, e.g., 10 s. Besides accurate aerodynamic models, which are not

considered for improvements in this thesis, radiation pressure force models are required. An error in the radiation pressure force modelling maps linearly into the accelerometer-derived thermospheric neutral density. The impact of applying the extended radiation pressure force model in the density estimation will be discussed mainly by comparing the thermospheric neutral density estimates to results from other institutions with different force modelling. Besides accelerometer-derived densities, orbit-integrated corrections for the thermospheric neutral density can be obtained within POD in terms of scale factors. This method, where no accelerometer data are required, will be applied for GRACE as well as for selected spherical satellites at low altitudes.

**5. Attempting to solve for radiation-related parameters based on the extended radiation pressure force model**
Corrections for existing data sets of the Earth's outgoing radiation would be beneficial for quantifying EEI. Radiation data sets are required in the forward modelling of the ERP and it is tempting to ask, whether an inverse estimation allows to estimate corrections for existing radiation data. Hakuba et al. (2018) proposed to monitor EEI from accelerometer measurements on-board a highly reflective or perfectly absorbing spherical satellite by relating the radial acceleration to the flux. In Vielberg and Kusche (2020) first attempts to correct radiation data within an inverse approach have been published. In this thesis, the research in this direction is intensified. Besides applying updated radiation pressure force models and finding a stable parametrization, the suitability of the accelerometer calibration for such inverse estimations will be discussed. Furthermore, radiation pressure scale factors will be estimated within a POD for selected spherical satellites and their interpretation as a correction for radiation data sets will be assessed. These findings are expected to pave the way to a geodetic EEI estimate.

## 1.5 Thesis outline

The workflow of this thesis is summarized in Fig. 1.4. On the left hand side, the measured and modelled non-gravitational accelerations are presented for GRACE. These modelled accelerations will be compared to each other and they are required for the inverse estimations. On the right hand side, the ideal force modelling for spherical SLR satellites is shown. For both GRACE and SLR, a validation of the modelled non-gravitational acceleration will be conducted by estimating a dynamic orbit and evaluating the residuals to SLR range measurements.

Based on this workflow, the structure of this thesis is as follows. In Ch. 2, the physical background on satellite dynamics, thermospheric neutral density, as well as the concept of EEI are introduced. Then, Ch. 3 presents the observations used in this thesis. First, the focus is on the twin-satellite mission GRACE. After providing an overview of the mission itself and relevant data products, the principle and challenges of accelerometer measurements are outlined and calibration methods are explained. Then, the measurement principle of SLR is presented before providing an overview of the selected missions relevant for this thesis.

The analytical non-gravitational force models for satellites with given geometry and material properties is outlined in detail in Ch. 4. After presenting the aerodynamic model, the focus is on the radiation pressure force modelling. Here, the state-of-the-art models are introduced, inconsistencies are discussed and extensions for the models are suggested. Additionally, satellite-induced forces are described briefly since they contribute to the non-gravitational forces as well. Ch. 4 concludes with suggested definitions of standard and extended non-gravitational force models.

The results of the forward non-gravitational force modelling are presented in Ch. 5. This includes the visualization and discussion of the impact of suggested model extensions on the radiation pressure accelerations. Here, the focus is on the GRACE-A satellite during the year 2008, where the aerodynamic signal was exceptionally low. Even though GRACE-FO provide more recent data, GRACE-FO is not evaluated in this thesis since GRACE already covers more than a full solar cycle and the accelerometer data quality of GRACE-FO is not as good as expected (McCullough et al., 2019). Even though the validation of the radiation pressure force model is challenging, two approaches are presented. (1) a comparison of modelled non-gravitational accelerations against ac-

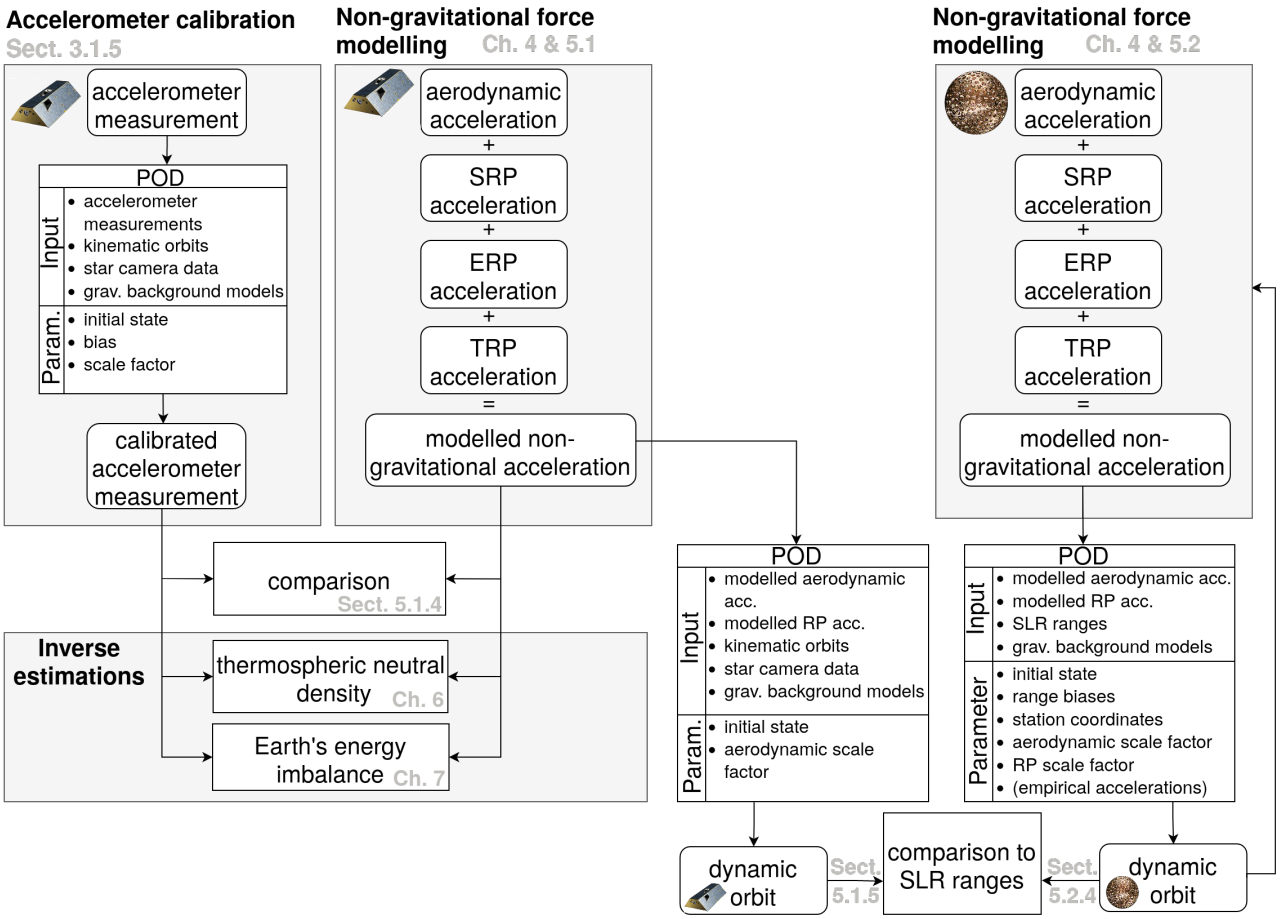



Figure 1.4: Workflow of this thesis.

celerometer measurements is shown, and (2) a validation with independent SLR data is performed. In addition to GRACE, the non-gravitational force modelling is discussed for spherical satellites. The results are shown for selected missions and a validation is performed based on a POD as well.

In the remaining chapters, the inverse modelling is addressed. The determination of the thermospheric neutral density is selected as a first example for an inverse estimation using precise non-gravitational force models. Ch. 6 outlines the parametrization and algorithm of the inverse approach using GRACE accelerometer measurements. The resulting thermospheric neutral density is compared to the results from other groups. Additionally, a POD is performed for GRACE and SLR satellites, which allows for the estimation of corrections in terms of daily scale factors for a model density. The comparability to accelerometer-derived thermospheric neutral density is discussed and comparisons are shown in terms of scale factors.

As a second example, an inverse estimation is performed with the aim to solve for radiation-related parameters in Ch. 7. In case of GRACE, the inverse estimation is based on non-gravitational force models and accelerometer measurements. The challenge of finding a suitable accelerometer calibration and a stable parametrization is discussed. In addition, a POD is performed with SLR measurements as input, where scale factors for the radiation pressure acceleration are estimated and their suitability as a correction for existing radiation data as well as its comparability to the first approach are discussed.

Finally, Ch. 8 summarizes the main findings from this thesis and discusses the achievement of the objectives. An outlook as well as suggestions for future missions are provided, which is expected to aid in further improving the radiation pressure force modelling.

# Chapter 2

# Physical background

This chapter provides an overview of the physics, which are relevant for this thesis. Since the force modelling of satellites is the main topic, the relation between the satellite's motion and the forces acting on it is outlined in Sect. 2.1. Background knowledge on the thermosphere as well as Earth's radiation budget are introduced in Sects. 2.2 and 2.3, respectively.

## 2.1 Satellite dynamics

The motion of a satellite is directly related to the forces acting on it. This can be expressed using Newton's second gravitational law: "When a body is acted upon by a force $\boldsymbol{f}$, the time rate of change of its momentum $\dot{\boldsymbol{p}}$ equals the force." In an inertial system, this can be formulated (Seeber, 2003) as

$$\dot{\boldsymbol{p}}(t) = \boldsymbol{f}(t, \boldsymbol{r}, \dot{\boldsymbol{r}}), \tag{2.1.1}$$

where the force depends not only on time $t$, but also on the position $\boldsymbol{r}$ and velocity $\dot{\boldsymbol{r}}$ of the body (here: the satellite). The momentum at time $t$ acting on the body with mass $m$ is defined as

$$\boldsymbol{p}(t) = m(t)\dot{\boldsymbol{r}}(t). \tag{2.1.2}$$

Then, the time rate of change of the momentum inserted in Eq. (2.1.1) reads

$$m\ddot{\boldsymbol{r}}(t) + \dot{m}\dot{\boldsymbol{r}}(t) = \boldsymbol{f}(t, \boldsymbol{r}, \dot{\boldsymbol{r}}). \tag{2.1.3}$$

The mass change is usually assumed to be negligible even though the spacecraft looses a very small amount of fuel. Considering this assumption yields the equation of motion

$$m\ddot{\boldsymbol{r}}(t) = \boldsymbol{f}(t, \boldsymbol{r}, \dot{\boldsymbol{r}}). \tag{2.1.4}$$

With the definition $\boldsymbol{a} := \frac{1}{m}\boldsymbol{f}$, where $\boldsymbol{a}$ is the force related to the unit mass, the differential equation simplifies to

$$\ddot{\boldsymbol{r}}(t) = \boldsymbol{a}(t, \boldsymbol{r}, \dot{\boldsymbol{r}}). \tag{2.1.5}$$

In the following, the contributions to the force $\boldsymbol{f}$ will be outlined (Seeber, 2003; Hofmann-Wellenhof and Moritz, 2006; Montenbruck and Gill, 2012). The dominating force acting on a satellite orbiting the Earth is the Earth's gravitational attraction. Beginning with Newton's law of universal gravitation, the Earth and the satellite can be assumed as two point masses $m_1$ and $m_2$ attracting each other with a force

$$\boldsymbol{f}_{12} = Gm_1m_2\frac{\boldsymbol{r}_2 - \boldsymbol{r}_1}{|\boldsymbol{r}_2 - \boldsymbol{r}_1|^3}. \tag{2.1.6}$$

This force acts along the connecting line of the Earth and the satellite, which are located at positions $\boldsymbol{r}_1$ and $\boldsymbol{r}_2$, respectively. The gravitational constant $G$ has the value $6.6742{\times}10^{-11}\,\mathrm{m^3\,kg^{-1}\,s^{-2}}$. Since the satellite's mass is only a fraction of the Earth's mass, the attraction of the Earth w.r.t.

the satellite is negligible. Consequently, one can define the Earth as the attracting mass (with mass $M$), while the satellite is the attracted mass. Additionally introducing the distance $l$ between the two objects, the force $\boldsymbol{f}_{12}$ simplifies to the gravitational field strength

$$\boldsymbol{g} = GM\frac{\boldsymbol{r}_2 - \boldsymbol{r}_1}{l^3}. \tag{2.1.7}$$

With the Earth as a point mass, the force is radially symmetric and the satellite orbits the Earth on a fixed plane. The satellite's position then follows Kepler's laws and the satellite moves on a Kepler ellipse with the Earth in its focal point. However, in reality the Earth's gravitational field is much more complex than a point mass due to its irregular shape and mass distribution leading to orbit perturbations. The gravitational potential can be written as the volume integral of the individual contributions of the mass elements $\mathrm{d}m = \rho \mathrm{d}v$ at distance $l$

$$V = G\iiint_v \frac{\mathrm{d}m}{l} = G\iiint_v \frac{\rho}{l}\mathrm{d}v. \tag{2.1.8}$$

With this definition, the gravitational field strength is commonly expressed as the gradient of the gravitational potential

$$\boldsymbol{g} = \nabla V. \tag{2.1.9}$$

This relation is valid since the gravitational field is a conservative field. Then, the gravitational potential at an arbitrary point in the Earth's exterior with the spherical coordinates $\lambda, \theta, r$ is a solution of Laplace's equation and can be expressed as a series of spherical harmonic functions

$$V(\lambda,\theta,r) = \frac{GM}{R}\sum_{n=0}^{\inf}\sum_{m=0}^{n}\left(\frac{R}{r}\right)^{n+1}\left[c_{nm}C_{nm}(\lambda,\theta) + s_{nm}S_{nm}(\lambda,\theta)\right]. \tag{2.1.10}$$

Here, $\lambda$ is the geographical longitude, $\theta$ denotes the colatitude and $r$ is the distance to the origin of the Earth-fixed coordinate system. $R$ is the Earth's radius, $c_{nm}$ and $s_{nm}$ are the spherical harmonic coefficients, i.e., the weights of the spherical base functions, depending on degree $n$ and order $m$ of the expansion. The base functions are surface spherical harmonics

$$C_{nm}(\lambda,\theta) = \cos(m\lambda)P_{nm}(\cos\theta), \tag{2.1.11}$$

$$S_{nm}(\lambda,\theta) = \sin(m\lambda)P_{nm}(\cos\theta), \tag{2.1.12}$$

providing a complete orthogonal system on the surface of a sphere with Legendre Polynomials $P_{nm}(\cos\theta)$. The gravitational potential is commonly truncated at a certain degree depending on the desired resolution.

Besides the Earth's gravitational field strength, the orbit of the satellite is perturbed by a variety of other forces (Montenbruck and Gill, 2012). The gravitational attraction of other celestial bodies especially the Sun and the Moon induce a tidal potential. These so-called third body perturbations act on the Earth as well as on the satellite and are denoted as direct tides $\boldsymbol{a}_{\mathrm{T}}$. Additionally, indirect tides result from the gravitational attraction of third bodies leading to mass redistribution on land as well as in the oceans and the atmosphere. These effects are known as solid Earth tides $\boldsymbol{a}_{\mathrm{ST}}$, ocean tides $\boldsymbol{a}_{\mathrm{OT}}$ and atmospheric tides $\boldsymbol{a}_{\mathrm{AT}}$. The latter are strictly speaking largely thermally driven and only to a small part is of gravitational origin.

Further tidal effects result from the polar motion, which is the motion of the rotational axis of the Earth w.r.t. a terrestrial reference frame. The resulting centrifugal force acts on the solid Earth and on the oceans leading to changes in the gravitational potential. These effects are known as solid Earth pole tides $\boldsymbol{a}_{\mathrm{SPT}}$ and ocean pole tides $\boldsymbol{a}_{\mathrm{OPT}}$. Additionally, non-tidal short term variations of atmosphere, ocean, hydrosphere and cryosphere $\boldsymbol{a}_{\mathrm{ntS}}$ are considered as well as long-term variations $\boldsymbol{a}_{\mathrm{ntL}}$ of the solid Earth due to glacial isostatic adjustment, and episodic accelerations $\boldsymbol{a}_{\mathrm{ntE}}$ caused by earthquakes.

Besides these gravitational effects, the satellite's orbit is perturbed by non-gravitational effects. For LEO satellites, the aerodynamic acceleration $\boldsymbol{a}_{\mathrm{aero}}$ is dominating, followed by the radiation

pressure of the Sun $\boldsymbol{a}_{\mathrm{SRP}}$ and the Earth $\boldsymbol{a}_{\mathrm{ERP}}$ as well as the satellite's thermal re-radiation pressure acceleration $\boldsymbol{a}_{\mathrm{TRP}}$. In addition, satellite-related forces $\boldsymbol{a}_{\mathrm{sat}}$ such as thruster firings perturb the orbit.

Considering the mentioned effects, the equation of motion of a satellite can be formulated with the contributions from gravitational $\boldsymbol{a}_{\mathrm{g}}$ and non-gravitational accelerations $\boldsymbol{a}_{\mathrm{ng}}$ as

$$\ddot{\boldsymbol{r}} = \boldsymbol{a}_{\mathrm{g}} + \boldsymbol{a}_{\mathrm{ng}} \tag{2.1.13}$$

$$= \boldsymbol{g} + \boldsymbol{a}_{\mathrm{T}} + \boldsymbol{a}_{\mathrm{ST}} + \boldsymbol{a}_{\mathrm{OT}} + \boldsymbol{a}_{\mathrm{AT}} + \boldsymbol{a}_{\mathrm{SPT}} + \boldsymbol{a}_{\mathrm{OPT}} + \boldsymbol{a}_{\mathrm{ntS}} + \boldsymbol{a}_{\mathrm{ntL}} + \boldsymbol{a}_{\mathrm{ntE}} + \boldsymbol{a}_{\mathrm{aero}} + \boldsymbol{a}_{\mathrm{SRP}} + \boldsymbol{a}_{\mathrm{ERP}} + \boldsymbol{a}_{\mathrm{TRP}} + \boldsymbol{a}_{\mathrm{sat}} + \epsilon, \tag{2.1.14}$$

where $\epsilon$ denotes remaining modelling errors. This equation provides the basis for POD also in this thesis as well as for gravity field estimation (e.g., Mayer-Gürr, 2006; Löcher, 2011; Lück, 2022).

## 2.2 The thermosphere and thermospheric neutral density

This section provides a brief introduction to the atmospheric structure with a focus on the thermosphere before introducing the thermospheric neutral density, its variability and models to obtain the thermospheric density empirically and physically.

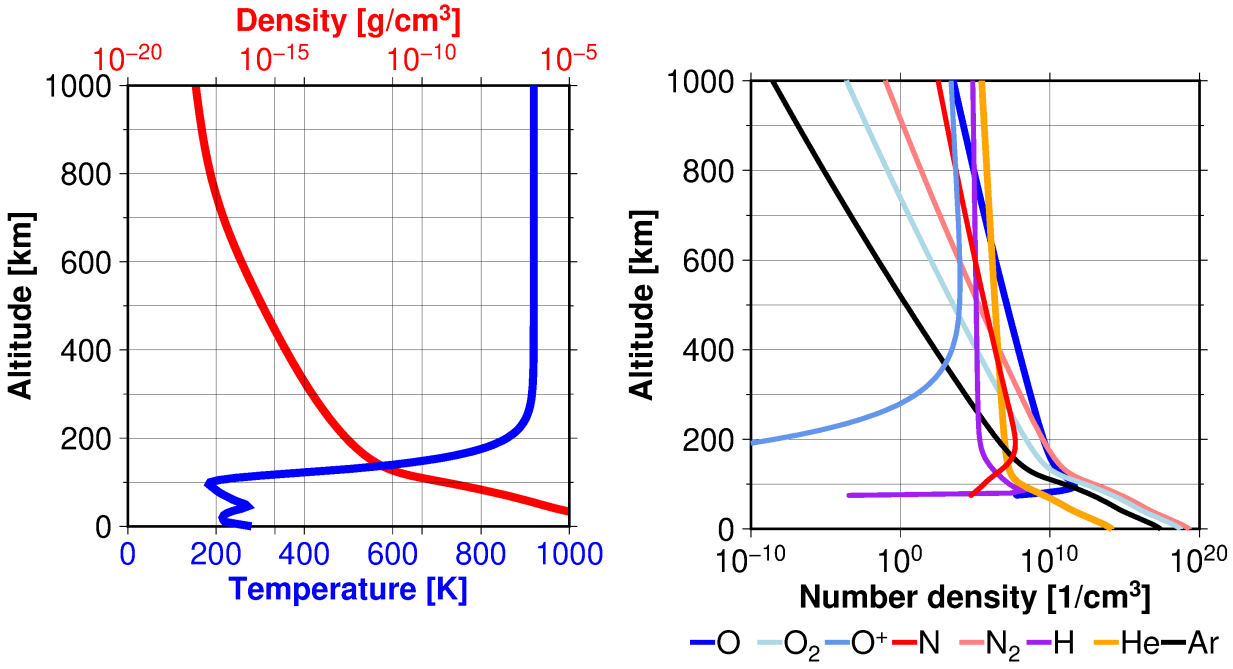
### 2.2.1 Vertical structure of the atmosphere

The Earth's atmosphere is a gas hull surrounding our planet (Prölss, 2012). Vertically, it can be divided into different layers based on its temperature. The temperature profile is presented exemplarily at the location of Bonn on April 1, 2017, at 1:50 a.m. in blue in Fig. 2.1a. Local temperature minima and maxima bound the four layers: troposphere (0-10 km), stratosphere (10-50 km), mesosphere (50-100 km), thermosphere (>100 km). The layer of interest for this thesis is the thermosphere, where LEO satellite missions orbit the Earth and experience the drag acceleration due to the collision of the gas molecules with the satellites surface leading to orbital decay. The thermosphere begins at around 100 km, where the temperature in the Earth's atmosphere reaches its minimum due to radiative cooling. Above 100 km, the temperature increases nearly asymptotically. The upper limit of the thermosphere is not clearly defined. The temperature is inversely proportional to the atmospheric composition shown in Fig. 2.1b. Below 100 km, the composition is well mixed (homosphere), whereas above 100 km (heterosphere) heavier gases dominate within the next 100 km and lighter gases are found above. This separation is due to molecular diffusion and gravity (Emmert, 2015). The dominating gases within the thermosphere at LEO altitudes between 200-600 km are atomic oxygen (O), dinitrogen (N2) and helium (HE). Summing up the mass of the neutral gases within a predefined volume results in the neutral mass density, also known as thermospheric (neutral) density, neutral density, or mass density. The thermospheric density profile (Fig. 2.1a, red) differs from the temperature profile as it decreases nearly exponentially with increasing altitude.

### 2.2.2 Variation of the thermospheric neutral density

The thermospheric neutral density varies not only with altitude, but also on different temporal scales between seconds and several years (e.g., Doornbos, 2012; Emmert, 2015). Depending on the positions of the Earth and the Sun, the thermospheric neutral density underlies diurnal and seasonal periodicities. The ultraviolet radiation of the Sun heats up the atmosphere, which causes not only changes in temperature and neutral density, but also ionizes the atmosphere. The ionized part of the atmosphere is known as ionosphere and is immersed in the upper atmosphere interacting with the neutral part of the atmosphere (Prölss, 2012). The thermospheric neutral density is strongest on the day side and reaches its maximum at daytime following the sub-solar point with a delay of approximately two hours. Besides the seasonal variations due to the varying Earth-Sun distance, the inclined Earth orbiting the Sun causes latitude-dependent density changes.

Thermospheric neural density variations depend not only on the geometry, but also on the solar activity. The extreme ultraviolet band of the Sun's radiation varies with the solar cycle reaching a



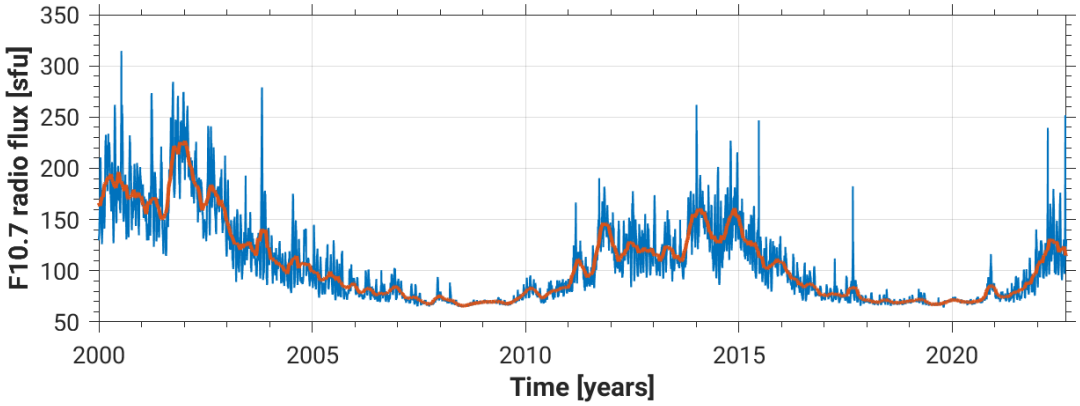

(a) Temperature and neutral density profiles

(b) Atmospheric composition

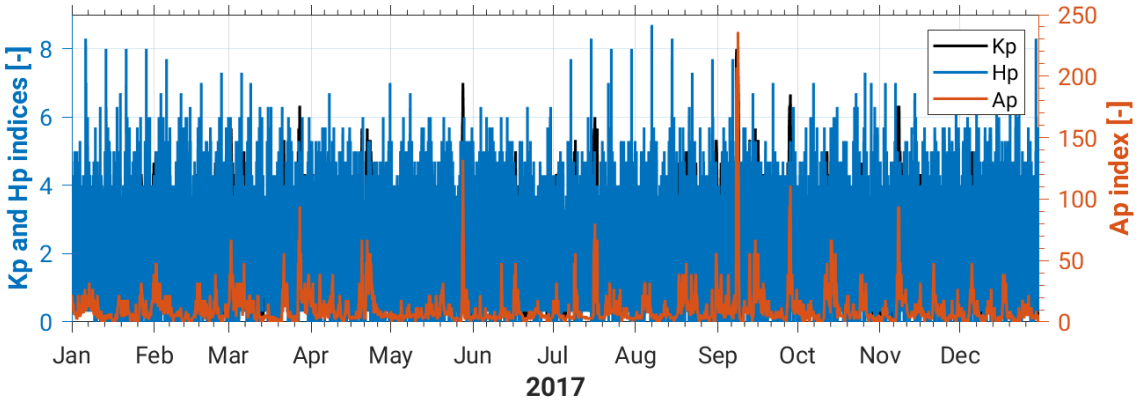
Figure 2.1: Vertical profiles of (a) temperature and thermospheric neutral density, and (b) atmospheric composition from the Naval Research Laboratory Mass Spectrometer Incoherent Scatter radar (NRLMSISE-00) model in Bonn (50.73°N, 7.10°E) on April 1, 2017, at 1:50 a.m..

maximum approximately every 11 years, where regions of high solar activity called sunspots occur. During high solar activity the thermospheric neural density can be around ten times larger than during solar minimum. Moreover, the rotation of the Sun of about 27 days impacts the atmospheric composition and temperature. The $F_{10.7}$ index (Tapping, 2013), which is a measure of the extreme ultraviolet solar radiation at a wavelength of 10.7 cm, is commonly used to represent the solar activity within density models. Nowadays, the Canadian National Research Council provides $F_{10.7}$ values measured at their Dominion Radio Astrophysical Observatory in Penticton, Canada, which are available since 1947. The time series of the daily $F_{10.7}$ index and its 81-day average are shown from 2000 until September 2022 in Fig. 2.2a covering nearly two solar cycles. Relating specific spectral measurements to the solar activity is an ongoing challenge, hence, new indices underlie a recent development (e.g., Ermolli et al., 2013; Dudok de Wit et al., 2014).

In addition, the thermosphere changes on short time scales due to sudden magnetic storms directed towards the Earth, i.e., coronal mass ejections of the Sun or solar flares, which are found to influence the geomagnetic field conditions and cause irregularities in atmospheric temperatures and densities, as well as the ionization in the ionosphere. These changes are not at all periodic and are complicated to model. Therefore, the global geomagnetic variation can be described by proxies in empirical and physical models with $Kp$ and $Ap$ indices (Mayaud, 1980; Matzka et al., 2021a), which are shown in Fig. 2.2b. The planetary geomagnetic index $Kp$ has been developed by Bartels (1949) and is derived from the standardised $K$ index. It varies between 0 at low geomagnetic activity and 9 during extreme geomagnetic storms on a quasi-logarithmic scale and is measured by 13 observatories. The planetary amplitude index $Ap$ is the linearized $Kp$ index. Both indices are provided three-hourly by the National Geophysical Data Center. However, their resolution is relatively coarse for the detection of sudden changes. Therefore, the $Hp$ index has been developed recently, which is similar to the $Kp$ index, but with a temporal resolution of 90, 60 and 30 minutes (Stolle et al., 2019). Fig. 2.2a exemplarily shows the geomagnetic $Kp$ and $Ap$ indices with a temporal resolution of 3 hours and daily, respectively, as well as the new $Hp$ index with a resolution of 30 min during the year 2017.




(a) Time series of the $F_{10.7}$ index (blue) and its 81-day average (red) in solar flux units (1 sfu = $10^{-22}$ W/m$^2$/s). Data from `ftp://ftp.geolab.nrcan.gc.ca/data/solar_flux/daily_flux_values/fluxtable.txt`, last access September 6, 2022.




(b) Geomagnetic $Kp$ and $Ap$ indices (Matzka et al., 2021b) with a temporal resolution of 3 h and daily, respectively, as well as the $Hp$ index with a resolution of 30 min (Stolle et al., 2019) during the year 2017.

Figure 2.2: Time series of solar and geomagnetic indices.

### 2.2.3 Overview of thermospheric neutral density models

To obtain the thermospheric neutral density at arbitrary positions and times, empirical and physical models have been developed and improved since the availability of the first TLE-derived thermospheric neutral density observations in the 1960s (e.g., Emmert, 2015). Empirical models represent an average stage of the atmosphere, which is obtained from fitting mathematical equations to measurements. Most measurements are integrated quantities, since in-situ data are sparse. The need for in-situ atmospheric compositions has also led to a mission proposal for the European Space Agency (ESA) Earth Observation program's 10th Earth Explorer (Sarris et al., 2020). However, it has not been selected and measurements of the atmospheric composition are only available from the Atmosphere Explorer satellites in the 1970s. Based on these data together with integrated thermospheric neutral densities and selected indices, a variety of empirical models have been developed, of which the ones from the Mass Spectrometer Incoherent Scatter (MSIS), Jacchia and DTM series are most frequently used (e.g., Vallado and Finkleman, 2014; Emmert, 2015). The MSIS series beginning with Hedin et al. (1977) applies temperature data from incoherent scatter radar measurements, which benefit from the incoherent backscattering of free electrons. Additionally, the thermospheric neutral density derived from orbit data is used in the most recent versions NRLMSISE-00 (Picone et al., 2002) and NRLMSIS 2.0 (Emmert et al., 2020) together with atmospheric composition measurements from the Solar Maximum mission. As input $Ap$ and $F_{10.7}$ indices are required. The most recent Jacchia model JB2008 (Bowman et al., 2008) is fitted to 20 years of orbit-derived density data up to 1000 km altitude and requires also $Ap$ and $F_{10.7}$ indices in addition to the disturbance storm time index $Dst$. Thermospheric neutral density from accelerometry serve

for validation purposes only. Another series are the DTMs, of which the operational and research DTM2020 models are the latest (Bruinsma and Boniface, 2021). Both are based on accelerometer-derived thermospheric neutral density data from GOCE, CHAMP, GRACE, and Swarm-A, as well as daily TLE-derived densities since 1967. The input to the operational model are $Kp$ and $F_{10.7}$ indices, whereas the more accurate research model requires hourly $Hp$ and $F_{30}$ indices, where the latter is a measure of the extreme ultraviolet solar radiation at a wavelength of 30 cm.

On the other hand, physical models can simulate the thermospheric neutral density based on continuity, energy and momentum equations of the ionosphere-thermosphere system without measurement constraints (Emmert, 2015). These models are generally much more complex than empirical models, however, they are still a simplification of the real physics (Schunk et al., 2012). The output of physical models depends similar to the empirical models on the input parameters, which are basically solar and geomagnetic indices and in addition time-varying boundary conditions. There exist multiple general circulation models (e.g., TIE-GCM, Qian et al., 2014), of which the whole atmosphere models (e.g., Whole Atmosphere Community Climate Model With Thermosphere and Ionosphere Extension (WACCM-X 2.0), Liu et al., 2018) allow for predictions from the ground. The upper altitude depends on the current solar conditions varying for TIE-GCM around 600 km. The spatial resolution of TIE-GCM can be up to 2.5°. The thermospheric neutral density from physical and empirical models are currently at similar accuracy, however, the advantage of physical models is that they allow for better analyses of physical processes in the atmosphere (Emmert, 2015), whereas empirical models are generally used for orbit predictions due to their simplicity.

In addition to the density models, horizontal winds can be obtained from empirical wind models (e.g., Horizontal Wind Model 14 (HWM14), Drob et al., 2015). The wind velocities, which are usually below 200 m/s and thus relatively small compared to the satellite's velocity of about 7 km/s at LEO altitudes, can disturb the satellite's motion in the cross-track direction.

In this thesis, the empirical model NRLMSIS 2.0 will be applied in the forward modelling of the aerodynamic acceleration since the models from the NRLMSIS series are most widely used. Wind models will be neglected since their effect is relatively small (Sutton, 2008; Mehta et al., 2017).

## 2.3 Earth's radiation budget

The energy entering and leaving the Earth's system is not in balance due to anthropogenic climate change. This imbalance of the Earth's energy is the most important variable to quantify global warming (von Schuckmann et al., 2023). It can be obtained from the difference between the incoming solar radiation and the outgoing longwave and shortwave radiations at the Earth's Top Of Atmosphere (TOA). This section provides a brief introduction on this broad topic, beginning with the concept of radiation. Then, the radiation of Sun and Earth are introduced before presenting and discussing current measurements of Earth's energy imbalance.

### 2.3.1 Concept of radiation

Radiation is known as the propagation of energy through a medium in the form of electromagnetic waves or particles (Taylor, 2005; Petty, 2006; Wendisch and Yang, 2012). Fig. 2.3 illustrates this propagation for a radiating surface element $dA$ of a sphere with radius $r$ and solid angle $d\Omega$. The spherically radiated energy $E$ [J = Ws] is the same at distances $r_1$ and $r_2$ from the surface element. In contrast, the flux $F$ [W m$^{-2}$], which is the energy flow per unit area, follows the inverse square law

$$\frac{F_1}{F_2} = \left(\frac{r_2}{r_1}\right)^2 . \tag{2.3.1}$$

For example, when the flux $F_2$ at distance $r_2$ is twice as far from the source than $r_1$, it is four times smaller than the flux $F_1$ at distance $r_1$. The flux per solid angle $d\Omega$ is the intensity $I$, which is again independent from the distance. The intensity of an object's emitted radiation varies over the entire electromagnetic spectrum and depends on the object's temperature.

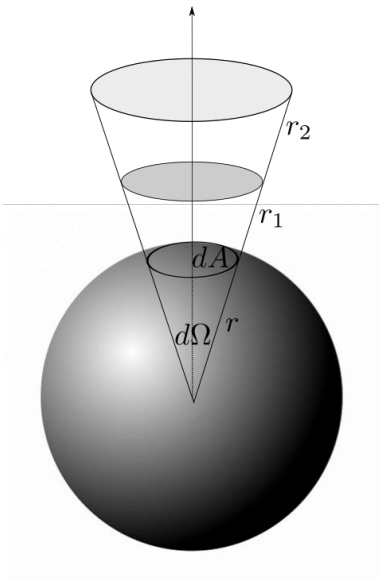



Figure 2.3: The surface element $dA$ spherically radiates energy at the surface angle $d\Omega$. At distance $r_2$, which is twice as far from $dA$ than $r_1$, the flux decreased four times according to the inverse square law.

The radiance of a surface area per unit wavelength is known as spectral radiance. For a black body, it can be computed according to Planck's radiation law, which is outlined in the following according to Wendisch and Yang (2012). A black body is a theoretical concept, which assumes an object in thermal equilibrium with a surface that absorbs the incoming radiation at all wavelengths. According to Kirchhoff's law (Kirchhoff, 1860), the absorbed radiation of a black body is completely emitted for each wavelength. Then, Planck's law (Planck, 1914) provides the spectral radiance $B$ as a function of the wavelength $\lambda$ and the object's surface temperature $T$

$$B(\lambda, T) = \frac{2hc^2}{\lambda^5} \frac{1}{e^{\frac{hc}{\lambda k T}} - 1}, \tag{2.3.2}$$

with Planck's constant $h = 6.62607015 \times 10^{-34}\,[\mathrm{J\,Hz^{-1}}]$, the Boltzmann constant $k = 1.380649 \times 10^{-23}\,[\mathrm{J\,K^{-1}}]$, and speed of light $c = 299792458\,[\mathrm{m\,s^{-1}}]$. Instead of writing Planck's law as a function of the wavelength, formulations in dependency of the frequency or wavenumber are common as well (Marr and Wilkin, 2012).

The integration of Planck's law over the whole spectrum and over $2\pi$ of a hemispheric solid angle results in the Stefan-Boltzmann law

$$S = \sigma T^4 \tag{2.3.3}$$

with the Stefan-Boltzmann constant $\sigma = 5.670374419 \cdot 10^{-8}\,\frac{\mathrm{J}}{\mathrm{m^2 K^4 s}}$. Planck's law describes the spectral radiance (or irradiance) $S$ emitted per time and area from an object with surface temperature $T$. Accordingly, every object with a temperature $T$ above 0 K radiates energy, thus, the Sun, Earth and even satellites radiate energy depending on temperature, material and geometry.

### 2.3.2 Radiation of the Sun

The electromagnetic radiation from the Sun transports energy and drives the Earth's climate system (Petty, 2006; Wendisch and Yang, 2012).

With an approximate surface temperature of the Sun of $T_S = 5778\,\mathrm{K}$, the emitted energy from the Sun's surface is $4{\cdot}10^{26}\,\mathrm{W/s}$. Applying Planck's law from Eq. (2.3.2) to compute the ideal solar spectrum received at the Earth under the assumption that the Sun is a black body with temperature $T_S$ results in the black body spectrum as shown by the black line in Fig. 2.4. Due to the Sun's high temperature, the irradiance peaks with $1.75\,\mathrm{W/m^2/nm}$ in the visible domain at around 520 nm.

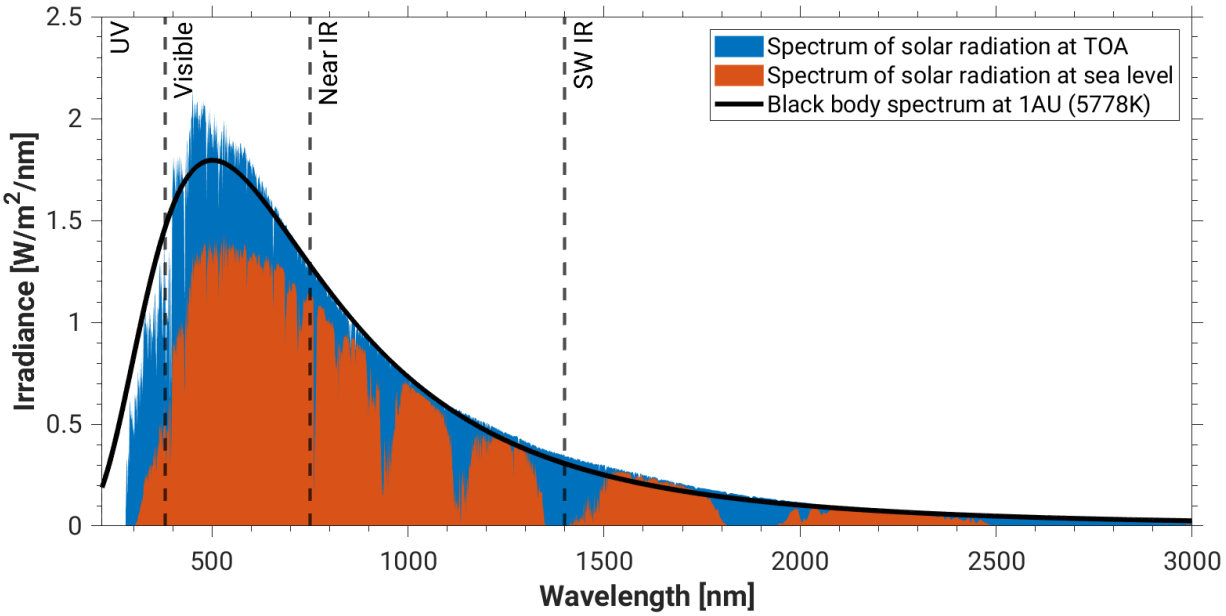



Figure 2.4: Spectral irradiance of the Sun at TOA and at sea level with data from National Renewable Energy Laboratory (`https://www.nrel.gov/grid/solar-resource/spectra-am1.5.html`, last access: November 17, 2021). Black body spectrum at the distance of 1 AU with the assumption of a solar surface temperature of 5778 K. Horizontal lines mark the regions of UltraViolet (UV), visible and InfraRed (IR) radiation.

Since the Sun is not a perfect black body in reality, the computed spectral irradiance is only an approximation of the actual one. Based on model data from the National Renewable Energy Laboratory, the solar spectral irradiance is also shown at Earth's TOA and at sea level in Fig. 2.4. At a first glance the solar irradiance at TOA matches the black body curve quite well especially in the IR domain. In the visible domain, the observed solar irradiance peaks already at around 450 nm with values of 2.1 $W/m^2/nm$. Due to the interaction of the solar radiation with atmospheric constituents, it is partly absorbed, reflected or scattered in the Earth's atmosphere, resulting in the solar irradiance at sea level differing from that at TOA.

Integrating the solar irradiance over the entire electromagnetic spectrum yields the Total Solar Irradiance (TSI). The average TSI at the mean distance of the Earth is known as solar constant, which has a value of 1360.8 $W/m^2$ according to Wild et al. (2013). The time series of the TSI at 1 AU since January 2000 is shown in Fig. 2.5. These daily TSI measurements from radiometers were obtained and combined from multiple missions, e.g., from the Total Irradiance Monitor (TIM) on-board SOlar Radiation and Climate Experiment (SORCE), and are available at `https://ceres.larc.nasa.gov/documents/TSIdata/CERES_EBAF_Ed2.8_DailyTSI.txt`. An overview of missions carrying radiometers for TSI is provided in Kopp and Lean (2011) and Dewitte and Clerbaux (2017). It is obvious that the TSI varies with the 11-year solar cycle. During solar maxima, the TSI shows larger variations and reaches nearly 1363 $W/m^2$, whereas the time series is much smoother during the solar minimum in 2008 with values near 1360.8 $W/m^2$.

At the Earth's TOA, the mean incoming solar radiation is quantified with 340 $W/m^2$ (Wild et al., 2015), which corresponds to a quarter of the TSI. The TSI is valid for the effective cross section of the Earth. Since the Earth is in first approximation a rotating sphere, the solar energy reaching this cross section is distributed over the entire surface of the surrounding sphere. The surface area of the cross section and the sphere differ by a factor of four such that the energy reaching the Earth's surrounding surface is four times smaller. The surrounding surface mentioned here is usually referred to as the Earth's TOA, which is defined at 20 km altitude (Loeb et al., 2002). Considering an oblate Earth, the factor is 4.003 (Loeb et al., 2018). The resulting spatial distribution of the incoming solar radiation at TOA is depicted in Fig. 2.6 and shows a pure

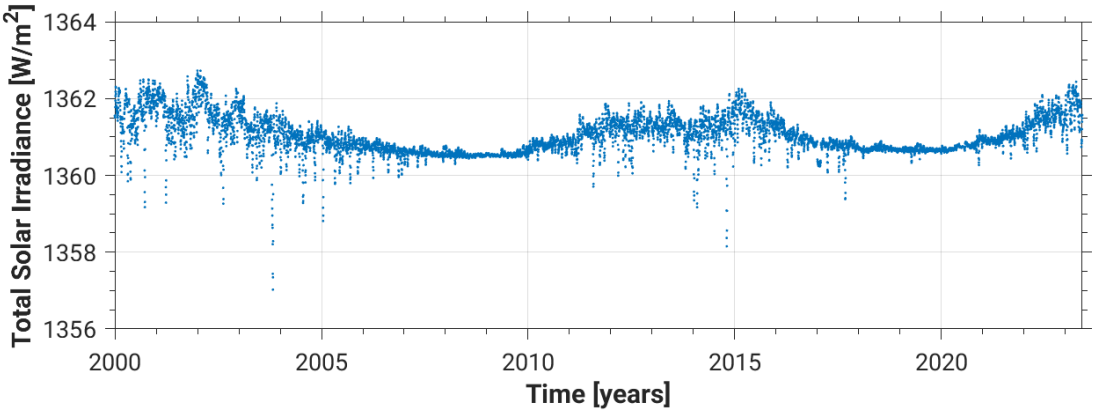



Figure 2.5: TSI between January 2000 and May 2023. The data were obtained from `https://ceres.larc.nasa.gov/documents/TSIdata/CERES_EBAF_Ed2.8_DailyTSI.txt`, last access: June 26, 2023.

latitude-dependency with minimal fluxes at the poles of about 170 $\mathrm{W/m^2}$ and maximal fluxes at the equator of 415 $\mathrm{W/m^2}$. According to Kopp and Lean (2011), the uncertainty of the incoming solar radiation is 0.13 $\mathrm{W/m^2}$.

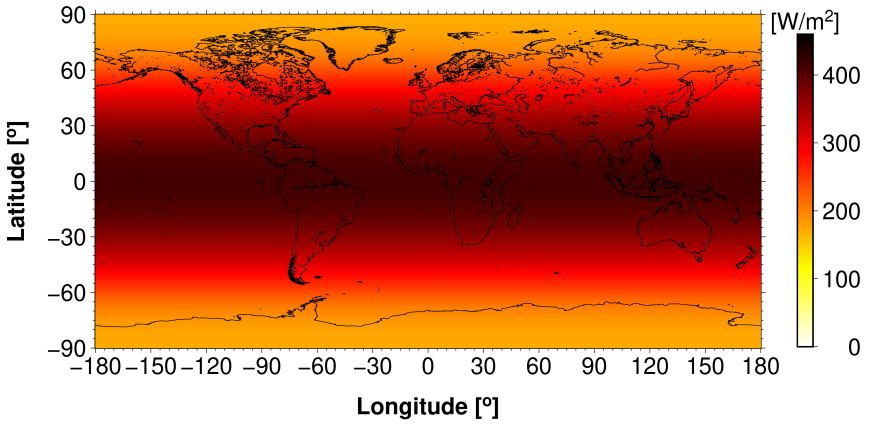



Figure 2.6: The incoming solar radiation from CERES SYN1deg data averaged over the period July 2005 - June 2015.

### 2.3.3 Outgoing radiation of the Earth

The solar radiation reaching the Earth's system is either reflected or absorbed in the atmosphere and at the Earth's surface. The ratio of the reflected $F_{\mathrm{refl},\nu}$ and incoming radiation $F_{\mathrm{in},\nu}$ at a specific wavelength $\nu$ is known as spectral albedo

$$a_\nu = \frac{F_{\mathrm{refl},\nu}}{F_{\mathrm{in},\nu}}. \tag{2.3.4}$$

For the Earth, the albedo usually corresponds to the ratio of reflected and incoming solar radiation over the whole solar spectrum. Surface albedo considers the ratio of the fluxes per unit area, i.e., radiosity divided by irradiance, at the Earth's surface.

The albedo of the Earth depends on the properties of the Earth's surface. For oceans, which absorb a large amount of the incoming solar radiation, the albedo is around below 0.1 (Goode et al., 2021). In contrast, ice and bright deserts reflect most of the incoming radiation leading to an albedo around 0.9. For the entire Earth, the current albedo is 0.29, however, its changes over time, e.g., due to sea ice variations, need further investigations (Stephens et al., 2015). Interestingly, Earth's albedo cannot only be monitored with Earth orbiting satellites measuring incoming and

reflected solar radiation (Wild et al., 2013), but also by evaluating the so-called Earth shine on the lunar surface, which results from the reflected sunlight at the Earth illuminating the dark parts of the Moon facing the Earth (Goode et al., 2021). The resulting trend (1998-2017) in albedo is 0.5 W/m$^2$ (Goode et al., 2021).

The reflected solar radiation leaving the Earth is commonly known as outgoing shortwave radiation. In addition, the Earth emits energy in the infrared domain denoted as outgoing longwave radiation. The corresponding spectrum under the assumption of the Earth as a black-body with a temperature of 288 K is shown in Fig. 2.7. In comparison to the solar irradiance (Fig. 2.4),

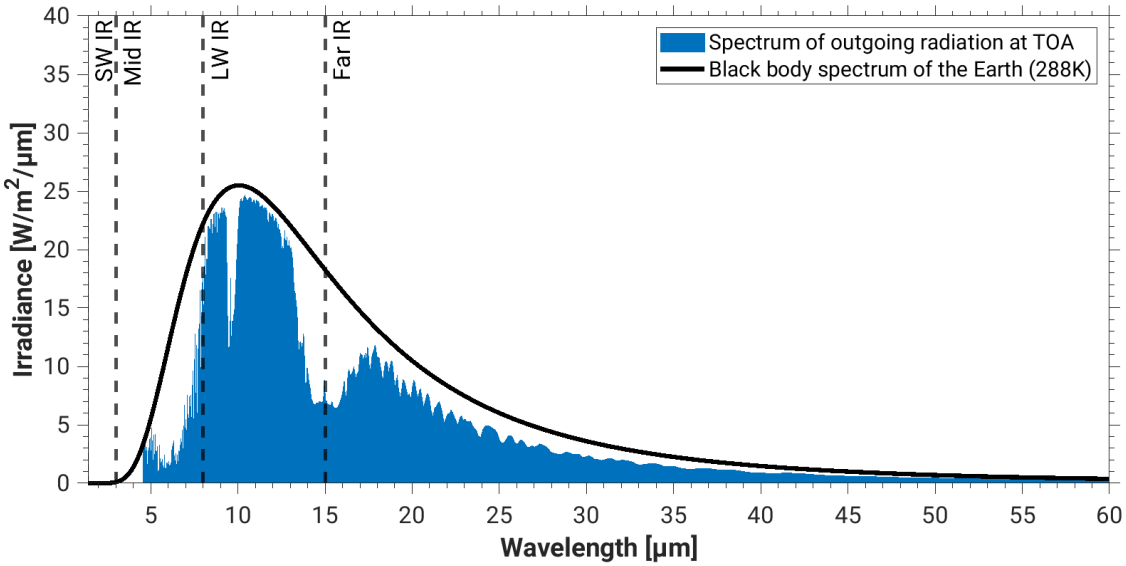



Figure 2.7: Black body spectrum of the Earth with the assumption of a surface temperature of 288 K together with the spectral irradiance of the outgoing radiation at TOA with data from the MODTRAN model assuming a standard atmosphere (`http://climatemodels.uchicago.edu/modtran/`, last access: June 1, 2023). Horizontal lines mark the regions of the subcategories of infrared (IR) radiation: shortwave (SW), mid, longwave (LW), and far.

the irradiance of the Earth peaks at a much larger wavelength of about 10 µm due to the lower temperature. The irradiance of the Earth covers the mid to far IR bands. Fig. 2.4 also shows the spectral irradiance of the outgoing radiation at TOA, which has been modelled with MODTRAN (at `http://climatemodels.uchicago.edu/modtran/`, last access: July 18, 2023) under the assumption of a standard atmosphere. The resulting irradiance is generally smaller than the black-body spectrum. The window at around 10 µm and 15 µm is due to ozone and carbon dioxide, respectively, as they are important absorber of the Earth's outgoing radiation. This window increases with increasing carbon dioxide levels in the atmosphere, leading to a larger amount of energy remaining in the Earth's system. Consequently, for every 1000 $GtCO_2$ anthropogenic emission, the global surface temperature rises by about 0.27-0.63°C as reported in the latest Intergovernmental Panel on Climate Change (IPCC) report (IPCC, 2023).

In order to get an idea of the magnitude of the Earth's outgoing radiation, Fig. 2.8 illustrates the Earth's global annually averaged energy budget (Wild et al., 2015). It is visible that the incoming solar radiation is not only reflected at the Earth's surface, but also partly at TOA due to clouds, atmospheric constituents and aerosols. Thus, one needs to differentiate between the Earth's outgoing shortwave radiation at the surface (25 W/m$^2$) and at TOA, which amounts to 100 W/m$^2$. In contrast, the Earth's outgoing longwave radiation is much larger at the Earth's surface with 398 W/m$^2$ than at TOA with 239 W/m$^2$, since the atmosphere absorbs large parts of this radiation. Additionally taking the incoming solar radiation at TOA of 340 W/m$^2$ into account, the so-called net radiative flux can be obtained from the difference of the incoming and outgoing radiation at TOA. Since this amounts to about 0.6 W/m$^2$ rather than 0, the Earth's energy budget is in imbalance.

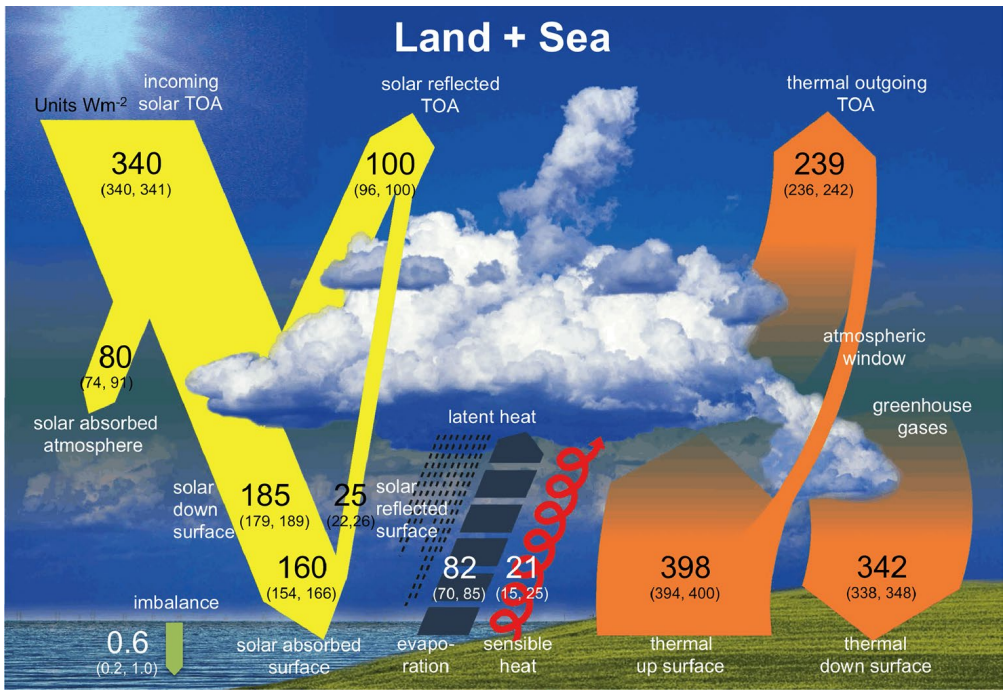



Figure 2.8: The global annual mean energy budget of the Earth in units W/m$^2$ from Wild et al. (2015).

### 2.3.4 Earth's energy imbalance

The Earth's energy is in imbalance since the incoming energy flux is larger than the outgoing energy flux. Measuring the EEI as well as its changes over time is highly important to quantify global warming (Loeb et al., 2018; Meyssignac et al., 2019; von Schuckmann et al., 2020; Loeb et al., 2021; Hakuba et al., 2021; Marti et al., 2022; von Schuckmann et al., 2023). Recently published estimates of EEI are listed in Tab. 2.1. The reported estimates vary between 0.47 and 0.94 W/m$^2$. Differences can occur due the period of evaluation indicating that the imbalance increased further during the last two decades. The current requirement for EEI estimates is an annual mean accuracy

Table 2.1: Overview of EEI estimates obtained from selected studies during various periods.

| EEI [W/m$^2$] | Period | Reference | Method /data |
|---|---|---|---|
| 0.48±0.1 | 1971-2020 | von Schuckmann et al. (2023) | observation-based |
| 0.76±0.2 | 2006-2020 | von Schuckmann et al. (2023) | observation-based |
| 0.74±0.22 | Aug. 2002 - Aug. 2016 | Marti et al. (2022) | space geodetic observations |
| 0.94±0.25 | 2005-2019 | Hakuba et al. (2021) | space geodetic observations |
| 0.50±0.47 | mid-2005 - mid-2019 | Loeb et al. (2021) | CERES and in-situ data |
| 0.47±0.1 | 1971-2018 | von Schuckmann et al. (2020) | observation-based |
| 0.87±0.12 | 2010-2018 | von Schuckmann et al. (2020) | observation-based |

of 0.1 W/m$^2$ (Meyssignac et al., 2019).

Basically four different methods exist to obtain EEI (Trenberth et al., 2009; von Schuckmann et al., 2016). (1) The evaluation of radiative fluxes of incoming and outgoing radiation at TOA is the most direct approach. Details on this approach will be outlined and discussed below, since the fluxes are considered in the ERP force modelling and correcting these fluxes will be addressed in Ch. 7. (2) Second, the exchange of energy between the Earth's surface and the atmosphere in terms of sensible and latent heat fluxes can be used to obtain EEI. However, the global coverage of available measurements on the Earth's surface is sparse and space observations of heat exchange on the Earth's surface have large uncertainties (von Schuckmann et al., 2016). (3) The third approach focusses on the oceans, where 90 % of the excess heat is stored. The Ocean Heat Content

(OHC) can be obtained from the evaluation of space geodetic and in-situ ocean observations before converting it to EEI. Since these OHC estimates are partly used to constrain the fluxes used in the first approach, an overview of different methods to obtain OHC is provided below. (4) Finally, EEI can be diagnosed from climate model simulations, which are not applied in this thesis and therefore not further discussed.

As already mentioned above, EEI is defined as the difference between the incoming and outgoing radiation at TOA

$$\mathrm{EEI} = \mathrm{SW}\downarrow - \mathrm{SW}\uparrow - \mathrm{LW}\uparrow, \tag{2.3.5}$$

with incoming shortwave flux SW ↓, outgoing shortwave flux SW ↑ and outgoing longwave flux LW ↑. Thus, evaluating radiative flux measurements at TOA as suggested in approach (1) is the direct way to obtain EEI.

Measurements of these fluxes at TOA with a spatial resolution of up to 1° can be derived from radiometers on-board LEO satellites, such as Nimbus 6/7, NOAA 9/10 or TRMM, since the 1970s (see e.g., Dewitte and Clerbaux, 2017). Since March 2000, measurements of the nadir-pointing CERES instrument on-board the Terra and Aqua satellites are available as part of National Aeronautics and Space Administration (NASA)'s CERES project (Wielicki et al., 1996). Data are available from `https://ceres.larc.nasa.gov/data/`, last access: July 18, 2023. The Terra satellite operates in a descending sun-synchronous orbit crossing the equator at 10:30 a.m. local time, whereas the orbit of Aqua is ascending with an equator crossing at 1:30 p.m. local time (*CERES_SYN1deg_Ed4A Data Quality Summary (10/3/2017)* 2017). The CERES instrument is launched on two satellites at once to allow for the synchronous measurement in different scan modes. In the cross-track scan mode, the radiances are measured, whereas in a biaxial scan mode with a rotating azimuth angle data of the radiance's angular distribution are collected (Smith et al., 2004). The CERES instrument is pointing towards the Earth and measures the radiance at three spectral channels. The combination of shortwave (0.2-5 µm), total (0.2-100 µm) and "window" (8-12 µm) channels allows to differentiate between the outgoing shortwave and longwave radiation (Wielicki et al., 1996). The window channel has been introduced to resolve the longwave radiation at the Earth's surface. The outgoing longwave radiation at TOA can be obtained from the residuals of total and shortwave measurements. The instruments have a narrow field of view of 20 km.

Since the radiances are measured in slant view along the orbit of the satellite, adequate processing is required to obtain global fluxes (Loeb et al., 2018). Within the processing from Level 0 (raw data) to Level 3 (gridded fluxes and cloud properties), hourly imager data from the MODerate resolution Imaging Spectroradiometer (MODIS) and Visible Infrared Imaging Radiometer Suite (VIIRS) instruments are considered in addition to CERES measurements to allow for the time interpolation of cloud changes. This is also known as diurnal correction. The processing of global fluxes also requires a careful calibration of the instruments. Furthermore, instantaneous radiance measurements are converted to fluxes by considering so-called ADMs for both longwave and shortwave radiation (Suttles et al., 1988; Suttles et al., 1989). These models consider the angular dependence of the radiation due to varying surface and cloud conditions. Additionally, filtering, temporal interpolation and spatial averaging are required to obtain global fluxes on a 1° grid at hourly resolution and monthly mean time steps. Besides surface fluxes, the fluxes are obtained at TOA, which is a pre-defined reference level of 20 km altitude (Loeb et al., 2002). A lot of effort has been made to improve the Level 0 to 3 processing during the past years (Su et al., 2015a; Su et al., 2015b; Doelling et al., 2016; Kato et al., 2018; Loeb et al., 2018). Nevertheless, the requirement to obtain EEI with an accuracy of $0.1\,\mathrm{W/m^2}$ is not met with Level 3 products. Consequently, further effort is made to constrain the net fluxes to long-term planetary heat uptake resulting in Level 3b products (Loeb et al., 2018). The differences between Level 3 and Level 3b products are summarized in the following and remaining uncertainties and biases are discussed.

CERES SYN1deg data result from Level 3 processing, where fluxes from Terra and Aqua are combined with fluxes derived from geostationary satellites to increase the temporal resolution of the resulting global fluxes to one hour (Doelling et al., 2016). The CERES SYN1deg product provides all-sky and clear-sky solutions, the latter having clouds removed. The global all-sky fluxes at TOA

from monthly CERES SYN1deg data during the period June 2005 - July 2015 are presented in the left column of Fig. 2.9. The outgoing shortwave radiation is largest over deserts, ice and mountain

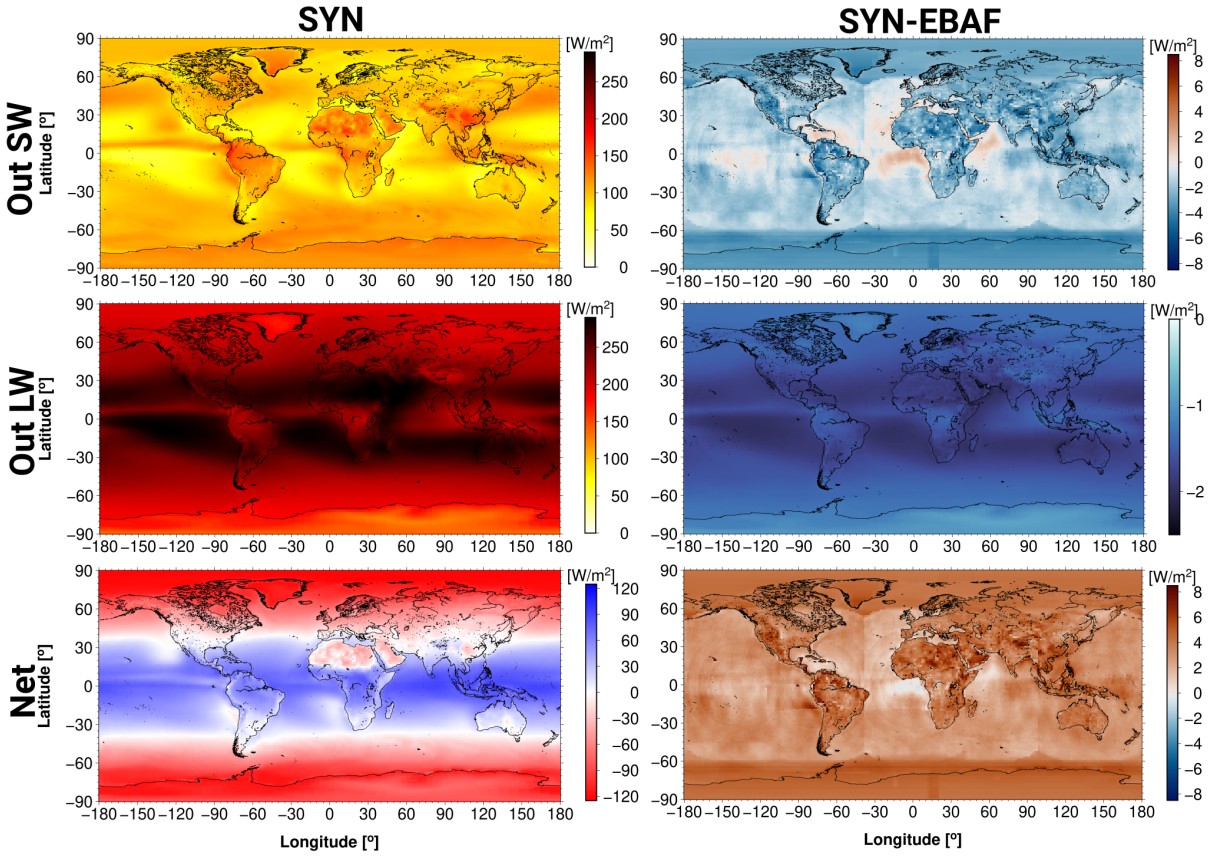



Figure 2.9: CERES all-sky fluxes at TOA from CERES SYN1deg (left) and the difference to EBAF (right). The global maps are averages from the monthly fluxes for the period July 2005 - June 2015. The outgoing shortwave and longwave radiation are shown in the first and second row, respectively. The third row depicts the net flux (EEI). Please note the different colour scales for most of the maps.

ranges with fluxes of up to 176 W/m$^2$. The pattern of the outgoing longwave radiation is inverse with the largest fluxes of up to 300 W/m$^2$ over the equatorial oceans. The incoming solar radiation has already been presented in Fig. 2.6. The net flux, which is directly provided within the CERES SYN1deg data, is negative at high latitudes above ±40° as well as in the deserts reaching fluxes of -123 W/m$^2$, and positive at low latitudes with fluxes of up to 106 W/m$^2$. Since the CERES SYN1deg TOA fluxes still contain biases, the globally averaged net flux amounts to 4.3 W/m$^2$ for the period 2005 to 2015 (Loeb et al., 2018), which is significantly larger than the expected EEI.

Therefore, the CERES Level 3b EBAF product has been developed by constraining the fluxes within their range of uncertainty (Loeb et al., 2009; Loeb et al., 2018) such that the net flux at TOA for the period July 2005 to June 2015 results in 0.71 W/m$^2$ according to Johnson et al. (2016). This value has been obtained from a combination of so-called OHC estimates of 0.61 W/m$^2$ from Argo data above 1800 m, OHC reconstructions below 2000 m of 0.07 W/m$^2$, and heating from non-ocean contributions of 0.03 W/m$^2$. According to Loeb et al. (2018), the shortwave and longwave fluxes at TOA increase by 2 W/m$^2$ and 1.5 W/m$^2$, respectively.

The differences between the CERES SYN1deg and EBAF fluxes for the period July 2005 to June 2015 are presented in the left column in Fig. 2.9. The shortwave fluxes contain relatively small differences below ±2W/m$^2$ between ±60° latitude, which corresponds the inclination of the geostationary imager data considered within the CERES SYN1deg processing. In the polar regions the differences are about three times larger. The outgoing longwave radiation from EBAF is on

average 1.5 $W/m^2$ larger than from CERES SYN1deg. Consequently, the net flux is 3.6 $W/m^2$ smaller when using the adjusted fluxes from EBAF resulting in an EEI of 0.71±0.1 $W/m^2$ for the period 2005 to 2015 as in Johnson et al. (2016). The spatial pattern from the differences in the outgoing shortwave flux dominate also the pattern of the net flux.

According to Loeb et al. (2018), the uncertainty in monthly all-sky longwave and shortwave EBAF TOA fluxes is 2.5 $W/m^2$ during the Terra-Aqua period (after July 2002). Smith et al. (2004) reports that ADMs are the largest error source in the conversion of measured radiances to instantaneous fluxes. The error after averaging the data spatially and temporally still limits the overall accuracy such that remaining errors from the radiance-to-flux conversion are 0.75 $W/m^2$ and 1 $W/m^2$ for EBAF longwave and shortwave fluxes, respectively (Su et al., 2015b). Moreover, the diurnal correction of EBAF data contribute to the overall uncertainty as well as calibration uncertainties of 1.8 $W/m^2$ and 1 $W/m^2$ for longwave and shortwave fluxes (Loeb et al., 2018). In summary, the remaining uncertainties in the CERES fluxes still limit the accuracy of the EEI estimates from this approach.

Besides CERES, the fluxes at TOA can be obtained from atmospheric reanalyses. Here, the atmospheric state is estimated using numerical weather prediction models together with available measurements since 1950. TOA fluxes from the European Centre for Medium-Range Weather Forecasts (ECMWF) reanalysis version 5 (ERA5) data set (Hersbach et al., 2020) are available hourly on a 0.25 grid. Despite the high spatio-temporal resolution and continuous improvement of the reanalysis products (Hersbach et al., 2020), fluxes from reanalyses are no measured fluxes and biases are likely. Therefore, ERA5 data are not further considered in this thesis.

As mentioned above, the CERES EBAF data have been constrained to OHC estimates. OHC is the amount of heat stored in the oceans (von Schuckmann et al., 2023). To better understand this constrain, the link between EEI and OHC is outlined before methods to obtain OHC are briefly summarized.

The excess heat in the Earth's system is mainly stored in the oceans (89 %), whereas land, cryosphere and atmosphere store 6 %, 4 % and 1 %, respectively (von Schuckmann et al., 2023). Consequently, the heat uptake of the oceans, which leads to the steric (volumetric) sea level rise, provides valuable information on the Earth's energy budget (Trenberth et al., 2016; WCRP Global Sea Level Budget Group, 2018; Hakuba et al., 2021; Marti et al., 2022; von Schuckmann et al., 2023).

Converting OHC to EEI can be conducted with different complexity (e.g., Trenberth et al., 2016; Aschenneller, 2021). The non-ocean contributions, i.e., the energy from ice, land, and the atmosphere can be obtained from observations, models or reanalyses (Trenberth et al., 2016). A rather simplistic approach suggests to scale OHC according to the amount of stored energy in the total system, i.e., multiplying with 1.11, to obtain EEI. Additionally, it makes sense to account for the difference of the surface area of oceans and TOA.

Ocean Heat Uptake (OHU), which is the change of OHC over time, can be obtained from different approaches (von Schuckmann et al., 2016; Meyssignac et al., 2019). Argo floats, which measure the temperature and salinity profiles of the oceans, allow for in-situ ocean observations down to 2000 m depth (Riser et al., 2016). These sub-surface temperature measurements can be used to obtain OHC (von Schuckmann et al., 2016), which requires the temperature integration over the vertical profiles. However, measurements in deep oceans are scarce in particular over time. Another challenge is the non-homogenous distribution of the floats, which requires adequate interpolation techniques. Moreover, changes in the instrumentation contribute to biases in OHC (von Schuckmann et al., 2016).

Secondly, geodetic space observations from satellite altimetry and GRACE gravimetry can be used to construct the sea level budget. The resulting steric sea level change can be converted to OHU by applying the global mean conversion factor $\epsilon = 0.52 W/m^2/mm/yr$, which describes the ocean's expansion efficiency of heat (e.g., Russell et al., 2000). This space geodetic approach has been applied in Rietbroek (2014); Dieng et al. (2015); Rietbroek et al. (2016); Meyssignac et al. (2019); Hakuba et al. (2021); Uebbing (2022).

A third approach to obtain OHC is the evaluation of ocean models and ocean reanalyses (Tren-

berth and Fasullo, 2017; Zuo et al., 2017; Zuo et al., 2019). The integration of vertical temperature profiles, e.g., from ORAS5 (Zuo et al., 2017), allow for the computation of global OHC.

As mentioned above, CERES EBAF outgoing fluxes are constrained to a net flux at TOA of $0.71\,\mathrm{W/m^2}$ for the period July 2005 to June 2015, which has been obtained from Argo data, OHC reconstruction and a non-ocean component (Loeb et al., 2018). Even though these contributions have been carefully selected and their uncertainty is at the lower end (Loeb et al., 2018), the EBAF fluxes might differ when constraining the data to OHC from other sources.

To summarize, due to the importance of quantifying global warming there is the necessity to estimate EEI with an accuracy of $0.1\,\mathrm{W/m^2}$. Different methods exist to obtain EEI, which all have their own advantages and challenges. Consequently, a need for independent estimates of EEI remains to overcome weaknesses in existing approaches.

# Chapter 3

# Satellite observations

This chapter provides an overview of satellite-based observations relevant for this thesis. The first part introduces the GRACE mission (Sect. 3.1) with a focus on accelerometer measurements. Second, SLR measurements are outlined (Sect. 3.2).

## 3.1 The GRACE(-FO) mission

An overview of the GRACE and GRACE-FO missions, their instruments and data is provided in the following. Since the accelerometer measurements are the most important data from this mission for this thesis, the final part of this section will focus on the measurement principle of space-borne accelerometery, its challenges and calibration procedures.

### 3.1.1 Mission overview

With the launch of the GRACE mission (Tapley et al., 2004) on March 17, 2002, measurements of the Earth's mean gravity field and its time-variability are available with unprecedented accuracy. The twin satellite mission consisting of the identical satellites GRACE-A and GRACE-B operated until October 12, 2017, which was about 10 years longer than originally planned due to the unexpected low solar activity causing a slower orbit decay. Its follow-on mission (Landerer et al., 2020) consisting of GRACE-C and GRACE-D continued measuring mass changes with its launch on May 22, 2018. Both GRACE and GRACE-FO are joint satellite missions of NASA and Deutsches Zentrum für Luft- und Raumfahrt e.V., engl. German Aerospace Centre (DLR).

The two satellites of each mission follow the same orbit with an inclination of $89.5° \pm 0.5°$ and an eccentricity of $e < 0.005$, which is nearly circular. Its orbital period is approximately 90 minutes. The initial altitude was about 500 km and the satellites keep an along-track distance of approximately 220 km$\pm$50 km (Case et al., 2010). Due to the orbit design, the satellites cover nearly the whole globe within 30 days, which allows for the estimation of monthly time-variable gravity fields.

The science community benefits from the time-variable gravity fields derived from both missions, since they enable the analysis of mass changes of the Earth over approximately two decades. The observed mass variations contribute to our understanding of global warming (Tapley et al., 2019).

### 3.1.2 Measurement principle and instruments

The primary measurement quantity is the precise distance between the satellites in terms of ranges, range-rates and range-accelerations. Due to the inhomogeneity of the Earth's gravity field and their separation in the along-track direction, the satellites experience the gravitational signal slightly differently, which leads to changes in their distance. Subsequently, the measured distance changes provide information on the higher-frequency variation of the gravitational signals (Kim and Tapley, 2002). Besides multiple other instruments (see Fig. 3.1), the satellite pair is equipped with the K-Band Ranging System (KBR) to measure the distance between the two satellites also known as low-low satellite-to-satellite tracking. From the ranging horn on the front panel (Fig. 3.1), the KBR

sends and receives a microwave signal with frequencies of 24 GHz (K-band) and 32 GHz (Ka-band). The two frequencies allow for the elimination of ionospheric signals and are both generated by an ultra-stable oscillator. The received signal phase change is the measurement quantity, which is transformed into the range. The accuracy of the measured range is below 10 µm (Tapley et al., 2004). In addition, GRACE-FO is equipped with a Laser Ranging Interferometer (LRI) (Heinzel et al., 2017), which allows for measuring the satellites' distance 10 times more precisely with the aim of measuring gravitational changes at smaller scales.

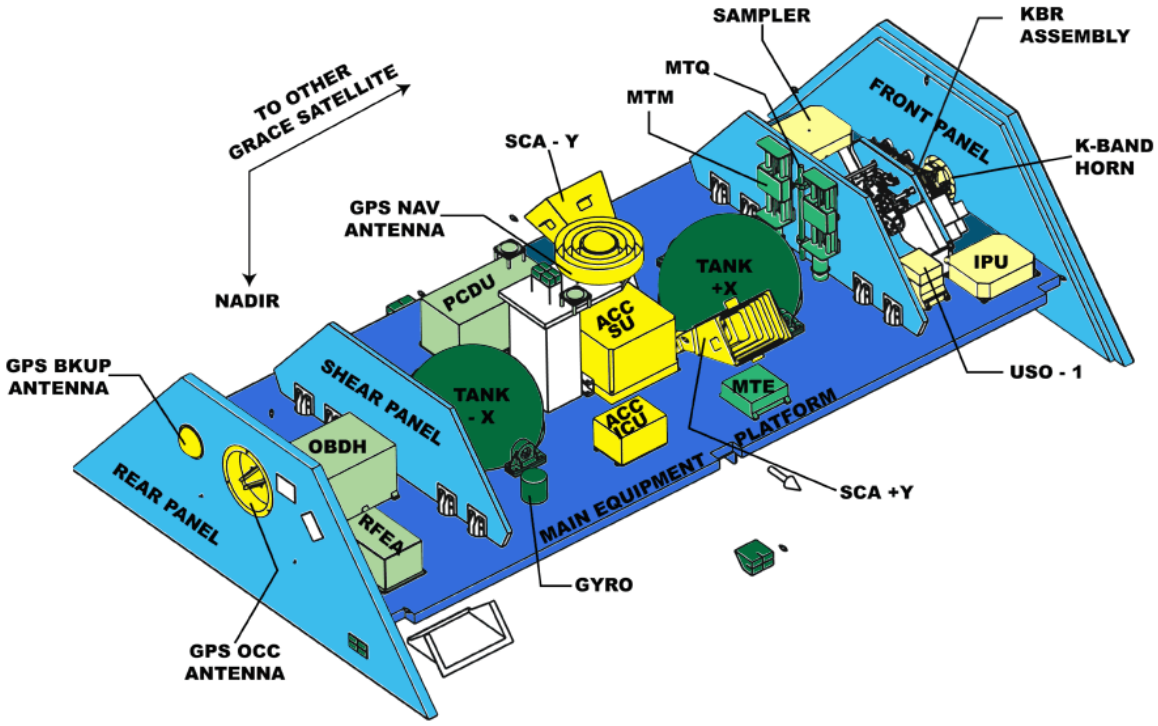



Figure 3.1: Internal instrument overview of a GRACE satellite. Source: `http://www2.csr.utexas.edu/grace/spacecraft/a1.html`, last access: June 1, 2022.

Since the measured ranges are not only sensitive to changes in the gravitational signal, but also to changes in the non-gravitational ones, each satellite carries an on-board accelerometer (Fig. 3.1). This instrument is located at the satellite's centre of mass. The measured non-gravitational accelerations are then used to separate them from the gravitational signal for gravity field recovery (Tapley et al., 2004).

In addition, high-low satellite-to-satellite tracking is required to locate each satellite at cm-accuracy. Therefore, both satellites are equipped with a Global Positioning System (GPS) receiver (Fig. 3.1). These instruments are additionally used for time-tagging the payload data and for radio occultation measurements, which provide vertical atmospheric temperature and humidity profiles for GRACE and GRACE-FO (Wen et al., 2019). A laser retro reflector is installed to validate the orbit determination with SLR measurements.

The star camera assembly provides the satellite's inertial orientation by comparing the star constellation to the star catalogues. It consists of two (three) star camera sensors on-board each GRACE (GRACE-FO) satellite, where the sensors are arranged such that they are not blinded by the Sun or the Moon at the same time. The star cameras are pointing 45° left and right of the satellite's zenith vector (Fig. 3.1).

### 3.1.3 Data

This section provides an overview of the data levels used in the GRACE community. GRACE and GRACE-FO data are governed by the Science Data Service (SDS), which is a cooperation of

Jet Propulsion Laboratory (JPL), University of Texas Center for Space Research (UTCSR) and Deutsches GeoForschungsZentrum (GFZ). They generate, distribute and archive the data products from Level-0 (L0) to Level-3 (L3) (Bettadpur, 2012; Wen et al., 2019).

**Level-0**
L0 data contain the science instrument and spacecraft housekeeping data, which are collected at DLR in Neustrelitz from each down-link pass.

**Level-1**
Level-1A (L1A) data are the first stage of processed L0 data. At this stage, sensor calibration factors and preliminary time tagging are applied to obtain the measurements in engineering units at satellite receiver clock time. The final L1A data, which are only publicly available for GRACE-FO, are reformatted and contain quality flags. In a second step within Level-1 processing, the measurements are correctly time-tagged and sampling rates are reduced resulting in Level-1B (L1B) data, which also include ancillary data from Level-1 processing. L1A and L1B data products are separated into Instruments Processing Unit (IPU), Interface Control Unit (ICU) and spacecraft housekeeping data. IPU provides measurements from the KBR, star camera and GPS instruments. ICU includes accelerometer data, and additional data are provided as housekeeping data collected by the On-Board Data Handler (OBDH). L1B data are publicly available at JPL's Physical Oceanography Distributed Active Data Center (PODAAC) (`https://podaac-tools.jpl.nasa.gov/drive`, last access: January 10, 2023) and GFZ's Information System and Data Center (ISDC) (`https://isdc.gfz-potsdam.de`, last access: January 10, 2023). These data are documented for GRACE and GRACE-FO in Case et al. (2010) and Wen et al. (2019), respectively.

**Level-2**
Further processing results in Level-2 (L2) data, which include the Earth's time-variable gravity field in terms of monthly Spherical Harmonic (SH) potential coefficients as well as ancillary data from L2 processing such as monthly means of the Atmosphere and Ocean De-aliasing L1B (AOD1B) de-aliasing products. More information on the official gravity fields can be found in Dahle et al. (2019a, 2019b) and Yuan (2019). Besides the official L2 gravity fields, several institutes apply their own processing from L1B to L2 data resulting in multiple monthly time-variable gravity field solutions, e.g., ITSG-Grace2018 from the Institute of Geodesy, Graz, Austria (Kvas et al., 2019a). The International Centre for Global Earth Models (ICGEM) (Ince et al., 2019) collects and distributes the solutions.

**Level-3**
Finally, L3 data contain gridded geopotential functionals in terms of equivalent water height processed from the L2 SH coefficients as described in Landerer and Cooley (2021).

There exist different releases of the data. Here, I apply L1B Release 03 (RL03) data (Bettadpur, 2012). The L1B data are the most basic ones, which are publicly available for GRACE. The L1B accelerometer data are provided in GPS-time and in the Satellite Reference Frame (SRF) (Wen et al., 2019). The SRF is located at the centre of mass of each satellite. The body-fixed reference frames are presented in Fig. 3.2. The axes of the SRF are parallel to the Accelerometer Frame (AF) and the Satellite Frame (SF). Following this, the $x$-axis of the SRF points towards the horn of the KBR, which is equal to the along-track direction of the trailing satellite and the anti-along-track direction of the leading satellite. The $z$-axis is directed to the surface normal of the main equipment platform and the normal to $x$-axis and is positive towards the satellite radiator. The $y$-axis completes the right-handed triad.

The L1B data, which are used in this thesis, are briefly summarized in the following. The ACC1B accelerometer product provides linear and angular non-gravitational accelerations with a resolution of 1 s. The satellite's orientation in space resulting from the star camera assembly is provided at 5 s resolution in the SRF in terms of quaternions as SCA1B data. These measurements are required for transformations between the SRF and Celestial Reference Frame (CRF). Precise positions and velocities at 10 s sampling are provided in the GNV1B data product derived from a reduced-dynamic orbit determination procedure. Additionally, there exist kinematic orbits processed by several institutes (Švehla and Rothacher, 2003; Visser and Van Den IJssel, 2003; Švehla

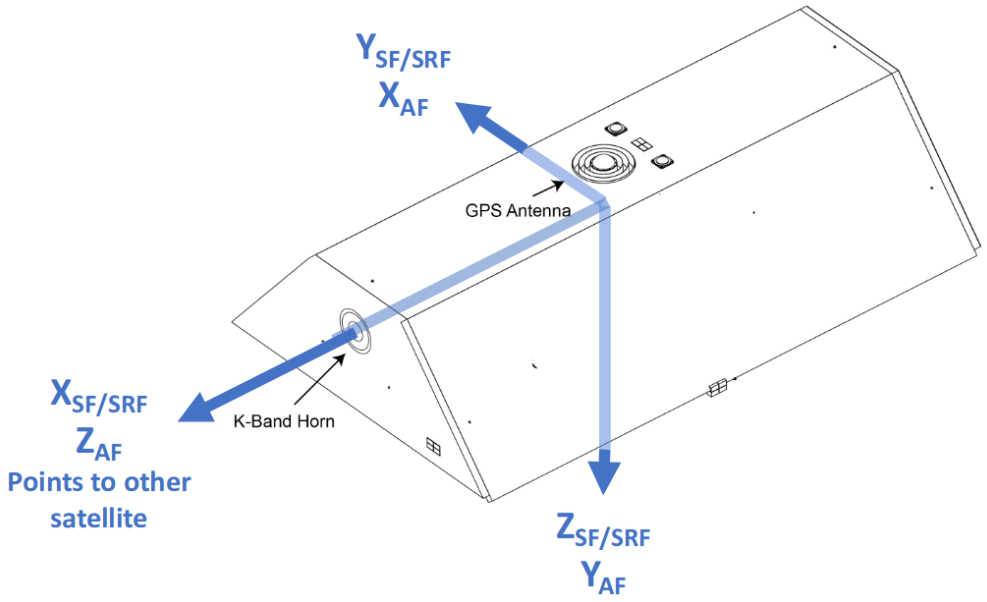



Figure 3.2: Illustration of the satellite-body fixed frames SF, SRF, AF from Wen et al. (2019).

and Rothacher, 2005; Weinbach and Schön, 2013; Arnold and Jäggi, 2020). The latest ones are available from Graz University of Technology (Zehentner and Mayer-Gürr, 2016; Zehentner, 2017; Suesser-Rechberger et al., 2022). Kinematic orbits are determined from the carrier phase measurements of the GPS instrument without accounting for any additional forces. Generally, dynamic and kinematic orbits have similar accuracies of 1-3 cm nowadays (Švehla and Földváry, 2006). Orbital positions can be converted from CRF to Earth Centered Earth Fixed reference frame (ECEF) using Standards Of Fundamental Astronomy (SOFA) routines as described in App. A.

Further, the mass product MAS1B provides mass measurements of the satellite based on (a) thruster firing, and (b) pressure and temperature sensors in the tanks (Bettadpur, 2012). The measurement error of (a) is 0.2 kg, whereas the error of (b) is stated zero for the entire mission in the MAS1B data. Therefore, I apply mass data from tank sensors in this thesis although an error of zero seems too optimistic. Finally, thruster events need to be considered. Theses are required to adjust the satellite's orbit and orientation, such that the KBR instruments point at each other precisely. The thrusts cause so-called satellite-induced non-gravitational accelerations, which contaminate the accelerometer measurements of the remaining non-gravitational forces in terms of spikes. Therefore, information on the activation of the 14 on-board thrusters are required and extracted from the THR1B thruster data.

### 3.1.4 Macro-model

The geometry and thermo-optical material properties of a satellite are ideally provided by the manufacturers and stored in a macro-model. The GRACE macro-model according to Bettadpur (2012) is presented in Tab. 3.1. The thermo-optical material properties of GRACE are provided for visible and infrared radiation including properties for specular and diffuse reflection as well as absorption. Limitations of such macro-models are discussed in detail in Sect. 4.2 as their accuracy limits the quality of the non-gravitational force modelling.

Table 3.1: GRACE macro-model (Bettadpur, 2012) including area, surface normal, and thermo-optical material properties for specular and diffuse reflection of visible (Vis) and infrared (IR) radiation for each panel. If two material properties are provided, they correspond to operating and non-operating solar arrays.

| Panel | Area [m$^2$] | Unit Normal | | | Emiss | Absorp | Refl (Vis) [-] | | Refl (IR) [-] | |
|---|---|---|---|---|---|---|---|---|---|---|
| | | x | y | z | (IR) | (Vis) | Spec. | Diff. | Spec. | Diff. |
| front | 0.9551567 | 1 | 0 | 0 | 0.62 | 0.34 | 0.40 | 0.26 | 0.23 | 0.15 |
| rear | 0.9551567 | -1 | 0 | 0 | 0.62 | 0.34 | 0.40 | 0.26 | 0.23 | 0.15 |
| starboard (outer) | 3.1554792 | 0 | 0.766044 | -0.642787 | 0.81 | 0.65/0.72 | 0.05 | 0.30 | 0.03 | 0.16 |
| starboard (inner) | 0.2282913 | 0 | -0.766044 | 0.642787 | 0.62 | 0.34 | 0.40 | 0.26 | 0.23 | 0.15 |
| port (outer) | 3.1554792 | 0 | -0.766044 | -0.642787 | 0.81 | 0.65/0.72 | 0.05 | 0.30 | 0.03 | 0.16 |
| port (inner) | 0.2282913 | 0 | 0.766044 | 0.642787 | 0.62 | 0.34 | 0.40 | 0.26 | 0.23 | 0.15 |
| nadir | 6.0711120 | 0 | 0 | 1 | 0.75 | 0.12 | 0.68 | 0.20 | 0.19 | 0.06 |
| zenith | 2.1673620 | 0 | 0 | -1 | 0.81 | 0.65/0.72 | 0.05 | 0.30 | 0.03 | 0.16 |

### 3.1.5 Space-borne accelerometry

Space-borne accelerometers measure the sum of the non-gravitational forces acting on a satellite along its three orthogonal axes. The individual accelerations are due to the aerodynamics $\boldsymbol{a}_{\text{aero}}$, the radiation pressure $\boldsymbol{a}_{\text{RP}}$, and satellite-induced effects $\boldsymbol{a}_{\text{sat}}$ resulting in the total non-gravitational acceleration

$$\boldsymbol{a}_{\text{ng}} = \boldsymbol{a}_{\text{aero}} + \boldsymbol{a}_{\text{RP}} + \boldsymbol{a}_{\text{sat}}. \tag{3.1.1}$$

Originally, the accelerometer measurements are required to remove the non-gravitational forces from the gravitational ones in gravity field recovery. However, accelerometer data can also be used for inverse applications such as the determination of the thermospheric neutral density (see Ch. 6).

#### 3.1.5.1 Measurement principle

Space-borne accelerometers contain a free-floating proof mass at the satellite's centre of mass. The proof mass experiences the same gravitational forces as the satellite itself, thus, the mass does not change its position relative to the satellite. In comparison, the non-gravitational forces only act on the satellite and not on the proof mass, since the non-gravitational forces are compensated by the accelerometer to keep the proof mass in the satellite's centre of mass. The required electrostatic force to do so is proportional to the mass' electrical potential. The sensor unit of the accelerometer provides electrode voltages, which are finally converted into accelerations. Locating the proof mass in the centre of mass also avoids the effect of centrifugal and angular accelerations (Touboul et al., 1999).

The SuperSTAR accelerometer on-board GRACE is not the only satellite mission making use of this measurement principle. Fig. 3.3 provides an overview of the LEO satellite missions equipped with ultra-sensitive accelerometers, since the beginning of the CHAMP mission in July 2000 (Reigber et al., 2002). CHAMP was designed to measure the Earth's gravity and magnetic field. It carried a Space Triaxial Accelerometer for Research missions (STAR) accelerometer, which is the

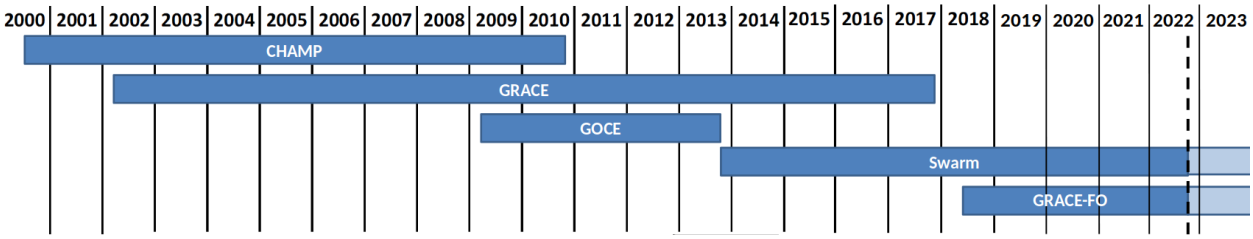


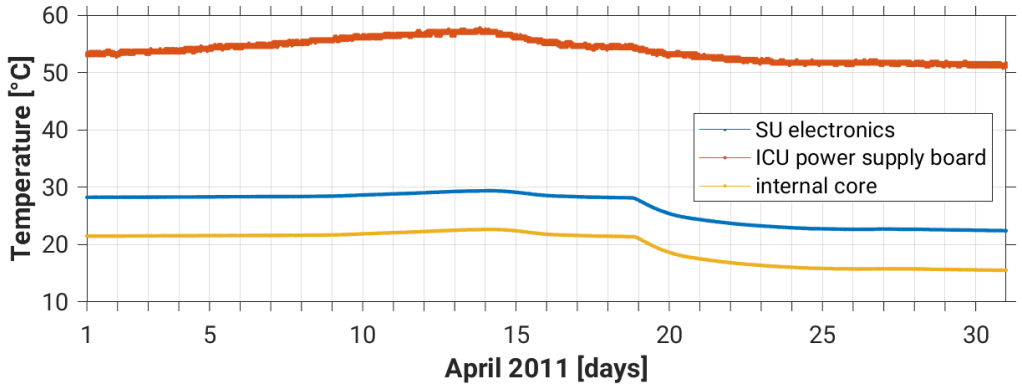

Figure 3.3: Timeline of LEO satellite missions equipped with space-borne accelerometers

predecessor of the SuperSTAR instrument on-board GRACE. Both have been developed by Office National d'Etudes et de Recherches Aérospatiales (ONERA). The SuperSTAR accelerometer had a precision of $10^{-10}\,\mathrm{m/s^2}/\sqrt{\mathrm{Hz}}$ for the radial and along-track axes, and one order of magnitude smaller for the cross-track axis (Flury et al., 2008). The noise level of both highly sensitive axes is 2-3 times larger than specified, however, it is similar for both satellites (Frommknecht, 2007). The GOCE mission (Drinkwater et al., 2006) measured the Earth's static gravity field successfully with an electrostatic gravity gradiometer consisting of six space-borne accelerometers, which are similar to the SuperSTAR accelerometer. However, their proof mass was about 4.6 times heavier, which constrained the missions' design and implementation. Moreover, ESA's Swarm mission (Friis-Christensen et al., 2008; Friedl and Sulla-Menashe, 2015) continues the CHAMP mission to measure the Earth's magnetic field. The scientific payload on-board the three identical satellites includes an accelerometer, which enables gravity field recovery in addition to the original mission purpose and bridging the data gap between GRACE and GRACE-FO (Lück et al., 2018). However, the accelerometers on-board Swarm are a low-cost variant (not by ONERA) and it turned out that they perform worse than expected showing several disturbances such as strong temperature-dependent bias variations (Siemes et al., 2016). Accelerometer data have been sophisticatedly improved for Swarm-C by evaluating calibration manoeuvres (Siemes et al., 2016). GRACE-FO is again equipped with an improved version of the SuperSTAR accelerometer to be more temperature-stable and operationally reliable (Christophe et al., 2015).

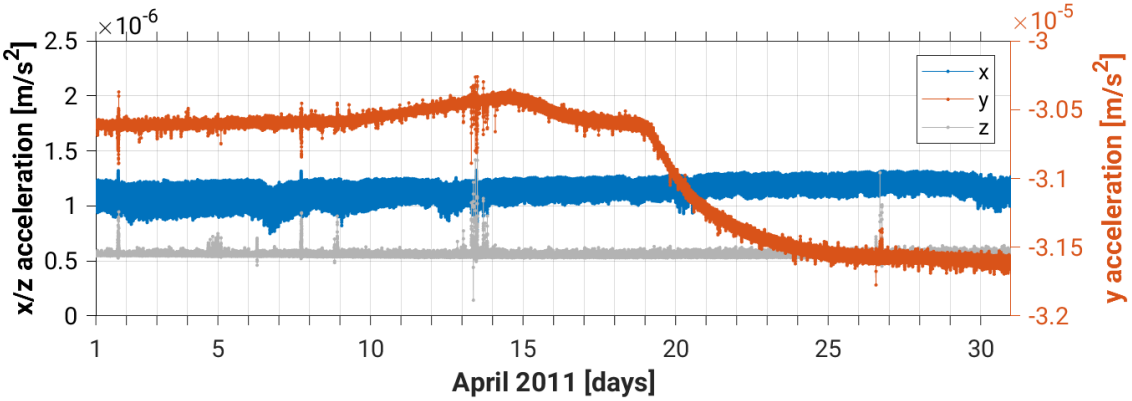
#### 3.1.5.2 Challenges

The performance of the accelerometers on-board GRACE and GRACE-FO posed several challenges during the mission lifetime. The main challenge for GRACE was the decreasing battery capacity since April 2011 (Herman et al., 2012). Not only the ability to run the measurement instruments depends on the capacity, but also the possibility to fly manoeuvres for adjusting the satellite's orientation and altitude. Since then, the mission was only fully operational when enough solar energy was available. Due to the precession of the orbital plane of about $-1.117°$ per day, the Sun traverses the orbital plane every 161 days (`http://www2.csr.utexas.edu/grace/operations/mission_status/`, last access: July 7, 2023). Following this, enough solar energy was available in case the angle between the orbital plane and the vector pointing from the Earth to the Sun ($\beta'$ angle) was between $\pm 69°$. When the solar energy and thus the battery capacity were limited, the satellites were only partly operational. Accordingly, the temperature control of the accelerometer was switched off in April 2011 for the first time. However, the maximum temperature variations should be kept below 0.1°C per orbital revolution (Touboul et al., 1999). Thus, since the accelerometer is very temperature sensitive, the quality of the measurements degraded during these periods. The temperature sensitivity of the accelerometer measurements is clearly visible in Fig. 3.4. Switching off the battery causes decreasing temperatures in the electronic parts of the accelerometer (Accelerometer Housekeeping L1B (AHK1B) data) especially after April 19, 2011 (Fig. 3.4a). The accelerometer measurements show a similar behaviour in the cross-track direction, which is the least sensitive instrument axis. Recently, McGirr et al. (2022) eliminated the thermal noise in the along-track component by applying low-pass filtered cross-track accelerations, however, this approach removes also signal, which is, e.g., required for the determination of cross-wind speeds (Siemes et al., 2023).

Since September 2016, the accelerometer on GRACE-B has been switched off during the complete $\beta'$ angle cycle due to the limited battery capacity. In order to still enable gravity field recovery, accelerometer measurements of GRACE-A had to be adapted to GRACE-B. Save et al. (2006) already investigated an accelerometer transplant approach between the satellites, when the accelerometer on-board GRACE-B had some instrument anomalies for a few weeks. Their approach is similar to Dahle et al. (2011), who transplanted the data to the other satellite by considering the time shift. Alternatively, Kim and Tapley (2015) applied a weighted moving average filter on the measurements from multiple epochs. Bandikova et al. (2019) further improved the transplant by considering a correction for thruster spikes. This approach became the processing standard of the ACT1B product.




(a) Temperature measurements.




(b) Along-track (x), cross-track (y) and radial (z) raw accelerometer measurements. The coloured right $y$-axis is introduced for the cross-track (y) data.

Figure 3.4: Temperature measurements from AHK1B data (top) and raw accelerometer measurements from Accelerometer L1B (ACC1B) data (bottom) for GRACE-A during April 2011.

For the accelerometer on-board GRACE-D, which is the trailing satellite of GRACE-FO, the noise characteristics worsened after June 21, 2018. Thus, the accelerometer transplant became relevant again. In addition, the GRACE-FO accelerometer data show phantom accelerations, i.e., spurious linear accelerations of unknown origin, which are treated as outliers in the processing of the ACT1B data (McCullough et al., 2019). For GRACE-FO, the accelerometer data product is ACT1B (instead of ACC1B as for GRACE). In October 2022, JPL published an updated and improved hybrid transplant product of the accelerometer data called ACX for the whole GRACE-FO mission. Alternatively, Behzadpour et al. (2021) processed Accelerometer L1A (ACC1A) data to obtain an improved transplant product for gravity field recovery and further research is still on-going.

Besides the issues related to the general satellite performance, there are so-called satellite-induced effects (Flury et al., 2008; Peterseim et al., 2012), which impact the accelerometer measurements. These effects, which are typically visible in terms of spikes, are generally ascribed to a combination of thruster firings, heater switches, twanks, current changes within the magnetic torquers, and antenna thrusts. Further details on these effects and the possibility of modelling them is outlined in Sect. 4.3.

Moreover, it should be mentioned here that a slight dislocation of the proof mass from the satellite's centre of mass leads to measurable linear and angular accelerations (Frommknecht, 2007). The non-orthogonality of the accelerometer axes causes additional systematic errors in the measurements. According to these constructional characteristics and the resulting systematics, a calibration of the measurements is necessary.

#### 3.1.5.3 Accelerometer calibration

On-board accelerometer measurements need to be calibrated before using the data for further studies, such as gravity field recovery (e.g., Reigber et al., 2003), precise orbit determination (e.g., Van Helleputte et al., 2009), or the estimation of thermospheric neutral densities (see e.g., Doornbos, 2012, and Ch. 6 ). Calibrating the ultra-sensitive space-borne accelerometers before the satellite's launch is not possible, since gravity on the Earth's surface is too large and simulating the space environment is extremely difficult. Therefore, several approaches have been developed during the last two decades to ensure in-orbit calibration of accelerometer measurements. For example, Kim (2000); Tapley et al. (2004), and Klinger and Mayer-Gürr (2016) calibrate GRACE accelerometer observations within a gravity field recovery procedure. Bezděk (2010) and Calabia et al. (2015) apply numerical differentiation techniques, e.g., developed by Reubelt et al. (2003), to compute accelerations from precise kinematic orbits, which are then used to estimate calibration parameters and their uncertainties. Alternatively, calibration parameters can be estimated within the precise orbit determination procedure (Bettadpur, 2009; Van Helleputte et al., 2009; Van den IJssel, 2014; Visser and Van den IJssel, 2016). Recently, temperature sensor data are also used within the calibration procedure to account for the above mentioned temperature variations (Siemes et al., 2023). Each method mentioned above yields different calibration parameters and their uncertainty as well as their influence on the final products such as the thermospheric neutral density estimation has not yet been systematically investigated.

In Vielberg et al. (2018), three different calibration procedures have been tested and compared, which are briefly summarized in the following. The calibration procedures have been performed on GRACE-A accelerometer data, however, they can be applied to any space-borne accelerometer measurements.

Calibrating accelerometer measurements $\boldsymbol{a}_{\mathrm{m}}$ requires an equation to link non-gravitational accelerations $\boldsymbol{a}_{\mathrm{ng}}$ with a set of calibration parameters. The parametrization is commonly formulated to estimate daily biases $\boldsymbol{b} = [b_x, b_y, b_z]^T$, and scale factors $\boldsymbol{S} = diag[s_x, s_y, s_z]$ for the x-, y-, and z-directions, respectively (e.g., Bettadpur, 2009; Van Helleputte et al., 2009; Calabia et al., 2015). More advanced parametrizations such as a fully populated scale factor matrix (Klinger and Mayer-Gürr, 2016) or a bias drift are possible. However, the classical parametrization is considered here. The scale factor is expected to be stable within the mission lifetime, whereas biases are expected to vary at relatively short time scales. Then, the calibration equation reads

$$\boldsymbol{a}_{\mathrm{ng}} = \boldsymbol{b} + \boldsymbol{S}\,\boldsymbol{a}_{\mathrm{m}} + \boldsymbol{v}, \tag{3.1.2}$$

where $\boldsymbol{a}_{\mathrm{ng}}$ contains modelled non-gravitational accelerations, $\boldsymbol{a}_{\mathrm{m}}$ denote the measured ones and finally $\boldsymbol{v}$ represents deviations from the simple bias-scale model plus measurement errors.

One common procedure to estimate the calibration parameters from Eq. (3.1.2) is to adjust the on-board measurements to analytically modelled non-gravitational accelerations (see e.g., Sutton et al., 2007; Doornbos, 2012; Wöske et al., 2019). In Vielberg et al. (2018), the aerodynamic acceleration is considered together with the radiation pressure acceleration due the radiation of Sun and Earth. Since the modelled accelerations should be as realistic as possible, the consideration of thermal radiation pressure accelerations as in Wöske et al. (2019) is beneficial, but has not yet been considered in Vielberg et al. (2018). Here, as well as in the other approaches, the kinematic orbit positions are used since they are free from measured or modelled non-gravitational accelerations.

As a second procedure, the multi-step numerical estimation approach (Vielberg et al., 2018) is based on the numerical differentiation of kinematic orbits and mainly follows Bezděk (2010). The idea is to apply a second numerical differentiation of precise kinematic orbit positions, which yields the satellite's total acceleration. Subtracting the gravitational accelerations (see Tab. 2 in Vielberg et al., 2018) from the total acceleration yields the non-gravitational acceleration acting on the satellite, which can be used to estimate the calibration parameters according to Eq. (3.1.2). When applying a numerical differentiation operator, the main challenges are the noise amplification and the temporal correlation. Numerical differentiation techniques have not only been used in the calibration procedure suggested by Bezděk (2010), but they have also been applied and tested in gravity retrieval studies (e.g., Reubelt et al., 2003). In Vielberg et al. (2018), similar to Bezděk

(2010), the Savitzky–Golay filter (with a window length of 11 data points and polynomial degree 5) is applied to mitigate the impact of noise, since it combines smoothing and differentiation operators. The temporal auto-correlation is reduced by iteratively fitting an AutoRegressive (AR) process to the residuals of the least squares estimation of the calibration parameters. Here, the difference to Bezděk (2010) is that auto-correlations are treated differently. Since the application of the least squares estimation together with the AR process has already reduced the correlation errors, the calibration parameters are directly estimated from adjusting the accelerations instead of converting the accelerations to positions before performing the estimation as in Bezděk (2010).

Accelerometer calibration parameters can also be estimated within a dynamic POD procedure. In dynamic POD, orbits are estimated from observables, while accounting for the forces acting on the satellite including the non-gravitational forces from accelerometer measurements and gravitational background models. Here, kinematic orbits from GNSS, e.g., from TU Graz available at `http://ftp.tugraz.at/outgoing/ITSG/tvgogo/orbits/GRACE/`, last access on July 7, 2023, (Zehentner and Mayer-Gürr, 2016), are applied as a simplification of the primary observables from GNSS. In the variational equation approach (e.g., Tapley, 1973), the dynamic POD is estimated by solving the equation of motion (see Eq. (2.1.5)) together with the associated variational equations. Besides the time, position and velocity of the satellites, the force model parameters $\boldsymbol{p}$ consisting of gravitational and non-gravitational accelerations including accelerometer calibration parameters need to be considered. The partial derivatives of the equation of motion with respect to the force model parameters $\boldsymbol{p}$ can be used to build the variational equations (Löcher, 2011) written as

$$\frac{d^2}{dt^2}\left(\frac{\partial \boldsymbol{r}}{\partial \boldsymbol{p}}\right) = \frac{\partial \boldsymbol{a}\left(t, \boldsymbol{r}, \dot{\boldsymbol{r}}, \boldsymbol{p}\right)}{\partial \boldsymbol{r}} \frac{\partial \boldsymbol{r}}{\partial \boldsymbol{p}} + \frac{\partial \boldsymbol{a}\left(t, \boldsymbol{r}, \dot{\boldsymbol{r}}, \boldsymbol{p}\right)}{\partial \dot{\boldsymbol{r}}} \frac{d}{dt}\left(\frac{\partial \boldsymbol{r}}{\partial \boldsymbol{p}}\right) + \frac{\partial \boldsymbol{a}\left(t, \boldsymbol{r}, \dot{\boldsymbol{r}}, \boldsymbol{p}\right)}{\partial \boldsymbol{p}}, \tag{3.1.3}$$

and the partial derivatives of the equation of motion with respect to the initial state $\boldsymbol{x_0} = [\boldsymbol{r}_0\, \dot{\boldsymbol{r}}_0]^T$ as

$$\frac{d^2}{dt^2}\left(\frac{\partial \boldsymbol{r}}{\partial \boldsymbol{x_0}}\right) = \frac{\partial \boldsymbol{a}\left(t, \boldsymbol{r}, \dot{\boldsymbol{r}}, \boldsymbol{p}\right)}{\partial \boldsymbol{r}} \frac{\partial \boldsymbol{r}}{\partial \boldsymbol{x_0}} + \frac{\partial \boldsymbol{a}\left(t, \boldsymbol{r}, \dot{\boldsymbol{r}}, \boldsymbol{p}\right)}{\partial \dot{\boldsymbol{r}}} \frac{d}{dt}\left(\frac{\partial \boldsymbol{r}}{\partial \boldsymbol{x_0}}\right). \tag{3.1.4}$$

In Eqs. (3.1.3) and (3.1.4), $\boldsymbol{a}\left(t, \boldsymbol{r}, \dot{\boldsymbol{r}}, \boldsymbol{p}\right)$ corresponds to the equation of motion introduced in Eq. (2.1.5). Then, the variational equations need to be integrated along the approximate orbit. The resulting system of equations reads

$$\bar{\boldsymbol{r}}(t) = \left.\frac{\partial \boldsymbol{r}}{\partial \boldsymbol{p}}\right|_{\tilde{\boldsymbol{r}}} \Delta \boldsymbol{p} + \left.\frac{\partial \boldsymbol{r}}{\partial \boldsymbol{x_0}}\right|_{\tilde{\boldsymbol{r}}} \Delta \boldsymbol{x_0} + \tilde{\boldsymbol{r}}(t), \tag{3.1.5}$$

where $\bar{\boldsymbol{r}}(t)$ is the given kinematic orbit and $\tilde{\boldsymbol{r}}(t)$ states the computed orbit using approximate values of $\boldsymbol{p}$ and $\boldsymbol{x_0}$ (Löcher, 2011). According to Eq. (3.1.5), the parameters, which include the satellite's position $\boldsymbol{r}$, velocity $\dot{\boldsymbol{r}}$, and accelerometer calibration parameters $\boldsymbol{b}$ and $\boldsymbol{S}$, are improved iteratively in a least squares adjustment. Convergence is reached as soon as the starting position changes less than 1 mm, since beyond this threshold the calibration parameters will not change significantly.

The resulting calibration parameters of the measured accelerations can be used according to Eq. (3.1.2) to calibrate the measured accelerations. However, since the simultaneous estimation of biases and scale factors yields highly (anti-)correlated calibration parameters, which cannot be physically interpreted, an iterative estimation of the calibration parameters is performed as recommended by Van Helleputte et al. (2009). During this procedure, (1) daily calibration parameters are estimated following Eq. (3.1.2), then (2) the scale factors from step (1) are temporally averaged for each direction for the whole period of available data, and finally (3) daily biases are re-estimated with the constant scales computed in step (2).

Applying the estimated biases and scale factors on the accelerometer measurements (see Eq. (3.1.2)) results in calibrated accelerometer data. The results of the three approaches were analysed in Vielberg et al. (2018) and differences between the estimation procedures are visible for each axis. In the radial direction, the differences in the biases from the three approaches are around 30 %, which is remarkable as the chosen calibration strongly impacts the further processing. In the along-track and cross-track directions, the POD-based calibration parameters provide the most stable biases.

Since the along-track biases are most important for the neutral density estimation, this method has been selected in Vielberg et al. (2018). However, for other purposes these calibration parameters might not be the best choice as the radial component is quite unstable. Consequently, the choice of the accelerometer calibration procedure and the resulting calibration parameters differ depending on the application. This appears unphysical since the calibration of an instrument should be non-ambiguous. However, in the context of the calibration of physical models such as the WaterGAP global hydrological model (Döll et al., 2023), calibrating all required parameters for each purpose at once is known to be extremely challenging due to the so-called equifinality property.

In this thesis, the calibration parameters (daily biases and mission scale factors) are obtained within a POD using the three-step procedure mentioned above following Vielberg et al. (2018) with updated background models as shown in Tab. 3.2.

Table 3.2: Geophysical background models used in POD-based accelerometer calibration. Modifications w.r.t. Vielberg et al. (2018) are marked with *.

| Parameters | Temporal resolution |
|---|---|
| Earth gravity field* | Static part*: GOCO06s (Kvas et al., 2019b) up to d/o 120<br>Time variable part*: ITSG2018 (Kvas et al., 2019a) up to d/o 60 |
| Sub-monthly non-tidal atmosphere and ocean gravity field disturbances* | AOD1B RL 06 (Dobslaw et al., 2017) |
| Direct tides | JPL DE-421 ephemerides: Sun, Moon, Planets |
| Solid Earth tides | IERS Conventions 2010 |
| Ocean tides* | FES2014b (Carrere et al., 2015) |
| Ocean pole tide | Desai (2002) |
| Solid Earth pole tide | IERS Conventions 2010 |
| Permanent tides | IERS Conventions 2010 |

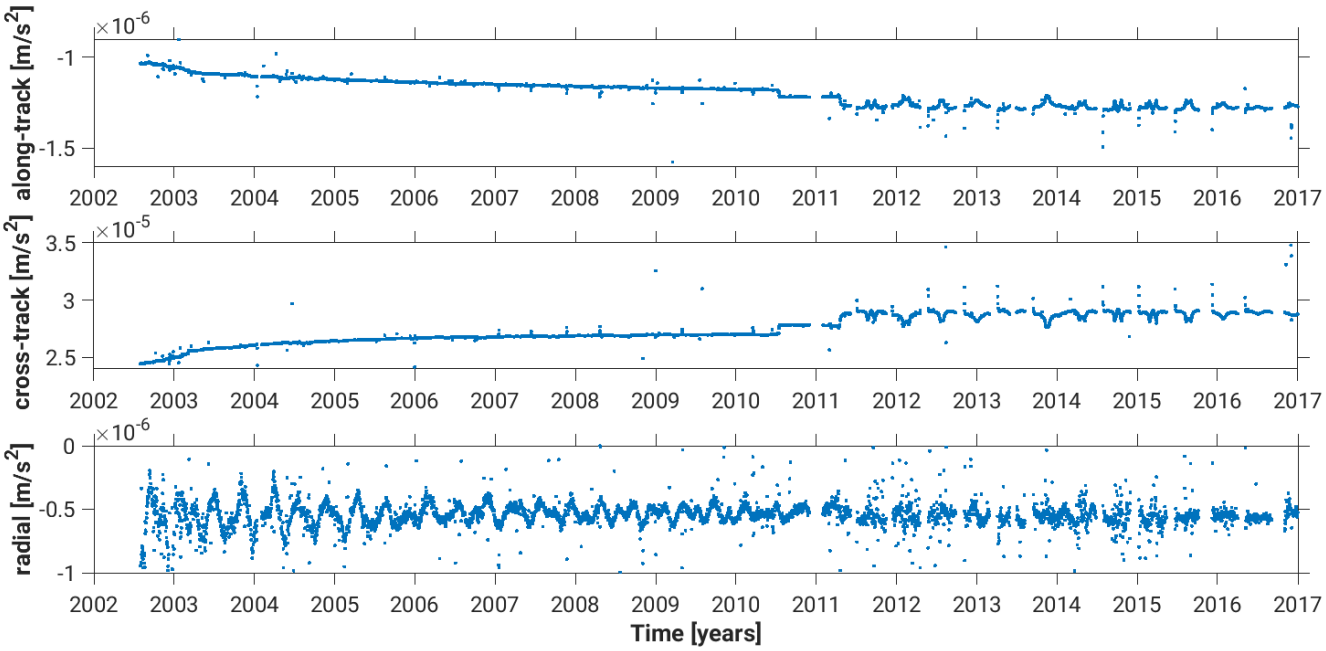



Figure 3.5: Accelerometer bias in the along-track (top), cross-track (middle), and radial directions (bottom) estimated within a POD using a three-step approach: (1) Estimation of daily biases and scale factors, (2) averaging the scale factors for the whole mission resulting in the scale factors 0.94 (along-track), 0.91 (cross-track), 0.93 (radial), (3) estimating daily biases with constrained scale factors from (2).

The resulting biases in along-track, cross-track and radial directions for GRACE-A during the mission lifetime are shown in Fig. 3.5. The along-track and cross-track biases are generally quite smooth until the switch-off of the satellite's thermal control in April 2011, where a cyclic behaviour due to variations of the $\beta'$ angle becomes visible. Beforehand biases of around -1.1×10$^{-6}$ m/s$^2$ and 2.7×10$^{-5}$ m/s$^2$ occur in along-track and cross-track directions, respectively. The radial biases vary strongly between -1×10$^{-6}$ m/s$^2$ and -0.3×10$^{-6}$ m/s$^2$ during the satellite's lifetime with smaller variations during solar minimum. This suggests that bias variations depend on thermospheric neutral density variations, which implies that the simple bias model is likely insufficient. The variations show a cyclic behaviour of roughly four months. The behaviour is also visible within the biases from Siemes et al. (2023) (Fig. 5) before constraining the radial component. The reason for this behaviour is not fully clear. What can be said is that there is a strong correlation between the along-track and radial directions due to the orbital physics: decelerations in the along-track direction lead to an orbital decay. Thus, the cyclic behaviour of the radial biases is likely related to the along-track biases. Further experiments are required, to understand and solve the cyclic behaviour of the radial biases. These should include analyses in the frequency domain, e.g., using a fast Fourier transform.

## 3.2 Satellite laser ranging (SLR)

SLR is a geodetic measurement technique, which allows to determine the precise position of satellites equipped with laser retro reflectors (e.g., Pearlman et al., 2019b). Geodetic SLR missions are spherical satellites at least partly covered with retro reflectors. Due to their small area to mass ratio the aerodynamic acceleration is reduced, which enables a long mission lifetime at around 1000 km altitude. Nowadays, a variety of remote sensing and navigation satellites are also equipped with a retro reflector to allow precise positioning from a combination of measurement techniques.

### 3.2.1 Measurement principle

From a ground station, a laser pulse leaves the telescope in the direction of a satellite, where it is reflected at the laser retro reflector back to the telescope. The measurement quantity is the two-way travel time $\Delta\tau$ of the laser pulse, which can be converted into the measured range $\rho$ between satellite and ground station

$$\rho + \epsilon = \frac{c\Delta\tau}{2} \tag{3.2.1}$$

with speed of light $c$ and measurement error $\epsilon$. These range measurements are generally stored in terms of normal points and are available from the International Laser Ranging Service (ILRS) (Pearlman et al., 2019b) at `https://ilrs.gsfc.nasa.gov/`, last access: July 18, 2023. To obtain the geometrical range between the station and the satellite, the range measurement needs to be corrected, e.g., for tropospheric refraction, relativistic, the system delay in the ground system and the satellite's mass centre offset. Within a POD, modelled ranges are fitted to the observations within an iterative least squares estimation.

Minimizing the observation residuals within a POD also allows for the estimation of several parameters such as the satellite orbits at cm-accuracy, coordinates of the ground stations, Earth rotation parameters, gravity field coefficients, and the centre of mass of the Earth (Pearlman et al., 2019b). Together with DORIS, GNSS, and Very Long Baseline Interferometry (VLBI), the SLR measurements contribute to the International Earth Rotation and Reference Systems Service (IERS) with the aim to provide realizations of reference system as well as Earth orientation parameters and further standards.

The SLR processing (Löcher and Kusche, 2019; Löcher and Kusche, 2021) as it is used in this thesis has been implemented and prepared by Anno Löcher at Institute of Geodesy and Geoinformation (IGG) and is part of the in-house Gravity Recovery Object Oriented Programming System (GROOPS) software.

### 3.2.2 Overview of SLR missions

Within this thesis, the six spherical SLR satellites Ajisai, LAGEOS 1 and 2, Larets, Starlette, and Stella are considered. These satellites, illustrated in Fig. 3.6, have been launched between 1975 and 2003 beginning with Starlette and are still in orbit (Pearlman et al., 2019a).



(a) Ajisai (b) LAGEOS 1 and 2 (c) Larets (d) Starlette/Stella

Figure 3.6: Selected SLR satellites. Images from Pearlman et al. (2019).

Ajisai is covered with mirrors and Corner Cube Reflectors (CCRs) to reflect the laser, whereas LAGEOS 1 and 2, Larets, Starlette, and Stella are covered with CCRs only. The main characteristics of the selected missions including the orbital parameters are summarized in Tab. 3.3. The selected satellites orbit above 650 km, of which Larets has the lowest orbital altitude of 691 km and LAGEOS 1 and 2 have the highest orbit of about 5700 km. The altitude difference between perigee and apogee depends on the orbit design especially on the eccentricity and is relatively large for Starlette with 0.021 leading to altitude variations of about 200 km. These six satellites are selected for the forward force modelling of spherical satellite as well as their validation in Sect. 5.2. Further, the satellites are utilized in the inverse estimations in this thesis.

Table 3.3: Overview of the characteristics of selected geodetic SLR missions modified from Pearlman et al. (2019) with additional surface information from Otsubo and Appleby (2003).

| | Ajisai | LAGEOS 1 | LAGEOS 2 | Larets | Starlette | Stella |
|---|---|---|---|---|---|---|
| Launch date | Aug. 12, 1986 | May 4, 1976 | Oct. 22, 1992 | Sep. 27, 2003 | Feb. 6, 1975 | Sep. 26, 1993 |
| Perigee altitude [km] | 1479 | 5845 | 5616.73 | 675 | 812 | 804 |
| Apogee altitude [km] | 1497 | 5955 | 5950.68 | 696 | 1114 | 812 |
| Mass [kg] | 685 | 406.965 | 405.380 | 23.3 | 47.29 | 48 |
| Radius [cm] | 108 | 30 | 30 | 12 | 12 | 12 |
| Orbital period [min] | 115.7 | 225.7 | 222.46 | 98 | 104.2 | 101 |
| Eccentricity [-] | 0.002 | 0.004 | 0.014 | 0.002 | 0.021 | 0.001 |
| Inclination [°] | 50 | 109.83 | 52.65 | 98.2 | 49.83 | 98.68 |
| Number of CCRs | 1436 | 426 | 426 | 60 | 60 | 60 |
| Material of CCRs | fused silica | fused silica (422)<br>germanium (4) | fused silica (422)<br>germanium (4) | fused silica | fused silica | fused silica |
| Number of mirrors | 318 | 0 | 0 | 0 | 0 | 0 |
| Surface area | 7.1% CCRs,<br>7.5% aluminium,<br>7.8% mirrors,<br>7% glass fibre<br>reinforced plastic | 43% CCRs,<br>57% aluminium | 43% CCRs,<br>57% aluminium | not found | not found | not found |

# Chapter 4

# Non-gravitational satellite force modelling

This chapter presents the modelling of the individual non-gravitational accelerations acting on a satellite due to aerodynamics $\boldsymbol{a}_{\text{aero}}$ (Sect. 4.1), radiation pressure $\boldsymbol{a}_{\text{RP}}$ (Sect. 4.2) and satellite-induced effects $\boldsymbol{a}_{\text{sat}}$ (Sect. 4.3). The sum of these individually modelled accelerations (see Eq. (3.1.1))

$$\boldsymbol{a}_{\text{ng}} = \boldsymbol{a}_{\text{aero}} + \boldsymbol{a}_{\text{RP}} + \boldsymbol{a}_{\text{sat}}$$

yields the modelled total non-gravitational acceleration $\boldsymbol{a}_{\text{ng}}$ acting on a satellite. In the context of satellite dynamics, the non-gravitational force models are commonly expressed in terms of accelerations, which can easily be converted to forces $\boldsymbol{f}_{\text{ng}}$ by multiplying with the satellite's mass $m$

$$\boldsymbol{f}_{\text{ng}} = m\,\boldsymbol{a}_{\text{ng}}. \tag{4.0.1}$$

First, the aerodynamic model applied in this thesis is presented. Then, the focus of this chapter is on the detailed discussion of the radiation pressure force modelling, where different stages of complexity are presented with a focus on a GRACE-like satellite, i.e., a satellite with flat surface panels. My own contributions to improving the radiation pressure force models are outlined as well. Parts of this section are already published in Vielberg and Kusche (2020). Afterwards, satellite-induced forces, which also perturb the satellite's motion, are discussed. The results of the modelled non-gravitational forces will be presented in Chap. 5.

## 4.1 Aerodynamics

The interaction of particles in the atmosphere with the satellite's surface is mainly directed anti-along-track, thus, causing a deceleration of the satellite. In addition, the wind velocity in the thermosphere impacts the satellite's motion. The aerodynamic signal is largest for satellites at low altitudes due to the thermospheric neutral density, which decreases nearly exponentially with altitude (see Fig. 2.1).

Since the beginning of the satellite era, aerodynamic models have been developed (e.g., Sentman, 1961; Cook, 1965) considering the incident particle flux as well as the reflected particle flux. More recently, several studies (Moe and Moe, 2005; Sutton, 2009; Doornbos, 2012; Pilinski et al., 2010; Walker et al., 2014; March et al., 2017; Mehta and Linares, 2018; Bernstein and Pilinski, 2022) investigated the improvement of the reflected particle flux and its angular distribution by developing more realistic gas-surface interaction models, however, the data base is still sparse and several assumptions are required. In addition, high-fidelity models of the satellite's shape enable a further improvement of the satellite's aerodynamic modelling (March et al., 2019a; March, 2020). This thesis does not aim at improving aerodynamic force models. The focus here is on the altitude range of LEO satellites, where certain molecular flow conditions are predominant.

The aerodynamic acceleration acting on a single surface of the satellite can be modelled analytically (Sentman, 1961; Montenbruck and Gill, 2012; Sutton, 2009; Doornbos, 2012) in the SRF as

$$\boldsymbol{a}_{\text{aero}} = \frac{1}{2}\frac{A_{\text{ref}}}{m}\boldsymbol{C}_{\text{a}}\rho v_{\text{r}}^2. \tag{4.1.1}$$

The aerodynamic acceleration is proportional to the thermospheric neutral density $\rho$ at the position of the satellite, which can be obtained from physical or empirical models. In this thesis, the neutral density is extracted from NRLMSIS 2.0 (Emmert et al., 2020). The interaction of the atmospheric particles with the satellite's surface is accounted for within the aerodynamic coefficient vector $\boldsymbol{C}_{\text{a}} \in \mathbb{R}^{3\times 1}$, which is explained in detail in Sect. 4.1.1. In addition, the satellite's area projected into flight direction $A_{\text{ref}}$ needs to be determined because it varies with the satellite's attitude. Even small attitude variations, e.g., approximately 2° for GRACE, impact the aerodynamic acceleration. The satellite's mass $m$ is considered here as in the Radiation Pressure (RP) modelling (see Sect. 4.2.1) and the satellite's velocity relative to the Earth's atmosphere $v_{\text{r}}$ is taken into account as explained in Sect. 4.1.2). Evaluating and summing up the aerodynamic acceleration (Eq. (4.1.1)) for each panel of the satellite yields the total aerodynamic signal.

The aerodynamic acceleration is often simplified by the drag acceleration, which results from the projection of the aerodynamic acceleration in flight direction. This can be implemented by introducing the drag coefficient

$$C_{\text{D}} = \boldsymbol{C}_{\text{a}} \cdot \hat{\boldsymbol{v}}_{\text{r}} \tag{4.1.2}$$

as a scalar resulting from the projection of the aerodynamic coefficient in the normalized direction of the satellite's velocity vector relative to the atmosphere $\hat{\boldsymbol{v}}_{\text{r}}$. Then, the drag acceleration acting on one panel of the satellite reads

$$\boldsymbol{a}_{\text{D}} = \frac{C_{\text{D}}A_{\text{ref}}}{m}\frac{1}{2}\rho v_{\text{r}}^2\hat{\boldsymbol{v}}_{\text{r}}. \tag{4.1.3}$$

For spherical satellites, only the drag acceleration is considered in the force modelling because the perpendicular forces (lift and side effects) are negligible due to the symmetrical shape (Doornbos, 2012).

### 4.1.1 Aerodynamic coefficient

The aerodynamic coefficient vector is modelled in this thesis following Doornbos, 2012. The model accounts for the gas-surface interaction according to Sentman (1961) in combination with the energy flux accommodation coefficient from Moe et al. (2004). Sentman (1961) assumes a Maxwell distribution of the thermal motion of the incident gas particles and their purely diffuse reflection at the satellite's surface.

The aerodynamic coefficient (Doornbos, 2012)

$$\boldsymbol{C}_{\text{a}} = \sum_{j=1}^{M}\frac{\rho_j}{\rho}\left(C_{\text{D},j}\hat{\boldsymbol{u}}_{\text{D}} + C_{\text{L},j}\hat{\boldsymbol{u}}_{\text{L}}\right) \tag{4.1.4}$$

results from the sum over the contribution of drag as well as lift and side effects for each atmospheric constituent $j$ interacting with one panel of the satellite. The thermospheric neutral density $\rho$ at the position of the satellite as well as the number density $\rho_j$ of the $M = 8$ species helium (He), hydrogen (H), oxygen (O, $O_2$, $O^+$), nitrogen (N, $N_2$), argon (Ar) are extracted from NRLMSIS 2.0. In Eq. (4.1.4), $C_{\text{D},j}$ denotes the drag force coefficient and $C_{\text{L},j}$ is the coefficient for lift and side forces. The unit directions of these force coefficients are considered by

$$\hat{\boldsymbol{u}}_{\text{D}} = \frac{\boldsymbol{v}_{\text{r}}}{||\boldsymbol{v}_{\text{r}}||} \tag{4.1.5}$$

with relative velocity vector $\boldsymbol{v}_{\text{r}}$ and

$$\hat{\boldsymbol{u}}_{\text{L}} = \frac{(\hat{\boldsymbol{u}}_{\text{D}} \times \hat{\boldsymbol{n}}) \times \hat{\boldsymbol{u}}_{\text{D}}}{||\,(\hat{\boldsymbol{u}}_{\text{D}} \times \hat{\boldsymbol{n}}) \times \hat{\boldsymbol{u}}_{\text{D}}||}. \tag{4.1.6}$$

Here, the lift vector $\hat{\boldsymbol{u}}_{\mathrm{L}}$ is orthogonal to the plane defined by the unit surface normal $\hat{\boldsymbol{n}}$ and the drag vector $\hat{\boldsymbol{u}}_{\mathrm{D}}$. For the computation of the force coefficients, the angle $\gamma$ between the inward normal of the satellite's surface panel and the drag vector as well as the angle $l$ between the inward normal and the lift vector are required

$$\gamma = -\hat{\boldsymbol{u}}_{\mathrm{D}} \cdot \hat{\boldsymbol{n}}, \tag{4.1.7}$$

$$l = -\hat{\boldsymbol{u}}_{\mathrm{L}} \cdot \hat{\boldsymbol{n}}. \tag{4.1.8}$$

Then, the drag force coefficient is expressed as

$$C_{\mathrm{D},j} = \left[\frac{P_j}{\sqrt{\pi}} + \gamma Q_j Z_j + \frac{\gamma}{2}\frac{v_{\mathrm{re}}}{v_{\mathrm{inc}}}\left(\gamma\sqrt{\pi}Z_j + P_j\right)\right]\frac{A}{A_{\mathrm{ref}}} \tag{4.1.9}$$

and the lift and side force coefficient results from

$$C_{\mathrm{L},j} = \left[lG_j Z_j + \frac{l}{2}\frac{v_{\mathrm{re}}}{v_{\mathrm{inc}}}\left(\gamma\sqrt{\pi}Z_j + P_j\right)\right]\frac{A}{A_{\mathrm{ref}}}. \tag{4.1.10}$$

Here, $A$ is the area of the surface panel of the satellite and $A_{\mathrm{ref}}$ is the satellite's area projected in flight direction. Then, the ratio $\frac{v_{\mathrm{re}}}{v_{\mathrm{inc}}}$ with the velocity of the re-emitted particles $v_{\mathrm{re}}$ and the velocity of the incoming particles $v_{\mathrm{inc}}$ can be obtained from

$$\frac{v_{\mathrm{re}}}{v_{\mathrm{inc}}} = \sqrt{\frac{1}{2}\left[a + \alpha\left(\frac{4RT_w}{v_{\mathrm{inc}}^2} - 1\right)\right]} \tag{4.1.11}$$

according to Koppenwallner (2009) with an accommodation coefficient of $\alpha = 0.93$ for GRACE. The universal gas constant is denoted by $R$, and the temperature of the wall $T_w$ is assumed to be 273 K following (Doornbos, 2012). For the computation of the drag and lift coefficients, the following expressions are required

$$G_j = \frac{1}{2S_j^2}, \tag{4.1.12}$$

$$P_j = \frac{1}{S_j}\exp\left(-\gamma^2 S_j^2\right), \tag{4.1.13}$$

$$Q_j = 1 + G_j, \tag{4.1.14}$$

$$Z_j = 1 + \operatorname{erf}\left(\gamma S_j\right), \tag{4.1.15}$$

with the error function

$$\operatorname{erf}(x) = \frac{2}{\sqrt{\pi}}\int_0^x \exp\left(-y^2\right)\mathrm{d}y. \tag{4.1.16}$$

Here, speed ratio $S_j$ is a relevant flow characteristic of the incident particle flow, which can be obtained from

$$S_j = \frac{v_{\mathrm{r}}}{c_{\mathrm{mp},j}} = \frac{v_{\mathrm{r}}}{\sqrt{2\frac{\sigma}{m_j}T}} \tag{4.1.17}$$

with the relative velocity of the satellite $v_{\mathrm{r}}$ and the so-called most probable thermal velocity of the particles $c_{\mathrm{mp},j}$, which depends on the Stefan Boltzmann constant $\sigma$, the molecular mass $m_j$ of the particle and the atmospheric temperature $T$. The last two are obtained from NRLMSIS 2.0 in this thesis similar to Sutton (2008).

### 4.1.2 Relative Velocity

The satellite's relative velocity denotes it's velocity relative to the atmosphere (Doornbos et al., 2010). It can be obtained from

$$\boldsymbol{v}_{\mathrm{r}} = -\boldsymbol{R}_{c2s}\boldsymbol{v} + \boldsymbol{R}_{c2s}\boldsymbol{v}_{\mathrm{c}} \tag{4.1.18}$$

and is provided in the SRF. The inertial velocity vector of the satellite $\boldsymbol{v}$ in the CRF is rotated by $\boldsymbol{R}_{c2s}$ to the SRF using star camera data. The velocity vector of the co-rotating atmosphere results from the average Earth rotation $\boldsymbol{\omega} = [0, 0, 0.7292115 \cdot 10^{-4}]^T \frac{\mathrm{rad}}{\mathrm{s}}$ and the position of the satellite $\boldsymbol{r}$

$$\boldsymbol{v}_{\mathrm{c}} = \boldsymbol{\omega} \times \boldsymbol{r}, \tag{4.1.19}$$

which is also rotated from CRF to SRF by applying the rotation matrix $\boldsymbol{R}_{c2s}$. Then, $v_{\mathrm{r}} = ||\boldsymbol{v}_{\mathrm{r}}||$ is the satellite's relative velocity. Different from Doornbos et al. (2010), the horizontal wind velocities are neglected in this thesis.

## 4.2 Radiation pressure

The interaction of the electromagnetic radiation reaching the satellite's surface causes a force, which is known as radiation pressure force. A satellite orbiting the Earth is not only exposed to the solar radiation leading to a SRP acceleration, but also to the sunlight reflected from the Earth's surface, which is the outgoing shortwave radiation, and Earth's thermal infrared radiation, known as outgoing longwave radiation. The last two are summarized as ERP acceleration, which decreases with increasing distance from the Earth's surface and is therefore especially relevant for LEO satellites. The SRP acceleration depends on the distance from the Sun and is thus not necessarily altitude-dependent, but it becomes prevalent at higher altitudes (above 500 km) because the ERP effect decreases. In addition, the sunlight is not only reflected at the Earth's surface, but also at the Moon causing a Lunar Radiation Pressure (LRP) acceleration, which is comparably small for Earth orbiting satellites. The radiation, which is absorbed at the satellite's surfaces, heat up the satellite in addition to the heat generated by internal processes and cause temperature variations. Consequently, the satellite radiates a varying amount of energy into space resulting in the TRP acceleration. Then, the total radiation pressure acceleration acting on a satellite results from the summation of the SRP $\boldsymbol{a}_{\mathrm{SRP}}$, ERP $\boldsymbol{a}_{\mathrm{ERP}}$, LRP $\boldsymbol{a}_{\mathrm{LRP}}$, and TRP $\boldsymbol{a}_{\mathrm{TRP}}$ accelerations

$$\boldsymbol{a}_{\mathrm{RP}} = \boldsymbol{a}_{\mathrm{SRP}} + \boldsymbol{a}_{\mathrm{ERP}} + \boldsymbol{a}_{\mathrm{LRP}} + \boldsymbol{a}_{\mathrm{TRP}}. \tag{4.2.1}$$

Before presenting the analytical models of the individual forces, I show the general radiation pressure equation for an arbitrary radiation acting on a single flat surface of the satellite following Montenbruck and Gill (2012).

The radiation pressure $P$

$$P = \frac{\Phi}{c} = \frac{\Delta E}{A \Delta t c} \tag{4.2.2}$$

depends on the energy flux $\Phi$ and the speed of light $c$ (e.g., Milani et al., 1987; Montenbruck and Gill, 2012; Doornbos, 2012). Here, the energy flux is equal to the energy amount $\Delta E$ passing through area $A$ during time interval $\Delta t$. The energy flux can be the one of Sun, Earth, or Moon, at the position of the satellite. Following Eq. (4.2.2) and considering that the pressure $P$ is defined as the force $f$ per area $A$, the radiation pressure force $f_{\mathrm{RP}}$ can be obtained from

$$f_{\mathrm{RP}} = AP = A\frac{\Phi}{c}. \tag{4.2.3}$$

Since the incident radiation is not always perpendicular on the satellite's surface, the cross-section of the incident light beam is considered by $\cos(\gamma)$, where $\gamma$ is the angle between the incident radiation $\mathbf{s}$ and the normal vector $\mathbf{n}$ of the surface panel, i.e., $\cos(\gamma) = \mathbf{s} \cdot \mathbf{n}$. Then, assuming that the incident radiation reaching the satellite can be reflected or absorbed, a multiplication with the

radiation pressure coefficient $\boldsymbol{c}_\mathrm{R}$ is required. Adding these considerations to Eq. (4.2.3) yields the three dimensional radiation pressure force vector

$$\boldsymbol{f}_\mathrm{RP} = A \cos(\gamma)\, \boldsymbol{c}_\mathrm{R} P. \tag{4.2.4}$$

Since the radiation pressure acting on a satellite is often expressed in terms of an acceleration $\boldsymbol{a}_\mathrm{RP}$, rewriting Eq. (4.2.4) yields the radiation pressure acceleration for one surface panel

$$\boldsymbol{a}_\mathrm{RP} = \frac{A}{m} \cos(\gamma)\, \boldsymbol{c}_\mathrm{R} P \tag{4.2.5}$$

with the satellite's mass $m$. The radiation pressure acceleration experienced by the whole satellite can be obtained by evaluating Eq. (4.2.5) for each surface individually and summing them up. In case of a spherical satellite, such summation is not required. Instead, the area $A$ in Eq. (4.2.5) represents the cross-sectional area of the satellite with the assumption that the surface normal points in the direction of the incoming radiation such that $\gamma = 0$.

All radiation pressure accelerations are commonly expressed in the CRF and then transformed to the SRF. For GRACE, the rotation matrix from CRF to SRF can be built column-wise from the quaternions provided by the star camera data. Spherical satellites are usually not equipped with star cameras, thus, star camera data can be simulated from orbital positions and velocities as explained in App. B.

### 4.2.1 Solar radiation pressure

The electromagnetic radiation of the Sun interacts with the satellite's surface causing a SRP acceleration on the satellite. Each photon reaching the satellite contributes to this acceleration by absorption and reflection depending on the satellite's surface material and area. With changing constellation of Earth, Sun and satellite, the satellite's illumination and thus the resulting acceleration varies being largest in sunlight and zero in umbra. The SRP acceleration is the largest radiation pressure acceleration acting on a satellite.

Generally, radiation pressure accelerations can be modelled empirically or analytically. Empirical models for SRP accelerations have been further developed in the GNSS community during the last decades (Springer et al., 1999; Rodriguez-Solano et al., 2014; Montenbruck et al., 2015; Steigenberger et al., 2015; Arnold et al., 2015; Montenbruck et al., 2017; Wang et al., 2019). The advantage of the empirical models is that the satellite's thermo-optical material properties as well as their mass, attitude, and geometry, which can be highly complex for GNSS satellites, are not necessarily required. Instead, a chosen number of empirical parameters are estimated within an orbit determination procedure. However, these parameters also absorb the mismodelling of other forces (Ziebart, 2004) and mismodelling of SRP propagates to other parameters.

On the other hand, the analytical model allows for the precise computation of the SRP acceleration by considering the physical interaction between the solar radiation and the satellite's surface (Milani et al., 1987). Besides the availability of a precise macro-model including surface areas and material properties, the satellite's mass and attitude information are essential. For analytical models, the requirement of a precise macro-model is also the limitation of this approach, since they are not necessarily provided by the manufacturers and the accuracy of the available thermo-optical properties is not known. In contrast to empirical models, the possible correlation between the orbit and other parameters is reduced in the analytical approach (Arnold et al., 2015).

The analytical model is applicable to spherical satellites (cannonball model) or satellites with flat panels, for which macro-models are available or their shape is approximated by a box or box-wing model to simplify the computations (Marshall et al., 1992; Rodriguez-Solano et al., 2012). Macro-models are also the basis for the very detailed high-fidelity models, which have been developed recently for different satellites and also allow for the application of analytical radiation pressure models (Marshall et al., 1992; Ziebart, 2004; Kenneally, 2016; March et al., 2019a; Wöske et al., 2019). The advantage of these complex models is that they allow for including shadowing effects and thermal radiation in more detail, however, the computational effort can be very large.

Besides analytical and empirical models, semi-empirical SRP models have been developed since the 1990s. Fliegel et al. (1992) and Fliegel and Gallini (1996) tried to reduced the complexity of the analytical SRP computation for a GPS satellite based on a Fourier expansion of the x- and z-components depending on the Sun's elongation. This procedure is similar to the one by McMahon and Scheeres (2012) and McMahon and Scheeres (2014), who derive a truncated Fourier series from an analytical model to account for variations over the course of a year, which decreases the computational effort. These models are similar to the semi-empirical models, such as the adjustable box-wing model (Rodriguez-Solano et al., 2012; Rodriguez-Solano et al., 2014), which combine the estimation of empirical parameters with the use of analytical models. However, the unavailability of surface area and thermo-optical properties again limits this approach (Montenbruck et al., 2015).

Before discussing the individual components, which are required for modelling the SRP acceleration analytically, the general RP model for one surface panel (Eq. (4.2.5)) is specified for the general analytical SRP acceleration

$$\boldsymbol{a}_{\mathrm{SRP}} = \frac{A}{m} \cos(\gamma)\, \nu \int_{\lambda} \boldsymbol{c}_{\mathrm{R}}^{\odot}(\lambda) P_{\odot}(\lambda) \mathrm{d}\lambda. \tag{4.2.6}$$

Here, Eq. (4.2.5) is modified by combining it with the wavelength-dependent representation of the flux (e.g., Prölss, 2012). Then, both the radiation pressure coefficient $\boldsymbol{c}_{\mathrm{R}}$ and the radiation pressure $P$ depend on the wavelength $\lambda$, and the spectrum of $P$ is specified for the Sun $\odot$. Additionally, the SRP depends on the shadow function $\nu$, which indicates whether the satellite is located in direct sunlight, in shadow or in semi-shadow. In the remaining section, the approximations and the consistency of the individual components of the SRP model and commonly used data sets are discussed with a focus on a GRACE-like satellite.

### Surface area

The area $A$ of the satellite's surface panels and the panels' orientation in a satellite frame forms the geometric satellite model. For GRACE, the macro-model by Bettadpur (2012) (see Tab. 3.1) is applied. While very recent studies (March et al., 2019a; Wöske et al., 2019) consider finite-element models, the 8-panel model from Bettadpur (2012) is used in this thesis. Errors in these models are usually not specified, even though they would be helpful for developing a realistic error budget.

### Satellite's mass

The satellite's mass $m$ in Eq. (4.2.6) is required to convert the radiation pressure forces to accelerations. During a mission's lifetime, the mass decreases due to the consumption of fuel as it is shown in Fig. 4.1 for GRACE-A and GRACE-B.

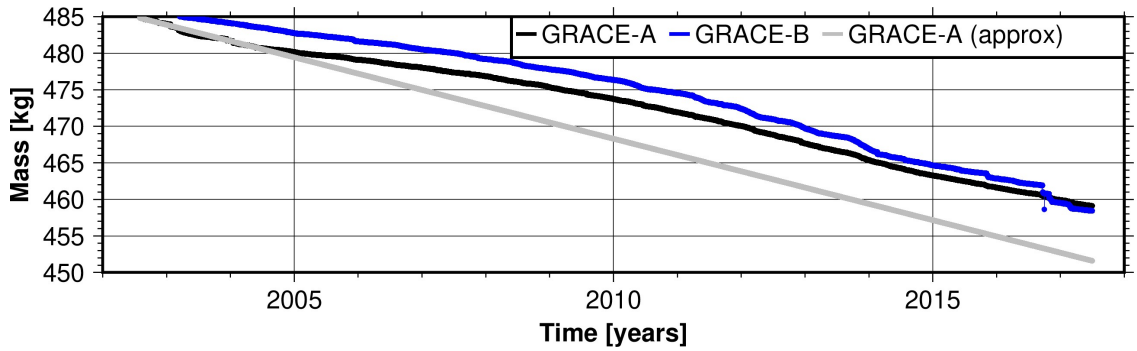



Figure 4.1: Mass of GRACE-A and GRACE-B during the mission lifetime from Mass L1B (MAS1B) product and a linear approximation for GRACE-A as suggested in Tapley et al. (2007).

Assuming a linear mass loss [kg] as in Tapley et al. (2007)

$$m_{\mathrm{GRACE-A}} = 482.6 - 0.0061\,(T - 52850)\,[\mathrm{kg}] \tag{4.2.7}$$

with current time $T$ in Modified Julian Date (MJD) might be helpful for approximating the mass during short time spans, however, it can only be seen as a rough approximation and is not recommended for the whole lifetime. In this thesis, I apply the mass from tank sensors, which is available from the MAS1B product (see Sect. 3.1.3).

**Wavelength-dependency**

Photon energy depends on the wavelength $\lambda$, and the SRP acceleration thus depends on the solar irradiance spectrum. Integrating over all wavelengths of the spectrum yields the total solar irradiance of approximately $1362\,\mathrm{W/m^2}$ averaged between mid 1970s to 2017 (Dewitte and Clerbaux, 2017) and $1360.5\,\mathrm{W/m^2}$ during the solar minimum in 2008 (Kopp and Lean, 2011), respectively. SRP models commonly use visible wavelengths only (e.g., Sutton et al., 2007; Cerri et al., 2010; Doornbos, 2012; Wöske et al., 2019) as input, which is - at least for GNSS satellites - due to the lack of thermal material properties (e.g., Ziebart, 2004; Hackel et al., 2017). When the material properties are given in the visible and infrared domain, the $\lambda$-integration in Eq. (4.2.6) can be discretized by an equally weighted summation of visible and infrared light

$$\boldsymbol{a}_{\mathrm{SRP}} = \frac{A}{m}\cos(\gamma)\,\nu\frac{1}{2}\left(\boldsymbol{c}^{\odot}_{\mathrm{R_{SW}}} + \boldsymbol{c}^{\odot}_{\mathrm{R_{LW}}}\right) P_{\odot}(\lambda). \tag{4.2.8}$$

However, there is usually no information provided on the wavelength-band, at which given material properties are strictly valid, e.g., Robertson (2015) splits the solar spectrum at the visible/IR boundary of 700 nm when accounting for the solar flux in the SRP computations with appropriate material coefficients in the visible and IR domain.

Similar integration over all wavelengths of the solar spectrum is also used in thermosphere modelling (e.g., TIE-GCM, Qian et al., 2014) to account for the interactions of thermospheric constituents with the solar irradiance at discrete spectral lines. For this, typically a solar extreme ultraviolet proxy model, e.g., EUVAC (Richards et al., 1994), is applied. Providing the thermo-optical material coefficients for multiple wavelengths such as UV radiation would thus allow to discretize the integration over all wavelengths in more detail for future missions, and consistent with thermosphere density modelling.

**Radiation pressure**

The radiation pressure of the Sun $P_{\odot}(\lambda)$ is commonly computed from the solar radiation pressure at one astronomical unit (1 AU), which is related to the radiation pressure at the current position of the satellite using the inverse square law

$$P_{\odot}(\lambda) = \left(\frac{1\,\mathrm{AU}}{r_{\odot,\mathrm{sat}}}\right)^2 P_{1\,\mathrm{AU}}(\lambda), \tag{4.2.9}$$

where $r_{\odot,\mathrm{sat}}$ is the distance from the Sun to the satellite, and the position of the Sun can be obtained, e.g., from JPL DE421 ephemerides (Folkner et al., 2008). Solar radiation pressure at 1 AU is commonly approximated by the ratio of the solar constant $\Phi_{\mathrm{sc}}$ and the speed of light $c$ (e.g., Montenbruck and Gill, 2012)

$$P_{1\,\mathrm{AU}} = \frac{\Phi_{\mathrm{sc}}}{c}. \tag{4.2.10}$$

However, the solar constant is only a temporal average of the Sun's energy flux integrated over all wavelengths $\lambda$. In reality, this energy flux varies with the solar rotation and the solar cycle, the solar constant of $1362\,\mathrm{W/m^2}$ (e.g., Dewitte and Clerbaux, 2017). Therefore, daily TSI measurements, which was already shown in Fig. 2.5, are applied in this thesis. The TSI varies between $1357.0\,\mathrm{W/m^2}$ and $1362.7\,\mathrm{W/m^2}$ since the year 2000.

To account for the temporal variation of the Sun's radiation pressure, Eq. (4.2.9) then becomes additionally time-dependent

$$\boldsymbol{a}_{\mathrm{SRP}} = \frac{A}{m}\cos(\gamma)\,\nu\frac{1}{2}\left(\boldsymbol{c}^{\odot}_{\mathrm{R_{SW}}} + \boldsymbol{c}^{\odot}_{\mathrm{R_{LW}}}\right) P_{\odot}(\lambda, t) \tag{4.2.11}$$

with

$$P_{\odot}(\lambda, t) = \left(\frac{1\,\mathrm{AU}}{r_{\odot,\mathrm{sat}}}\right)^2 P_{1\,\mathrm{AU}}(\lambda, t). \tag{4.2.12}$$

Theoretically, the radiation reaching the satellite depends also on the atmosphere, since radiation can be absorbed, transmitted or scattered by the gases and clouds in the atmosphere (Taylor, 2005; Petty, 2006). This effect is expected to be small for the solar radiation reaching the satellite due to the small amount of gases in the satellite's surrounding. However, it might be larger for the Earth's outgoing radiation, which reaches the satellite after propagating through the atmosphere. In the LEO satellite force modelling, this effect has - at least to my knowledge - not been investigated before and will also not be treated in this thesis because modelling radiative transfer in the atmosphere is a broad and complex topic (Taylor, 2005).

### Radiation pressure coefficient

The radiation pressure (force) coefficient provides the direction of the force resulting from the interaction of the incoming radiation and the satellite's surface. As shown in Fig. 4.2, the photons can be absorbed or reflected at the satellite's surface and the reflection is assumed to be either diffuse or specular depending on the thermo-optical material properties. Other reflection types such as quasi-specular, quasi-Lambertian, or complex reflection are usually not considered. The incoming radiation is usually not only diffusely or specularly reflected, it is rather a combination both. For example, the nadir panel of GRACE (see Sect. 3.1.4) presumably reflects 68 % of the incident radiation specularly and 20 % diffusely, while 12 % are absorbed. The direction of the resulting force depends also on the normalized direction of the incoming radiation $\boldsymbol{s}$, the surface normal $\boldsymbol{n}$ and the angle $\gamma$ between.

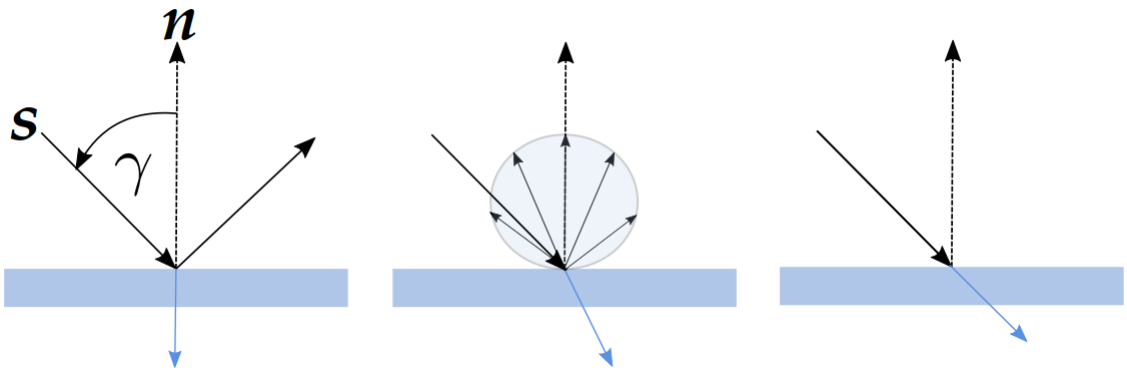



Figure 4.2: Geometrical illustration of specular (left) and diffuse (middle) reflection, and absorption (right) with the direction of incoming photons $\boldsymbol{s}$, the surface normal $\boldsymbol{n}$, and the angle $\gamma$ in between. The direction of the resulting radiation pressure acceleration is shown in blue. This illustration is similar to Doornbos (2012) (Fig. 3.6).

To derive the solar radiation pressure coefficient $\boldsymbol{c}_R^{\odot}$, I assume for now that it only depends on a single wavelength. The three-dimensional radiation pressure coefficient $\boldsymbol{c}_R^{\odot}$ for one surface panel is the sum of the three individual radiation pressure coefficients described below following Fliegel et al. (1992); Doornbos (2012) and Montenbruck and Gill (2012)

$$\boldsymbol{c}_R^{\odot} = \boldsymbol{c}_{R,a}^{\odot} + \boldsymbol{c}_{R,d}^{\odot} + \boldsymbol{c}_{R,s}^{\odot}. \tag{4.2.13}$$

In case the surface material is a mirror, the photons are specularly reflected. The impulse resulting from the specularly reflected radiation acts against the direction of the surface normal $\boldsymbol{n}$ and is twice as large as the incoming radiation

$$\boldsymbol{c}_{R,s}^{\odot} = -c_s 2\cos\gamma \boldsymbol{n}. \tag{4.2.14}$$

It considers the thermo-optical material coefficient for specular reflection $c_s$.

In case of a matt surface material, the incoming radiation is diffusely reflected, where one may assume Lambert's cosine law. Thus, the incoming light is reflected equally into all directions. Integrating over the half sphere results in an impulse that acts against the direction of the surface normal with two-thirds of the incoming radiation. In addition, the impulse in the direction of the incoming radiation needs to be considered, which results in the diffuse radiation pressure coefficient

$$\boldsymbol{c}_{R,d}^{\odot} = c_d \left( \boldsymbol{s}^{\odot} - \frac{2}{3}\boldsymbol{n} \right), \tag{4.2.15}$$

where $c_d$ is thermo-optical material coefficient for diffusely reflected photons. Since the photons, which are not reflected, are absorbed, the absorption coefficient $c_a$ can be directly computed from

$$c_a = 1 - c_s - c_d. \tag{4.2.16}$$

The absorption is taken into account by

$$\boldsymbol{c}_{R,a}^{\odot} = c_a \boldsymbol{s}^{\odot} \tag{4.2.17}$$

as the impulse follows the direction of the incident radiation.

Following this, the three radiation pressure coefficients can be inserted into the general equation of the radiation pressure coefficient (Eq. (4.2.13)) and rearranged to

$$\begin{aligned} \boldsymbol{c}_{R}^{\odot} &= c_d \left( \boldsymbol{s}^{\odot} - \frac{2}{3}\boldsymbol{n} \right) - c_s 2\cos\gamma \boldsymbol{n} + c_a \boldsymbol{s}^{\odot} && (4.2.18)\\ &= c_d \boldsymbol{s}^{\odot} - \left( \frac{2}{3} c_d + c_s 2\cos\gamma \right) \boldsymbol{n} + (1 - c_s - c_d)\boldsymbol{s}^{\odot} && (4.2.19)\\ &= -2\left( \frac{c_d}{3} + c_s \cos\gamma \right) \boldsymbol{n} + (1 - c_s)\, \boldsymbol{s}^{\odot}. && (4.2.20) \end{aligned}$$

The radiation pressure coefficient is zero, if the incident angle $\gamma$ between $\boldsymbol{s}$ and $\boldsymbol{n}$ is larger than 90°. Including the wavelength-dependency of the thermo-optical material coefficients in Eq. (4.2.20) yields the final radiation pressure coefficient

$$\boldsymbol{c}_{\mathrm{R}}^{\odot}(\lambda) = -2\left( \frac{c_d(\lambda)}{3} + c_s(\lambda)\cos\gamma \right) \boldsymbol{n} + (1 - c_s(\lambda))\, \boldsymbol{s}^{\odot}. \tag{4.2.21}$$

**Thermo-optical properties**

As mentioned above, the thermo-optical material coefficients of the satellite's materials are essential for the computation of the RP coefficient. In theory, for each surface material the amount of photons that are reflected (specularly $c_s$ or diffusely $c_d$) and absorbed $c_a$ is required for each wavelength. However, in practice the thermo-optical material coefficients are - if available at all - either assumed to be constant for all wavelengths, or separated for visible and infrared radiation, which simplifies the integration over the wavelengths in Eq. (4.2.6).

During the mission lifetime, the thermo-optical material properties are generally assumed to be constant, even though the ageing of the material in space has already been studied since the 1990s (Stuckey, 1993; Reddy, 1995; Silverman, 1995a), e.g., with the Long Duration Exposure Facility (LDEF) mission. From these studies, material changes are known to depend on the time of UV radiation exposure measured in equivalent solar hours, on the thickness of the coating material and subsequently on the atomic oxygen erosion. The interaction of atomic oxygen on different surface materials of spacecrafts has also been analysed in Reddy (1995); Silverman (1995). The density of atomic oxygen in LEO-altitudes is quite low, nevertheless, the high velocities enable erosion and mass loss leading to changes in the surface material.

Consequently, changes of the thermo-optical material coefficients during the mission lifetime should ideally be considered. Since macro-models themselves are hardly available, this is usually not the case. One exception is the Swarm mission, where absorption coefficients for visible radiation

are provided for a few materials for beginning and end of lifetime (Siemes, 2020), which differ by up to 18%.

In case of GRACE(-FO), the thermo-optical material coefficients are provided for visible and infrared radiation within the macro-model (see Tab. 3.1). Even though, the coefficients are documented for these two bands of the spectrum, the exact wavelengths of the bands are not provided. Thus, it remains unclear, if the IR properties are valid for Near-IR only, which would make them suitable to consider the ERP longwave radiation, or if they can be assumed for wavelengths beyond the visible domain of the solar radiation as well. As mentioned above, Robertson (2015) assumes that the visible coefficients are valid for wavelengths below 700 nm and infrared coefficients above 700 nm to account for the solar spectrum in the these bands. To further this idea, I experimentally design a macro-model with material coefficients for selected wavelengths based on the original macro-model for GRACE, which is tested later in Ch. 5. First, the wavelengths for which the given thermo-optical material properties are valid need to be defined. The provided coefficients for visible radiation are assumed to be valid for the visible band (350-780 nm, see Fig. 2.4), and infrared coefficients are assumed to be valid for wavelengths above the mid-IR band (3 µm, see Fig. 2.7). Thus, I suggest to fix the visible coefficients to 580 nm, and the infrared coefficients to 11.5 µm, which corresponds to the central wavelength of the visible and longwave IR bands, respectively. Then, the coefficients are interpolated for the near and shortwave IR bands with central wavelengths of 1.075 µm and 2.2 µm, respectively. Since I suggested above that the visible coefficients are only valid for the visible band, the coefficients for the UV-band (<380 nm) are extrapolated. Tab. 4.1 provides an overview of the resulting coefficients of the materials used in the GRACE macro-model. When applying this model in the SRP modelling, one needs to know the amount of solar radiation, which can be assigned to these bands. Therefore, the percentage of the integrated measured solar spectral irradiance at TOA for the assumed bands is listed in the table as well. CERES data, which are later on used in the ERP model, are assumed to be valid for the same central wavelength as the given visible and infrared material coefficients. Thus, outgoing radiation at TOA, which already consider ADMs, are interpolated to the central wavelengths from Tab. 4.1 as well when applying the suggested interpolated macro-model.

Table 4.1: Assumptions of wavelength-dependent material coefficients for materials from the GRACE macro-model. Thermo-optical material coefficients for visible and longwave IR are taken from the original macro-model (Bettadpur, 2012), whereas the remaining coefficients result from linear inter- or extrapolation. Absorption coefficients can be computed from $1-\rho_s-\rho_d$. SiOx/Kapton is the material of front, rear, starboard (inner), and port (inner) panels; Teflon is the material of the nadir panel; Si Glass Solar Array is the material of starboard (outer), port (outer), and zenith panels.

| Name | Near UV | Visible | Near IR | SW IR | Mid IR | LW IR | Far IR |
|---|---|---|---|---|---|---|---|
| Wavelength [µm] | 0.315-0.380 | 0.38-0.78 | 0.78-1.4 | 1.4-3 | 3-8 | 8-15 | >15 |
| Central wavelength [µm] | 0.3475 | 0.58 | 1.075 | 2.2 | 5.5 | 11.5 | 22 |
| Solar radiation [%] | 6.0 | 48.4 | 30.3 | 13.6 | 0 | 0 | 0 |
| Earth SW radiation [%] | 6.0 | 48.4 | 30.3 | 13.6 | 0 | 0 | 0 |
| Earth LW radiation [%] | 0 | 0 | 0 | 0 | 14.4 | 42.5 | 43.1 |
| SiOx/Kapton $\rho_s$ | 0.404 | 0.4 | 0.392 | 0.375 | 0.323 | 0.23 | 0.067 |
| SiOx/Kapton $\rho_d$ | 0.262 | 0.26 | 0.255 | 0.244 | 0.210 | 0.15 | 0.044 |
| Teflon $\rho_s$ | 0.69 | 0.68 | 0.658 | 0.607 | 0.459 | 0.19 | 0 |
| Teflon $\rho_d$ | 0.203 | 0.2 | 0.194 | 0.179 | 0.137 | 0.06 | 0 |
| Si Glass Solar Array $\rho_s$ | 0.05 | 0.05 | 0.049 | 0.047 | 0.041 | 0.03 | 0.01 |
| Si Glass Solar Array $\rho_d$ | 0.303 | 0.3 | 0.294 | 0.279 | 0.237 | 0.16 | 0.025 |

In addition, for GRACE(-FO) the absorption coefficient for visible radiation of the solar panels is reported to increase by 7 % in case they are not operating (Bettadpur, 2012). According to Eq. (4.2.16), the sum of the thermo-optical material coefficients has to be equal to 1, however, changes in the reflection coefficients due to operating solar arrays are not documented, and reflection coefficients only for operating panels are provided. Thus, one can either assume that the solar panels are always operating, or specular and diffuse reflection increase (e.g., equally by 3.5 %) in case of non-operating solar panels. Since no explicit data set on the status of the solar panels is available, the solar panels can be assumed to be switched off in the Earth's shadow, where the operation of the solar arrays is not beneficial and visible radiation does not reach the satellite.

Additionally, Siemes et al. (2023) found from the inspection of photographs of the satellites before launch that the material of GRACE and GRACE-FO clearly differs, even though the provided macro-model is identical. Since the material of GRACE-FO appears similar to Swarm, Siemes et al. (2023) suggest corrections for the material based on the Swarm macro-model. Ideally, the thermo-optical material properties should be determined and provided by the manufacturers using spectrometers.

Another issue is the accuracy of the thermo-optical material coefficients, which is usually not provided. Within the GRACE-community, the material properties are often assumed to be incorrect by a few tens of percent (personal communication with Srinivas Bettadpur). For GNSS satellites, Rodriguez-Solano et al. (2012) mention that the optical properties are also inaccurately known. For CHAMP, Bruinsma and Biancale (2003) report that the accuracy of the thermo-optical coefficients is limited due to the coverage with thermal foil after the measurement of these parameters.

**Bidirectional reflectance**

In geodesy and POD, the satellite's surface is traditionally assumed to reflect isotropically. The dependency of the scattered reflection at the satellite's surface on the angle of illumination is rarely considered in satellite force modelling. Other disciplines have more experience in accounting for such anisotropic reflections. For example in computer graphics, an object's reflection has been investigated in consideration of the illumination conditions and the surface material in order to generate photorealistic images (e.g., Pharr et al., 2016). This process is also known as rendering and requires analytical reflection models - so-called Bidirectional Reflectance Distribution Functions (BRDFs), which have been continuously improved during the last decades (e.g., Blinn, 1977; Cook and Torrance, 1982; Schlick, 1994; Ashikhmin and Shirley, 2000; Ashikhmin and Premože, 2007).

The geometry of a BRDF is shown in Fig. 4.3. As BRDFs have originally been developed for rendering images, the direction of the incoming light from an arbitrary source such as the Sun and the direction of the observer, e.g., a camera, are relevant. A BRDF (Pharr et al., 2016) is generally defined as a function of the surface point $\boldsymbol{x}$ and a particular pair of the incoming and outgoing directions of the light $\boldsymbol{\omega}_i$ and $\boldsymbol{\omega}_o$ as

$$f_r\left(\boldsymbol{x}, \boldsymbol{\omega}_o, \boldsymbol{\omega}_i\right) = \frac{\mathrm{d}L_0\left(\boldsymbol{x}, \boldsymbol{\omega}_o\right)}{\mathrm{d}E\left(\boldsymbol{x}, \boldsymbol{\omega}_i\right)} = \frac{\mathrm{d}L_0\left(\boldsymbol{x}, \boldsymbol{\omega}_o\right)}{L_i\left(\boldsymbol{x}, \boldsymbol{\omega}_i\right)\cos\theta_i \mathrm{d}\boldsymbol{\omega}_i}. \tag{4.2.22}$$

It describes the amount of radiance leaving the surface $L_0\left(\boldsymbol{x}, \boldsymbol{\omega}_o\right)$ in dependency of the incident radiance $L_i\left(\boldsymbol{x}, \boldsymbol{\omega}_i\right)$. Here, the differential irradiance $\mathrm{d}E\left(\boldsymbol{x}, \boldsymbol{\omega}_i\right)$ can be described as the incident radiance with the assumption that the direction $\boldsymbol{\omega}_i$ is a differential cone of directions, which are accounted for by $L_i\left(\boldsymbol{x}, \boldsymbol{\omega}_i\right)\cos\theta_i \mathrm{d}\boldsymbol{\omega}_i$. In addition, the proportionality of the reflected differential radiance $\mathrm{d}L_0\left(\boldsymbol{x}, \boldsymbol{\omega}_o\right)$ to the irradiance $\mathrm{d}E\left(\boldsymbol{x}, \boldsymbol{\omega}_i\right)$ is considered.

Physics-based BRDFs fulfil reciprocity and conservation of energy (Pharr et al., 2016). Due to reciprocity, the equation

$$f_r\left(\boldsymbol{x}, \boldsymbol{\omega}_o, \boldsymbol{\omega}_i\right) = \left(\boldsymbol{x}, \boldsymbol{\omega}_i, \boldsymbol{\omega}_o\right) \tag{4.2.23}$$

is valid for all pairs of incoming and outgoing directions $\boldsymbol{\omega}_i$ and $\boldsymbol{\omega}_o$. Energy conservation means in case of BRDFs that the total energy of the light leaving the surface is equal to or smaller than the energy of the incoming light integrated over the hemisphere $H^2$

$$\int_{H^2} f_r\left(\boldsymbol{x}, \boldsymbol{\omega}_o, \boldsymbol{\omega}_i\right)\cos\theta_i \mathrm{d}\boldsymbol{\omega}_i \leq 1. \tag{4.2.24}$$

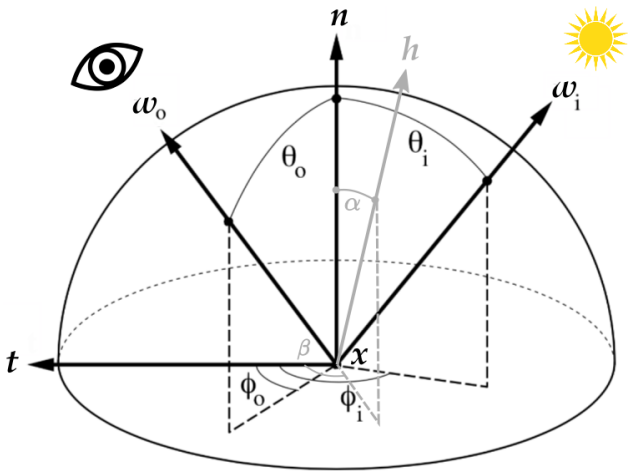



Figure 4.3: Geometry of a BRDF modified from Kenneally and Schaub (2019) (Fig. 4). $\boldsymbol{\omega}_i$ denotes the direction of the incident radiance, e.g., the Sun, on the surface point $\boldsymbol{x}$. $\boldsymbol{\omega}_o$ is the direction of the outgoing radiance as viewed from a camera or observer. The angles between the surface normal $\boldsymbol{n}$ on $\boldsymbol{x}$ and the incident and outgoing radiances are denoted as $\theta_i$ and $\theta_o$, respectively. The angles between the tangential vector $\boldsymbol{t}$ on $\boldsymbol{x}$ and the incident and outgoing radiances are denoted as $\phi_i$ and $\phi_o$, respectively. The vector $\boldsymbol{h}$ is the bisector between the incoming light and the observer. The angles $\alpha$ and $\beta$ are defined between $\boldsymbol{h}$ and the surface normal $\boldsymbol{n}$ and the tangential vector $\boldsymbol{t}$, respectively.

There exist a large variety of BRDFs (e.g., Blinn, 1977; Cook and Torrance, 1982; Schlick, 1994; Ashikhmin and Shirley, 2000; Ashikhmin and Premože, 2007), which have their own applications and purposes. For example, the function developed by Ashikhmin and Shirley (2000) accounts for anisotropy, energy conservation, diffuse and specular bidirectional reflectance, and the Fresnel effect, which considers the reflectance at the interface of different materials such as diffusely reflecting materials below specular surfaces. Rendering images requires the integration of the BRDF over all incident directions. In case there is no analytical solution of this integral, it can be solved numerically, which is however computationally expensive. In computer graphics, numerical solutions are obtained from Monte Carlo algorithms (Pharr et al., 2016).

BRDFs have recently become important for applications beyond computer graphics. For example, in the context of space situational awareness, Linares et al. (2010) suggested the use of BRDFs to obtain orbit, attitude and shape information of space objects. Additionally, Ceniceros et al. (2015) applied BRDFs to compute light curves, i.e., the temporal brightness, of geostationary space objects, which allow for the prediction of telescope observations.

During the last decade, first studies presented the application of BRDFs in RP force modelling, since this is expected to make the force models more realistic provided the underlying assumptions of the BRDF are correct. Kenneally and Schaub (2017) and Kenneally and Schaub (2019) applied BRDFs in the SRP force modelling of LAGEOS 2 and the Mars Reconnaissance Orbiter. The evaluation of the BRDFs is performed numerically with a Monte Carlo importance sampling integration method on a Graphic Processing Unit (GPU), which allows for parallelized and highly efficient computations. The advantage of this method is that it does not only account for realistic reflections of the incoming light, but also for self-reflections and self-shadowing, which become relevant for satellites with complex shapes.

In addition, first investigations of applying the rendering software *Mitsuba 2* (Nimier-David et al., 2019) for SRP modelling of rather simply-shaped satellites have been performed in Börger (2021), where a bias between the SRP acceleration from the analytical force models and the ray-tracing has been identified. The reason is likely related to the consideration of a specific amount of photons in the ray-tracing algorithm, which might not necessarily represent the flux used in analytical force models.

Instead of solving the integration over the BRDFs numerically, Wetterer et al. (2014) solved selected BRDFs analytically, which are then used to derive correction factors for the thermo-optical material properties in the SRP force modelling. This approach does not account for self-shadowing or multiple reflections, however, it has the advantage of including the bidirectional surface reflections in a simplistic way.

In this thesis, the approach by Wetterer et al. (2014) has been implemented for the GRACE satellite in SRP force modelling. In the following, the consideration of the Ashikhmin-Shirley BRDF (Ashikhmin and Shirley, 2000) in terms of correction factors for the thermo-optical material coefficients within the computation of the radiation pressure coefficient is described according to Wetterer et al. (2014).

Following Wetterer et al. (2014), the general BRDF can be written as

$$f_r = dR_d + sR_s. \tag{4.2.25}$$

Here, $d$ and $s$ are the fractions of diffuse and specular reflection, respectively, so that $d + s = 1$. These fractions can be obtained using the reflection coefficients $c_d$ and $c_s$ from the macro-model

$$d = \frac{c_d}{c_d + c_s} \tag{4.2.26}$$

$$s = \frac{c_s}{c_d + c_s}. \tag{4.2.27}$$

Thus, it is possible to obtain the correction factors for visible and infra-red material coefficients separately. Since the transmission of light is not relevant for the satellite's surface materials, the bidirectional transmittance distribution functions (Pharr et al., 2016), which are also important for physics-based rendering, can be neglected in SRP force modelling.

The Ashikhmin and Shirley (2000) BRDF accounts for anisotropic reflection and is a progression of the widely used Phong model Phong (1975). For diffuse and specular bidirectional reflectance, the BRDFs by Ashikhmin and Shirley (2000) read

$$R_d = \frac{28 c_d}{23\pi} (1 - s c_s) \left(1 - \left(1 - \frac{\boldsymbol{n} \cdot \boldsymbol{\omega}_i}{2}\right)^5\right) \left(1 - \left(1 - \frac{\boldsymbol{n} \cdot \boldsymbol{\omega}_o}{2}\right)^5\right), \tag{4.2.28}$$

$$R_s = \frac{\sqrt{(n_u + 1)(n_v + 1)}}{8\pi} \frac{F}{(\boldsymbol{\omega}_o \cdot \boldsymbol{h})\, max\left[\boldsymbol{n} \cdot \boldsymbol{\omega}_i, \boldsymbol{n} \cdot \boldsymbol{\omega}_o\right]} (\cos\alpha)^{n_u \cos^2\beta + n_v \sin^2\beta}, \tag{4.2.29}$$

respectively. The diffuse term (Eq. (4.2.28)) is a non-Lambertian BRDF and energy conservation is guaranteed by the leading term. The specular term (Eq. (4.2.29)) accounts for Fresnel reflectance $F$ given by Schlick's approximation (Schlick, 1994)

$$F(\theta, s, c_s) = c_s + \left(\frac{1}{s} - c_s\right)(1 - \cos\theta_i)^5, \tag{4.2.30}$$

which considers the reflectance at the interface of different materials such as diffusely reflecting materials below specular surfaces. In Eq. (4.2.29), $\boldsymbol{h} = \frac{\boldsymbol{\omega}_i + \boldsymbol{\omega}_o}{|\boldsymbol{\omega}_i + \boldsymbol{\omega}_o|}$ is the bisector vector between the incoming light and the observer. The angles $\alpha$ and $\beta$ are defined between the vector $\boldsymbol{h}$ and surface normal $\boldsymbol{n}$, and between $\boldsymbol{h}$ and the tangential vector $\boldsymbol{t}$, respectively (see Fig. 4.3). $n_u$ and $n_v$ are the Phong-like exponents (Shirley and Wang, 1992) to control the shape of the specular lobe. Increasing values of $n$ indicate that the reflection behaviour is closer to a mirror. Small values of $n$ yield unrealistic energy conservation properties, however, I found that setting the exponents to one minimizes the difference to the radiation pressure coefficient from Eq. (4.2.20).

Based on the BRDFs by Ashikhmin and Shirley (2000), Wetterer et al. (2014) derive correction factors for the reflection terms of the radiation pressure coefficient (Eq. (4.2.20)). For the diffuse component (see also Eq. (4.2.15)), the correction term reads

$$\Delta_d = \left[\frac{31}{32}(1 - s c_s)\right] \frac{1573}{1426} \left(1 - \left(1 - \frac{\cos\theta_i}{2}\right)^5\right). \tag{4.2.31}$$

For the specular component (see also Eq. (4.2.14)), Wetterer et al. (2014) formulate two correction terms based on the Ashikhmin-Shirley BRDF (Eq. (4.2.29))

$$\Delta_{s1} = \Delta_{AS1}(n)\Delta_{AS2}(\theta_i, s, c_s)\delta_{s1}(\theta_i, n, c_s), \tag{4.2.32}$$

$$\Delta_{s2} = \Delta_{AS1}(n)\Delta_{AS2}(\theta_i, s, c_s)\delta_{s2}(\theta_i, n, c_s), \tag{4.2.33}$$

with $n_v = n_u = n$ and the analytical equations

$$\Delta_{AS1}(n) = 1 - \frac{2^{3-(n+1)/2} + 8(n+1)}{(n+5)(n+3)}, \tag{4.2.34}$$

$$\Delta_{AS2}(\theta_i, s, c_s) = \frac{F(\theta_i, s, c_s)}{c_s}. \tag{4.2.35}$$

Obtaining the $\delta$ terms in Eqs. (4.2.32) and (4.2.33) requires two steps. First, a numerical formulation can be obtained from

$$\Delta_{s1}(\theta_i, c_s)_{\text{numerical}} = \frac{(\boldsymbol{\omega}_i' \cdot \boldsymbol{n})\cos\theta_i - (\boldsymbol{\omega}_i' \cdot \boldsymbol{\omega}_i)}{c_s \sin^2\theta_i}, \tag{4.2.36}$$

$$\Delta_{s2}(\theta_i, c_s)_{\text{numerical}} = \frac{(\boldsymbol{\omega}_i' \cdot \boldsymbol{n}) - (\boldsymbol{\omega}_i' \cdot \boldsymbol{\omega}_i)\cos\theta_i}{2c_s \cos\theta_i \sin^2\theta_i}, \tag{4.2.37}$$

with the integration of the BRDF (Eq. (4.2.25)) over all viewing angles

$$\boldsymbol{\omega}_i' = \int_{2\pi} f_r \cos\theta_o \boldsymbol{\omega}_o \mathrm{d}\omega_o, \tag{4.2.38}$$

where $p$ are the parameters in the BRDF. In a second step, the $\delta$ terms are formulated as the residuals between the numerical and the analytical formulations

$$\delta_{s1}(\theta_i, n, c_s) = \Delta_{AS1}(n) - \Delta_{s1}(\theta_i, c_s)_{\text{numerical}}, \tag{4.2.39}$$

$$\delta_{s2}(\theta_i, n, c_s) = \Delta_{AS2}(n) - \Delta_{s2}(\theta_i, c_s)_{\text{numerical}}. \tag{4.2.40}$$

The correction factors $\Delta_d, \Delta_{s1}, \Delta_{s2}$ can be stored in a look-up table, which requires the computations for several combinations of illumination angles and material properties.

Finally, including the BRDF (Ashikhmin and Shirley, 2000) in terms of correction factors $\Delta_d, \Delta_{s1}, \Delta_{s2}$ for the thermo-optical material properties leads to the following extension of the radiation pressure coefficient from Eq. (4.2.20)

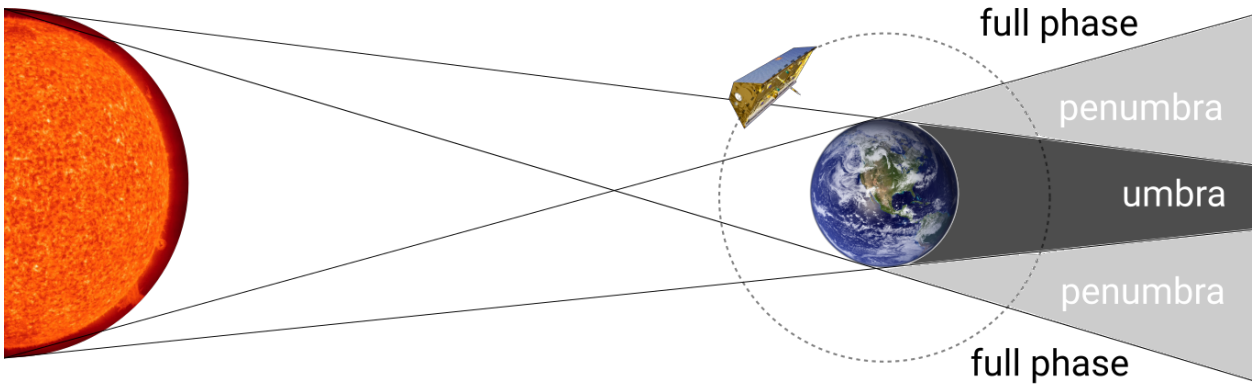
$$\boldsymbol{c}_{\mathrm{R}}^{\odot}(\lambda) = -2\left(\frac{c_d(\lambda)\Delta_d(\lambda)}{3} + c_s(\lambda)\Delta_{s2}(\lambda)\cos\gamma\right)\boldsymbol{n} + (1 - c_s(\lambda)\Delta_{s1}(\lambda))\,\boldsymbol{s}^{\odot}. \tag{4.2.41}$$

Here, the correction factors are included in dependency of the wavelength because they can be computed for different material properties of visible and infrared radiation.

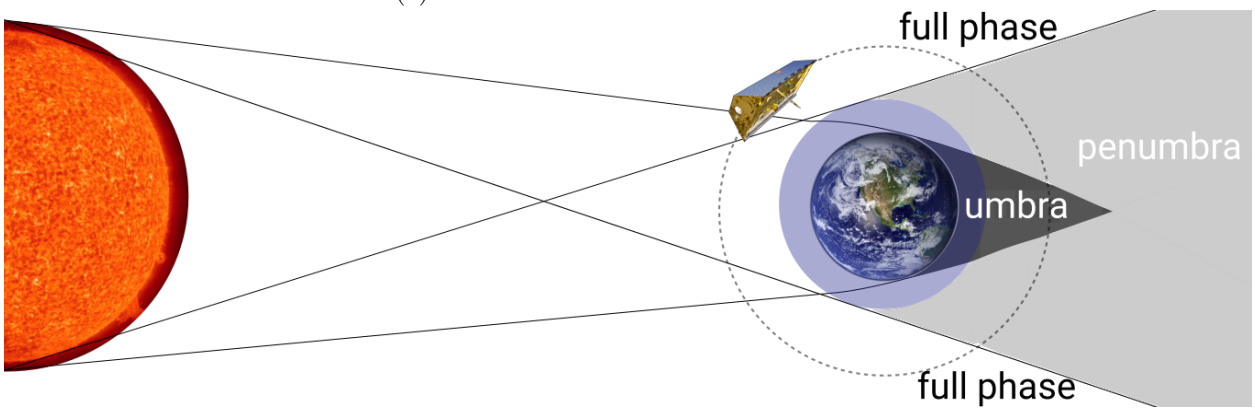
### Shadow function

In Eq. (4.2.6), the shadow function $\nu$ indicates whether the satellite is located in direct sunlight, in shadow or in semi-shadow. As shown in Fig. 4.4a, the amount of solar radiation reaching the satellite depends on the constellation of Earth, Sun and satellite. The shadow function is zero in umbra, where SRP is not relevant, one in full sunlight, and deviates between zero and one in between. For GRACE, the penumbra transition lasted nearly two minutes during January 2010, when the $\beta'$ angle was about 37°.

There exist different shadow functions from simple geometrical to complex physical. The most basic shadow function is a cylindrical model that only distinguishes between sunlight and shadow (e.g., Hubaux et al., 2012) with values of 1 and 0, respectively. However, as also demonstrated in Fig. 4.4, penumbra regions exist, which should not be ignored. Geometrically more advanced are conical models that enable to distinguish between sunlight, shadow, and semi-shadow. These




(a) Sketch of a conical shadow function.




(b) Sketch of a shadow function that considers the physical processes that the light experiences by travelling through the atmosphere.

Figure 4.4: Geometrical sketch of the shadow function in case of (a) a conical model and (b) a model considering the effects of the atmosphere on the light's path. The dimensions in both figures are exaggerated here for demonstration purposes.

conical models often assume a spherical Earth (Montenbruck and Gill, 2012), and sometimes an oblate Earth (Adhya et al., 2004; Srivastava et al., 2014), which is obviously physically more correct.

Nevertheless, all geometrical models lack the consideration of the physical processes that the light experiences by travelling through the atmosphere. Especially in the lower atmosphere, the light's absorption, scattering, and refraction, lead to changes in the travelling direction of the light, its intensity as well as its spectral composition and shape. As exemplarily demonstrated in Fig. 4.4b, these effects have an impact on the penumbra and umbra regions, even though the effect is highly exaggerated in the drawing for demonstration purposes. Physical models considering the light's absorption, scattering, and refraction have for example been developed by Vokrouhlický et al. (1993); Robertson (2015) and Li et al. (2018), of which the two recent ones are addressed in the following. Recently, Li et al. (2018) developed the perspective projection based shadow function with atmospheric effects (PPM_atm) that applies a reduction coefficient, which is a linear function to account for the reduction of the solar flux after travelling through the atmosphere, together with a precise geometrical approach to account for the oblate Earth. The model is freely available on GitHub at `https://github.com/whulizhen/PPM_atm_shadow_function`, last access on July 6, 2023. A physically more complex model called Solar radiation pressure with Oblateness and Lower Atmospheric Absorption, Refraction, and Scattering (SOLAARS) has been developed by Robertson (2015). It considers the light's absorption, scattering, and refraction together with the assumption of an oblate Earth. Due to the complexity and computational effort of the original model, he developed a curve-fitted model Solar radiation pressure with Oblateness and Lower Atmospheric Absorption, Refraction, and Scattering Curve Fit (SOLAARS-CF) (Robertson, 2015), which is also applied in this thesis and summarized in the following.

To simplify the SOLAARS model, the SOLAARS-CF model assumes a global average atmosphere, constant visible material properties of the satellite's surface, and neglects the tilt of the Earth's axis with respect to the ecliptic. The curve fit is based on two distances. At first, the projection of the satellite's position on the Earth-Sun direction is required

$$x_R = -\boldsymbol{x}_{\text{sat}} \cdot \bar{\boldsymbol{x}}_{\text{sun}}, \tag{4.2.42}$$

which results from the dot product of the satellite's position $\boldsymbol{x}_{\text{sat}}$ and the normalized position of the Sun $\bar{\boldsymbol{x}}_{\text{sun}}$ both in a geocentric inertial system. Secondly, the satellite's position is projected on the plane perpendicular to the Earth-Sun direction

$$\boldsymbol{x}_e = \boldsymbol{x}_{\text{sat}} - (\boldsymbol{x}_{\text{sat}} \cdot \bar{\boldsymbol{x}}_{\text{sun}})\, \bar{\boldsymbol{x}}_{\text{sun}}. \tag{4.2.43}$$

Then, the vector $\boldsymbol{x}_e$ is separated into the components parallel $x_{\text{e}\parallel}$ and perpendicular $x_{e\perp}$ to the unit normal of the ecliptic $\bar{\boldsymbol{e}}$ as

$$x_{e\parallel} = \bar{\boldsymbol{e}} \cdot \boldsymbol{x}_e, \tag{4.2.44}$$

$$x_{e\perp} = \sqrt{x_e^2 - x_{e\parallel}^2}. \tag{4.2.45}$$

A scaling factor considering the Earth's oblateness according to World Geodetic System 1984 (WGS84)

$$s_O = \frac{6378137.0}{6356752.3142} \tag{4.2.46}$$

is applied on $x_{e\parallel}$ to adjust the distance $x_e$ and to account for the oblateness before the curve fit

$$x'_e = \sqrt{x_{e\perp}^2 + \left(s_0 x_{e\parallel}\right)^2}. \tag{4.2.47}$$

The curve fit is performed by fitting the function

$$\nu = \frac{1 + a_1 + a_2 + a_1 \tanh\left(a_3\left(x'_e - a_4\right)\right) + a_2 \tanh\left(a_5\left(x'_e - a_6\right)\right) + \tanh\left(a_7\left(x'_e - a_8\right)\right)}{2 + 2a_1 + 2a_2} \tag{4.2.48}$$

for each $x_R$ (Eq. (4.2.42)) before fitting each $a$ coefficient as a function of $x_R$. This yields the $a_1$ to $a_8$ coefficients as listed in Tab. 4.2. Note that the units of $x_R$ and $x'_e$ are in $10^6$ meters.

Table 4.2: Curve fitting equations to compute the $a$ coefficients, which are required for evaluating the SOLAARS-CF shadow function (Robertson, 2015).

| Equation | $b_1$ | $b_2$ | $b_3$ | $b_4$ |
|---|---|---|---|---|
| $a_1 = b_1 e^{b_2 x_R} + b_3 e^{b_4 x_R}$ | 0.1715 | -0.1423 | 0.01061 | -0.01443 |
| $a_2 = b_1 x_R + b_2$ | 0.008162 | 0.3401 | - | - |
| $a_3 = b_1 e^{b_2 x_R} + b_3 e^{b_4 x_R}$ | 260.9 | -0.4661 | 27.81 | -0.009437 |
| $a_4 = b_1 x_R^{b_2} + b_3$ | -0.006119 | 1.176 | 6.385 | - |
| $a_5 = b_1 e^{b_2 x_R} + b_3 e^{b_4 x_R}$ | 87.56 | -0.09188 | 19.3 | -0.01089 |
| $a_6 = b_1 x_R + b_2$ | 0.002047 | 6.409 | - | - |
| $a_7 = b_1 e^{b_2 x_R} + b_3 e^{b_4 x_R}$ | 61.98 | -0.1629 | 27.87 | -0.02217 |
| $a_8 = b_1 e^{b_2 x_R} + b_3 e^{b_4 x_R}$ | 6.413 | -0.0002593 | -0.01479 | -0.1318 |

In Fig. 4.5, different shadow functions are evaluated during the first penumbra transition in July 2010 for GRACE-A at a 10 s resolution. Using the conical model, the satellite requires less than 20 s to cross the penumbra region. In comparison, the penumbra transition with the physical model PPM_atm lasts twice as long. With the SOLAARS-CF model, the penumbra transition takes four minutes, however, the first and last values deviate less than 1 % from one and zero, respectively, and are thus not shown in the figure. For comparison, the shadow function is derived by normalizing measured accelerometer data as suggested in Li et al. (2018)

$$\nu_{\text{a}} = \frac{a_{\text{t}} - a_{\text{s}}}{a_{\text{u}} - a_{\text{s}}} \tag{4.2.49}$$

with the acceleration $a_t$ at time $t$, the acceleration in umbra $a_u$ and in sunlight $a_s$. Even though the results of the most advanced model SOLAARS-CF are closest to the accelerometer-derived function, the results of the latter have to be treated with care since they strongly depend on the choice of the first and last data point. However, looking at further penumbra transitions confirms that they last approximately two times longer when using physical models, which causes a difference of $2 \times 10^{-9}\,\mathrm{m/s^2}$ in the modelled acceleration during one transition.

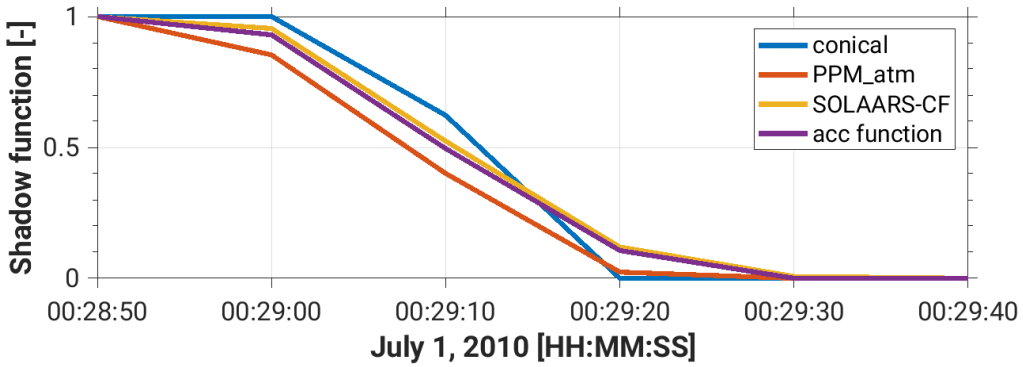



Figure 4.5: Penumbra transition from sunlight to umbra in July 2010 for GRACE-A at a 10 s resolution from four different approaches. (1) conical model (Montenbruck and Gill, 2012), (2) PPM_atm model (Li et al., 2018), (3) SOLAARS-CF model (Robertson, 2015), (4) shadow derived from accelerometer data as suggested in Li et al. (2018).

Besides the Earth, the Moon can shadow the sunlight reaching the satellite. In this thesis, lunar eclipses are accounted for with the conical model by Montenbruck and Gill (2012) with the assumption of a spherical Moon. Since overlapping of the Earth's and the Moon's shadow is very rare (Zhang et al., 2019), these events are neglected here. For modelling the shadow of the Earth and the Moon, the planetary and lunar ephemeris DE 421 (Folkner et al., 2008) are applied.

Another shadowing effect is the self-shadowing, which is often ignored in satellite force modelling. Mazarico et al. (2009) found that the effect of this phenomenon strongly depends on the shape of the satellite. Löcher and Kusche (2018) apply self-shadowing within an SRP model for the Lunar Reconnaissance Orbiter (LRO) spacecraft. As mentioned in the context of BRDFs, Kenneally and Schaub (2017) apply ray-tracing models from graphics rendering software to consider self-shadowing, as well as self-reflection, for the Mars Reconnaissance Orbiter. Both orbiters mentioned above had a complex shape as compared to GRACE, and SRP plays a much larger role in the lunar and Mars force models.

For the GRACE satellites, self-shadowing has been considered in Wöske et al. (2019), but was found to cause a rather small effect. Here, the self-shadowing is only relevant for a very short time span, when the aprons shadow the satellite's nadir panel, which leads to changes in the cross-track acceleration of the satellite. Therefore, the self-shadowing of both solar and Earth radiation is neglected in this study, however, the influence of self-shadowing and multiple reflections has to be reviewed when transferring the model to other spacecraft as considered, e.g., in List et al. (2015).

### 4.2.2 Earth radiation pressure

The interaction of the outgoing radiation of the Earth and the satellite's surface lead to the ERP acceleration. The Earth's outgoing flux is about $280\,\mathrm{W/m^2}$, of which the longwave flux, i.e. the Earth's thermal infrared radiation, contributes twice as much as the sunlight reflected at the Earth's surface and atmosphere known as shortwave flux. Both the Earth's outgoing longwave and shortwave radiation reaching the satellite depend on the constellation of Sun, Earth, and satellite including the satellite's altitude above the Earth's surface. Similar to SRP, the radiation can be reflected or absorbed depending on the surface material of the satellite. The contribution of the Earth's outgoing radiation to the ERP acceleration is also related to the satellite's mass and surface area.

The ERP acceleration is generally modelled analytically. The analytical model from Knocke et al. (1988) and Knocke (1989) is still widely used and combines the findings from Rubincam and Weiss (1986) and McCarthy and Martin (1977), which were the most advanced approaches until then. To discretize the Earth's surface, Knocke et al. (1988) follow the suggestion by McCarthy and Martin (1977) to divide the satellite's Field of View (FoV) into segments. The FoV or sometimes called footprint is the part of the Earth, which is geometrically visible from the satellite. For each segment of the footprint, Knocke et al. (1988) model the Earth's outgoing fluxes by approximating seasonal averages of satellite-derived albedo and emissivity data from Stephens et al. (1981) with second degree zonal harmonic functions similar to Rubincam and Weiss (1986) to account for the latitude-dependency dominating the data. Albedo is here the ratio of outgoing to incoming shortwave fluxes, and emissivity is the ratio of outgoing longwave flux to incoming shortwave flux. Knocke et al. (1988) assume that the outgoing radiation behaves perfectly diffuse so that Lambert's cosine law can be applied to obtain the radiation at the satellite's position. Summing up the ERP acceleration due to radiation originating from each segment yields the total ERP acceleration.

After Knocke et al. (1988), several studies applied more sophisticated albedo and emissivity maps derived from the Earth Radiation Budget Experiment (ERBE) mission as in Martin and Rubincam (1996); Ziebart et al. (2005), or from the CERES project as in Ziebart et al. (2005); Ziebart et al. (2007); Rodríguez-Solano et al. (2012); Montenbruck et al. (2018); Bury et al. (2019); Visser et al. (2019); Wöske et al. (2019); Wöske (2020) and Bhattarai et al. (2022), which also enable a higher resolution of the discretization of the Earth's surface. These updated models are generally applied in the force modelling of LEO satellites (e.g., Visser et al., 2019a; Wöske et al., 2019), and even though the magnitude is small at Medium Earth Orbit (MEO) altitudes, ERP should not be neglected for GNSS satellites (e.g., Ziebart et al., 2007; Rodríguez-Solano et al., 2012; Li et al., 2017; Bhattarai et al., 2022). For altimetry satellites, accurate ERP models are essential since systematics in the radial orbit position directly impact the measured sea surface height. However, high resolution radiation data are rarely considered (Mao et al., 2021; Rudenko et al., 2023). In addition, attempts to account for the anisotropic reflection at the Earth's surface have been made by Taylor and Stowe (1984); Rubincam et al. (1987) and Vokrouhlický and Farinella (1995). Martin and Rubincam (1996) applied the most sophisticated approach, where albedo data from ERBE were transformed to the satellite's position with the consideration of solar zenith angle, surface area, and cloud coverage. A further development of this approach has been published in Vielberg and Kusche (2020), which is outlined below.

Empirical methods are mainly applied to absorb the mismodelling of SRP accelerations. Assuming that some of the empirical parameters are related to the solar flux, others need to be estimated consistently with the ERP modelling. A combination of empirical SRP and analytical ERP models is widely used in the GNSS community (e.g., Ziebart et al., 2007; Rodríguez-Solano et al., 2012).

Based on the general RP model for one surface panel (Eq. (4.2.5)), the analytical ERP acceleration reads

$$\boldsymbol{a}_{\mathrm{ERP}} = \frac{A}{m} \int_{\Delta} \cos(\gamma) \int_{\lambda} \boldsymbol{c}_{\mathrm{R}}^{\oplus}(\lambda) P_{\oplus}(\lambda) \mathrm{d}\lambda \mathrm{d}\omega. \tag{4.2.50}$$

In Eq. (4.2.50), $A/m$ denotes the area to mass ratio and $\gamma$ is the angle between the incident radiation and the normal vector of the surface panel. In line with the SRP model, a wavelength-dependent representation of the flux is considered. The radiation pressure coefficient $\boldsymbol{c}_{\mathrm{R}}$ and the radiation pressure $P$ depend on the wavelength $\lambda$, and the spectrum of $P$ is specified for the Earth $\oplus$. As mentioned above, the RP accelerations are commonly computed in an inertial coordinate system and are transformed to a satellite body-fixed coordinate system using the satellite's attitude data.

To be consistent with SRP modelling, the satellite's mass $m$, surface area $A$, and the radiation pressure coefficient $\boldsymbol{c}_{\mathrm{R}}$ are considered in ERP modelling in the same way, thus, please refer to Sect. 4.2.1 for details. The integration over the satellite's FoV ($\Delta$ in Eq. (4.2.50)) is discretized by accumulating the ERP acceleration over each surface element. This means that the Earth's surface is divided into segments, for which the outgoing radiation for each wavelength needs to be derived from satellite-based radiation data sets. Thus, in the following the integration of the radiation

pressure of the Earth

$$\int_{\Delta}\int_{\lambda} P_{\oplus}(\lambda)\mathrm{d}\lambda\mathrm{d}\omega \tag{4.2.51}$$

will be derived and explained in detail including the discussions of current standards and suggestions of possible extensions. First, the radiation pressure for one segment of the Earth's surface acting on the satellite is derived from the radiance, then different wavelengths of the Earth's outgoing radiation are considered and finally, the discretization of the satellite's field of view is introduced.

**From radiance to radiation pressure**

Following Knocke et al. (1988) and Nicodemus et al. (1977), the radiance $L$ is the portion of the flux $\mathrm{d}\Phi$ leaving a surface element per solid angle $\mathrm{d}\Omega$ and per area projected normal to the given beam direction $\mathrm{d}\omega\cos\alpha$

$$L = \frac{\mathrm{d}\Phi}{\mathrm{d}\Omega\mathrm{d}\omega\cos\alpha}. \tag{4.2.52}$$

Rearranging the definition of the radiance for the flux and considering that the flux reaches a surface area $A$ (e.g., of a satellite) orthogonal to the beam direction at distance $r$ from the radiating surface element yields

$$\mathrm{d}\Phi = L\frac{A}{r^2}\mathrm{d}\omega\cos\alpha. \tag{4.2.53}$$

Linking the flux and the radiation pressure, which is the flux divided by the speed of light $c$ and a surface area, which cancels out, leads to

$$P = L\frac{\mathrm{d}\omega\cos\alpha}{cr^2}. \tag{4.2.54}$$

This equation can be adopted for the ERP caused by the wavelength-dependent outgoing radiance $L_{\oplus}(\lambda)$ of a discretized segment $\mathrm{d}\omega$ on the Earth's surface with area $\Delta\omega$

$$\int_{\lambda} P_{\oplus}(\lambda)\mathrm{d}\lambda = \int_{\lambda} L_{\oplus}(\lambda)\frac{\mathrm{d}\omega\cos\alpha}{c|\boldsymbol{x}-\boldsymbol{x}_{\mathrm{E}}|^2}\mathrm{d}\lambda. \tag{4.2.55}$$

The angle between the segment's surface normal and the satellite is denoted with $\alpha$, and $|\boldsymbol{x}-\boldsymbol{x}_{\mathrm{E}}|$ is the distance from the surface segment of the Earth to the satellite (see Fig. 4.6).

**Integration over all wavelengths**

As mentioned above, the Earth's outgoing radiation consists of a shortwave and a longwave part. Thus, the integration over different wavelengths simplifies to

$$\int_{\lambda} P_{\oplus}(\lambda)\mathrm{d}\lambda = \left(L_{SW\uparrow} + L_{LW\uparrow}\right)\frac{\mathrm{d}\omega\cos\alpha}{c|\boldsymbol{x}-\boldsymbol{x}_{\mathrm{E}}|^2}. \tag{4.2.56}$$

The computation of the shortwave and longwave radiances $L_{SW\uparrow}$ and $L_{LW\uparrow}$ at a surface element will be described in the following according to Knocke et al. (1988) based on albedo and emissivity, before alternative formulations will be presented.

**Knocke's formulation of the shortwave radiance**

Beginning with the shortwave part, Knocke et al. (1988) introduce the albedo of a surface element

$$a = \frac{\Phi_{\mathrm{SW}\uparrow}}{\Phi_{\mathrm{SW}\downarrow}} \tag{4.2.57}$$

as the ratio of outgoing and incoming shortwave fluxes $\Phi_{\mathrm{SW}\downarrow}$ and $\Phi_{\mathrm{SW}\uparrow}$. The shortwave flux leaving the surface element $\mathrm{d}\omega$ can be obtained from the integration of the flux (Eq. (4.2.53)) over the total

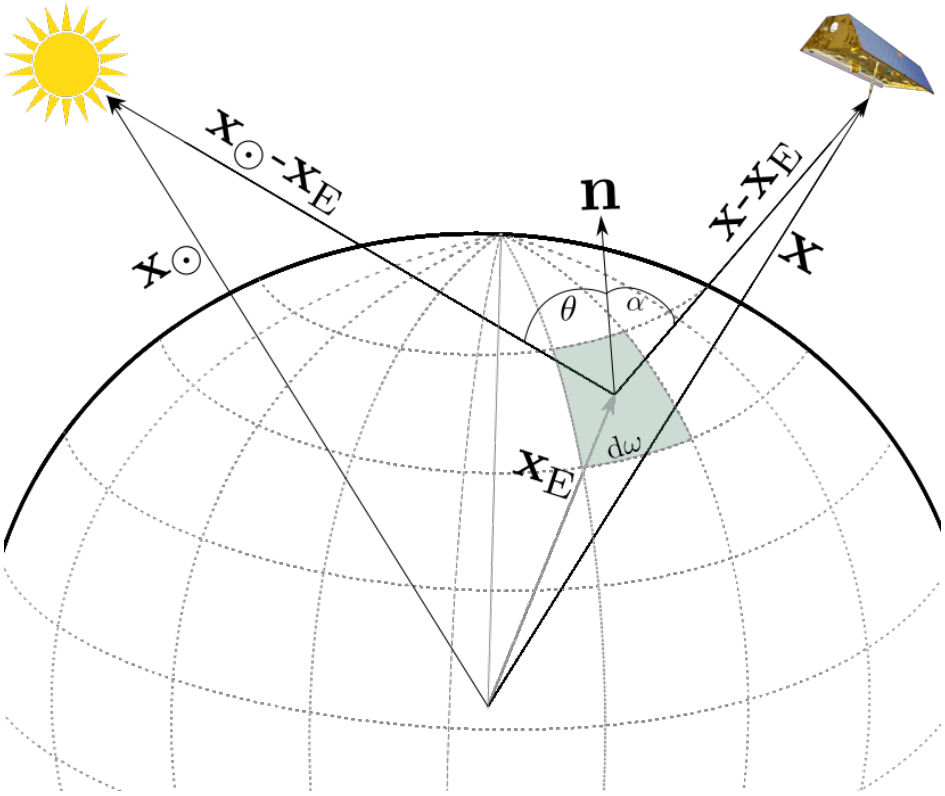



Figure 4.6: Geometry of the ERP for one discretized surface element $\mathrm{d}\omega$. $\boldsymbol{x}$ is the vector pointing from the Earth's centre to the position of the satellite, $\boldsymbol{x}_\odot$ is the vector pointing from the Earth's centre to the Sun, and $\boldsymbol{x}_\mathrm{E}$ is the vector pointing from the Earth's centre to the centre of the segment on the Earth's surface. Then, the vector from the centre of the surface element to the Sun and the satellite result from $\boldsymbol{x}_\odot - \boldsymbol{x}_\mathrm{E}$ and $\boldsymbol{x} - \boldsymbol{x}_\mathrm{E}$, respectively. The angle between the surface normal $\boldsymbol{n}$ and $\boldsymbol{x} - \boldsymbol{x}_\mathrm{E}$ is denoted with $\alpha$.

hemisphere

$$\mathrm{d}\Phi_{\mathrm{SW}\uparrow} = \int_{H^2} L_{\mathrm{SW}\uparrow} \frac{A}{r^2} \mathrm{d}\omega \cos\alpha \tag{4.2.58}$$

$$= \mathrm{d}\omega \int_{H^2} L_{\mathrm{SW}\uparrow} \cos\alpha \frac{r\mathrm{d}\alpha \sin\alpha \mathrm{d}\psi}{r^2} \tag{4.2.59}$$

$$= \mathrm{d}\omega \int_{\alpha=0}^{\frac{\pi}{2}} \int_{\psi=0}^{2\pi} L_{\mathrm{SW}\uparrow} \sin\alpha \cos\alpha \mathrm{d}\alpha \mathrm{d}\psi. \tag{4.2.60}$$

Assuming that the Earth's surface reflects purely diffuse, Lambert's law can be applied. Thus, the outgoing flux is independent of the angles $\alpha$ and $\psi$, and simplifies to

$$\mathrm{d}\Phi_{\mathrm{SW}\uparrow} = L_{\mathrm{SW}\uparrow} \mathrm{d}\omega \int_{\alpha=0}^{\frac{\pi}{2}} \int_{\psi=0}^{2\pi} \sin\alpha \cos\alpha \mathrm{d}\alpha \mathrm{d}\psi \tag{4.2.61}$$

$$= \pi L_{\mathrm{SW}\uparrow} \mathrm{d}\omega. \tag{4.2.62}$$

The incoming shortwave flux $\Phi_{\mathrm{SW}\downarrow}$ on the surface element in Eq. (4.2.57) with angle $\theta$ between the surface normal and the incoming flux (see Fig. 4.6) can be expressed as

$$\Phi_{\mathrm{SW}\downarrow} = E_s \cos\theta \mathrm{d}\omega, \tag{4.2.63}$$

with

$$E_s = \frac{\Phi_{\mathrm{sc}}}{4\pi r^2}. \tag{4.2.64}$$

Here, $\Phi_{\text{sc}}$ is the total solar flux, which is directly related to the solar irradiance $E_s$. Inserting the formulations for the outgoing fluxes (Eqs. (4.2.62), (4.2.63)) in the expression for the albedo (Eq. (4.2.57)) and rearranging it for the shortwave radiance yields

$$L_{\text{SW}\uparrow} = \frac{aE_s \cos\theta}{\pi}. \tag{4.2.65}$$

**Knocke's formulation of the longwave radiance**

The longwave radiance $L_{\text{LW}\uparrow}$ at a single surface element of the Earth is based on the emissivity

$$e = \frac{M_{\text{LW}\uparrow}}{M_B \uparrow}. \tag{4.2.66}$$

Emissivity is defined as the ratio of the longwave exitance $M_{\text{LW}\uparrow}$ and the exitance $M_B$, which results from the assumption that the solar radiation is instantaneously re-emitted into space isotropically, i.e., the Earth is assumed to be a black body (Knocke et al., 1988). Under this assumption, the exitance $M_B$ can be obtained from a quarter of the solar irradiance $E_s$, which corresponds the solar radiation reaching the Earth's cross sectional area

$$M_B = \frac{E_s}{4}. \tag{4.2.67}$$

The longwave exitance $M_{\text{LW}\uparrow}$ can be related to the radiance $L_{\text{LW}\uparrow}$ with the assumption that the Earth's surface is a perfect diffuse emitter similar to the outgoing shortwave flux in Eqs. (4.2.58) - (4.2.62) as

$$M_{\text{LW}\uparrow} = \frac{\Phi_{\text{LW}\uparrow}}{\mathrm{d}\omega} \tag{4.2.68}$$

$$= \frac{L_{\text{SW}\uparrow}\mathrm{d}\omega \int_{\alpha=0}^{\frac{\pi}{2}} \int_{\psi=0}^{2\pi} \sin\alpha\cos\alpha \mathrm{d}\alpha\mathrm{d}\psi}{\mathrm{d}\omega} \tag{4.2.69}$$

$$= \pi L_{\text{LW}\uparrow}. \tag{4.2.70}$$

Combining the equations for the exitances Eqs. (4.2.67) and (4.2.70) with the expression of the emissivity (Eq. (4.2.66)) yields the outgoing longwave radiance

$$L_{\text{LW}\uparrow} = \frac{eE_s}{4\pi}. \tag{4.2.71}$$

**Knocke's radiation pressure formulation**

Now both the outgoing shortwave and longwave radiances (Eqs.(4.2.65), (4.2.71)) can be inserted into the formulation of the radiation pressure of a single surface element (Eq. (4.2.56)), which yields

$$\int_\lambda P_\oplus(\lambda)\mathrm{d}\lambda = \left(\tau a E_s \cos\theta + \frac{eE_s}{4}\right) \frac{\mathrm{d}\omega\cos\alpha}{c\pi|\boldsymbol{x} - \boldsymbol{x}_{\text{E}}|^2}. \tag{4.2.72}$$

Since the albedo depends on the illumination of the surface area, an illumination factor $\tau$, which is zero during night and one during day, is considered here.

**Knocke's representation of albedo and emissivity**

To compute the radiation pressure according to Eq. (4.2.72), the albedo $a$ and emissivity $e$ need to be obtained at the Earth's surface element. A second degree zonal harmonic function is used in Knocke et al. (1988) to approximate the seasonally averaged satellite-derived albedo and emissivity maps from Stephens et al. (1981) as

$$a = a_0 + a_1 P_1(\sin\phi) + a_2 P_2(\sin\phi), \tag{4.2.73}$$

$$e = e_0 + e_1 P_1(\sin\phi) + e_2 P_2(\sin\phi), \tag{4.2.74}$$

with the Legendre polynomial $P_n(\sin\phi)$ depending on latitude $\phi$ and

$$a_1 = c_0 + c_1 \cos\left(\frac{t-t_0}{365.25}\right) + c_2 \sin\left(\frac{t-t_0}{365.25}\right), \tag{4.2.75}$$

$$e_1 = k_0 + k_1 \cos\left(\frac{t-t_0}{365.25}\right) + k_2 \sin\left(\frac{t-t_0}{365.25}\right). \tag{4.2.76}$$

Here, $t$ denotes the time given in Julian date and $t_0$ is set to December 22, 1981 (Knocke et al., 1988). The coefficients resulting from the fit mentioned above are $a_0 = 0.34$, $c_0 = 0$, $c_1 = 0.1$, $c_2 = 0$, $a_2 = 0.29$ for albedo, and $e_0 = 0.68$, $k_0 = 0$, $k_1 = -0.07$, $k_2 = 0$, $e_2 = -0.18$ for emissivity. This harmonic representation is not able to account for long-term changes in the radiation, e.g., due to variations in snow coverage or vegetation.

**Alternative representation of albedo and emissivity**

Since albedo and emissivity are indeed strongly latitude-dependent, the formulation of the radiation pressure from Knocke et al. (1988) based on albedo and emissivity is still a good approximation. However, the representation of albedo and emissivity has gone through a considerable development due to the availability of the CERES measurements at TOA. The data sets used for albedo and emissivity differ in recent publications. For example, Rodríguez-Solano (2009) derives albedo and emissivity from monthly CERES data with a latitude-dependent approximation similar to Knocke et al. (1988) and Montenbruck et al. (2018) use a harmonic representation based on CERES EBAF TOA data.

Such harmonic representations are still very efficient, however, since the computational efficiency improved immensely since 1980s, one has to balance the efficiency against the accuracy, which can be improved by applying albedo and emissivity from satellite data at the position of the Earth's surface element directly. For example, Bury et al. (2019) apply monthly CERES EBAF TOA data, Visser et al. (2019) use monthly SYN1deg data, and Wöske et al. (2019) and Vielberg and Kusche (2020) use hourly SYN1deg data. As mentioned before, unlike the EBAF product, the SYN1deg product is not constrained to the heat content from ocean reanalysis (Loeb et al., 2018) and thus contains average biases around 1-2 $\mathrm{W/m^2}$. Adding $1\,\mathrm{W/m^2}$ to the global average of the Earth's outgoing longwave or shortwave radiation changes the radial ERP acceleration by up to 1 %. The EBAF product has a monthly resolution, whereas the SYN1deg data is available hourly, which means that one no longer requires using an illumination function to consider the shortwave flux only at the dayside.

**Alternative representation of the radiance**

With the availability of CERES observations of the Earth's outgoing radiation TOA, there is no need to approximate the radiances by expressions of albedo and emission in the RP computation (Eq. (4.2.56)) any more. Thus, in Vielberg and Kusche (2020) we suggested an alternative formulation of the shortwave and longwave radiances $L_{\mathrm{SW}\uparrow}$ and $L_{\mathrm{LW}\uparrow}$. This model has already been adopted for applications such as the estimation of precise orbits or the thermospheric density (Krauss et al., 2020; Wang et al., 2023) and is derived in the following.

According to Eq. (4.2.70), the longwave exitance $M_{\mathrm{LW}}$ can be related to the longwave radiance with the assumption of diffuse emissivity by

$$L_{\mathrm{LW}\uparrow} = \frac{M_{\mathrm{LW}\uparrow}}{\pi}. \tag{4.2.77}$$

Combining Eq. (4.2.62) $\mathrm{d}\Phi_{\mathrm{SW}\uparrow} = \pi L_{\mathrm{SW}\uparrow}\mathrm{d}\omega$ with the definition of the exitance, which is related to the flux $\Phi_{\mathrm{SW}\uparrow}$ by

$$M_{\mathrm{SW}\uparrow} = \frac{\Phi_{\mathrm{SW}\uparrow}}{\mathrm{d}\omega}, \tag{4.2.78}$$

results in the same relation for the shortwave radiance

$$L_{\mathrm{SW}\uparrow} = \frac{M_{\mathrm{SW}\uparrow}}{\pi}. \tag{4.2.79}$$

The exitance $M_{\mathrm{SW}\uparrow}$ and $M_{\mathrm{LW}\uparrow}$ can be obtained from CERES data directly. Using these variables, the integrated radiation pressure in Eq. (4.2.56) becomes

$$\int_{\lambda} P_{\oplus}(\lambda)\mathrm{d}\lambda = \left(M_{\mathrm{SW}\uparrow} + M_{\mathrm{LW}\uparrow}\right) \frac{\mathrm{d}\omega \cos\alpha}{c\pi|\boldsymbol{x} - \boldsymbol{x}_{\mathrm{E}}|^2}. \tag{4.2.80}$$

In this thesis, the fields of observed hourly outgoing shortwave and longwave fluxes at TOA from CERES SYN1deg Ed4.1 are applied (NASA/LARC/SD/ASDC, 2017). This is possible since the term *flux* in the CERES processing is defined as the energy flow per unit area over unit time and is given in $\mathrm{W/m^2}$, which is the same as the exitance. Another advantage of applying the observations of the outgoing longwave flux directly is that the delay between the incoming radiation and emitted thermal radiation is automatically considered, which is not the case in Knocke et al. (1988), where instantaneous emission of the incoming radiation has been assumed.

**Extended representation of the radiance with ADMs**

Strictly speaking, the formulation of the Eq. (4.2.82) misses an important point namely the consideration of the angular dependence of Earth's outgoing radiation. In the CERES data processing, so-called ADMs (Su et al., 2015a; Su et al., 2015b) are applied in the estimation of the global fluxes from in-situ radiances from space. Thus to be consistent, computing ERP accelerations at the position of a satellite requires the back-projection from CERES fluxes to radiances with the same ADMs as in the CERES data processing.

Then, the relation between the exitance $L$ (both shortwave and longwave) at one surface element of the Earth and the radiance $M$ with the consideration of ADM anisotropic factor $R$ (Su et al., 2015a, Eq. (2)) reads

$$L\left(\theta, \alpha, \Phi\right) = \frac{M\left(\theta\right) R\left(\theta, \alpha, \Phi\right)}{\pi}. \tag{4.2.81}$$

Here, the dependency on the geometry according to Fig. 4.7 is introduced as well. The radiance depends on the solar zenith angle $\theta$ only, whereas the exitance and the anisotropic factor additionally depend on the instrument's viewing zenith angle $\alpha$ and relative azimuth angle $\Phi$. The concept of the ADMs is similar to that of the BRDFs, which was used above to consider the anisotropic reflection at the satellite's surface. Instead of the thermo-optical material coefficient of the satellite's surface, the reflection properties of the Earth as seen from space are required. Thus, besides the constellation of satellite, Sun, and Earth as shown in Fig. 4.7, ADMs, and thus the anisotropic factor $R$, depend on the land coverage and cloud properties, which make the concept more complex.

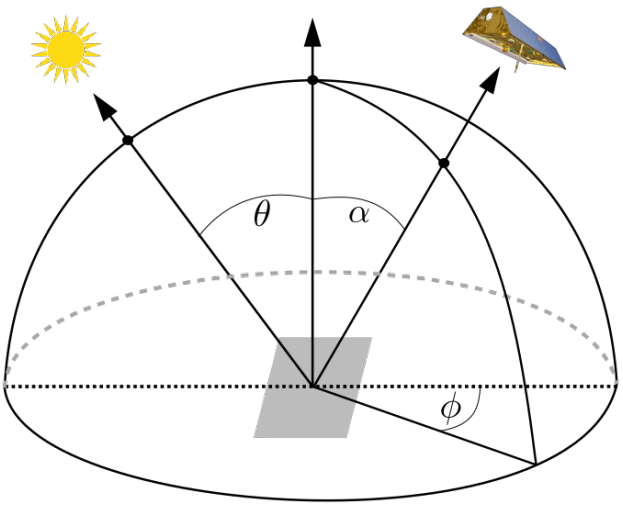



Figure 4.7: Geometry required for applying ADMs according to Suttles et al. (1988) (Fig. 1) with solar zenith angle $\theta$, instrument's viewing zenith angle $\alpha$ and relative azimuth angle $\Phi$. The grey area assigns the target area.

With the consideration of the anisotropic reflection, the radiation pressure of the Earth for one surface element becomes

$$\int_{\lambda} P_{\oplus}(\lambda)\mathrm{d}\lambda = \left(M_{\mathrm{SW}\uparrow}R_{\mathrm{SW}\uparrow} + M_{\mathrm{LW}\uparrow}R_{\mathrm{LW}\uparrow}\right)\frac{\mathrm{d}\omega\cos\alpha}{c\pi|\boldsymbol{x}-\boldsymbol{x}_{\mathrm{E}}|^2}. \tag{4.2.82}$$

The equation is written without the angular dependency for better readability.

Most recently, Vielberg and Kusche (2020) considered ADMs consistently in ERP modelling with CERES data. Applying the state-of-the-art ADMs (Su et al., 2015a; Su et al., 2015b) would be fully in line with the current CERES processing. However, they are not publicly available. The latest available ADMs are the CERES Terra ADMs (Loeb et al., 2007). Applying them in the CERES TOA data processing, the error due to radiance-to-flux conversion is $10\,\mathrm{W/m^2}$ for shortwave fluxes and $3-5\,\mathrm{W/m^2}$ for longwave fluxes (Loeb et al., 2007). For CERES TOA fluxes, the error due to radiance-to-flux conversion is $10\,\mathrm{W/m^2}$ for shortwave fluxes and $3-5\,\mathrm{W/m^2}$ for longwave fluxes (Loeb et al., 2007). Compared to the total error in radiance-to-flux conversion, the differences of monthly mean TOA fluxes when using the previous ERBE ADMs compared to Terra ADMs in the CERES processing result in larger monthly mean TOA fluxes of $1.8\,\mathrm{W/m^2}$ and $1.3\,\mathrm{W/m^2}$ for shortwave and longwave, respectively (Loeb et al., 2007). In this thesis following Vielberg and Kusche (2020), the ERBE ADMs developed by Suttles et al. (1988) and Suttles et al. (1989) are applied. However, the fact that older ADMs are likely to overestimate CERES TOA fluxes should be kept in mind.

In general, the ERBE ADMs depend on the viewing zenith angle (see Fig. 4.7) and on twelve scene types, which consider nine basic types of cloud coverage and land cover and three mixed types (Suttles et al., 1988). We use the cloud area fraction provided within the CERES SYN1deg data at the same temporal and spatial resolution as the used fluxes to distinguish between clear sky (0-5% coverage), partly cloudy (5-50% coverage), mostly cloudy (50-95% coverage), and overcast (95-100% coverage). The land cover type used to determine the scene type differentiates between ocean, land, snow, desert, and land-ocean mix. In this thesis, the global land cover map generated from *MODIS/Terra and Aqua Combined Land Cover Type CMG Yearly Global 0.05 Deg V006* (Friedl and Sulla-Menashe, 2015) in Vielberg and Kusche (2020) is used. Since the application of ERBE ADMs requires only five land cover types instead of 17 as assigned in the MODIS data, snow and ocean areas are adopted directly, whereas barren land with up to 10% vegetation are assigned to desert, and the remaining types correspond to land. Within a majority voting, which is required to obtain the land cover type at a spatial resolution of 1° (similar to the available fluxes) instead of 0.05°, grid cells are assigned as coastal region, if they contain at least 20% of ocean as well as any other land type (land, desert, snow). The MODIS land cover maps are available yearly since 2001, however, at a spatial resolution of 1° land cover changes are minor and are thus disregarded. In this thesis, the land cover maps of the year 2010 are used, which is approximately in the middle of the GRACE lifetime. Since the five final scene types are rather general, updating the land cover map is not expected to be necessary when extending the evaluation period. The final land cover map is presented in Fig. 4.8.

Since the assigned snow regions are permanently covered by snow, information on seasonal snow coverage is taken from the snow/ice percent coverage, which is available within the CERES auxiliary surface data derived from the National Snow and Ice Data Center.

Additionally, ADMs for the longwave flux depend on the season and the co-latitude, whereas shortwave ADMs depend on the relative azimuth angle and the solar zenith angle (see Tab. 2 in Suttles et al., 1988).

#### Integration over the satellite's FoV

Above, the radiation pressure acting on the surface panel of the satellite was formulated for one surface element of the Earth. To obtain the radiation pressure reaching the surface panel of a satellite, the integration over the satellite's FoV ($\Delta$ in Eq. (4.2.50)) is required. The surface area

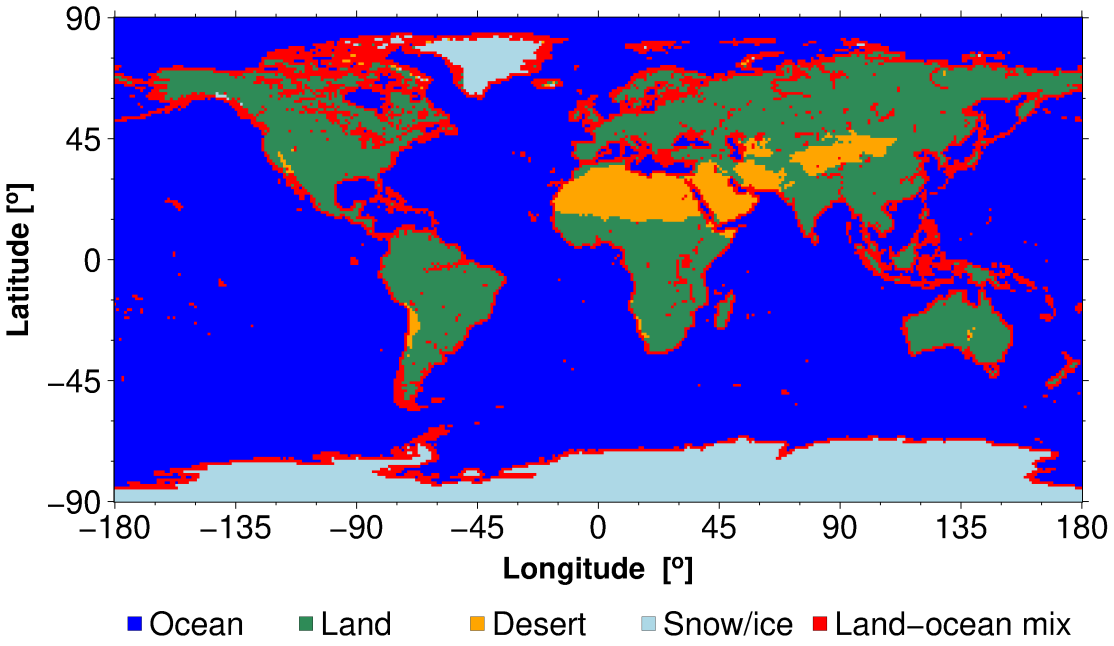



Figure 4.8: Land cover map used to determine the scene type for the angular distribution model in ERP modelling (Vielberg and Kusche, 2020).

$S_{\mathrm{FoV}}$ of the FoV (e.g., Girardin, 2016) can be computed from

$$S_{\mathrm{FoV}} = 2\pi|\boldsymbol{x}_{\mathrm{E}}|^2\left(1-\frac{|\boldsymbol{x}_{\mathrm{E}}|}{|\boldsymbol{x}|}\right), \tag{4.2.83}$$

where $|\boldsymbol{x}_{\mathrm{E}}|$ is the radius of Earth, and $\frac{|\boldsymbol{x}_{\mathrm{E}}|}{|\boldsymbol{x}|}$ is equal to $\cos\psi$, where $\psi$ is the opening angle seen from the Earth and the distance $|\boldsymbol{x}|$ from the centre of Earth to the satellite.

To discretize the FoV, Knocke et al. (1988) suggested a ring-like discretization, which results in 19 surface elements (more elements are possible) and is still a widely-used standard (e.g., Montenbruck and Gill, 2012). Each ring $k$ consists of $6k$ segments resulting in the total number of $m$ segments, so that $S_{\mathrm{FoV}} = \sum_j^m S_j$. Note that the first segment is equal to the cap of the sphere with surface area $S$. The area $S$ of each segment is computed as

$$S = \frac{S_{\mathrm{FoV}}}{m} = \frac{2\pi|\boldsymbol{x}_{\mathrm{E}}|^2}{m}\left(1-\frac{|\boldsymbol{x}_{\mathrm{E}}|}{|\boldsymbol{x}|}\right), \tag{4.2.84}$$

so that the segments of the footprint at a specific satellite position have the same area. Instead of dividing the footprint into rings and sections, Li et al. (2017) suggested to reorganize the 1° CERES data into 6 levels of triangles.

Other recent publications assume a grid of 2.5° in longitude and latitude (Doornbos et al., 2009; Rodríguez-Solano et al., 2012) to discretize the FoV. Since Earth's outgoing radiation data from CERES are currently available on a grid of 1° in longitude and latitude, in this thesis the FoV is divided into segments of the same size as, e.g., in Visser et al. (2019); Wöske et al. (2019). Thus, currently a grid of 1° appears sufficient, however, in case the spatial resolution of the Earth's outgoing radiation data increases, the resolution of the discretization of the FoV should increase as well. In any case, the area of a pixel of the global radiation map in row $r$ and column $c$ with index $j = c(r-1)/R$, which corresponds to the number of pixels of a global map with a resolution of $R \times C$ pixels (R= 180 and C= 360 for CERES data), is computed according to Doornbos et al. (2009) from

$$S = \frac{4\pi|\boldsymbol{x}_{\mathrm{E}}|^2}{R}\sin\left(\frac{\pi/2}{C}\right)\sin\left(\frac{(c-0.5)\pi}{C}\right). \tag{4.2.85}$$

The pixel in the top left of the map is defined as 90° in latitude and −180° in longitude. Since the CERES maps are defined at TOA, the surface elements are discretized at an altitude of 20 km

above the Earth's surface (Loeb et al., 2018). To conclude, approximating the discretizing by using rings or triangulation methods decreases the computational runtime, however, discretizing the grid at the resolution of the radiation data sets is more accurate.

Finally, combining the discretization of the wavelengths with the discretization of the surface integral, the ERP acting on one surface panel of the satellite from Eq. (4.2.51) can be written as

$$\int_{\Delta}\int_{\lambda} P_{\oplus}(\lambda)\mathrm{d}\lambda\mathrm{d}\omega = \sum_{j}\left(L^{j}_{SW\uparrow} + L^{j}_{LW\uparrow}\right)\frac{S_j\cos\alpha_j}{c|\boldsymbol{x}-\boldsymbol{x}_{\mathrm{E_j}}|^2} \tag{4.2.86}$$

$$= \sum_{j}\left(M^{j}_{\mathrm{SW}\uparrow}R^{j}_{\mathrm{SW}\uparrow} + M^{j}_{\mathrm{LW}\uparrow}R^{j}_{\mathrm{LW}\uparrow}\right)\frac{S_j\cos\alpha_j}{c\pi|\boldsymbol{x}-\boldsymbol{x}_{\mathrm{E_j}}|^2}. \tag{4.2.87}$$

Here, the integration over the satellite's FoV is discretized by the summation over all surface elements $j$ with the discretized area $S$ and the integration over all wavelengths is considered by the Earth's outgoing shortwave $L_{SW\uparrow}$ and longwave $L_{LW\uparrow}$ radiance for each surface element, which can be obtained in different ways as explained above. In Eq. (4.2.87), it is obtained from the combination of CERES data in $M$ with ADM anisotropic factor $R$.

### 4.2.3 Lunar radiation pressure

Not only the radiation of Sun and Earth can lead to radiation pressure accelerations on celestial objects, but also the radiation of the Moon. The so-called lunar albedo acceleration results from the reflected sunlight at the Moon's surface and effects the motion of space objects in the lunar vicinity. Strictly speaking, the sunlight reflected at the Earth's surface reaching the Moon also contributes to lunar albedo. As for the Earth, there is not only an outgoing shortwave, but also a longwave radiation, since its temperature is above 0 K. The resulting acceleration is known as lunar thermal emissivity (Lemoine et al., 2013; Wirnsberger et al., 2018).

Early studies (Kirpichnikov, 1968) on the motion of lunar satellites consider solar and lunar radiation pressure for models. Later on in the context of lunar gravity field determination, a few studies consider the lunar radiation pressure accelerations. Floberghagen et al. (1999) investigated the lunar albedo force modelling for low lunar orbits in the context of future lunar gravity field determination. Their model is based on the ERP model by Knocke et al. (1988) (see Sect. 4.2.2), i.e., the reflected radiation is derived from the incoming solar radiation at the position of the Moon and the albedo model Delft Lunar Albedo Model I (DLAM-1), which is provided in terms of spherical harmonic coefficients until degree and order 15. The same approach is applied in Wirnsberger et al. (2018) within the computation of the Graz Lunar Gravity field Model (GrazLGM) and in Löcher and Kusche (2018) within the precise orbit determination of LRO. In addition, Konopliv et al. (2013) and Wirnsberger et al. (2018) consider the acceleration due to the lunar thermal emissivity, which requires an assumption of the lunar emissivity coefficient. Racca (1995) studied the thermal characteristics of the Moon and derive different temperature models similar to those used for the computation of the satellite's surface temperature in the TRP modelling (Sect. 4.2.4) and obtain an average infrared emissivity coefficient of 0.97, which is applied in Wirnsberger et al. (2018). Instead of assuming a constant emissivity, Lemoine et al. (2013) apply a temperature-based emissivity depending on latitude and local time, where the temperature results from

$$T = \max\left(\mathrm{T_{max}}(\cos\phi)^{\frac{1}{4}}, \mathrm{T_{min}}\right), \tag{4.2.88}$$

with $T_{\max} = 375\,\mathrm{K}$, $T_{\min} = 100\,\mathrm{K}$ and the angle $\phi$ to the subsolar point. Applying Stefan-Boltzmann's law results in the emissivity coefficient

$$e = \frac{\sigma T^4}{c} \tag{4.2.89}$$

with speed of light $c$ and Stefan-Boltzmann constant $\sigma = 1.380649 \cdot 10^{-23}\mathrm{J/K}$. This emissivity model is, e.g., applied by Löcher and Kusche (2018) in the precise orbit determination of LRO.

With the availability of albedo and emissivity data for the Moon, the LRP acceleration can be computed following the same principle as the ERP model by Knocke et al. (1988) shown in Eq. (4.2.72) and is therefore not shown here again. In the low lunar orbit, the resulting acceleration reaches $\approx 20\%$ of the SRP acceleration peaking to $10\,\mathrm{nm/s^2}$ and causing orbit perturbations of 1-2 m per week (Floberghagen et al., 1999). For LEO satellites, the LRP acceleration is relatively small due to the large average distance between Earth and Moon of 378,000 km (Williams, 2021). For example, for GRACE-A on January 1, 2010, the lunar radiation pressure implemented with emissivity according to Lemoine et al. (2013) and albedo following Floberghagen et al. (1999) yields $2 \cdot 10^{-13}\,\mathrm{m/s^2}$, which is approximately 10,000 times smaller than the ERP acceleration. Consequently, LRP accelerations as well as accelerations from shortwave and longwave radiation of other celestial objects are commonly not considered in LEO force modelling.

### 4.2.4 Thermal re-radiation pressure

The electromagnetic radiation of the Sun as well as the reflected and emitted radiation of the Earth do not only cause a radiation pressure acceleration on the satellite. In addition, the electromagnetic radiation, which is absorbed at the satellite's surface, heats up the illuminated surface. According to the physics of heat transfer mechanisms, this leads to temperature variations of the whole spacecraft. The emissivity of the satellite's thermal energy following the Stefan-Boltzmann law causes an acceleration, which depends on the absorbed radiation, the satellite's internal and external geometry, and the thermo-optical material properties.

Different terminology for this effect can be found in the available literature (e.g., Ciufolini et al., 2018). On the one hand, this topic is treated in geodetic literature on POD, on the other hand there is astrophysics literature on the thermal balance of small bodies in the universe. The thermal radiation due to the solar radiation is often referred to as Yarkovsky or Yarkovsky-Schach effect, whereas the thermal effect due to Earth infrared radiation is known as Earth Yarkovsky or Yarkovsky-Rubincam effect, which has first been investigated by Rubincam (1987) and Rubincam (1988) when explanations for the unexpected orbit decay of LAGEOS became relevant for further applications (Bertotti and Iess, 1991; Scharroo et al., 1991; Rubincam et al., 1997). Since the resulting acceleration acts in the anti-along-track direction for non-rotating spherical satellites, this effect is sometimes referred to as thermal drag (Ciufolini et al., 2018). For rotating spherical satellites, the force resulting from the re-radiation is directed along the spin axis of the hotter part of the satellite (Scharroo et al., 1991). Due to the satellite's rotation, a thermal lag needs to be considered as well when modelling its thermal re-radiation (e.g., Scharroo et al., 1991). In this thesis, I use the term TRP acceleration for the re-radiation of heat considering the absorbed radiation due to the total electromagnetic radiation reaching the satellite.

The TRP acceleration acting on satellites with a panel model has already been investigated since the early 1990s in the context of POD for the TOPEX/POSEIDON spacecraft (e.g., Marshall et al., 1992; Antreasian and Rosborough, 1992). More recently, TRP models have been studied (Adhya, 2005; Bhattarai et al., 2022) and considered in simplistic ways (Montenbruck et al., 2015) for GNSS satellites. Additionally, Rievers (2012) developed high precision TRP models for complex satellites using finite element satellite models, which allow for the consideration of delayed thermal re-radiation due to rerouted heat generated by the satellite's electrical components. TRP force models for the lunar gravity field mission GRAIL applied finite element models as well (Fahnestock et al., 2012). A finite element approach for TRP modelling including transient heating and heat conduction for GRACE has been developed by Wöske et al. (2019). Such high-fidelity models rely on the information provided by the manufacturers.

Beyond the application of TRP modelling for satellite dynamics, recent publications investigate the orbits of asteroids under consideration of TRP (Bottke et al., 2006; Deo and Kushvah, 2017). In this context, the Yarkovsky-O'Keefe-Radzievskii-Paddack (YORP) effect has also been investigated, which is relevant for rotating spherical satellites due to the thermal torque that changes the object's spin rate and axis (Vokrouhlický and Bottke, 2012) caused by its irregular thermal radiation. Furthermore, this effect is relevant for comet outgassing caused by surface temperature rises (Hu and Shi, 2021).

Since the TRP acceleration is approximately at the same order of magnitude as the ERP acceleration for LEO satellites (see Fig. 1.1), this effect should be considered in precise non-gravitational force modelling. Thus, the next sections provide an overview of the analytical TRP modelling based on a static and an advanced model, where the latter accounts for transient heating and heat conduction for a GRACE-like satellite closely following the implementation by Wöske et al. (2019); Wöske (2020).

**General formulation**

The acceleration due to TRP can be derived from the general equation of the RP acceleration (Eq. (4.2.5))

$$\boldsymbol{a}_{\mathrm{RP}} = \frac{A}{m} \cos(\gamma)\, \boldsymbol{c}_{\mathrm{R}} P.$$

Since the TRP is a radiation leaving the satellite, the angle of the incoming radiation is no longer relevant. In addition, the radiation pressure coefficient $\boldsymbol{c}_{\mathrm{R}}$ simplifies to $-2/3\mathbf{n}$ (with surface normal $\mathbf{n}$) when assuming Lambertian re-radiation, $P$ becomes the absorbed radiation $P_{\mathrm{abs}}$, and the area to mass ratio $A/m$ needs to be considered. Then, the TRP acceleration $\mathbf{a}_{\mathrm{TRP}}$ acting on a single surface panel of the satellite can be written as

$$\mathbf{a}_{\mathrm{TRP}} = -\frac{2}{3}\frac{A}{m}\mathbf{n} P_{\mathrm{abs}}. \tag{4.2.90}$$

With Stefan-Boltzmann's law, the absorbed radiation is directly related to the temperature $T$ of the satellite's surface by

$$P_{\mathrm{abs}} = T^4 \epsilon \sigma, \tag{4.2.91}$$

with the panel's emissivity coefficient $\epsilon$ and the Stefan Boltzmann constant $\sigma$. Inserting this into Eq. (4.2.90) yields

$$\mathbf{a}_{\mathrm{TRP}} = -\frac{2}{3}\frac{A}{m}\epsilon \sigma T^4 \mathbf{n}, \tag{4.2.92}$$

which is also the basis for TRP computations in Wöske et al. (2019).

**Temperature from static (instantaneous) model**

Since the surface temperature of a satellite's panels is usually not measured, it has to be computed. There are different algorithms to derive the surface temperature from the absorbed radiation. The simplest formulation accounts for instantaneous re-radiation of the absorbed radiation at the satellite's surface (Montenbruck et al., 2015; Wöske et al., 2019). In this static case, the panel's temperature can be obtained from Stefan-Boltzmann's law (Eq. (4.2.91)) as it is done in Wöske et al. (2019) (Eq. (14)). Alternatively, instead of computing the temperature and then again the radiation from temperature, the TRP computation can be included in the absorption term of the radiation pressure coefficient for each panel of the satellite. In Montenbruck et al. (2015) and Vielberg and Kusche (2020), this static TRP formulation has been included into the computation of the radiation pressure coefficient (Eq. 4.2.21) for both SRP and ERP as

$$\boldsymbol{c}_{\mathrm{R}}^{\odot}(\lambda) = (1 - c_s)\, \boldsymbol{s} - 2\left(\frac{c_d}{3} + c_s \cos\gamma + \frac{c_a}{3}\right) \boldsymbol{n}. \tag{4.2.93}$$

**Temperature from transient heat-conductive model**

Instead of considering instantaneous re-radiation of heat, a more advanced approach is to account for the delayed re-radiation. Analytical formulations for the so-called thermal lag time have been determined empirically for LAGEOS (e.g., Lucchesi, 2002) resulting in a thermal lag time around 3000 s. Instead of computing the thermal lag time, the acceleration resulting from the delayed re-radiation of heat is formulated here following the advanced model by Wöske et al. (2019), which

is a transient temperature model including heat conduction. In this case, the partial differential equation (e.g. Elsner, 1988; Wöske et al., 2019, Eq. (16))

$$c_p \rho \frac{\partial T}{\partial t} = \lambda \frac{\partial^2 T}{\partial x^2} \tag{4.2.94}$$

needs to be solved for each panel with finite thickness $x$ to obtain the outer surface temperature $T$. Eq. (4.2.94) is also known as heat equation, which considers the material's thermal diffusivity (e.g. Elsner, 1988)

$$\alpha = \frac{\lambda}{c_p \rho}, \tag{4.2.95}$$

depending on the heat capacity $c_p$, the density $\rho$, and the conductivity $\lambda$ of the material. The thermal diffusivity describes the temporal temperature change of a material through heat conduction due to a temperature gradient. The assumptions for the GRACE satellite are summarized in Tab. 4.3 following Wöske et al. (2019), where $c_p \rho h$ was tuned so that the modelled and measured non-gravitational accelerations of GRACE agree well. Consequently, the parameters might absorb also the mismodelling of other non-gravitational accelerations and re-estimating the parameters might be beneficial in case of applying a slightly different force model than in Wöske et al. (2019). The parameters are assumed to be stable during the whole mission.

Table 4.3: Assumptions of heat capacity $c_p$, density $\rho$, and conductivity $\lambda$ of the panels of the GRACE satellite adopted from (Wöske et al., 2019, Tab. 2), who tuned $c_p \rho h$ such that the modelled and measured non-gravitational accelerations of GRACE agree well.

| Panel | Material | $c_p$ [J/kg K] | $\rho$ [kg/ m$^3$] | $h$ [mm] | $\lambda$ [W/m K] |
|---|---|---|---|---|---|
| Left, right and top | Solar panel | 540 | 2000 | 2.5 | 1.85 |
| | Insulation | 1000 | 30 | 70 | 0.023 |
| | Honey comb | 900 | 45 | 30 | 0.08 |
| Front and rear | Kapton | 1095 | 1400 | 0.1 | 0.2 |
| | Insulation | 1000 | 33 | 75 | 0.018 |
| | Honey comb | 900 | 45 | 30 | 0.08 |
| Nadir | Teflon foil | 1095 | 2000 | 0.1 | 0.2 |

To solve the partial differential equation (Eq. (4.2.94)), outer surface boundary condition and initial conditions need to be considered, which are adopted from Wöske et al. (2019). The condition that absorbed fluxes $P_{\text{abs}}$ and radiated fluxes are the same at the outer surface is considered as

$$P_{\text{abs}} - \epsilon \sigma T^4 = 0. \tag{4.2.96}$$

Further boundary conditions are not required as an infinite panel is assumed when solving the Partial Differential Equation (PDE). As initial condition, the internal heat production is assumed to be 250 W. Since the internal redistribution and production of heat strongly depends on the satellite's internal and external geometry, which is generally complicated to model, it would be desirable for the precise force modelling of future missions to have measurements of the material's thermal diffusivity, of the internal heat production, or ideally direct measurements of the outer surface temperature.

The solution of the partial differential equation (Eq. (4.2.94)) depends also on the initial temperature. From an initial test, I found that the solution of the partial differential equation depends on the initial temperature for approximately 15 orbital revolutions, when assuming initial temperature values of 280 K for every panel. Thus, to obtain stable results for the whole time period that should be evaluated, better estimates of the initial temperature of each panel are required. These

estimates are obtained here in an open loop run by solving the partial differential equation for 16 orbital revolutions assuming initial temperature values of 280 K for every panel.

Another idea to obtain the satellite's surface temperature, is using Coarse Earth Sun Sensor (CESS) measurements. CESS is a sensor invented by Doll and Pitz (1999) and can be found on-board GRACE, CHAMP and other missions. It consists of six sensor heads providing the satellite's orientation with respect to the Earth and the Sun, in case the star camera measurements are not available. Each sensor head consists of a small glass plate with one silvered part and one black part. The material properties of CESS on-board GRACE-A are $\alpha_B = 0.95$, $\epsilon_B = 0.85$ for the black plate, and $\alpha_M = 0.1$, $\epsilon_M = 0.86$ for the mirror-like surface (Qioptiq, 2023). The measured variable of CESS is the temperature. However, since the material of CESS is different from the satellite's surface, relating the measured temperature to the temperature of each surface might be possible but would require several assumptions. Since the temperature is a measure for the absorbed radiation at the sensor's surface, the absorbed radiation is directly related to CESS measurements and could be inserted in the TRP formulation under consideration of the varying absorption coefficients for different materials. However, this requires the availability of CESS data, which is currently not the case.

**Absorbed radiation**

As mentioned above, modelling the TRP acceleration according to both the static and the advanced model (Eqs. (4.2.93), (4.2.94)) requires information about the absorbed radiation at the satellite's surface. The amount of absorbed radiation basically depends on the amount of incoming radiation, the thermo-optical material properties and the satellite's geometry. Changes in the radiation lead to temperature variations, which in turn impact the acceleration. The computation of the absorbed radiation is outlined in the following with some differences to Wöske et al. (2019).

Generally, the total absorbed radiation $P_{abs}$ at each panel of the satellite results from the amount of absorption of the incoming radiation of the Sun $\odot$ and the Earth $\oplus$ weighted with the absorption coefficient $c_a$ of the panel's material. The incoming radiation at the position of the satellite has already been introduced in Eq. (4.2.11) for the Sun and in Eq. (4.2.87) for the Earth. In consideration with the absorption coefficients $c_{\mathrm{a_{vis}}}$ and $c_{\mathrm{a_{IR}}}$ from the macro-model for visible and infrared radiation, respectively, we obtain the absorbed radiation of each panel from

$$\begin{aligned} P_{\mathrm{abs}} =& P_{\mathrm{abs}\odot} + P_{\mathrm{abs}\oplus} && (4.2.97)\\ =& \left(\frac{1\,\mathrm{AU}}{r_{\odot,\mathrm{sat}}}\right)^2 P_{1\,\mathrm{AU}} \nu \frac{1}{2} \left(c_{\mathrm{a_{SW}}} + c_{\mathrm{a_{LW}}}\right) \cos\left(\gamma_\odot\right) + \\ & \sum_j \left(M^j_{\mathrm{SW}\uparrow} R^j_{\mathrm{SW}\uparrow} c_{\mathrm{a_{SW}}} + M^j_{\mathrm{LW}\uparrow} R^j_{\mathrm{LW}\uparrow} c_{\mathrm{a_{LW}}}\right) \frac{S_j \cos\alpha_j \cos\left(\gamma_{\oplus_j}\right)}{c\pi |\boldsymbol{x} - \boldsymbol{x}_{\mathrm{E_j}}|^2}. && (4.2.98) \end{aligned}$$

Here, $P_{\odot 1\,\mathrm{AU}}$ is the daily total solar irradiance at 1 AU, which requires the projection to the satellite's position by the inverse-square law with the distance $r_{\odot,\mathrm{sat}}$ between the satellite and the Sun. The solar radiation is split into visible and infrared by equally considering the absorption coefficients for shortwave and longwave radiation $c_{\mathrm{a_{SW}}}$ and $c_{\mathrm{a_{LW}}}$. This is different from Wöske et al. (2019), where the solar radiation is assumed to be constant and in the visible domain only. Then, $\nu$ denotes the shadow function, which is obtained in this thesis according to Robertson (2015). The panel's orientation is taken into account by $\cos(\gamma)$, where $\gamma$ denotes the angle between the incoming radiation and the surface normal. To obtain the total absorbed radiation of the Earth, the visible and infrared radiation for every surface element $j$ with a resolution of 1° in longitude and latitude are considered. $M$ is the Earth's outgoing flux in consideration of the ADMs denoted by $R$. Instead of obtaining the shortwave flux from CERES albedo data and the incoming solar flux as in Wöske et al. (2019), I include the outgoing fluxes from CERES SYN1deg data directly and in line with ADMs. $\alpha$ is the angle between the element's surface normal and the vector pointing from the centre of each element to the satellite. $S^j$ is the area of a discretized Earth surface element and $|\boldsymbol{x} - \boldsymbol{x}_{\mathrm{E_j}}|$ denotes the distance from the surface element to the satellite.

For GRACE, the macro-model provides the absorption coefficient for visible light $c_{\mathrm{a_{SW}}}$, which fulfils the condition $1 = c_{\mathrm{a_{SW}}} + c_{\mathrm{d_{LW}}} + c_{\mathrm{s_{LW}}}$. As already discussed above, (see Sect. 4.2.1), it is not defined for which wavelengths the provided thermo-optical material properties are valid. However, here it is assumed that $c_{\mathrm{a_{SW}}}$ can be used to obtain the absorbed visible solar radiation and the absorbed shortwave radiation of the Earth at each panel of the satellite. For infrared radiation, the macro-model provides an emission coefficient, which fulfils $1 = c_{\mathrm{e_{LW}}} + c_{\mathrm{d_{SW}}} + c_{\mathrm{s_{SW}}}$. Due to Kirchhoff's law, one can assume that emission and absorption are equal for a given wavelength, i.e., the absorption coefficient for infrared solar radiation and the longwave radiation of the Earth for each panel is the same as the given infrared emission coefficient. This is independent of the choice of the temperature model, which considers either instantaneous or delayed re-radiation.

## 4.3 Satellite-induced forces

In addition to the aerodynamics and radiation pressure forces, several satellite-induced non-gravitational forces act on a satellite. Their modelling is of importance for processing accelerometer measurements, since they introduce a disturbance signal. The order of magnitude of satellite-induced accelerations can be quite large as they occur in terms of spikes, however, their period is relatively small in the order of seconds.

### 4.3.1 Temperature sensitivity

As mentioned in Sect. 3.1, the accelerometer data are very temperature-sensitive. This heat sensitivity is also reported by Flury et al. (2008), who analysed spikes in the accelerometer data, which is related to the activation of the 64 heater circuits lasting up to 40 s. The resulting artificial accelerations have a complex pattern and can be up to $70\,\mathrm{nm\,s^{-1}}$. Flury et al. (2008) modelled the accelerations due to heater switches by applying a high-pass filter to the accelerometer measurements and extracting the data around the switch events.

### 4.3.2 Twanks

Twanks are another phenomenon, which effects the accelerometer data quality (Peterseim et al., 2012). The reason of the resulting 0.2 s signal consisting of a high amplitude peak, which generally fades out, is not clear yet. The twanks are visible in all three components with the largest effect in the radial direction.

### 4.3.3 Magnetic torquers

Some spikes in accelerometer data can also be related to magnetic torques and their current changes (Peterseim et al., 2012). Magnetic torquers are electromagnets used for attitude control. Peterseim et al. (2012) developed an empirical model of torque-related spikes.

### 4.3.4 Thruster firings

In addition, thruster firings are visible in the accelerometer measurements especially in the along-track and cross-track directions (Montenbruck and Gill, 2012). Thruster firings are required for orbit control. Modelling the impact and removing the additional acceleration is possible with knowledge of the timing and power of the thrusts using a suitable analytical model (see e.g., Montenbruck and Gill, 2012, pp. 105-107). Alternatively, the thruster events can be excluded from further analyses.

### 4.3.5 Antenna thrust

Another satellite-induced acceleration is the antenna thrust caused by the signal transmission. This includes the acceleration due to the up- and down link as well as the acceleration caused by other satellite-to-satellite tracking techniques such as the KBR measurement system on-board the GRACE satellites. Since the transmitted signals are also electromagnetic radiations at different wavelengths, the resulting antenna thrust acceleration can also be categorized as radiation pressure acceleration. During the mission's lifetime, this acceleration increases because the satellite's mass decreases due to the loss of fuel.

The acceleration due to antenna thrust

$$a_{\mathrm{AT}} = \frac{P}{cm} \tag{4.3.1}$$

depends on the transmit power $P$ of the antenna, the speed of light $c$ and on the satellite's mass $m$ (Milani et al., 1987; Eanes et al., 2000; Ziebart et al., 2004; Rodríguez-Solano, 2009; Steigenberger et al., 2018). Studies on the antenna thrust are usually available for GNSS satellites due to the continuous transmission of a large amount of radio navigation signals. Ziebart et al. (2007) found that including the antenna thrust in the force model for GPS satellites reduces the anomaly between SLR and International GNSS Service (IGS) orbits by 2 cm. For a *Block I GPS* satellite transmitting radio navigation signals with a power of about 80 W, the antenna thrust is especially relevant in the radial direction resulting in an acceleration of $5.3 \cdot 10^{-10} \frac{\mathrm{m}}{\mathrm{s}^2}$ (Rodríguez-Solano, 2009), which is larger than the ERP acceleration at the altitude of GPS satellites.

The antenna thrust has - at least to my knowledge - not yet been investigated for GRACE(-FO). Each GRACE satellite is equipped with antennas for up- and downlink using S-Band. Both are active during short-time fly-over periods of a few ground stations, e.g., the main downlink station for GRACE(-FO) is Ny-Ålesund, Norway (Falck et al., 2020). The resulting acceleration is expected to be multiple times smaller than the transmitting power of radio navigation signals for GNSS satellites. However, this effect cannot be considered in the experiments of this thesis, since reliable information about the receiver and transmitter power as well as their duration are not publicly available. Nevertheless, long-term perturbations of the orbit due to the thrust of the S-Band antenna cannot be excluded and should be kept in mind as a possible source of error in the force modelling.

In comparison to the occasional activity of up- and downlink antennas, the distance between the satellites is measured continuously using the KBR, and for GRACE-FO also a LRI system. For the GRACE-FO mission, the transmitted LRI signal has a power of 25 mW (Heinzel et al., 2017).The power of the signal reaching the other satellite is approximately 200 pW in case of perfect alignment of the transmitting and receiving antennas (Heinzel et al., 2017). Assuming a mass of 580 kg, the magnitude of the antenna thrust for the transmitting satellite in the along track direction is $1.44 \cdot 10^{-13} \frac{\mathrm{m}}{\mathrm{s}^2}$, which is about three orders of magnitude smaller than the along-track ERP acceleration. Since this is a very small value, the antenna thrust acceleration caused by the KBR or LRI systems is not modelled in further experiments of this thesis.

Strictly speaking, the electromagnetic signal from satellites above, such as GNSS satellites, causes also an acceleration on the satellites below, too. However, this anti-radial directed acceleration is expected to be negligible due to the already small amount of energy, which is transmitted, and the large distance of around 20,000 km to such satellites.

### 4.3.6 Electromagnetics

Since the satellite's electrical charge differs from its surrounding, the satellite experiences a Lorentz force depending on the angle between the Earth's magnetic field lines and the satellite's relative velocity (Sehnal, 1969; Vokrouhlický, 1989; Serra et al., 2018). As the satellite's electrical charge is relevant here, I categorize this acceleration as satellite-induced. According to Serra et al. (2018),

the Lorentz or electromagnetic acceleration can be computed from

$$\boldsymbol{a}_{\mathrm{em}} = \frac{q}{m}\boldsymbol{v} \times \boldsymbol{B}, \tag{4.3.2}$$

with the satellite's electrical charge $q$, its total mass $m$, its relative velocity $\boldsymbol{v}$ and the intensity of the magnetic field $\boldsymbol{B}$, which is related to the magnetic potential $V$ by

$$\boldsymbol{B} = -\nabla V. \tag{4.3.3}$$

The magnetic potential in up, south and east directions can be obtained from a spherical harmonic expansion of the recent International Geomagnetic Reference Field 13th generation (IGRF-13) (Alken et al., 2021). The transformation into the CRF first requires the rotation into ECEF coordinates (Laundal and Richmond, 2017) before rotating them to the CRF as described in App. A. The satellite's electrical charge $q$ results from

$$q = C\phi, \tag{4.3.4}$$

with the electrostatic capacitance $C$ and the surface potential $\phi$. The latter depends on the shadow function $\nu$ (see Sect. 4.2.1). The surface potential is has been measured on a few satellites only and is a rather critical quantity. For the van Allen Probes at medium Earth orbit, values vary generally between -10 and 10 Volt (Sarno-Smith et al., 2016). These results have been adopted for LEO satellites as well by Serra et al. (2018) resulting in the assumption that the surface potential can be obtained from $-5+10\nu$. To apply Eq. (4.3.4), the capacitance of a panel (Serra et al., 2018)

$$C = \frac{\epsilon_0 A}{2\lambda_{\mathrm{d}}} \tag{4.3.5}$$

depends on the vacuum permittivity $\epsilon_0 = 8.854 \cdot 10^{-12}\,\frac{\mathrm{F}}{\mathrm{m}}$, the area $A$ of the satellite's surface and the Debye length $\lambda_{\mathrm{d}}$, which is in the range of mm to cm for LEOs. Assuming $\lambda_{\mathrm{d}} = 5\,\mathrm{mm}$, and an area of $1\,\mathrm{m}^2$ for a GRACE-like satellite results in an acceleration at the order of $1 \cdot 10^{-12}$, which is about 1000 times smaller than the ERP acceleration and thus commonly not considered in satellite force modelling.

In addition, the rotation of the satellite in the Earth's magnetic field induces a magnetic momentum, which is especially relevant for rotating satellites such as LAGEOS (Sehnal, 1969; Vokrouhlický, 1989; Bertotti and Iess, 1991; Métris et al., 1997). Another acceleration related to the electromagnetics is caused by the interaction of the satellite with charged particles in the ionosphere. This has been discussed for spherical non-rotating satellites in Afonso et al. (1985).

## 4.4 Definition of standard and extended models

For comparing the acceleration resulting from different extensions of the RP models, it is prudent to define a "standard" for ERP and SRP models as a reference for the suggested model extensions. In Vielberg and Kusche (2020), we defined a standard RP model and an extended RP model, which are summarized below. Since this thesis includes additional suggestions to the extended model from Vielberg and Kusche (2020), I additionally introduce an extended RP model version as used in this thesis.

Based on the general SRP

$$\boldsymbol{a}_{\mathrm{SRP}} = \frac{A}{m}\cos(\gamma)\,\nu \int_{\lambda} \boldsymbol{c}_{\mathrm{R}}^{\odot}(\lambda) P_{\odot}(\lambda)\mathrm{d}\lambda$$

and ERP

$$\boldsymbol{a}_{\mathrm{ERP}} = \frac{A}{m}\int_{\Delta}\cos(\gamma)\int_{\lambda} \boldsymbol{c}_{\mathrm{R}}^{\oplus}(\lambda) P_{\oplus}(\lambda)\mathrm{d}\lambda\mathrm{d}\omega$$

formulations (see Eqs. (4.2.6) and (4.2.50)) for a single flat surface of the satellite, the standard and extended models are formulated with discretizations and details as discussed in Sects. 4.2.1 and 4.2.2. The SRP acceleration acting on the entire satellite can be obtained by evaluating and summing up the accelerations for all surface panels.

### 4.4.1 Standard model

The standard SRP model reads

$$\boldsymbol{a}_{\mathrm{SRP}} = \frac{A}{m}\cos(\gamma)\,\nu\boldsymbol{c}^{\odot}_{\mathrm{R_{SW}}}\left(\frac{1\,\mathrm{AU}}{r_{\odot,\mathrm{sat}}}\right)^2 P_{1\,\mathrm{AU}}. \tag{4.4.1}$$

It considers the Earth's shadow purely geometrically with the assumption of a spherical Earth according to Montenbruck and Gill (2012). In addition, the standard model uses a constant solar flux of $\Phi_{\mathrm{sc}}$ =1360.8 W/m$^2$ (Wild et al., 2013), which is assumed to be in the visible domain so that the radiation pressure coefficient for shortwave radiation $\boldsymbol{c}^{\odot}_{\mathrm{R_{SW}}}$ only is required, which considers absorption, specular and diffuse reflection.

The standard ERP model following Knocke et al. (1988) is based on latitude-dependent albedo and emissivity data and reads

$$\boldsymbol{a}_{\mathrm{ERP}} = \frac{A}{m}\sum_{j=1}^{19}\cos(\gamma_j)\left(\boldsymbol{c}^{\oplus}_{R_{\mathrm{LW,j}}}\frac{e_j E_s}{4} + \boldsymbol{c}^{\oplus}_{R_{\mathrm{SW,j}}}\tau_j a_j E_s\cos\theta\right)\frac{S_j\cos\alpha_j}{\pi|\boldsymbol{x}-\boldsymbol{x}_{\mathrm{E_j}}|^2}. \tag{4.4.2}$$

Here, the Earth's surface is discretized by 19 elements with same size $S$ (Eq. (4.2.84)). The solar irradiance $E_s = \Phi_{\mathrm{sc}}/c$ is computed from the same constant solar flux $\Phi_{\mathrm{sc}}$ =1360.8 W/m$^2$ as above. This differs from the original model by Knocke et al. (1988), where $\Phi_{\mathrm{sc}}$ =1367.05 W/m$^2$ is applied. Albedo and emissivity are computed according to Eqs. (4.2.73) and (4.2.74). The interaction of incoming radiation with the satellite's surface is modelled with specular and diffuse reflection as well as absorption using thermo-optical material properties for both longwave and shortwave radiation. TRP is not considered in the standard model defined here and LRP is throughout omitted in the RP force model of LEO satellites.

### 4.4.2 Extended model according to Vielberg and Kusche (2020)

Here, the extended unified analytical models for SRP and ERP accelerations according to Vielberg and Kusche (2020) are presented. The extended SRP acceleration acting on a single flat surface of the satellite can be modelled as

$$\boldsymbol{a}_{\mathrm{SRP}} = \frac{A}{m}\cos(\gamma)\,\nu\frac{1}{2}\left(\boldsymbol{c}^{\odot}_{\mathrm{R_{SW}}} + \boldsymbol{c}^{\odot}_{\mathrm{R_{LW\uparrow}}}\right)\left(\frac{1\,\mathrm{AU}}{r_{\odot,\mathrm{sat}}}\right)^2 P_{1\,\mathrm{AU}}(\lambda,t). \tag{4.4.3}$$

It differs from the standard model as it includes the dependency on at least two channels of the solar spectrum (visible and infrared) instead of visible wavelengths only. The solar constant is replaced by a time series of the total solar irradiance (see Fig. 2.5) to account for the temporal variability of the solar flux. The reflection at the satellite's surface is modified by additionally accounting for anisotropic reflection as in Wetterer et al. (2014) and static thermal re-radiation following Montenbruck et al. (2015). In addition, the applied shadow function considers processes in the Earth's atmosphere and the Earth as a spheroid following Robertson (2015).

The extended ERP acceleration model reads

$$\boldsymbol{a}_{\mathrm{ERP}} = \frac{A}{m}\sum_{j}\cos(\gamma_j)\left(\boldsymbol{c}^{\oplus}_{R_{\mathrm{SW,j}}}F_{\mathrm{SW,j}}R_{\mathrm{SW,j}} + \boldsymbol{c}^{\oplus}_{R_{\mathrm{LW,j}}}F_{\mathrm{LW,j}}R_{\mathrm{LW,j}}\right)\frac{\cos(\alpha_j)\,\Delta\omega_j}{\pi c r^2_{\mathrm{Sat},j}}. \tag{4.4.4}$$

To be consistent with the SRP model, the reflection at the satellite's surface is implemented as above. As mentioned in Sect. 4.2.2, hourly outgoing fluxes at the top of atmosphere from CERES are applied directly instead of albedo and emissivity maps. Additionally, angular distribution models (Suttles et al., 1988; Suttles et al., 1989) account for the angular dependency of Earth's radiation. Instead of discretizing the Earth's surface by a small number of elements (Knocke et al., 1988), the surface elements are discretized with a resolution of 1° in longitude and latitude.

### 4.4.3 Extended model as used in thesis

In this thesis, I further modified the extended version from Vielberg and Kusche (2020). For both ERP and SRP computations, the radiation pressure coefficient is modified, whereas the remaining model stays the same as above (Eqs. (4.4.3) and (4.4.4)). Instead of applying the static thermal re-radiation within the radiation pressure coefficient, the TRP is computed separately based on the temperature from the advanced TRP model considering heat conduction according to Wöske et al. (2019). To obtain the absorbed radiation, the solar and Earth radiation reaching the satellite are computed exactly as in the SRP and ERP force modelling, respectively. Additionally, anisotropic reflection is not considered in the extended model as used in this thesis as it turned out to bring the modelled accelerations further away from the measurements in Vielberg and Kusche (2020).

The extended model as defined here is expected to be the most realistic radiation pressure force model. This hypothesis will be carefully validated in Ch. 5, which includes a detailed analysis of the force model extensions and different validation approaches.

Adding the aerodynamic and satellite-induced acceleration to the above mentioned radiation pressure force models result in the total non-gravitational accelerations. From the satellite-induced accelerations, thruster firings are considered by removing the data 30 s around the thrusts as in Vielberg and Kusche (2020). The aerodynamic acceleration for GRACE in Vielberg and Kusche (2020) has been modelled as described in Vielberg et al. (2018). The model accounts for drag and lift forces as in Doornbos (2012) with an energy accommodation coefficient of 0.93. Thermospheric neutral densities are obtained from NRLMSISE-00 (Picone et al., 2002) and neutral winds were not considered. In this thesis, the same approach is applied, however, the density is obtained from NRLMSIS 2.0.

At IGG, the implementation of the non-gravitational forces has been developed in the context of the neutral density estimation within the D-SAT project (Bestimmung von thermosphärischen Dichteparametern mit Hilfe von Akzelerometermessungen an Bord verschiedener Satellitenmissionen sowie mit Hilfe von GPS-bestimmten Satellitenorbits, LZ 1402) in 2014. This software, which also included standard models of non-gravitational accelerations, has mainly been developed by my colleagues Ehsan Forootan and is based on earlier implementations by Anno Löcher. The implementations have been further developed since then by Christina Lück, Armin Corbin and me. Christina Lück implemented the drag acceleration after Doornbos (2012) and Sentman (1961). Armin Corbin integrated the new NRLMSIS 2.0 empirical atmospheric model into the software (Emmert et al., 2021). I extended the radiation pressure modelling of the Sun and the Earth, added the thermal radiation pressure estimation from Wöske et al. (2019) as described in Sect. 4.2, and implemented the iterative density estimation following Doornbos et al. (2010) (see Sect. 6.1).

# Chapter 5

# Results of forward non-gravitational force modelling

In this chapter, the results of the forward non-gravitational force modelling are presented with a focus on the GRACE satellite (Sect. 5.1). After introducing the results of the total radiation pressure accelerations, a comparison of the individual radiation pressure accelerations at different stages of extension. However, evaluating the skill of the radiation pressure force modelling and its suggested extensions from the previous chapter appears challenging because this would require perfectly measured non-gravitational accelerations and a perfect aerodynamic model. Therefore, a comparison of the modelled non-gravitational accelerations to observed ones is shown instead, before introducing a validation with independent SLR data.

Additionally, the forward modelling is applied to spherical SLR satellites in Sect. 5.2. Even though modelling the non-gravitational forces for a sphere might seem easier at a first glance, challenges for spherical satellites need to be discussed.The modelled non-gravitational accelerations are presented for six selected spherical SLR satellites. Finally, the modelled forces are validated within a POD.

## 5.1 Results for the satellite mission GRACE

The satellite mission GRACE collected data for approximately 15 years between 2002 and 2017. To get an idea of the magnitude of the non-gravitational accelerations acting on it during this period, Fig. 5.1 depicts the norm of the modelled aerodynamic and radiation pressure accelerations acting on GRACE-A during its lifetime. For these computations, the aerodynamic model as described in Sect. 4.1 is applied together with the extended radiation pressure model as defined in Sect. 4.4.3. The aerodynamic acceleration is usually the dominating non-gravitational acceleration during the GRACE lifetime and basically follows the solar cycle with a maximum in 2003 and 2015. Even though the solar maximum was more intense during 2003, the aerodynamic acceleration reaches a value of $400\,\mathrm{nm/s^2}$, which is less than half of the magnitude reached in 2015. The reason for this is the decreasing satellite altitude (see also Fig. 5.1) from around 500 km until nearly 350 km at the mission end. Thus, with decreasing altitude the atmosphere becomes more dense and the aerodynamic acceleration is larger. In contrast, the norm of the radiation pressure acceleration is usually below $65\,\mathrm{nm/s^2}$ and shows systematics, which are clearly related to the $\beta$ angle instead of the solar cycle. During the solar minimum around 2008, where the magnitude of the aerodynamic signal is about ten times smaller than during the solar maximum, the magnitude is similar and partly even below that of the radiation pressure acceleration. Since the similar magnitude of these accelerations is beneficial for the validation later on as it keeps errors due to the aerodynamic modelling to a minimum, the year 2008 is selected for further analyses as well. Furthermore, the chosen year 2008 is about in the middle of the mission lifetime, when the instrumentation and battery were still fully operational.

In Fig. 5.1, as well as in the following, the computation of the non-gravitational accelerations is based on the satellite's position taken from reduced dynamic orbits, but any orbit could be used.

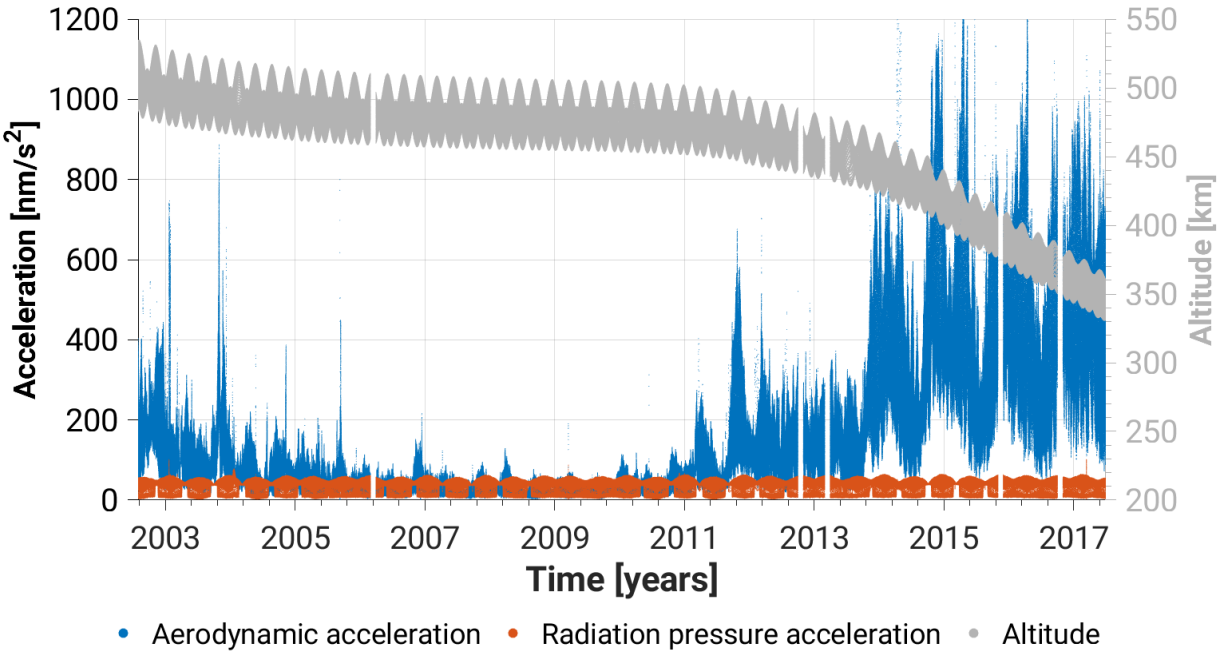



Figure 5.1: Norm of the modelled aerodynamic and radiation pressure acceleration in the SRF acting on GRACE-A together with the satellite altitude above the Earth's surface during the mission lifetime. For the computation of the radiation pressure acceleration, the extended model as defined in Sect. 4.4.3 is applied.

The non-gravitational accelerations are modelled in an inertial reference frame before transforming them to the SRF using star camera data. The results in this chapter are throughout represented in the SRF. The following comparisons are based on the results published in Vielberg and Kusche (2020) and complemented by adding the TRP acceleration.

Fig. 5.2 shows the norm of the modelled radiation pressure accelerations acting on GRACE-A with respect to the argument of latitude during the year 2008. The norm of the total RP acceleration is illustrated as well as the individual accelerations (SRP, ERP, TRP) contributing to it. Each acceleration is modelled using the standard model and the extended model as defined in Sects. 4.4.1 and 4.4.3, respectively. One column of each plot depicts the acceleration along one orbital revolution of the satellite, i.e., the argument of latitude is 0°, where the satellite passes the equator from south to north. Then, it reaches 90° at the north pole, from where the satellite descends until the south pole at 270° and finally reaches the equator again. One revolution lasts approximately 90 minutes. The illustration of time against argument of latitude allows for the detection of patterns in time and space such as the shadow regions, which are clearly visible in all images except of the standard TRP acceleration, which is assumed to be zero as it is commonly not considered at all. The shadow regions occur in the descending orbit between end of March to beginning of August. Here, the standard total radiation pressure acceleration acting on the satellite reaches nearly 30 $\mathrm{nm/s^2}$ resulting from the Earth's longwave radiation only. On the ascending orbit during the same period of the year, the standard RP acceleration reaches 51 $\mathrm{nm/s^2}$. It should be mentioned here that the norm of the RP acceleration is computed after summing up the individual accelerations. Thus, a positive SRP acceleration and a negative ERP acceleration in the same direction (here especially radial) leads to an RP norm, which is smaller than the norm of the SRP and ERP accelerations with 66 $\mathrm{nm/s^2}$ and 70 $\mathrm{nm/s^2}$, respectively.

The satellite is fully in sunlight for approximately one month before and after the eclipse, i.e. March and August, where the standard RP acceleration reaches 34 $\mathrm{nm/s^2}$. In the remaining time, the satellite is in the sunlight while descending and in umbra while ascending. The transition between umbra and sunlight area is quite small with a few seconds to a few minutes.

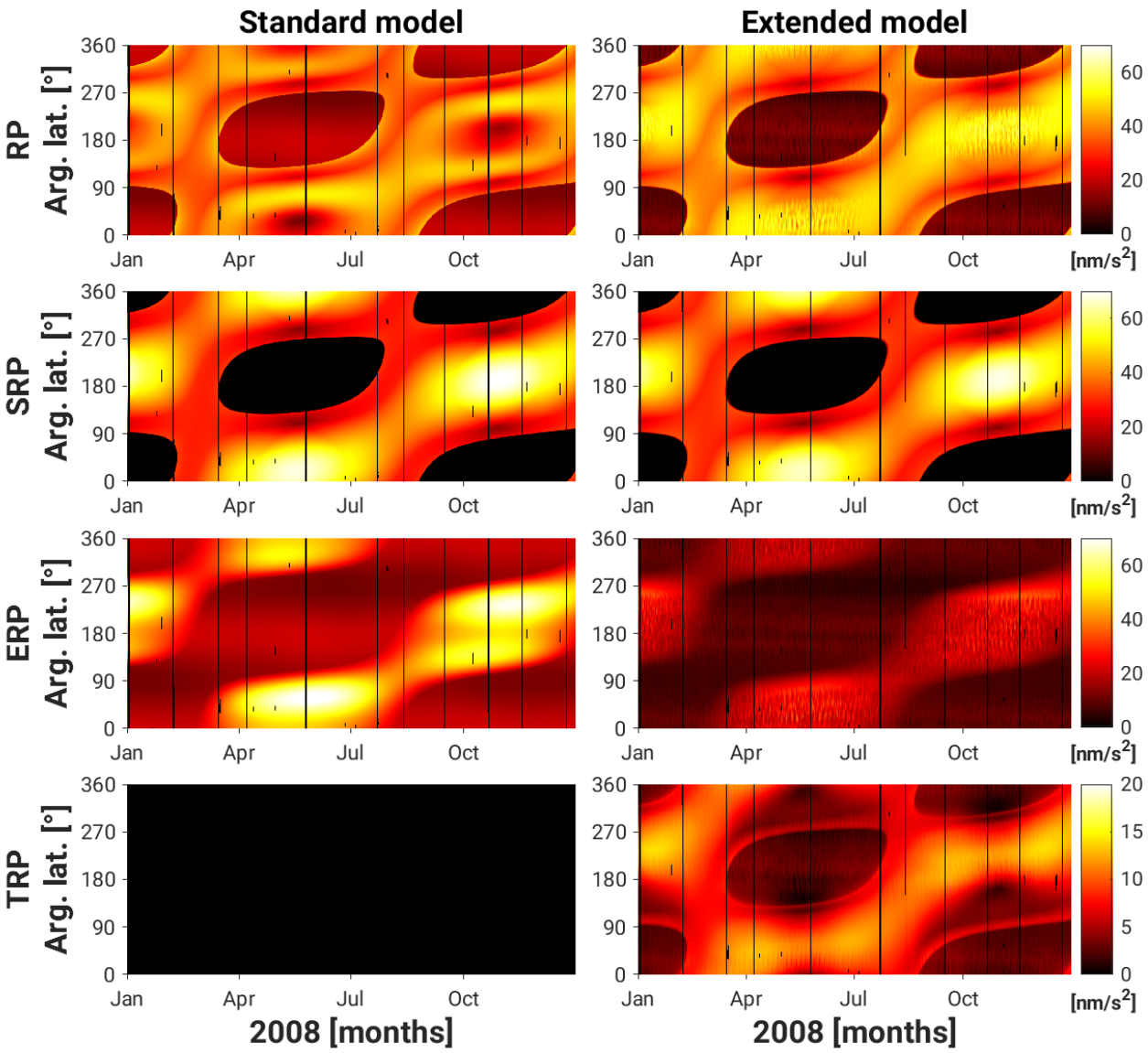



Figure 5.2: Norm of the modelled radiation pressure, SRP, ERP, and TRP accelerations acting on GRACE-A during the year 2008 in dependency of the argument of latitude. For the computation of the radiation pressure acceleration, the standard and extended models as defined in Sects. 4.4.1 and 4.4.3, respectively, are applied. The lower left image is black, since the TRP acceleration is not considered in the standard model.

In the extended model, the norm of the RP acceleration reaches 51 nm/s$^2$ in sunlight, which is similar to the standard model. However, in the shadow regions the RP norm is smaller with values well below 15 nm/s$^2$ even though the TRP acceleration contributes to these regions in the extended model as well, i.e., the ERP acceleration from the extended model are about two times smaller than in the standard model. At this point, I suspect that the standard ERP model may result in overestimated accelerations, however, further analyses are performed later in this chapter to verify this assumption. In addition, the extended ERP model provides more detailed structures due to the increased temporal resolution (hourly) of the radiation data sets. The extended TRP acceleration considers transient heating and heat conduction. Its norm reaches 11 nm/s$^2$ in the shadow regions and up to 14 nm/s$^2$ when the satellite is in sunlight, which is nearly 30% of the RP acceleration and should therefore not be neglected in the force modelling. In addition, the consideration of the TRP acceleration changes the patterns of the RP acceleration especially after leaving the shadow regions. The SRP acceleration does not show any visible differences in this first

comparison.

In the following, the three directions of the individual accelerations are shown and discussed in more detail. For each acceleration, different model scenarios are compared to each other.

### 5.1.1 SRP

Here, the results of the analytically modelled SRP acceleration at different stages of extension as outlined in Sect. 4.2.1 are presented. To allow for a systematic comparison, I introduce a code of five digits as shown in Tab. 5.1 to distinguish between different model versions. These versions allow for a comparison of the SRP acceleration using the solar constant or daily TSI, a geometrical or physical shadow function, isotropic or anisotropic reflection at the satellite, a varying amount of visible solar radiation, and operating or non-operating solar panels. For example, 00000 represents the standard model, whereas 11020 is the extended SRP model.

Table 5.1: Overview of the five-digit code of different SRP model extensions. Note that the weight of the visible incoming solar radiation is a value between 0 and 1 and the remaining amount is assigned to the infrared radiation. The "interp." scenario goes one step further and applies the suggested macro-model from Tab. 4.1, which is an interpolation of the original model for five spectral bands.

| | 1st digit | 2nd digit | 3rd digit | 4th digit | 5th digit |
|---|---|---|---|---|---|
| | Solar radiation | Shadow function | Reflection at the satellite | Scale of visible incoming solar radiation | $\alpha_{\text{vis}}$ of solar panel |
| 0 | solar constant | conical shadow | isotropic reflection | 1 | 0.65 |
| 1 | daily TSI from EBAF data | physical shadow | anisotropic reflection with BRDF | 0.45 | 0.72 |
| 2 | - | - | - | 0.5 | - |
| 3 | - | - | - | 0.55 | - |
| 4 | - | - | - | interp. (Tab. 4.1) | - |

The modelled SRP accelerations for the GRACE-A satellite are presented exemplarily between 5 and 8 a.m. on January 1, 2008, in Fig. 5.3. During this period, GRACE went through approximately two orbital revolutions as shown with the ground track in Fig. 5.4. Starting with the standard SRP model, extensions are added successively to study their impact on the SRP acceleration. During the selected time period, the magnitude of the SRP acceleration is largest in the radial direction with up to 61 nm/s$^2$. This is related to the satellite's orientation and its orbit, where the relatively small $\beta'$ angle of 24° results in an illumination from the top covering the satellite's largest areas. The magnitude in the along-track and cross-track directions of up 35 nm/s$^2$ and 33 nm/s$^2$, respectively, is smaller than in the radial direction. During eclipse transition the satellite is not illuminated and the SRP acceleration is zero in all directions. When using the physical shadow function (Robertson, 2015), passing the semi-shadowed regions takes nearly four minutes, whereas the shadow entry lasts below 20 seconds with the conical model for the same transit.

To take a closer look at the differences between the extensions of the SRP model, Fig. 5.5 shows the mean differences as well as the Root Mean Square Differences (RMSDs) between selected versions from Tab. 5.1 for January, 2008. The model extensions have the largest impact on the radial direction, whereas the impact on the along-track accelerations is minor, which is again related to the orbital plane orientation. This is also valid during other periods, e.g., January 2010 (Vielberg and Kusche, 2020). Including the BRDF shows the largest mean differences and RMSDs of up to 5.9 nm/s$^2$, which is about half of the SRP signal in that direction (see also Fig. 5.3). Increasing discrepancies when including the BRDF does not necessarily mean that these extensions

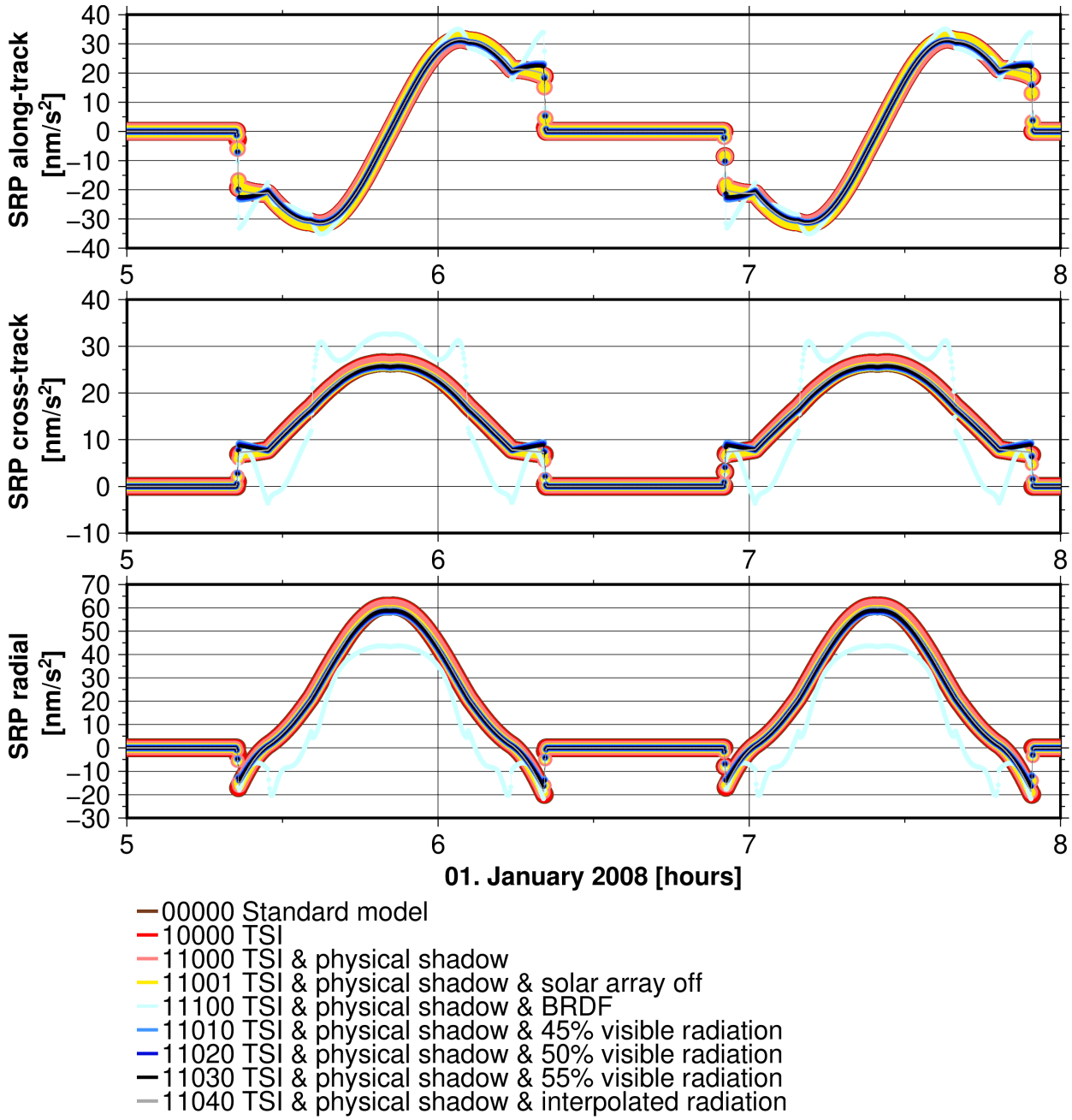



Figure 5.3: Different scenarios of modelled SRP acceleration acting on GRACE-A in the along-track (top), cross-track (middle), and radial (bottom) directions of the SRF during 3 hours (5–8 a.m.) on January 1, 2008. To look up modelling details, please see Tab. 5.1.

are unsuitable and further validation is required. Interestingly, the choice of the absorption coefficient for operating versus non-operating solar arrays (cases 11000 and 11001, respectively) has the second largest impact with a mean difference of 0.7 nm/s$^2$ in the radial direction. The fact that changing the absorption coefficient by 0.07 results in a difference of roughly 6 % in the radial SRP acceleration clarifies that the thermo-optical material properties have a large impact on the modelled acceleration. However, the material properties are known to be incorrect by a few tens of percent and can therefore be assumed to bring the largest weakness in radiation pressure force modelling. Including the physical shadow function causes the smallest mean difference and RMSD around 0.002 nm/s$^2$. Nevertheless, these changes are important when considering accelerations during penumbra transitions.

Mentioning that incorrect thermo-optical material properties are the major weaknesses in the

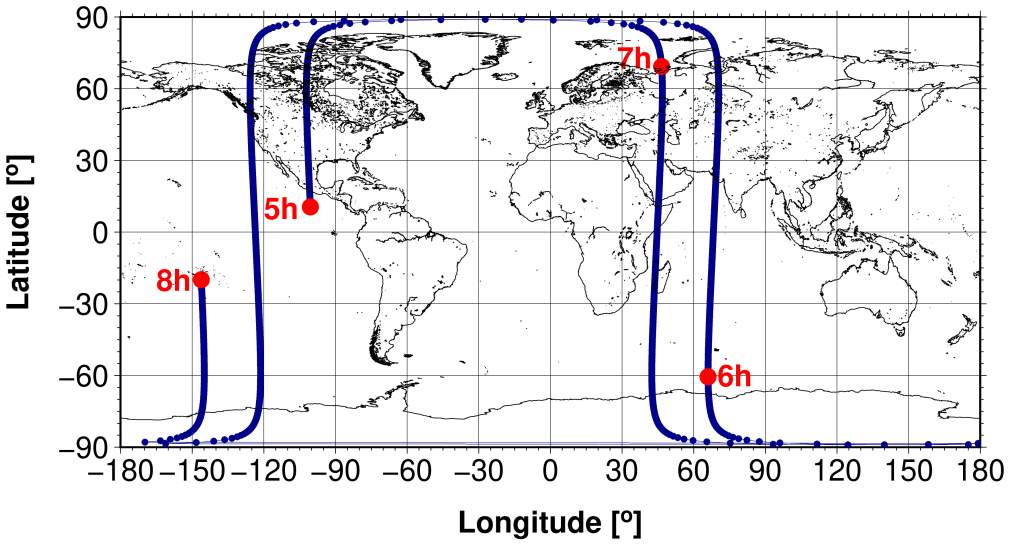



Figure 5.4: Ground track of GRACE-A between 5 and 8 a.m. on January 1, 2008.

radiation pressure force modelling, requires a closer look at the uncertainty of the modelled forces. Generally, an error of 5 % is assumed for the total radiation pressure (e.g., Doornbos et al., 2009; Siemes et al., 2023). Making a statement of the uncertainty of the individual radiation pressure forces could be derived from a variance propagation. However, this requires several assumptions about the uncertainty of the input data such as geometry, mass, thermo-optical material properties, and fluxes, which can only be estimated roughly. Therefore, this thesis does not show a variance propagation and instead focusses on the impact of the model extensions on the individual radiation pressure accelerations.

### 5.1.2 ERP

Similar to SRP, this section shows a comparison of modelled ERP accelerations at different stages of extension from Sect. 4.2.2. Again a code of five digits as shown in Tab. 5.2 is used to distinguish between different versions. Besides changing the discretization of the footprint and the consideration of active solar arrays, the focus is on the usage of different radiation data as well as the anisotropic reflection at TOA and at the satellite. The utilized CERES data, which are required for most extended ERP models, are shown in Fig. 5.6 and consist of the outgoing shortwave and longwave fluxes, cloud fraction, and snow coverage from the hourly available CERES SYN1deg data set.

The results are again displayed for GRACE-A during the same exemplary period between 5 and 8 a.m. on January 1, 2008. Fig. 5.7 shows the modelled ERP acceleration for the standard model and for different stages of extension. As expected, the signal is largest in the radial direction with accelerations of up to -66 $\mathrm{nm/s^2}$ for the standard model. This maximum is reached, e.g., around 6 a.m. when the satellite receives a large amount of reflected radiation from the Antarctic region, which has a very high albedo (see Fig. 5.6). The magnitude of the ERP accelerations with the extended model formalism are lower with up to -39 $\mathrm{nm/s^2}$ in the radial direction, thus, the standard model seems to overestimate the ERP acceleration due to the coarse discretization of the footprint, which has also been observed during other periods. Within the Earth's shadow, where the satellite experiences only the Earth's outgoing infrared radiation, the signal is generally smoother than in sunlight. This is related to the high variability in the shortwave fluxes (see Fig. 5.6), which is only visible in the hourly CERES data since the short-term variations average out in the monthly EBAF data as well as in the latitude-dependent representation used in the standard model. Thus, changing the radiation data leads to variations on small spatial scales especially, when the satellite is in sunlight. An attempt at finer discretization of the radiation pressure coefficient Eq. (4.2.21) with interpolated material properties according to Tab. 4.1 leads to the smallest ERP signal in

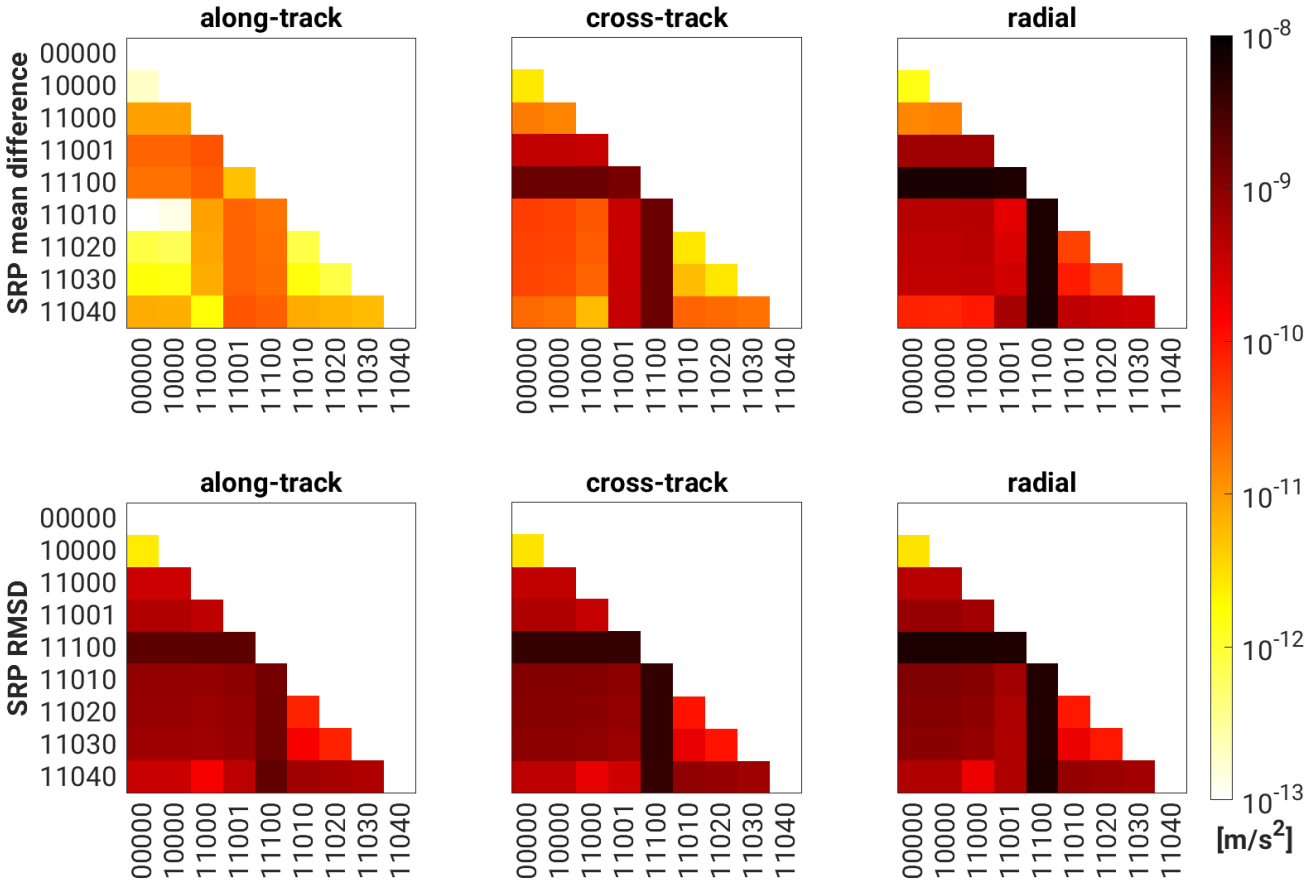



Figure 5.5: Mean differences (top) and RMSDs (bottom) between different SRP extensions applied to GRACE-A during January, 2008. To look up the five-digit code, please see Fig. 5.3 or Tab. 5.1 for details.

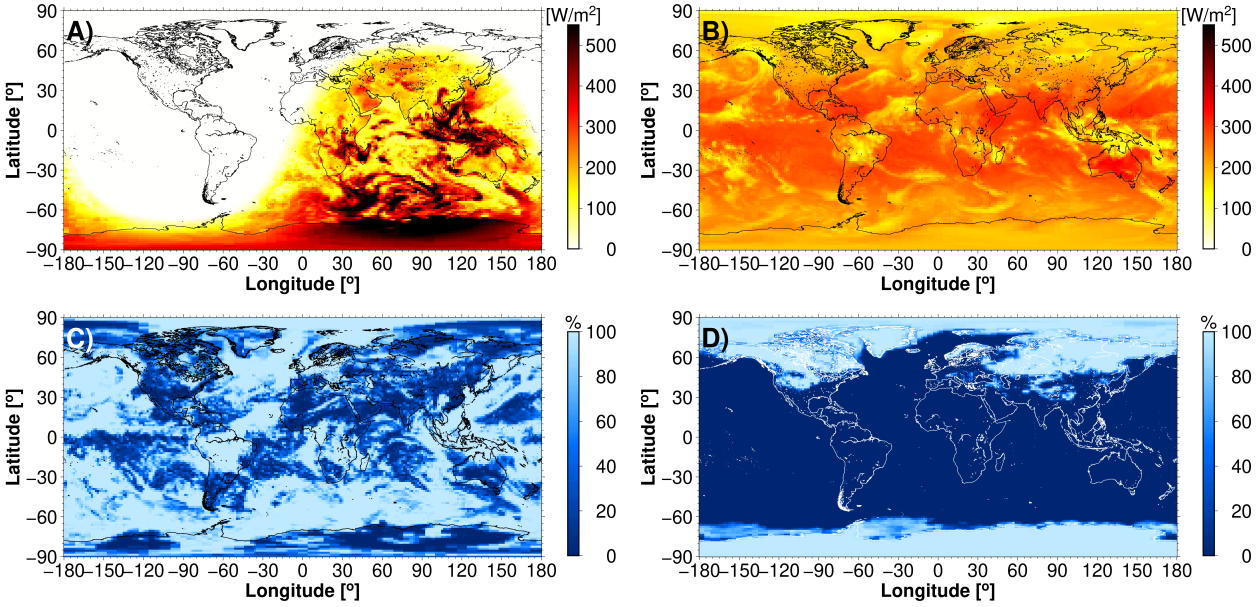



Figure 5.6: Outgoing shortwave (A) and longwave (B) flux, cloud fraction (C) and snow coverage (D) from CERES SYN1deg data on January 1, 2010, at 6 a.m.

Table 5.2: Overview of the five-digit code of different ERP model extensions. The scenario with interpolated fluxes applies the suggested macro-model from Tab. 4.1, which is an interpolation of the original model for seven spectral bands. The fluxes are interpolated to the same wavelengths in that scenario.

| | 1st digit | 2nd digit | 3rd digit | 4th digit | 5th digit |
|---|---|---|---|---|---|
| | Footprint | Radiation data | Reflection at TOA | Reflection at satellite | $\alpha_{\text{vis}}$ of solar panel |
| 0 | Discretization with 19 surface elements | Albedo, emission as in Knocke et al. (1988) | isotropic | isotropic | 0.65 |
| 1 | Discretization with $1^\circ \times 1^\circ$ grid | Albedo, emission from EBAF data | anisotropic with ADMs | anisotropic with BRDFs | 0.72 |
| 2 | - | Outgoing flux from EBAF data | - | - | - |
| 3 | - | Outgoing flux from SYN1deg data | - | - | - |
| 4 | - | Interp. outgoing flux from SYN1deg data | - | - | - |

the radial direction. The reason for this is that the interpolated coefficients for the nadir panel assume that the total radiation in the far infrared band is fully absorbed, which might not be a realistic assumption. However, it becomes clear that the thermo-optical material properties from the macro-model also have an impact on the magnitude of the ERP acceleration. Changing the thermo-optical material properties due to operating and non-operating solar panels does not have an impact on the ERP acceleration since the Earth's outgoing radiation hardly reaches the panels on top of the satellite.

In the along-track and cross-track directions, the magnitude of the ERP acceleration is usually below $1\,\text{nm/s}^2$. Here, larger variations are visible when including the anisotropic reflection at the satellite, which was already found to have a large impact on the SRP acceleration and it remains an open question, whether the selected BRDF to account for anisotropy is a good choice.

In addition to the time series, Fig. 5.8 shows the mean differences and RMSD between different model extensions during January 2008. The largest differences between the differently modelled ERP accelerations occur of course in the radial direction, where the signal is largest. The ERP mean differences and RMSD reach up to $1\,\text{nm/s}^2$ in the radial direction, when changing the discretization of the satellite's field of view from 19 surface elements as suggested by Knocke et al. (1988) to a grid of $1^\circ$ in latitude and longitude. Considering the outgoing radiation only on a coarse grid can easily lead to over- or underestimated radiation pressure accelerations, since the acceleration strongly depends on the radiation at the position of these surface elements. Changes in the radiation data and the anisotropic reflection at TOA yield smaller differences below $1\,\text{nm/s}^2$ in all directions. However, as observed above, the variations can locally exceed a few nanometres due to the strong albedo signal over Antarctic regions.

The findings for the SRP and ERP accelerations during this particular time agree well with the results from (Vielberg and Kusche, 2020), where January 2010 was selected instead, and TRP was not considered.

### 5.1.3 TRP

Finally, the TRP acceleration is compared at different stages of extension. Once again a code of five digits distinguishes between different extensions (see Tab. 5.3). Besides tuning the incoming radiation and considering active solar arrays, variations of the thermal diffusivity and the internal

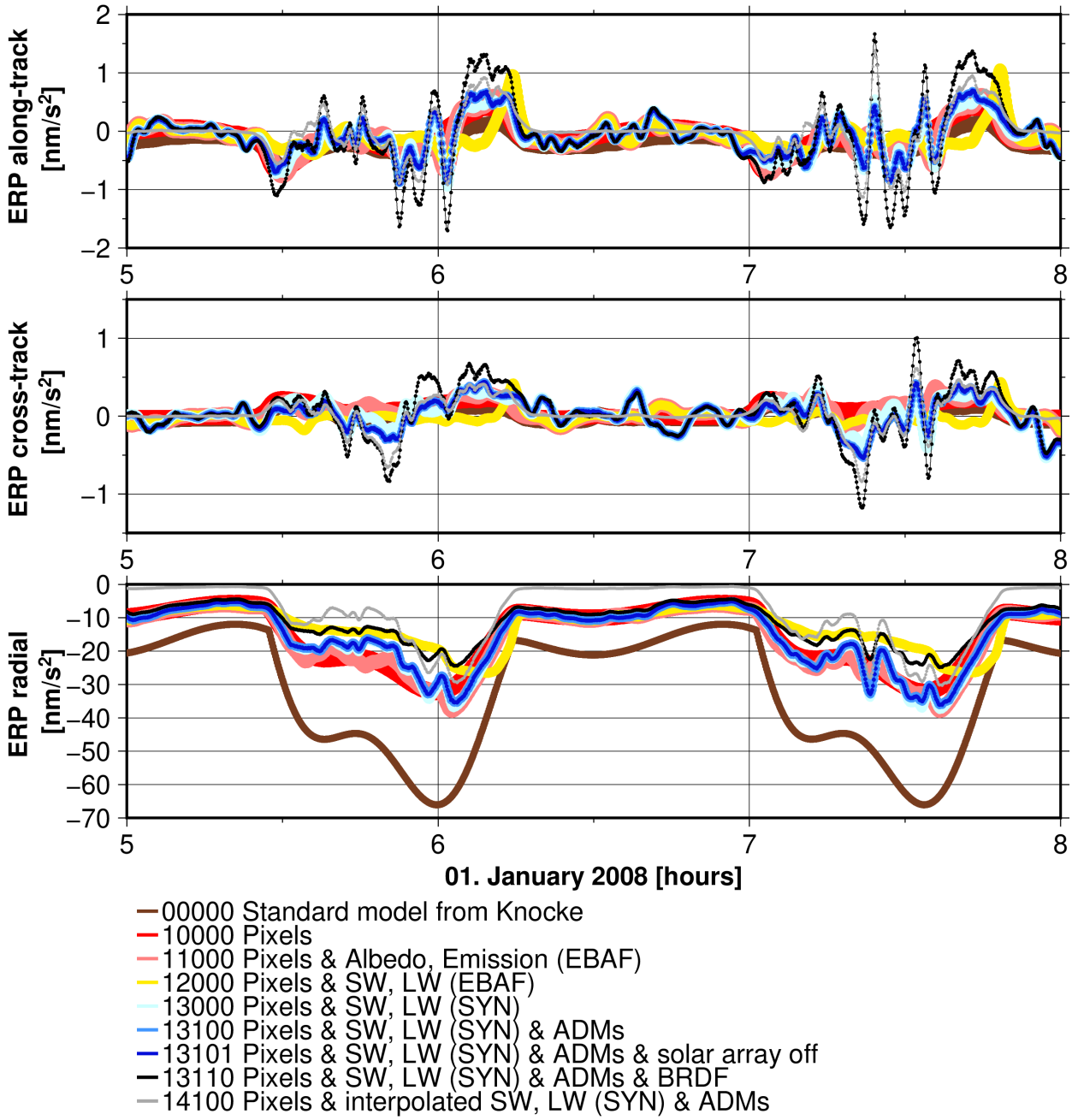



Figure 5.7: Different scenarios of modelled ERP acceleration acting on GRACE-A in the along-track (top), cross-track (middle), and radial (bottom) directions of the SRF during 3 hours (5–8 a.m.) on January 1, 2008. To look up modelling details, please see Tab. 5.2.

power are tested since these quantities are based on assumptions in the TRP model.

In Fig. 5.9, the differently modelled TRP accelerations are presented for GRACE-A between 4 and 8 a.m. on January 1, 2008. Here, the TRP acceleration is largest in the radial direction when considering the static case with instantaneous re-radiation, where the signal is up to 14 nm/s$^2$. The peak is reached eight minutes earlier and a few nm/s$^2$ larger than in case of considering transient temperatures and heat conduction using PDEs. The difference between the instantaneous and heat-conductive solutions shows also very large variations in the other directions. In the along-track direction, where the TRP acceleration varies up to $\pm$2.4 nm/s$^2$, the instantaneous TRP acceleration is similar to a sine curve. This is not the case for the PDE solution because it is close to zero for nearly 30 minutes when the satellite is in the Earth's shadow. This is physically more realistic because the satellite cools down and is only exposed to the Earth's outgoing IR radiation.

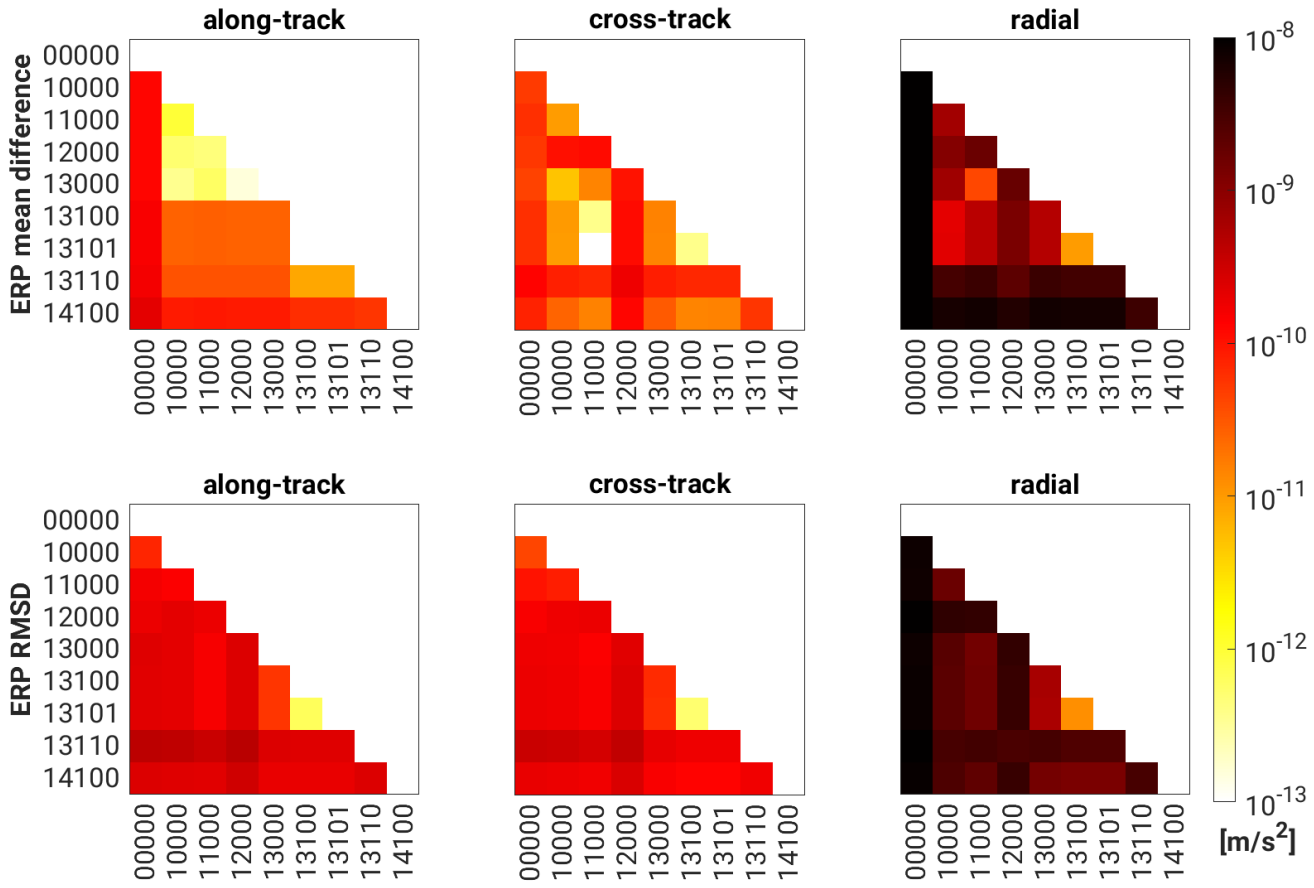



Figure 5.8: Mean differences (top) and root mean square differences (RMSD, bottom) between different ERP extensions applied to GRACE-A during January, 2008. To look up the digit codes, please see Fig. 5.7 or Tab. 5.2 for details.

Table 5.3: Overview of the five-digit code of different TRP model extensions. The interpolated scenario applies the macro-model from Tab. 4.1, which is an interpolation of the original model for seven spectral bands in total.

| | 1st digit | 2nd digit | 3rd digit | 4th digit | 5th digit |
|---|---|---|---|---|---|
| | Model | Scale of thermal diffusivity | Internal power [W] | Scale of visible incoming solar radiation | $\alpha_{vis}$ of solar panel |
| 0 | static (instantaneous)[1] | 1 | 250 | 1 | 0.65 |
| 1 | PDE: transient heat-conductive [2] | 0.5 | 300 | 0.45 | 0.72 |
| 2 | - | 1.5 | - | 0.5 | - |
| 3 | - | - | - | 0.55 | - |
| 4 | - | - | - | interp. Tab. 4.1 | - |

[1] Montenbruck et al. (2015)
[2] Wöske et al. (2019)

In the cross-track direction, the TRP acceleration is larger than in along-track and reaches at most $8\,\mathrm{nm/s^2}$. Within the shadow regions, the acceleration is close to zero. The instantaneous signal shows quite abrupt variations before and after the shadow entry and remains nearly constant in-between. On the other hand, the heat-conductive solution is much smoother. Changing the thermal diffusivity (see Eq. (4.2.95)) by a factor of 0.5 and 1.5 results in an earlier and delayed peak, respectively, in all directions. Especially in the cross-track and radial directions the shift is quite large with up to $0.5\,\mathrm{nm/s^2}$ and $2\,\mathrm{nm/s^2}$, respectively, which equals 7 % and 25 % of the signal in that direction. Whereas the variations in the cross-track acceleration are least critical for the orbit determination, a radial non-gravitational perturbation of $2\,\mathrm{nm/s^2}$ for GRACE yields an along-track orbit error of 65 cm after one day with the assumption of fixed initial values. (The radial and cross-track components of the orbital position are affected well below 1 cm.) Consequently, it is critical that the thermal diffusivity as well as the thickness and layers of the panels are not provided by the manufacturers and assumptions need to be made. However, changes in the internal power, which is assumed to be 250 W in the computations and exemplarily raised to 300 W in scenario 10100, lead to variations below 2 %. Then, the impact of wavelength-dependent incoming radiation on the TRP acceleration is assessed. Considering not only visible solar radiation but also infrared solar radiation results in an increased TRP acceleration in all directions. The variations are largest in the radial direction with up to $2\,\mathrm{nm/s^2}$, which corresponds to 25 % of the TRP acceleration in this direction. Interestingly, in the radial direction also a sudden decrease by nearly $5\,\mathrm{nm/s^2}$ can be observed when entering or leaving the shadow region, however, the reason remains unclear. Varying the amount of visible and infrared solar radiation as it has been done above for the SRP acceleration leads to changes below 2 %. Modelling the TRP acceleration with the interpolated macro-model, i.e., splitting the solar and terrestrial radiation into seven bands (scenario 10040), leads to large variations in the radial directions. This is related to the interpolated coefficients of the nadir panel, where the total radiation in the far infrared band is assumed to be fully absorbed, which might not be a realistic assumption. Changing thermo-optical material properties due to operating and non-operating solar panels has the same impact as considering visible and infrared solar radiation, i.e., the peaks increase by nearly 25 %. To summarize, changing the thermo-optical material properties from the macro-model impacts the magnitude of the TRP acceleration significantly.

Additionally, Fig. 5.10 provides the mean differences and RMSD between different TRP model extensions during January 2008. Similar to ERP, the largest differences between the differently modelled accelerations occur in the radial direction, where the signal is largest. As one would expect, the RMSD shows the largest values when changing from the instantaneous to heat-conductive solution with up to $0.4\,\mathrm{nm/s^2}$ in the radial direction. The largest mean differences are observed when considering the interpolation scenario, which was found above to be not suitable for considering the Earth's outgoing radiation correctly. Changing the wavelength-dependency of the solar radiation has a large impact on both the mean differences and the RMSD in all directions.

### 5.1.4 Validation using accelerometer data

As mentioned before, the validation of the radiation pressure force models is challenging because the radiation pressure cannot be measured directly. Instead, in case of GRACE accelerometer measurements are available, which allow for the validation of the total modelled non-gravitational accelerations. However, in this thesis a validation of the radiation pressure force model and its suggested extensions is aimed. Therefore, both the accelerometer calibration and the aerodynamic model are kept fixed during the following experiments to allow for the comparison of differently modelled radiation pressure accelerations. However, it should be mentioned here that perfectly calibrated accelerometer measurements as well as a perfect aerodynamic model cannot be achieved and that these choices may very well affect the outcome of the analyses.

In the following, the aerodynamic acceleration is modelled as described in Sect. 4.1 by accounting for drag and lift forces using a fixed energy accommodation coefficient of 0.93. Compared to the experiments in Vielberg and Kusche (2020) the applied empirical model is updated here, i.e., the thermospheric neutral density is obtained from NRLMSIS 2.0. The accelerometer calibration has been performed within a precise orbit determination procedure without making use of

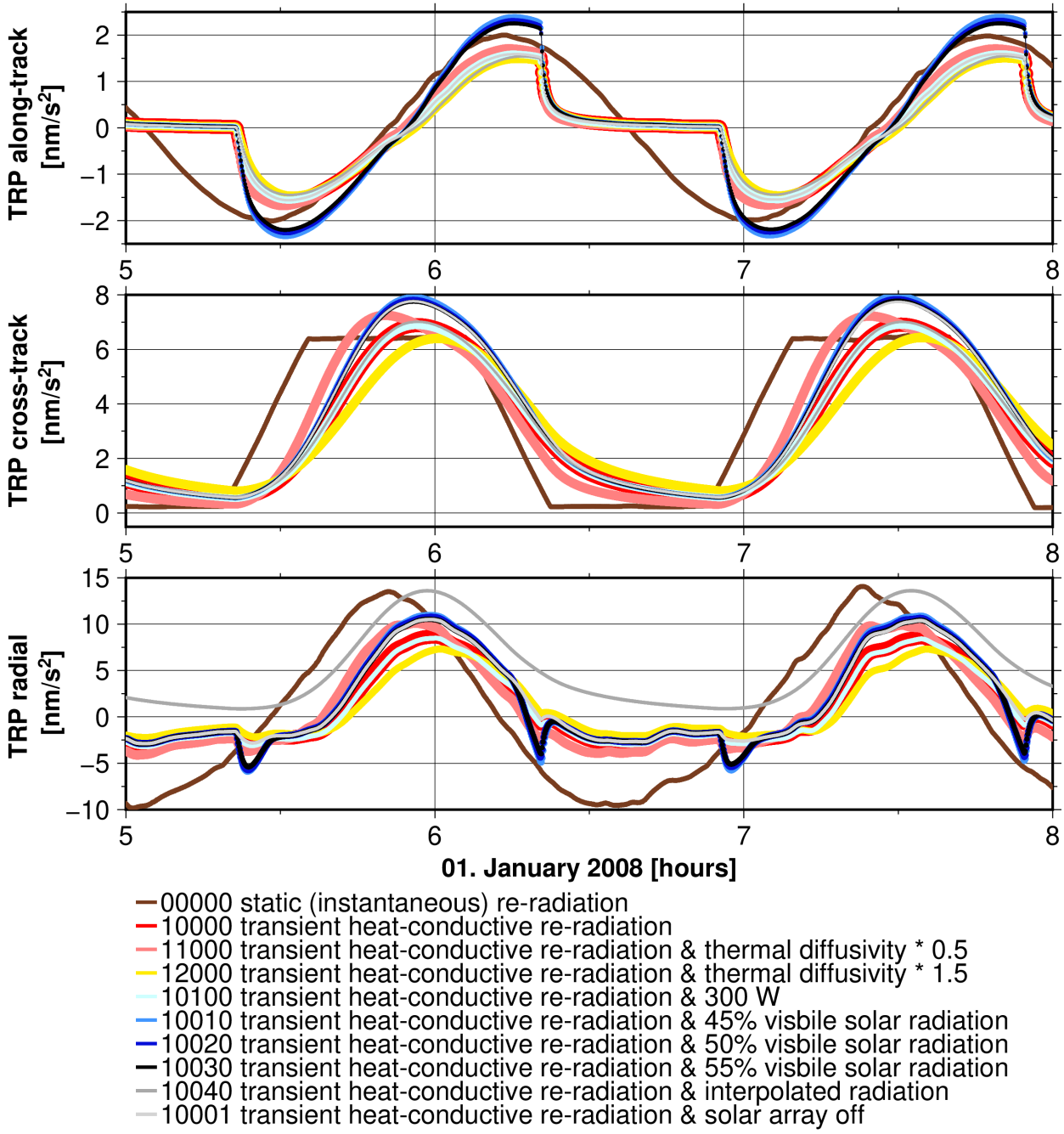



Figure 5.9: Different scenarios of modelled TRP acceleration acting on GRACE-A in the along-track (top), cross-track (middle), and radial (bottom) directions of the SRF during 3 hours (5–8 a.m.) on January 1, 2008. To look up modelling details, please see Tab. 5.3.

non-gravitational force models. This procedure is based on Vielberg et al. (2018) and has been introduced in Sect. 3.1.5. The estimation of the calibration parameters is based on a POD and considers a three-step approach resulting in daily biases and constant scale factors. In Vielberg and Kusche (2020) as well as in this thesis, the gravitational background models have been updated according to Tab. 3.2.

To avoid the impact of spiking accelerations due to thruster firings, accelerations 30 s before and after each thrust are eliminated based on the GRACE L1B thruster activation data. As a consequence, about 25 % of the data are excluded from the subsequent experiments. Other satellite-induced non-gravitational accelerations are not considered here.

To get an idea of the total non-gravitational signal from model and measurements, Fig. 5.11

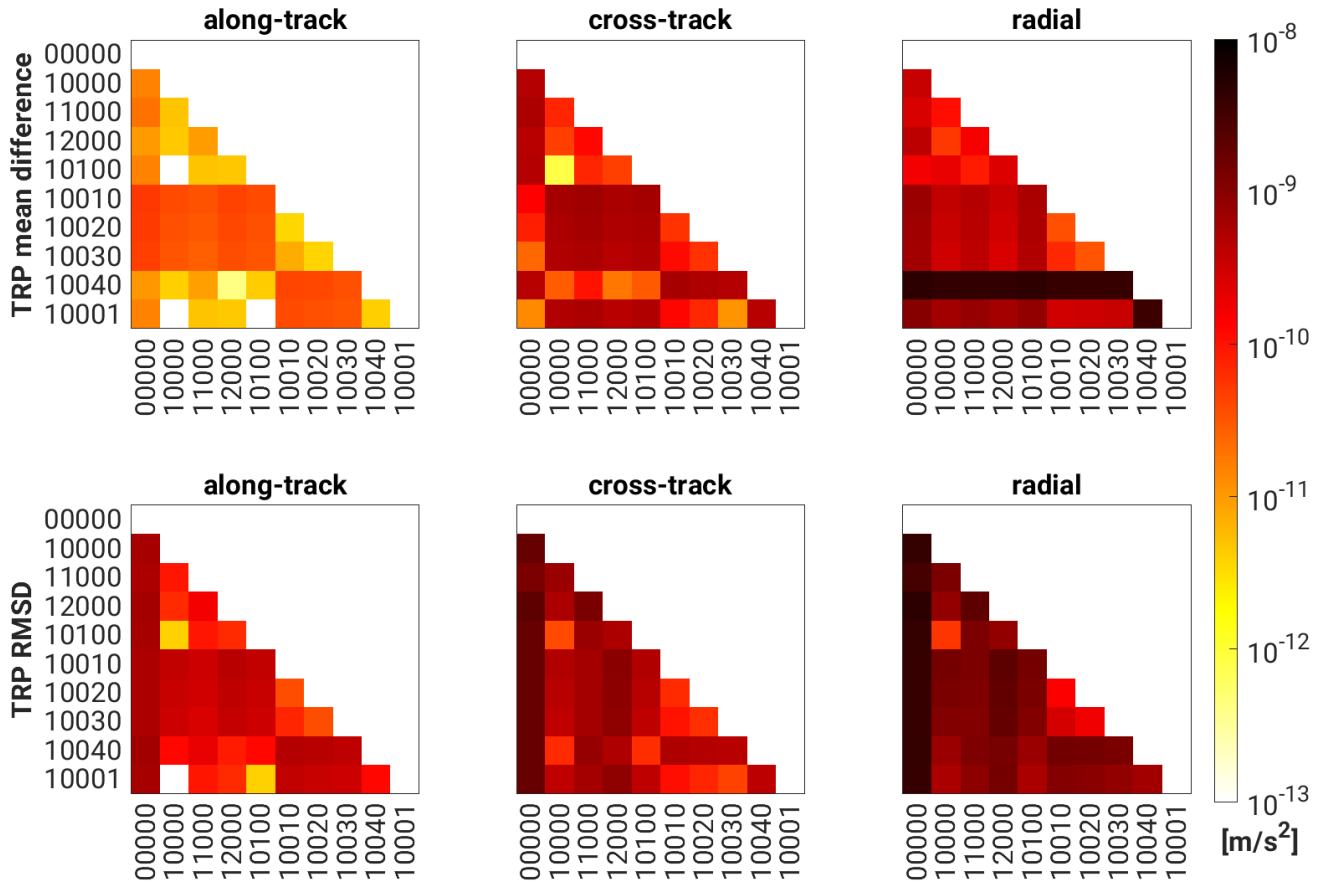



Figure 5.10: Mean differences (top) and root mean square differences (RMSD, bottom) between different TRP extensions applied to GRACE-A during January, 2008. To look up the digit codes, please see Fig. 5.9 or Tab. 5.3 for details.

shows the sum of the modelled non-gravitational accelerations for two selected scenarios as well as calibrated accelerometer measurements from this thesis. Since several institutes process their own calibration parameters, the calibrated accelerations by TU Delft (Siemes et al., 2023) courtesy of Christian Siemes are presented for comparison. In their calibration, a temperature correction is performed before estimating the calibration parameters from a POD using a three-step approach, which results in daily biases and constant scale factors. The cross-track and radial biases from Siemes et al. (2023) are constrained to reduce noise.

The selected model versions shown in Fig. 5.11 are the standard model (see Sect. 4.4.1) as well as the extended model as defined in Sect. 4.4.3, which includes advanced ERP and SRP model extensions and accounts for thermal re-radiation with transient heating and heat conduction.

In the along-track direction, the non-gravitational accelerations vary between -60 and 10 nm/s$^2$ during the selected three hours on January 1, 2008, where the SRP acceleration is prevalent. Within periods of high solar activity, the aerodynamic signal can be more than 10 times larger and thus dominates the along-track acceleration. In Fig. 5.11, the modelled and calibrated along-track accelerations agree very well shortly before and after the transit from shadow to sunlight, e.g., between 5:46 and 6:06 a.m.). However, when entering the shadow regions, the differences are larger with up to 10 nm/s$^2$. This is also the case when the SRP acceleration reaches its minimum around 5:40 a.m.. These discrepancies between modelled and calibrated accelerations might be related to shadowing effects, since the overhang of the satellite's side panels cause shadows on the nadir panel closely after emerging from the shadow regions, which is not accounted for when using the simplistic panel macro-model. As expected, the difference between the modelled accelerations

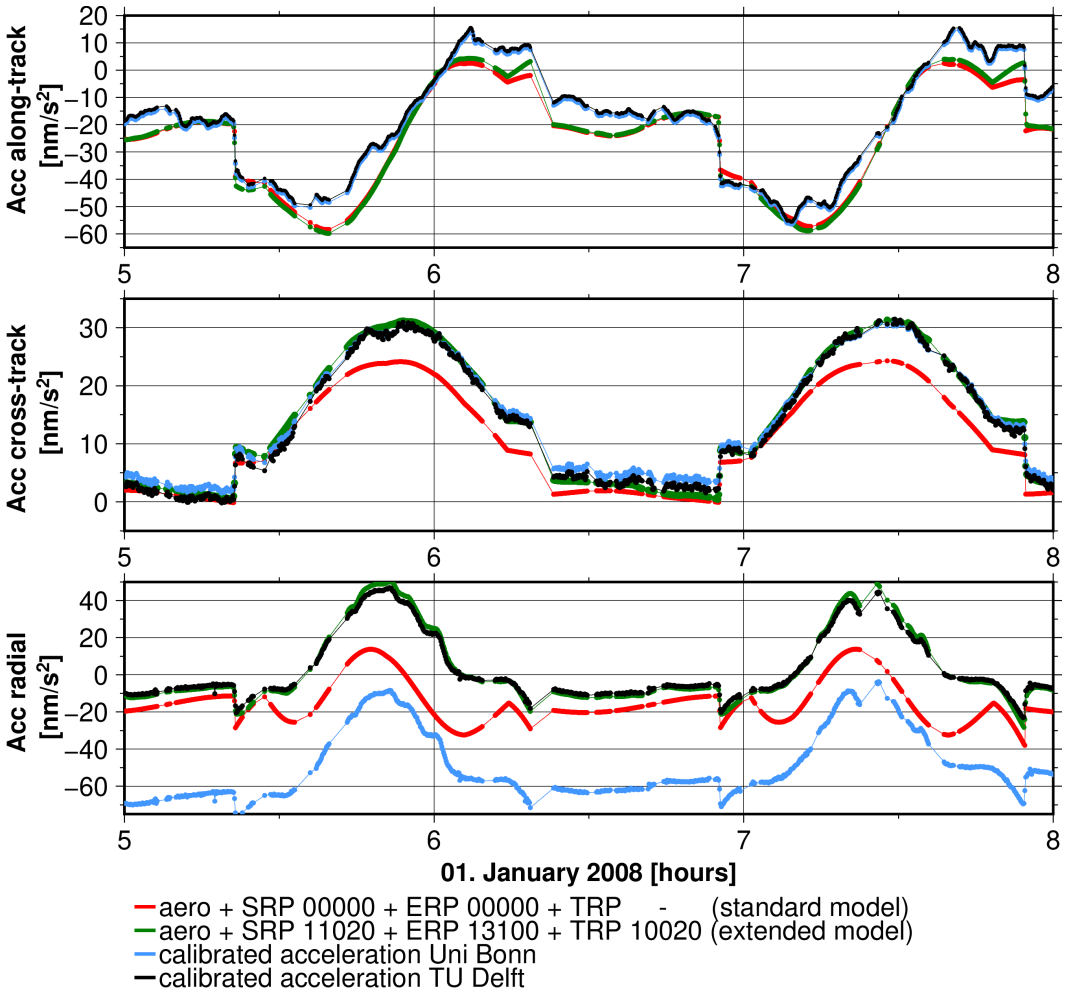



Figure 5.11: Modelled and calibrated non-gravitational accelerations of GRACE-A in the along-track (top), cross-track (middle), and radial (bottom) directions of the SRF during 3 hours (5–8 a.m.) on January 1, 2008. To look up the details of the combined five digit codes (SRP+ERP+TRP), see Tab. 5.1 for SRP, Tab. 5.2 for ERP, and Tab. 5.3 for TRP. Calibrated accelerations from Uni Bonn are introduced in Sect. 3.1.5. For details on the calibrated accelerations from TU Delft see Siemes et al. (2023).

with the standard and the extended radiation pressure model are small in the along-track direction, since the aerodynamic acceleration is dominating. The largest differences between the shown model versions are 4 nm/s$^2$ in the along-track direction shortly before the shadow entry, which is mainly related to the consideration of the TRP acceleration in the extension. Calibrated data from this thesis agree very well with the ones from Siemes et al. (2023) in this direction.

In the cross-track direction, where the signal reaches 31 nm/s$^2$, the modelled accelerations especially the selected extended version agree very well with the calibrated measurements from both institutes even though the performance of the accelerometer is less sensitive in this direction (Flury et al., 2008). The standard model does not match the observations well during increasing exposure to solar radiation. Most likely, the good agreement of the extended model to the observations is related to the use of the TRP model, which accounts for transient heating and heat conduction and brings the model closer to the observations around the shadow entry and during the exposure to solar radiation. Within the shadow regions, the calibrated accelerations from Siemes et al. (2023) agree slightly better with the extended model version than the calibration from this thesis.

In the radial direction, not only the differences between the modelled non-gravitational accelerations from the standard and extended version are large with 18 nm/s$^2$ on average. When assuming a non-gravitational perturbation of 18 nm/s$^2$ in the radial direction for GRACE, this leads to an

along-track orbit error of 6 m after one day under consideration of fixed initial values; the radial component is affected by about 5 cm and the impact on the cross-track component is negligible. In addition, the differences between the calibrated accelerations are remarkable. Here the calibration following Vielberg et al. (2018), contains a bias of nearly 60 $\mathrm{nm/s^2}$ w.r.t. the extended model, which is as large as the signal itself. This is not the case when comparing the modelled non-gravitational accelerations to the calibrated ones from Siemes et al. (2023), where especially the extended model version fits the observations very well and only a small offset remains around the peak of the SRP acceleration, e.g., at 5:51 a.m., which is below 0.5 $\mathrm{nm/s^2}$. Thus, the bias correction following Vielberg et al. (2018) seems to be insufficient in the radial direction during the shown period, which is most likely related to the variations in the radial biases presented in Fig. 3.5. Here, the calibration parameters were obtained within three-step approach using a POD as outlined in Sect. 3.1.5 similar to Siemes et al. (2023), however, Siemes et al. (2023) constrained the cross-track and radial biases, which is not the case when following Vielberg et al. (2018). A remaining offset between modelled and calibrated non-gravitational accelerations in the radial direction (without constraining the radial biases) has also been observed in Wöske (2020). The reason for this is related to the orbit mechanics, i.e, the orbit energy is primarily changed by along-track signals, whereas changes in the radial acceleration have a minor effect leading to a small orbital tilt (see Fig. 6.5 in Wöske, 2020), which makes it also challenging to obtain good estimates in this direction. Thus, constraining the radial bias as done in Siemes et al. (2023) seems reasonable for this application. Alternatively, one could correct the calibrated accelerometer data again by estimating a daily bias from a fit to modelled data as suggested by Wöske (2020). Both approaches are not further tested in this thesis. Moreover, combining the accelerometer calibration and the inverse radiation pressure modelling in a joint approach as suggested above might also be helpful to overcome remaining discrepancies.

Regardless the offset in the calibration, the extended model shows the same signal variations as the observations, whereas the standard model is much smoother, which is especially related to the improvements in the ERP modelling (see Sect. 4.2.2). The shift of the standard model w.r.t. calibrated data when the satellite is exposed to sunlight is likely related to the consideration of the TRP in the extended model version. To conclude, extending the radiation pressure modelling shows the largest effect in the radial direction of the total non-gravitational acceleration, whereas the model extensions are least relevant in the along-track direction.

In a further step, modelled radiation pressure accelerations at a variety of different stages of extension are added to the modelled aerodynamic acceleration. This allows a validation with calibrated accelerations in terms of mean differences, RMSD and RMSD reduction as shown in Fig. 5.12. The RMSD reduction

$$\mathrm{RMSD}_{\mathrm{reduction}} = 1 - \frac{\mathrm{RMSD}_2}{\mathrm{RMSD}_1} \tag{5.1.1}$$

emphasizes the impact of each model extension. Here, it is computed for different model extensions $\mathrm{RMSD}_2$ with respect to the standard model $\mathrm{RMSD}_1$, i.e., the positive percentages mean that accelerations from the extended model version are closer to calibrated accelerations than the standard model. The standard radiation pressure model is the first scenario shown in Fig. 5.12, where only basic models of the ERP and SRP accelerations are considered and TRP is omitted.

In Vielberg and Kusche (2020), a similar comparison has been performed, where the modelled non-gravitational accelerations are validated against the a priori calibration as recommended in Bettadpur (2009) and against the calibration following Vielberg et al. (2018). We found that the validation against a priori calibrated accelerations is not suitable due to remaining biases especially in the along-track and cross-track directions. Since it turned out in the previous comparisons that there is still a remaining bias between the modelled and calibrated accelerations following Vielberg et al. (2018) in the radial direction, Fig. 5.12 validates the modelled data not only w.r.t. these data, but also w.r.t. calibrated accelerations from Siemes et al. (2023) in the lower plot.

The absolute mean differences when comparing modelled data with the calibration following Vielberg et al. (2018) are at the order of 2 $\mathrm{nm/s^2}$ in the along-track and 9 $\mathrm{nm/s^2}$ in the cross-track direction. In the along-track direction, the mean differences and RMSD, which is at the order of 5 $\mathrm{nm/s^2}$, remain constant due to the relatively low impact of the model extensions in this direction.

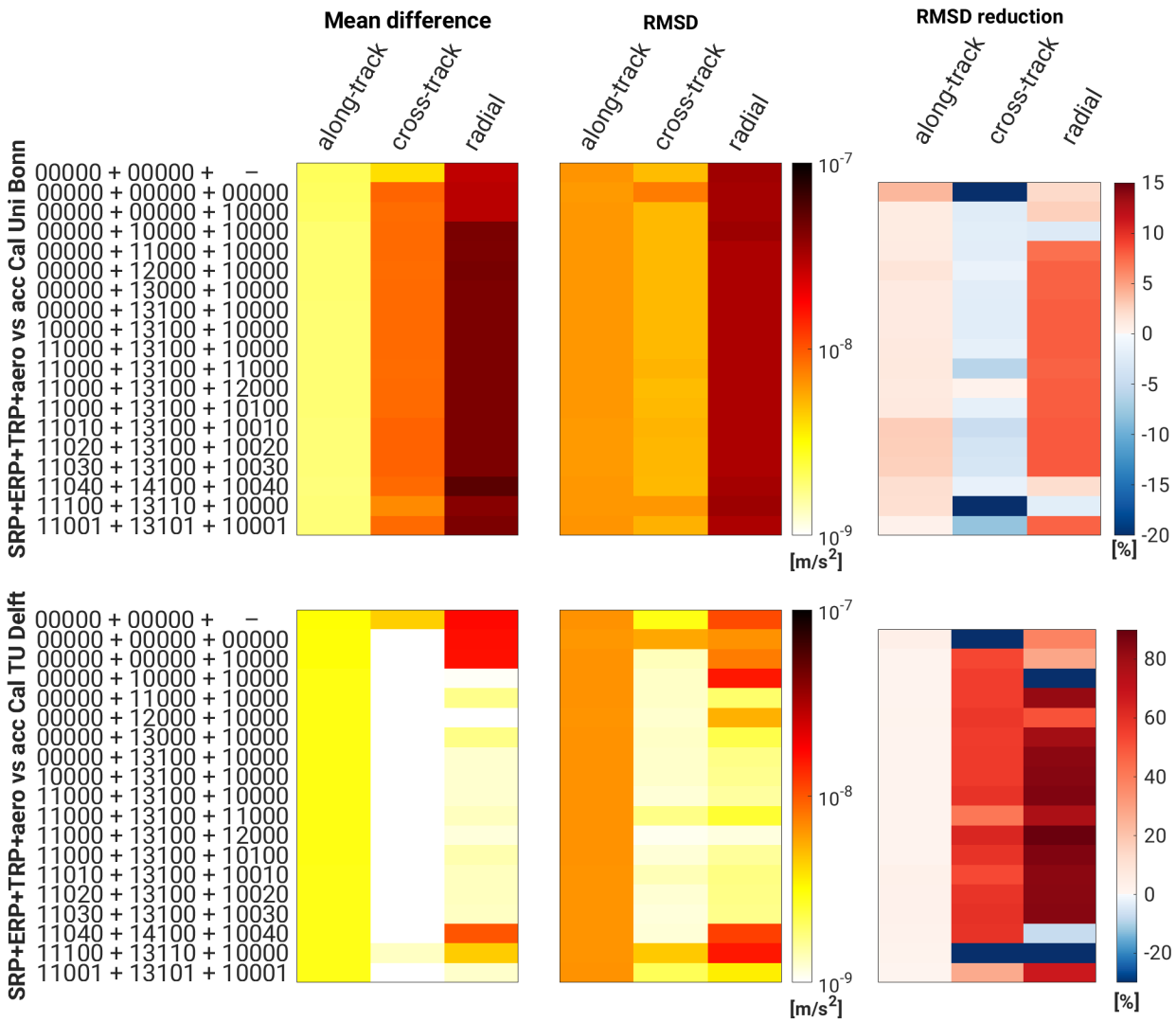



Figure 5.12: Mean differences (left), RMSDs (middle) and RMSDs reduction (right) between modelled and calibrated accelerations of GRACE-A during January, 2008. Top: calibrated accelerations as outlined in Sect. 3.1.5 are used as a reference. Bottom: calibrated accelerations from TU Delft (Siemes et al., 2023) are utilized instead. Please note that the RMSD reduction, which is computed w.r.t. the first scenario, uses different colour scales. To look up the combined five digit codes (SRP+ERP+TRP), see Tab. 5.1 for SRP, Tab. 5.2 for ERP, and Tab. 5.3 for TRP. The first version is the standard model as defined in Sect. 4.4.1, where TRP is not considered at all. The extended model version from Sect. 4.4.3 corresponds to scenario 11020 + 13100 + 10020.

Applying more advanced aerodynamic models, which is not part of this thesis, is expected to reduce the mean differences in the along-track direction, however, introducing horizontal winds from HWM14 turned out to impact the result by less than 0.1 %. The RMSD reduction reveals that considering the thermal re-radiation as well as accounting for visible and infrared wavelengths of the incoming solar radiation instead of considering visible wavelengths only, has indeed an impact in the along-track direction and reduces the difference to the calibrated accelerations.

In the cross-track direction, introducing the BRDFs impacts the mean differences and RMSD in terms of an increase in the difference between model and observations by nearly 2 $nm/s^2$. These data suggest that the effects of realistic anisotropic reflection deserve further study to find, develop, calibrate, and test BRDFs for satellite force modelling based on manufacturer information of the surface materials. The cross-track direction is also very sensitive to changes of the TRP model and

its thermal diffusivity. The thermal diffusivity is the ratio of conductivity to density and capacity of the material. Decreasing the thermal diffusivity by 50 % increases the RMSD reduction by up to 5 %, whereas increasing the thermal diffusivity leads to a decrease of only 2 % and brings the model closer to the standard model. In addition, accounting for visible and infrared solar radiation increases the RMSD reduction by 2 %, which does not necessarily mean that this extension is unsuitable, however, it brings the model further away from the standard model.

In the radial direction, where the impact of the force model extensions is largest, the mean differences and RMSD vary around 43 $\mathrm{nm/s^2}$ and 31 $\mathrm{nm/s^2}$, respectively, which is nearly as large as the signal itself. This makes the validation of the radiation pressure modelling difficult, although the radial direction is the most important one for the validation, since the different model extensions of ERP and TRP vary a lot in this direction as presented in Figs. 5.7 and 5.9, respectively. Consequently, only model extensions such as including the TRP acceleration and the discretization of the footprint to a detailed resolution of $1^\circ \times 1^\circ$ grid as well as considering BRDFs at the satellite's surface cause variations, which are large enough to be detected when comparing to calibrated accelerations following Vielberg et al. (2018).

With the calibrated accelerometer data from Siemes et al. (2023), the results in the along-track direction are very similar, however, the results differ from the validation with the calibration following Vielberg et al. (2018) in cross-track and radial directions with much smaller mean differences of about 0.6 $\mathrm{nm/s^2}$ and 1 $\mathrm{nm/s^2}$, respectively. It becomes clear that the calibration parameters from Siemes et al. (2023) and the resulting accelerations fit the modelled accelerations better than the calibration following Vielberg et al. (2018), which is especially in the cross-track direction likely related to the temperature correction in the Siemes et al. (2023) dataset. In the radial direction, the calibration from Siemes et al. (2023) fits the modelled results better as already discussed above due to the constrained radial bias. The largest impact on the mean differences can be found when increasing the discretization of the footprint to a $1^\circ \times 1^\circ$ grid, which reduces the absolute mean differences from 16 $\mathrm{nm/s^2}$ to 1 $\mathrm{nm/s^2}$. Interestingly, the mean differences are smallest with 0.02 $\mathrm{nm/s^2}$ after using outgoing fluxes from EBAF instead of albedo and emission from the same dataset. Further applying the CERES SYN1deg data instead of EBAF data increases the mean differences again, however, the RMSD decreases to 0.1 $\mathrm{nm/s^2}$ revealing that the high resolution of the dataset captures more details. From the RMSD reductions resulting from the TU Delft calibration it becomes clear that including the heat-conductive TRP modelling reduces the RMSD reduction by 10 % to 28 %. Also changing the thermal diffusivity within the TRP modelling has a large impact in the cross-track and radial directions with up to 23 % and 17 % RMSD reduction, respectively.

In summary, the validation of the radiation pressure force models is challenging due to shortcomings in the accelerometer calibration as well as imperfect aerodynamic modelling. Consequently, it is not possible to draw a satisfying conclusion as to which radiation pressure force model is most suitable. Instead, the impact of different model extensions on the difference to calibrated accelerations were pointed out. The largest impact on the selected statistics were found from introducing the heat-conductive TRP acceleration, changes in the discretization of the Earth's footprint as well as considering visible and infra-red solar radiation. To overcome remaining discrepancies in the force model and in the accelerometer calibration in the future, the development of a joint estimation would be desirable.

### 5.1.5 Validation using SLR data

In addition to the validation of the radiation pressure force models with accelerometer measurements, an independent validation is performed in the following using SLR data. The advantage of this procedure is that SLR measurements do not require such calibration as the accelerometer data in the previous validation, where errors in the radiation pressure force models were difficult to separate from the residual effects of the necessary accelerometer calibration procedure (see Fig. 5.12). On the other hand, it is disadvantageous that the SLR validation temporally averages out many effects. The validation performed here has also been presented at the EGU General Assembly 2023 (Vielberg et al., 2023).

A similar validation was performed in Wang et al. (2023) for GRACE-FO, where the success

of the reduced-dynamic orbit determination using differently modelled solar and thermal radiation pressure accelerations was assessed with SLR data. In this thesis, the validation against SLR data is performed as follows. In a first step, a dynamic orbit is estimated by solving the equation of motion together with the associated variational equations (Löcher, 2011). Thus, this procedure is similar to the calibration of the accelerometer data described in Sect. 3.1.5, however, the setup is different here. Similarly, kinematic orbits from GNSS and its covariance information processed here from TU Graz (Zehentner and Mayer-Gürr, 2016; Zehentner, 2017) serve as observations, which are processed in orbits of 1 day length. To account for the forces acting on the satellite, gravitational background models are applied as listed in Tab. 3.2. The non-gravitational forces combine the radiation pressure forces modelled with different extensions and an aerodynamic model, which uses thermospheric densities from NRLMSIS 2.0. The aerodynamic force model is kept fixed during the following experiments and a parameter (scale factor) to account for aerodynamic mismodelling in all three directions is co-estimated hourly. Additionally, the year 2008 is selected again, where the radiation pressure signal is at the same order of magnitude as the aerodynamic signal.

In a second step, the residuals between the SLR measurements and the dynamic orbit resulting from the previous step are computed. This requires the conversion of the SLR normal points to ranges. Normal points are a specific data format to store the original range measurements averaged over several minutes, which are available from the ILRS. On the other hand, computed ranges are required, which consider International Terrestrial Reference System (ITRF) positions and velocities of each station as well as the vector from the subsequent position to the reference point of the laser system. The positions need to be corrected for time-dependent effects, which are mostly geophysical ones, as listed in Tab. 5.4. Then, the corrected range measurements are compared to the dynamic

Table 5.4: Data and models as applied in the SLR processing. Adopted from Löcher and Kusche (2021) (Tab. 2).

| Parameters | Description |
|---|---|
| Normal points | ILRS (Pearlman et al., 2019b) |
| Station coordinates | SLRF2014 |
| Solid Earth tides | IERS Conventions 2010 (Petit and Luzum, 2010) |
| Ocean tidal loading | FES2014b (Carrere et al., 2015) |
| Ocean nontidal loading, atmosphere tidal and nontidal loading | EOST Strasbourg (Boy et al., 2009) |
| Tropospheric delay | Mendes and Pavlis (2004) |
| Relativistic delay | IERS Conventions 2010 |

orbit from the first step in terms of ranges. Since we assume the SLR observations as the truth, small residuals indicate that the modelled non-gravitational accelerations represent reality well. To guarantee a high quality of the SLR ranges, only observations from the 12 high-performing ILRS stations according to Arnold et al. (2019) are used. The validation is performed with the software GROOPS. The utilized parts of the software were already implemented by my colleague Anno Löcher and I conducted the experiments.

The two-fold approach is performed several times with a varying parametrization of the radiation pressure force model. The resulting residuals between the SLR range and the range computed from the dynamic orbit are used to compute the RMS per pass. Its annual mean is computed after removing outliers (RMS$>$ 30 cm, i.e., 3.8 % of the data are removed) and is summarized in Tab. 5.5. From all tested radiation pressure scenarios, the largest RMS of 4.5 cm is reached with the standard model for ERP and SRP and without applying the thermal re-radiation. Introducing the instantaneous TRP model (TRP version 00000) already decreases the result by more than 1.5 cm. Interestingly, the RMS increases again when switching to the heat-conductive TRP model (TRP version 10000). This is most likely related to the unsuitability of the standard ERP model. When extending the ERP model (ERP version 13100), the RMS reduces to around 2.4 cm, whereas extending the SRP model does not impact the result. Thus, additionally the extended ERP and SRP model (SRP version 11000, ERP version 13100) without TRP and with instantaneous TRP

Table 5.5: Annual average of the Root Mean Square (RMS) per pass of the residuals between SLR range measurements and the estimated dynamic orbit for the whole year 2008. Outliers, i.e., RMS values above 30 cm, have been removed, thus, the averaging is performed for 96.2 % of the data. For the POD, the kinematic orbits serve as observations and the gravitational background models are summarized in Tab. 3.2. Then, different versions of modelled RP forces serve as input. To look up their combined five digit codes (SRP+ERP+TRP), see Tab. 5.1 for SRP, Tab. 5.2 for ERP, and Tab. 5.3 for TRP. The first version is the standard model as defined in Sect. 4.4.1, where TRP is not considered at all. The extended model version from Sect. 4.4.3 corresponds to scenario 11020 + 13100 + 10020. The annual average of the hourly estimated scale factor for the modelled aerodynamic acceleration is also listed. Three additional scenarios are added in this validation at the bottom, where TRP version 13000 represents the fitted thermal diffusivity.

| Version | | | RMS | Aerodynamic scale factor | Standard deviation of aerodynamic scale factor |
|---|---|---|---|---|---|
| SRP | ERP | TRP | [cm] | [-] | [-] |
| 00000 | 00000 | - | 4.500 | 0.74 | 0.37 |
| 00000 | 00000 | 00000 | 2.965 | 0.70 | 0.25 |
| 00000 | 00000 | 10000 | 3.451 | 0.72 | 0.30 |
| 00000 | 10000 | 10000 | 2.348 | 0.70 | 0.19 |
| 00000 | 11000 | 10000 | 2.350 | 0.70 | 0.19 |
| 00000 | 12000 | 10000 | 2.616 | 0.70 | 0.22 |
| 00000 | 13000 | 10000 | 2.401 | 0.70 | 0.19 |
| 00000 | 13100 | 10000 | 2.403 | 0.70 | 0.19 |
| 10000 | 13100 | 10000 | 2.409 | 0.70 | 0.19 |
| 11000 | 13100 | 10000 | 2.409 | 0.70 | 0.19 |
| 11000 | 13100 | 11000 | 2.584 | 0.70 | 0.20 |
| 11000 | 13100 | 12000 | 2.335 | 0.70 | 0.19 |
| 11000 | 13100 | 10100 | 2.409 | 0.70 | 0.19 |
| 11010 | 13100 | 10010 | 2.391 | 0.70 | 0.20 |
| 11020 | 13100 | 10020 | 2.389 | 0.70 | 0.20 |
| 11030 | 13100 | 10030 | 2.387 | 0.70 | 0.20 |
| 11100 | 13110 | 10000 | 2.616 | 0.71 | 0.22 |
| 11001 | 13101 | 10001 | 2.436 | 0.70 | 0.20 |
| 11000 | 13100 | - | 2.737 | 0.70 | 0.22 |
| 11000 | 13100 | 00000 | 3.167 | 0.70 | 0.25 |
| 11000 | 13100 | 13000 | 2.314 | 0.70 | 0.19 |

(TRP version 'non' and 00000) are evaluated and added to the bottom of Tab. 5.5. Here, it becomes clear that the instantaneous re-radiation increases the RMS by 14 % compared to applying no re-radiation at all. Applying a heat-conductive model for the thermal re-radiation decreases the RMS by 12 % compared to using no TRP model and by 24 % compared to considering instantaneous re-radiation of heat. Consequently, implementing a heat-conductive thermal model is highly recommended for precise non-gravitational force modelling. It should be mentioned here that the aerodynamic scale factor is estimated independently for all cases, but the differences are below 1 %.

Nevertheless, the heat-conductive TRP modelling relies on the assumptions of the materials' conductivity, capacity and density, which are considered in the thermal diffusivity term (see Eq. 4.2.95). In an attempt to adjust the thermal diffusivity, a scale factor of 0.5 (TRP version 11000) and 1.5 (TRP version 12000) of the thermal diffusivity are introduced. It turns out that the factor of 1.5 yields the smallest RMS of 2.335 cm. This reveals that a fine tuning of the

thermal diffusivity is likely to further improving the heat-conductive TRP model. Thus, when changing the scale factor in 0.1 steps, the minimal RMS of 2.314 cm is reached with a scale factor of 2.2. This scenario with fitted thermal diffusivity (TRP version 13000) is added at the bottom of Tab. 5.9. Including heat-conductive thermal re-radiation with fitted thermal diffusivity in the non-gravitational force model for GRACE decreases the SLR residuals by 36 % compared to using instantaneous re-radiation and by 4 % without fitting the thermal diffusivity. This scale factor of 2.2 is assumed to scale the thermal diffusivity of all panels. However, the thermal diffusivity is most likely different for solar panels and nadir or front panels. In addition, this scale factor might also absorb other error sources, e.g., missing information on the heat distribution in the satellite's interior, mismodelling of gravitational and remaining non-gravitational force models or weaknesses in the ranges. Consequently, increasing the number of parameters would be interesting, however, the aim of this experiment is still to validate the radiation pressure force models and not finding a perfect parametrization towards a reduced-dynamic POD.

Interestingly, the minimal RMS of 2.314 cm just mentioned above is reached in combination with the SRP model 11000 using daily TSI and a physical shadow function in combination with the ERP model 13100 using outgoing fluxes from hourly CERES SYN1deg data on a 1° grid. This differs from our definition of the extended model in Sect. 4.4 as the separation between visible and infrared radiation is not included. This again underlines the need of accurate thermo-optical material properties of the material including not only reflectivity and absorption, but also the thermal diffusivity. The non-gravitational accelerations obtained with the standard, extended and best (in terms of minimal SLR residuals) models for GRACE-A during 3 hours (5–8 a.m.) on January 1, 2008, are visualized in Fig. 5.13. The differences between the extended and the best model are small especially in the radial direction.

As mentioned above, changes in the ERP model reduce the RMS to about 2.4 cm, where increasing the discretization of the footprint to 1° (ERP scenario 00000 to 10000) has the largest impact as the RMS decreases by 32 %. The use of different CERES data sets and their parametrization (ERP scenarios 10000, 11000, 12000, 13000) leads to changes of 2.7 mm (11 %) and reveal that the CERES data processing has a significant impact on the radiation pressure force model. Interestingly, introducing the ADMs (ERP scenario 13100) increases the RMS by 0.2 mm. The applied ADMs are a simplification of the ones used in the CERES processing, thus, applying the original CERES ADMs might further reduce the RMS, which is not tested in this thesis due to the limited availability. Furthermore, the use of BRDFs to account for the light's anisotropic reflection at the satellite's surface increases the RMS by more than 2 mm (ERP scenario 13100 to 13110), which underline the findings from the comparison to accelerometer data that there is a need for finding suitable BRDFs for each material individually.

The impact of the SRP models on the SLR residuals is generally small ($\leq$1 mm). Changing the solar constant to daily TSI as well as replacing the conical shadow function by a physical one has hardly an impact on the RMS. In Tab. 5.5, changes in the incoming solar radiation (SRP scenarios 11000, 11010, 11020, 11030) lead to variations in the RMS of 0.2 mm. The radiation pressure version with interpolated radiation data (SRP scenario 11040) is left out here, since it already turned out to be unsuitable in the previous comparison. Finally, changing the absorption of the satellite's solar panel (SRP scenario 11001) increases the RMS by 0.5 mm, which underlines the need of accurate thermo-optical material properties. In comparison to Wang et al. (2023), the RMS is generally larger, however, Wang et al. (2023) co-estimate additional empirical parameters to absorb the remaining mismodelling of the non-gravitational forces, which is not done in the validation of this thesis.

To summarize the discussion of the RMS, the choice of the force model impacts the GRACE orbit during the year 2008 by more than 2 cm. This reveals that a careful selection of the radiation pressure force model is required to obtain precise orbits. The model version with the smallest RMS was found to be the SRP model 11000 using daily TSI and a physical shadow function in combination with the ERP model 13100 using outgoing fluxes from hourly CERES SYN1deg data on a 1° grid and the heat-conductive TRP model with a scale factor of 2.2. The largest improvements of 47 % and 24 % are achieved by discretizing the Earth's footprint on a 1° grid and

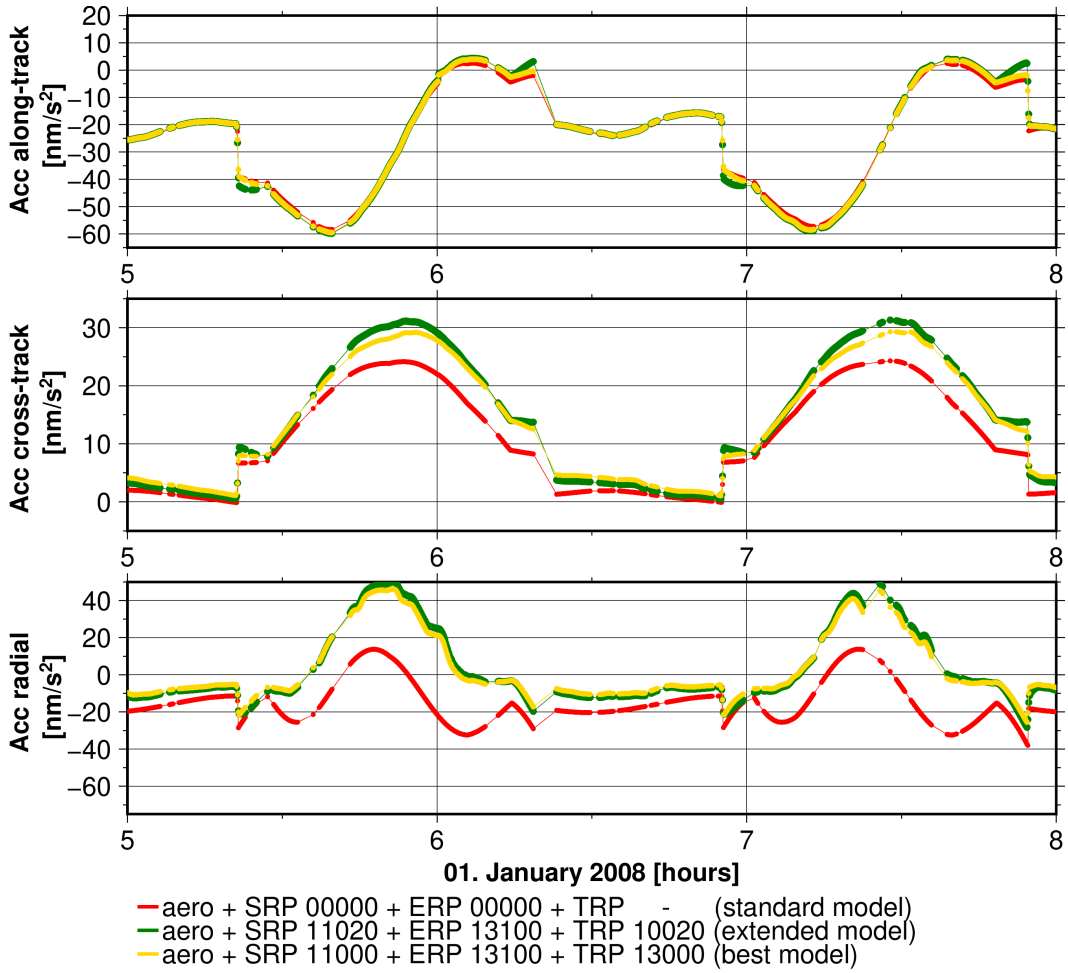



Figure 5.13: Modelled non-gravitational accelerations of GRACE-A in the along-track (top), cross-track (middle), and radial (bottom) directions of the SRF during 3 hours (5–8 a.m.) on January 1, 2008. The acceleration resulting from the standard and extended models are shown together with the best model according to the smallest SLR residuals. To look up the details of the combined five digit codes (SRP+ERP+TRP), see Tab. 5.1 for SRP, Tab. 5.2 for ERP, and Tab. 5.3 for TRP.

by introducing heat-conductive TRP, respectively. Nevertheless, more accurate information on the material characteristics are expected to further reduce the RMS.

Additionally, Tab. 5.5 presents the annual mean of the co-estimated aerodynamic scale factor together with its standard deviation. The aerodynamic scale factor varies between 0.70 and 0.74. Interpreting the aerodynamic scale factor as a correction for the thermospheric neutral density model (here: NRLMSIS 2.0) reveals that the model overestimates the density, which has also been found for extreme solar minimum conditions during 2008 (Solomon et al., 2010; Doornbos, 2012; Vielberg et al., 2018; Zeitler et al., 2021). In an additional test, the NRLMSIS 2.0 model is replaced with NRLMSISE-00. The resulting scale factors are generally smaller with values between 0.65 and 0.70 depending on the RP model version. At the same time, the RMS is about 2 mm larger when applying the NRLMSISE-00 model. These results confirm that the choice of the aerodynamic model indeed has an impact on the validation. Computing Pearson's linear correlation coefficient between the RMS and aerodynamic scale factors yields a correlation of 0.93. Thus, when using and interpreting the scale factor as a correction of the model density one should be aware of its correlation to the choice of the radiation pressure force model. The aerodynamic scale factor will be further discussed in Ch. 6.

Instead of applying modelled non-gravitational accelerations in the POD from the first step

of this validation, one can also use accelerometer measurements to assess the suitability of the modelled non-gravitational accelerations in comparison to measured ones. This means that the raw accelerometer data can serve as input, which requires the additional estimation of calibration parameters, or calibrated accelerometer data can be used directly. The results are summarized in Tab. 5.6 - again in terms of annual averages of the RMS per pass of the residuals between SLR range measurements and the estimated orbit for the year 2008. As a reference, the average RMS

Table 5.6: Annual average of the RMS per pass of the residuals between SLR range measurements and the estimated dynamic orbit or kinematic orbit for the whole year 2008. Outliers, i.e., RMS values above 0.3, have been removed, thus, the averaging is performed for approximately 96.2 % of the data. For the POD, the kinematic orbits serve as observations. The gravitational background models used in the POD are summarized in Tab. 3.2. In case of dynamic orbits as input, (calibrated) accelerometer observations serve as input for the non-gravitational forces. In case the raw accelerometer data are used, calibration parameters (bias and/or scale) are estimated.

| Orbit version | RMS [cm] |
|---|---|
| kinematic orbit | 1.29 |
| dynamic orbit (calibration Uni Bonn) | 4.75 |
| dynamic orbit (calibration TU Delft) | 8.72 |
| dynamic orbit (3h bias) | 2.54 |
| dynamic orbit (3h bias, 1d scale) | 2.24 |
| dynamic orbit (1h bias) | 1.85 |
| dynamic orbit (without any non-gravitational accelerations) | 754.17 |

per pass of the residuals between the SLR ranges and the kinematic orbit, which is used as input in the POD, is computed. It shows the smallest RMS of 1.29 cm and is thus nearly half of the RMS reached with modelled data.

Then, the calibrated accelerometer data with updated gravitational background models from Vielberg et al. (2018) are used as input in the POD, which yields an RMS of 4.75 cm. This is twice as large as the smallest RMS from our previous experiment with modelled non-gravitational accelerations as input. The large RMS here is most likely related to the remaining bias in the radial component of the calibrated accelerometer data discussed above (Fig. 5.11). In addition, the calibration from Siemes et al. (2023) is used as input in the POD resulting in an RMS of 8.72 cm. Further tests revealed that the large RMS is related to the constrained radial bias. The radial component is not further used in Siemes et al. (2023) as it is not required for the neutral density and cross-wind determination. Using the calibrated accelerometer data in a POD without constraining the radial bias yields an RMS of 2.66 cm for January 2008 (courtesy: Jose van den IJssel). This confirms that constraining the bias estimate in the radial direction is not useful when using calibrated accelerations within a POD. Thus, the calibration procedure seems to depend strongly on the application. Without the consideration of non-gravitational accelerations in the POD, the RMS reaches 7.5 m, which clearly shows that non-gravitational force models are essential for an accurate POD.

Additionally, raw accelerometer data are tested as input, which are calibrated within the POD using different parametrizations. For this experiment, biases hourly or every three hours are tested as well as a daily scale in addition to the three-hour bias. As expected, increasing the temporal resolution of the accelerometer bias estimate reduces the SLR residuals. When applying hourly biases, the solution is closest to the kinematic orbit with an RMS of 1.85 cm. However, the estimated orbit does still not reach the quality of the kinematic orbit. On the one hand, this questions the parametrization of the accelerometer in terms of bias and scales. On the other hand, the background models might still be imperfect.

To conclude, both method and parametrization of the accelerometer calibration strongly impact not only the comparison to modelled accelerations but also the orbit solution when using these data

in a POD. Thus, the calibration of accelerometer data and the adjustment of non-gravitational force model corrections should be ideally revised in an inverse model.

## 5.2 Results for spherical SLR satellites

SLR satellites are generally spherical satellites with a mission lifetime of several decades due to the thin atmosphere at altitudes above 800 km. In this section, the magnitude of the non-gravitational accelerations acting on the selected spherical satellites is outlined before discussing the differences in the force modelling of spherical satellites and satellites for which a panel model exists. Then, the impact of selected radiation pressure model scenarios is exemplarily shown for Starlette. Finally, a validation of the chosen radiation pressure force models for the six selected satellites is performed within a POD using SLR data.

As for non-spherical satellites, the non-gravitational forces acting on spherical SLR satellites depend mainly on the satellite's area to mass ratio and thermo-optical material properties, its altitude as well as on atmospheric and radiation conditions. To get an idea of the non-gravitational forces acting on spherical satellites, Tab. 5.7 provides the norm of the individual accelerations of six SLR satellites averaged during one orbital revolution on January 1, 2008.

Table 5.7: Non-gravitational accelerations acting on the spherical SLR satellites Ajisai, LAGEOS 1 and 2, Larets, Starlette, and Stella. Here, the long-term radiation pressure coefficients $C_r$ from Sośnica et al. (2015) are applied. The norm of the aerodynamic and radiation pressure accelerations is averaged for the first orbital revolution on January 1st, 2008, for each satellite.

| Satellite | Aerodynamic [nm/s$^2$] | SRP [nm/s$^2$] | ERP [nm/s$^2$] |
|---|---|---|---|
| Ajisai | 0.07 | 19.40 | 4.36 |
| LAGEOS 1 | 2.14 $\times 10^{-4}$ | 3.51 | 0.20 |
| LAGEOS 2 | 1.73 $\times 10^{-4}$ | 3.40 | 0.23 |
| Larets | 0.67 | 3.53 | 1.63 |
| Starlette | 0.10 | 3.16 | 0.97 |
| Stella | 0.20 | 3.58 | 0.89 |

The aerodynamic acceleration is the smallest non-gravitational acceleration acting on these satellites due to the thin atmosphere at high altitudes especially above 800 km. In the aerodynamic model, the neutral density is obtained from NRLMSIS 2.0. The neutral density during January 2008 at the altitude of Stella (around 810 km) is on average $3 \times 10^{-15}$ kg/m$^3$ resulting in an aerodynamic acceleration of 0.2 nm/s$^2$. The aerodynamic acceleration acting on Starlette and Ajisai is slightly smaller with 0.1 nm/s$^2$ and 0.07 nm/s$^2$, respectively, due to their higher altitude. The aerodynamic acceleration of Larets is largest due to the relatively low altitude of 691 km. At about 5900 km at the altitude of LAGEOS 1, the neutral density is even six orders of magnitude smaller and the resulting aerodynamic acceleration is well below 0.01 nm/s$^2$. Thus, the satellite's orbital altitude remains nearly the same since launch 50 years ago. Consequently, aerodynamics are usually not considered in the force modelling for LAGEOS 1 and 2.

The SRP acceleration in Tab. 5.7 is around 3.5 nm/s$^2$ for LAGEOS 1 and 2, Larets and the sun-synchronous satellite Stella. The SRP acceleration of Starlette is slightly smaller with 3.2 nm/s$^2$. For Ajisai, the SRP acceleration is largest with nearly 19 nm/s$^2$ due to its relatively large area to mass ratio.

The ERP acceleration (see Tab. 5.7) is smaller than the SRP acceleration but larger than the aerodynamic acceleration for each of the selected satellites. Here, the ERP acceleration is again largest for Ajisai with 4 nm/s$^2$ due to its large area to mass ratio. For the remaining satellites, which are of similar geometry and mass, the ERP accelerations clearly differs with altitude. Here, ERP accelerations vary around 0.2 nm/s$^2$ for the LAGEOS satellites at high altitudes, followed by

0.9 nm/s$^2$ for Starlette and Stella at around 810 km, and 1.6 nm/s$^2$ for Larets at the lowest orbital altitude below 700 km.

### 5.2.1 Challenges for spherical satellites

The modelling of the radiation pressure accelerations for spherical satellites differs slightly from that for a GRACE-like satellite. Instead of using a panel model, the satellite's cross-sectional area is assumed to well represent the area directed to the incoming radiation in case of radiation pressure modelling (and to the along-track direction in case of the aerodynamic modelling). Then instead of separating the terms for the diffuse and specular reflection and absorption as in case of GRACE, for a spherical satellite a fixed radiation pressure coefficient is applied. This is possible because the forces resulting from reflection and absorption act all in the same direction, i.e., following the incoming radiation. Thus, thermo-optical material properties are not required for the SRP model and consequently a distinction between visible and infrared radiation is not done. In the computation of the RP acceleration in Tab. 5.7, a long-term mean of the radiation pressure coefficient $C_r$ is assumed according to Sośnica et al. (2015). The orbit positions used to evaluated the forces are obtained from a dynamic POD.

The radiation pressure modelling is commonly performed within the CRF. For GRACE, the accelerations were rotated into the SRF with a rotation matrix build from star camera data. Since spherical satellites are not equipped with such instruments, the star camera data are simulated from orbital positions and velocities such that the radial direction points exactly in the direction of the Earth's centre (see App. B).

The thermal re-radiation is not shown in Tab. 5.7, since adequately modelling the TRP acceleration for rotating spherical satellites turned out to be more challenging than for a non-rotating GRACE-like satellite. For rotating spherical satellites, the force resulting from the re-radiation of heat is directed along the spin axis of the hotter part of the satellite (Scharroo et al., 1991). The force can be modelled from Lambert's cosine law considering the diffuse re-emission of heat and was found to be at the order of 70 nm/s$^2$ for the LAGEOS satellites (Andrés et al., 2006). This requires adequate information on the satellite's temperature distribution, which does not only depend on the thermo-optical and geometrical characteristics and on the internal power of the satellite, but also on its spin behaviour (Scharroo et al., 1991; Andrés et al., 2004; Vokrouhlický and Bottke, 2012; Kucharski et al., 2013; Visco and Lucchesi, 2018a). Consequently, there is a hemispheric temperature difference, in addition to the temperature variations between the CCRs and the aluminium surface. With known spin axis and rotational period of the satellite, the resulting force can be computed (Vokrouhlický and Bottke, 2012; Kucharski et al., 2013). However, both spin axis and period are not constant. Beginning with a high rotational period of less than 1 s for LAGEOS 1 and 2 at launch and a slow drift in the spin axis, the spin period decreased exponentially and the spin axis started wobbling rapidly after roughly one decade (Andrés et al., 2006).

The Lageos Spin Axis Model (LOSSAM) model (Andrés et al., 2004) has been developed to approximate this spin behaviour taking into account observations as well as analytical considerations of the Earth's geomagnetic and gravity field, the satellite's centre of pressure offset as well as the varying reflectivity of the satellite's southern and northern hemisphere. An updated version of the LOSSAM model including the spin for the spherical satellite LARES is published in Visco and Lucchesi (2018). There also exist approximations of the rotational period for LAGEOS 1 and 2 (Kucharski et al., 2013), which rotate clockwise and counter-clockwise respectively. Exemplarily, the rotational period in seconds for LAGEOS 1 can be obtained from

$$T = 0.6188667 e^{0.328951 \cdot Y}, \tag{5.2.1}$$

where $Y$ is the time in years since launch (at 1976.3415). In January 2008, the spin period decreased already to nearly six hours. Consequently, LAGEOS 1 rotates only 1.6° within ten minutes. Due to this very small rotational angles, the effort of implementing the full spin model for the TRP acceleration is not made in this thesis. However, for earlier evaluation periods the consideration of a spin model and an adequate temperature model is essential (e.g., Visco and Lucchesi, 2018a).

In the following, the instantaneous re-radiation of heat is assumed, which acts in the same direction as the remaining radiation pressure accelerations. The instantaneous TRP force is not modelled analytically. Instead, this acceleration is generally intercepted with the estimation of the radiation pressure scale factor $C_r$ within a POD.

### 5.2.2 SRP

Before validating the analytically modelled radiation pressure forces for spherical satellites, a selection of suitable model extensions is required. Due to the differences in the RP force modelling between satellites with a panel model and spherical satellites, it is not possible to evaluate the same model scenarios here as for GRACE. Consequently, only a few scenarios are selected for the spherical satellites beginning with the SRP acceleration.

For GRACE, the parametrization of the solar radiation (solar constant vs. daily TSI) as well as different the shadow models (conical vs. physical) have been selected. Applying these modifications is also possible for spherical satellites. Additionally, isotropic and anisotropic reflection at the satellite's surface have been discussed for GRACE. With perfectly known thermo-optical material coefficients, it would be possible to analytically model diffuse and specular reflections for SLR satellites as well. However, the radiation pressure coefficient $C_r$ for spherical satellites does not distinguish between diffuse and specular reflections as mentioned above. Therefore, the BRDFs are not applicable. For the same reason, a separation between visible and infrared radiation and different thermo-optical material properties is not practical for spherical satellites. With these limitations, the SRP five digit codes from Tab. 5.1 simplify to a four digit code, where the third and fourth digit are always 0. Consequently, three SRP scenarios are selected, which are shown in Fig. 5.14 exemplarily for the Starlette satellite during three hours on January 1, 2008, with the radiation pressure coefficient set to $C_r = 1.134$ according to Sośnica et al. (2015).

One orbital revolution of Starlette lasts 104 minutes, of which the satellite is exposed to sunlight for about 70 minutes. Within sunlight, the SRP acceleration for Starlette is largest in the along-track direction with amplitudes between -5.1 and 5.1 $\mathrm{nm/s^2}$. In the cross-track direction, the SRP acceleration is nearly constant with about 0.33 $\mathrm{nm/s^2}$, which is related to the orientation of the orbital plane in space. The radial SRP acceleration peaks at 5.1 $\mathrm{nm/s^2}$ and is smallest shortly before and after eclipse with -2 $\mathrm{nm/s^2}$. The different model versions do not show a visible difference in all directions, which has also been observed for GRACE in Sect. 5.1.1.

### 5.2.3 ERP

In addition to SRP, here the choice of the ERP model scenarios is outlined. Similar to the ERP force modelling for GRACE, the parametrization of the radiation pressure data can be varied, i.e., the discretization of the footprint, the radiation data set, and the consideration of the reflection at TOA. Similar to SRP, the anisotropic reflection at the satellite's surface using BRDFs is not possible, since applying the radiation pressure coefficient for spherical satellites does not allow for the distinction between different reflection types. For the same reason, different thermo-optical material properties are not considered for spherical satellites. Nevertheless, both Earth's outgoing longwave and shortwave radiation are considered using the same radiation pressure. Again, the five digit codes simplify to a four digit code for ERP, where the fourth digit is always 0.

Consequently, six ERP scenarios are selected for spherical satellites, which are shown in Fig. 5.14 for Starlette during the same period. The ERP acceleration is largest in the radial direction with up to -1.7 $\mathrm{nm/s^2}$, when the satellite is fully exposed to sunlight. This is more than 10 times smaller than for GRACE due to the larger distance from the Earth's surface. Within the Earth's shadow, the radial ERP acceleration decreases to 0.5 $\mathrm{nm/s^2}$. In the along-track and cross-track directions, the ERP acceleration is below -0.1 $\mathrm{nm/s^2}$. Differences between the model scenarios are visible in all directions, especially when the satellite is in sunlight. Here, the standard model has the largest amplitude of -1.9 $\mathrm{nm/s^2}$ in the radial direction. Whereas the amplitude is smallest with -0.9 $\mathrm{nm/s^2}$ for the scenario 1200 using the discretization with a 1° grid together with outgoing shortwave and longwave data from EBAF. Compared to GRACE, the impact on the model scenario on the ERP

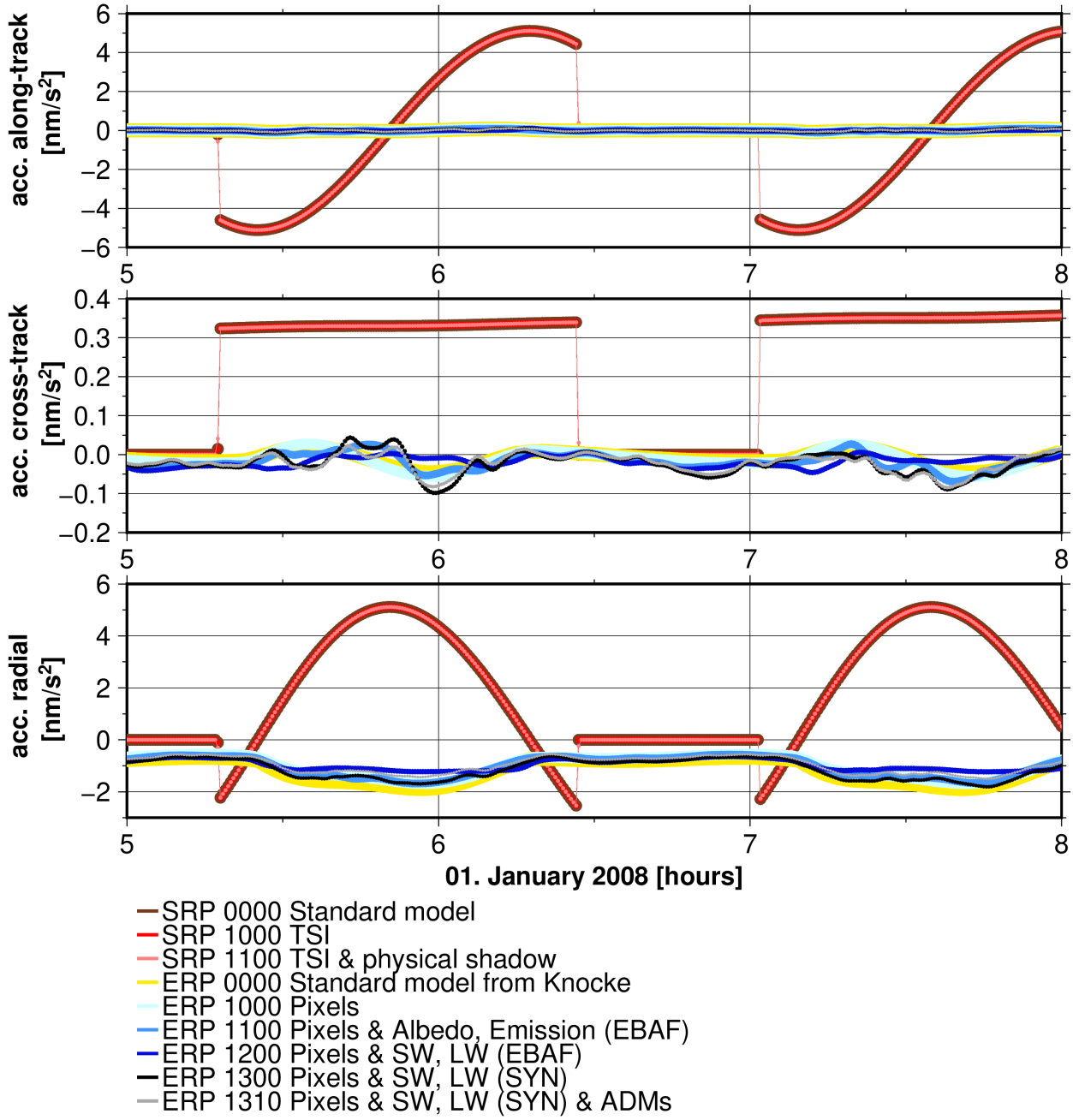



Figure 5.14: Different scenarios of modelled SRP and ERP accelerations acting on Starlette in the along-track (top), cross-track (middle), and radial (bottom) directions of the SRF during 3 hours (5–8 a.m.) on January 1, 2008. The radiation pressure coefficient is set to $C_r = 1.134$ (Sośnica et al., 2015). To look up modelling details, please see Tab. 5.1 and 5.2 for SRP and ERP, respectively.

acceleration is much smaller, which is most likely related to the high altitude of the SLR satellites, where details of the modelling become dispensable.

Since the differences between the scenarios has already been discussed for GRACE in detail and further insights are not expected, here a similar discussion is waived and the attention is directly turned to the validation.

### 5.2.4 Validation with POD

Validating the force models for spherical satellites turns out to be challenging. Non-spherical satellites are usually equipped with several instruments such as an accelerometer, which can be

used to validated the force models. The passive SLR satellites are designed as an ideal target for POD using SLR observations, i.e., independent measurements are not available. Therefore, a similar validation approach as for GRACE is conducted using SLR observations. Here, differently modelled radiation pressure accelerations serve as input for a POD together with SLR observations. Then, the residuals between the estimated dynamic orbit and the SLR ranges are computed. Smaller residuals indicate that the applied radiation pressure force model is more suitable than others.

The POD is again an iterative procedure, where orbit parameters are adjusted to minimize the observation residuals. At mentioned before, the software used in this thesis has been implemented by my colleague Anno Löcher and is part of the GROOPS software at IGG. The same method has also been applied in Zeitler et al. (2021); Löcher and Kusche (2021) with slightly different settings. Here, gravitational background models are applied according to Tab. 3.2. The normal points are converted to ranges as already explained in Sect. 5.1.5 by considering mostly geophysical effects (see Tab. 5.4). Observations are first modelled stochastically based on the provided accuracy in the normal point files. Then, a variance component estimation (Förstner, 1979) is applied for data weighting, which is organized by grouping the observations of each month by stations to account for different noise levels of the laser systems (Löcher and Kusche, 2021).

The non-gravitational force model combines different extensions of the radiation pressure force model as outlined in the previous section. The NRLMSIS 2.0 is selected as well to model the aerodynamic acceleration. To absorb the mismodelling of these forces, a careful parametrization is required. Commonly, either empirical parameters and/or scale factors are co-estimated within the POD (e.g., Hattori and Otsubo, 2019; Bloßfeld et al., 2015; Sośnica et al., 2015). Tab. 5.8 provides an overview of the parameters, which are estimated in this experiment, following Löcher and Kusche (2021).

Table 5.8: Parameter set for POD using SLR data as observations following Löcher and Kusche (2021).

| Parameter type | Frequency |
|---|---|
| Initial state vector | 1 per arc (10 days for LAGEOS, 3 days for Ajisai, Larets, Stella, Starlette) |
| Acceleration along-track, constant | 1 per arc (LAGEOS only) |
| Acceleration along-track, once per revolution | 1 set per arc (LAGEOS only) |
| Scale factor for radiation pressure | 1 per satellite and month |
| Scale factor for aerodynamics | 1 per satellite and day (Ajisai, Larets, Stella, Starlette) |
| Range biases | 1 per month per satellite and station |
| Station coordinates | 1 set per month for selected stations |

The POD is performed several times with a varying parametrization of the radiation pressure force model, which were already shown for Starlette in Fig. 5.14. The resulting residuals between the estimated dynamic orbit and the SLR ranges are used to compute the RMS per pass. Its annual mean is computed for the whole year 2008 and presented in Tab. 5.9.

The RMS is generally smallest for the LAGEOS satellites with around 1.293 and 1.139 cm for LAGEOS 1 and 2, respectively. This might be related to the selected parametrization, which includes constant as well as once per revolution accelerations in the along-track direction, in combination with the negligible aerodynamic signal at 5000 km. Due to the high altitude, the effect of the non-gravitational force modelling on the orbit is small with variations in the RMS below 0.1 mm for both satellites. Interestingly, LAGEOS 1 shows the smallest RMS with the standard SRP scenario and ERP scenario 1200, which uses EBAF radiation data on a 1° grid parametrized as outgoing fluxes. The opposite effect can be observed for LAGEOS 2, where ERP scenario 1200 has the largest RMS of 1.140 cm. Introducing the physical shadow function to the SRP modelling yields the smallest RMS of 1.133 cm. The sensitivity of LAGEOS 2 to the shadow function is most likely related to the orbit design, which has a larger ellipticity and lower inclination compared to LAGEOS 1 and consequently more eclipse transitions that necessitate the use of a physical shadow function.

The RMS for Starlette and Stella with around 1.465 and 1.484 cm is slightly smaller than for Larets and Ajisai with around 1.665 cm and 1.810 cm, respectively. For these satellites orbiting

Table 5.9: Annual average of the RMS per pass of the residuals between SLR ranges and the estimated dynamic orbit for the whole year 2008. For the POD, SLR measurements to six spherical satellites serve as observations, the gravitational background models are summarized in Tab. 3.2, estimated parameters are listed in Tab. 5.8. Then, different versions of modelled RP forces together with modelled aerodynamics for the satellites below 1000 km using NRLMSIS 2.0 serve as input for the non-gravitational force model. To look up the combined digit codes (SRP+ERP), see Tab. 5.1 for SRP, Tab. 5.2 for ERP, where the fifth digit is not required for spherical satellites. The estimated radiation pressure factor is also listed. The minimum per column is highlighted.

| Version | | LAGEOS 1 | | LAGEOS 2 | | Starlette | | Stella | | Ajisai | | Larets | |
|---|---|---|---|---|---|---|---|---|---|---|---|---|---|
| | | RMS | $C_r$ | RMS | $C_r$ | RMS | $C_r$ | RMS | $C_r$ | RMS | $C_r$ | RMS | $C_r$ |
| SRP | ERP | [cm] | [-] | [cm] | [-] | [cm] | [-] | [cm] | [-] | [cm] | [-] | [cm] | [-] |
| 0000 | 0000 | 1.294 | **1.11** | 1.139 | 1.10 | 1.472 | 1.15 | 1.508 | 1.16 | 1.820 | 1.00 | 1.680 | 1.02 |
| 0000 | 1000 | 1.294 | 1.11 | 1.138 | 1.10 | **1.462** | 1.14 | 1.489 | 1.14 | 1.815 | 1.00 | 1.667 | 0.99 |
| 0000 | 1100 | 1.294 | 1.11 | 1.139 | 1.10 | 1.465 | 1.13 | 1.490 | 1.14 | **1.800** | 1.00 | 1.667 | 0.99 |
| 0000 | 1200 | **1.291** | 1.11 | 1.140 | **1.09** | 1.463 | **1.11** | 1.489 | **1.11** | 1.910 | **0.98** | 1.660 | **0.97** |
| 0000 | 1300 | 1.293 | 1.11 | 1.138 | 1.10 | 1.464 | 1.13 | 1.484 | 1.14 | 1.812 | 1.00 | 1.663 | 0.99 |
| 0000 | 1310 | 1.293 | 1.11 | 1.139 | 1.10 | 1.465 | 1.13 | 1.483 | 1.13 | 1.808 | 0.99 | 1.663 | 0.99 |
| 1000 | 1310 | 1.293 | 1.11 | 1.138 | 1.10 | 1.465 | 1.13 | **1.483** | 1.13 | 1.808 | 0.99 | 1.663 | 0.99 |
| 1100 | 1310 | 1.294 | 1.12 | **1.133** | 1.10 | 1.466 | 1.13 | 1.483 | 1.13 | 1.805 | 0.99 | **1.658** | 0.99 |

below 1500 km, the variation of the ERP acceleration has a larger impact on the orbit than changes in the SRP modelling. When enhancing the discretization of the footprint on the Earth's surface from 19 elements (ERP scenario 0000) to a 1° grid in longitude and latitude (ERP scenario 1000), the RMS decreases for the three satellites by up to 0.02 cm. As expected, the effect is largest for Larets, which is the satellite with the lowest orbital altitude.

For Stella, Starlette and Larets, the RMS increases slightly when introducing the monthly EBAF radiation data (ERP scenario 1100) and then decreases again by up to 0.07 mm for Larets with the use of outgoing fluxes (ERP scenario 1200) instead of albedo and emissions. For Ajisai, the behaviour is contrary, which might be related to the large area to mass ratio, which makes the satellite more susceptible to surface forces. Consequently, the use of outgoing radiation data data instead of fluxes seems to improve the orbit. Replacing the monthly CERES EBAF data with hourly CERES SYN1deg data (ERP scenario 1300) slightly increases the RMS (except for Ajisai). The benefit of the high resolution data on the orbit probably diminishes by the fact that the CERES SYN1deg data are not energy balanced. For Stella, the RMS is smallest after introducing a daily value for the TSI in the SRP modelling. However, the TSI modification has the smallest impact on all satellites and seems negligible. As for LAser GEOynamics Satellite 2 or Laser Geometric Environmental Observation Survey 2 (LAGEOS 2), the physical shadow function decreases the RMS for Ajisai and Larets, which is most likely related to the orbit design.

Since the scenario with the minimal RMS differs for each of the selected missions, it is not possible to choose the best overall scenario. Nevertheless, from this experiment it can be concluded that detailed radiation pressure force modelling - especially the choice of the radiation data and the shadow function - impact the orbit of spherical satellites below 1500 km altitude by up to 1 mm. Even though this value is very small, these effects will likely become relevant in the future with increasing demands on the orbit accuracy.

In addition to the RMS, the variation of the co-estimated parameters within the POD might hint at the most suitable force model. Tab. 5.9 shows the resulting radiation pressure coefficient $C_r$, which is co-estimated monthly within the POD and here averaged for the year 2008. In case $C_r = 1$, the incoming radiation is re-radiated isotropically, whereas $C_r = 2$ indicates that the satellite is a perfect mirror (Rubincam and Weiss, 1986). In Tab. 5.9, the radiation pressure coefficient is 1.11 and 1.10 for LAGEOS 1 and 2, respectively. This fits the results from Hattori and Otsubo (2019) well, who found an average $C_r$ for LAGEOS 1 and 2 of 1.14 and 1.10, respectively. The

slight differences between the results presented in this thesis and Hattori and Otsubo (2019) for LAGEOS 1 are most likely related to the selected time span. In comparison to LAGEOS with a nearly constant value for $C_r$ in Tab. 5.9 (variations below 0.01), $C_r$ varies between 1.11 and 1.15 (1.16) with the parametrization of the ERP acceleration for Starlette (and Stella). The $C_r$ for Ajisai is smallest with values between 0.98 and 1.00, which is close to 1.04 found by Hattori and Otsubo (2019). Larets shows similar scales between 0.97 and 1.02. Interestingly, $C_r$ is smallest for all missions except LAGEOS 1 with the standard SRP scenario 0000 and ERP scenario 1200 (1° grid, outgoing fluxes from EBAF). For LAGEOS 1, $C_r$ is slightly smaller for the standard ERP scenario, which still rounds to a scale of 1.11. Fig. 5.15 depicts the monthly estimates of the radiation pressure coefficient $C_r$ using the standard SRP scenario 0000 and ERP scenario 1200 during the year 2008. It is clearly visible that $C_r$ is nearly constant throughout the year, except for LAGEOS 1, where $C_r$ varies between 0.8 and 1.3, which might be related to the once-per-revolution acceleration that is larger for LAGEOS 1 than for LAGEOS 2. In addition to the $C_r$ coefficient, other parameters have been co-estimated within the POD. However, analysing the variations of the empirical along-track accelerations for LAGEOS as well as the aerodynamic scale factor for the remaining satellites does not provide new insights to this discussion.

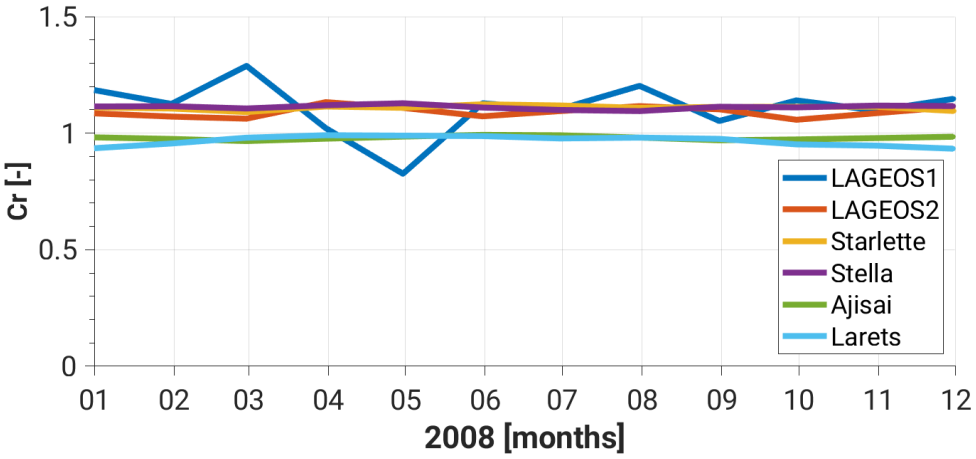



Figure 5.15: Time series of the radiation pressure coefficient $C_r$ for the year 2008 for the six selected satellites. The radiation pressure coefficient is estimated monthly with the POD using the standard SRP scenario in combination with the ERP scenario 1200 (1° grid, outgoing fluxes from EBAF) resulting in the smallest $C_r$ for all missions.

To conclude, the radiation pressure force modelling for spherical satellites is generally challenging due to the impact of the satellite's spin behaviour on the orbit dynamics. Therefore, a careful parametrization, i.e., the consideration of a radiation pressure scale factor and empirical acceleration, of the non-gravitational force model is required for a successful POD. A validation of selected radiation pressure scenarios for six spherical satellites at 700-1500 km altitude revealed that especially the choice of the radiation data and the shadow function improve the POD as it minimizes the difference between the estimated orbit and the SLR measurements. Improved radiation pressure force models decrease the RMS by up to 1 mm.

# Chapter 6

# Inverse estimation: Thermospheric neutral density

While the previous chapter focused on the forward modelling of the non-gravitational accelerations, the inverse estimation becomes the focus of attention for the remaining part of this thesis. As outlined before, there are several possibilities to apply an inverse estimation in the context of non-gravitational force modelling. The inverse estimations are based on modelled and measured non-gravitational accelerations. Ideally, all parameters, which are not sufficiently known, should be estimated in a joint procedure. This means that the accelerometer calibration and the estimation of other parameters, such as thermospheric neutral density, wind, and radiation-related parameters, would be performed jointly, either implemented one step or iteratively. This, albeit certainly innovative, approach would require very extensive numerical testing and complicated interpretation of estimates. Therefore, in this thesis the inverse estimation of selected parameters is outlined and performed with a fixed calibration.

In this chapter, the inverse estimation of the neutral density[1] from modelled and measured non-gravitational accelerations is outlined with a focus on GRACE data (Sect. 6.1). In addition, scale factors for a model density can be obtained from SLR measurements within a POD (Sect. 6.2). For both approaches, the parametrization as well as the applied algorithms are introduced before discussing the comparability of both methods and finally comparing the results in terms of scale factors.

## 6.1 Inverse estimation based on accelerometer data

Accelerometer measurements have been used to derive neutral density at a high temporal resolution (1-10 s) since the beginning of the CHAMP mission in 2000 (e.g., Bruinsma and Biancale, 2003; Bruinsma et al., 2004; Sutton et al., 2007; Doornbos, 2012; Mehta et al., 2017; March et al., 2019b). Even though the spatial resolution is low with one measurement per time-step, investigation of the thermosphere highly benefit from the global coverage resulting from the observation of longer time spans (e.g., one day or months). Besides from CHAMP, neutral densities have been derived from the accelerometer measurements on-board GOCE (e.g., Doornbos et al., 2013; Bruinsma et al., 2014; March et al., 2019a; March et al., 2019b), ESA's Swarm Mission (Swarm) (e.g., Siemes et al., 2016), GRACE (e.g., Tapley et al., 2007; Doornbos, 2012; Mehta et al., 2017; Vielberg et al., 2018; March et al., 2019a) and GRACE-FO (e.g., Krauss et al., 2020). Several solar and geomagnetic events have been investigated based on accelerometer-derived densities (Liu and Lühr, 2005; Sutton et al., 2005; Bruinsma et al., 2006; Sutton et al., 2006; Krauss et al., 2014; Krauss et al., 2020; Li and Lei, 2021).

Furthermore, accelerometer measurements were successfully used to derive the horizontal wind speed at satellite-altitude (Sutton et al., 2005; Sutton et al., 2007; Doornbos et al., 2010; Visser et al., 2013; Visser et al., 2019a; Visser et al., 2019b; Visser, 2019; March, 2020), which were used

[1] The thermospheric neutral density is abbreviated as neutral density in the following.

for atmospheric studies, e.g., to investigate the wind structure and their seasonal variation (Liu et al., 2016).

Recently, within the Thermosphere Observations from Low-Earth Orbiting Satellites (TOLEOS) project funded by ESA (Siemes et al., 2023), the neutral density and wind velocity were officially reprocessed for GRACE(-FO) and CHAMP with an improved processing as used for the official Swarm densities `https://swarm-diss.eo.esa.int`. The project was a collaboration of Delft University of Technology, Centre National d'Études Spatiales, engl. National Centre for Space Studies (CNES), DLR in Neustrelitz and University of Bonn, where I validated the radiation pressure force modelling. The final neutral density and wind estimates from this project are available at `http://thermosphere.tudelft.nl/` and will be applied in this thesis for comparison.

### 6.1.1 Parametrization

The basis for the inverse estimation here is the relation between measured $\boldsymbol{a}_{\text{meas}}$ and modelled non-gravitational acceleration under consideration of an error $\epsilon$

$$\boldsymbol{a}_{\text{meas}} = \boldsymbol{a}_{\text{aero}} + \boldsymbol{a}_{\text{RP}} + \boldsymbol{a}_{\text{sat}} + \epsilon. \tag{6.1.1}$$

The modelled non-gravitational accelerations result from the summation of the aerodynamic, radiation-pressure and satellite-induced accelerations (see Ch. 4). In the forward modelling, the neutral density within the aerodynamic acceleration is commonly obtained from empirical models for every time step, e.g., 10 s, at the position of the satellite.

In the inverse modelling, the aim is to solve Eq. 6.1.2 for the neutral density at a high temporal resolution to benefit the high resolution of the accelerometer measurements. Since the measured non-gravitational accelerations are on the left hand-side of the equation, the calibration of these measurements needs be considered as well. Ideally, accelerometer calibration parameters and the neutral density would be estimated in a joint procedure. The accelerometer calibration is commonly parametrized with a scale factor, e.g., for the whole mission, and a daily bias for each axis (see Sect. 3.1.5). However, with the aim of estimating the neutral density per time step, together with three daily biases, and scale factors jointly, the system of equations would be largely underdetermined.

Instead of aiming a joint estimation, a stepwise approach is more suitable (Doornbos et al., 2010). In this case, the accelerometer should be calibrated first resulting in an updated observation equation

$$\boldsymbol{a}_{\text{cal}} = \boldsymbol{a}_{\text{aero}} + \boldsymbol{a}_{\text{RP}} + \boldsymbol{a}_{\text{sat}} + \epsilon \tag{6.1.2}$$

that can be solved for the neutral density. In Vielberg et al. (2018), we confirmed that the accelerometer calibration procedure impacts the neutral density estimates significantly. Depending on the calibration approach, updating the neutral density within the calibration allows for an iterative procedure.

Besides the requirement of the accelerometer calibration, any modelling errors in Eq. (6.1.2) would directly impact the neutral density estimation. These include the mismodelling of the radiation pressure acceleration, e.g., due to errors in the thermo-optical material coefficients, as well as an imperfect consideration of satellite-induced accelerations, and inaccuracies in the modelled aerodynamic acceleration itself, where the aerodynamic coefficient (Doornbos et al., 2010) is known to be critical and the relative velocity is effected by inaccurate wind models. Parametrizing theses errors and including them in the inverse estimation would lead to an even more unstable system of equations and is thus not an option.

Within the stepwise procedure, horizontal wind velocities at satellite altitude can be estimated. The separate estimation of neutral density and winds is performed in a direct approach (Doornbos et al., 2010). Since neutral density and wind estimates depend on the alignment of the observed and modelled non-gravitational force vectors, Doornbos et al. (2010) developed a joint approach to estimate the neural density as well as the wind velocity vector in cross-track direction in an iterative procedure. Both the direct and iterative algorithms are explained in the next section.

Instead of estimating the neutral density, one could think of using a model density in the computation of the aerodynamic acceleration and solving for a neutral density correction in an inverse approach. This correction could be parametrized as a scale factor with a lower temporal resolution, e.g., daily. This would be similar to the approach applied in the second part of this chapter, where such scale factors for a model density are estimated within a POD. Estimating neutral density corrections from accelerometer measurements would indeed simplify the inverse estimation, however, the benefit of the high temporal resolution of the data would be disregarded.

Further, the estimated neutral density (correction) can be assimilated into empirical or physical models (Corbin and Kusche, 2022). The resulting updated neutral density might be applied again in the computation of the aerodynamic acceleration. This allows for an iterative combination with the inverse model.

### 6.1.2 Algorithm

The inverse estimation of in-situ neutral densities and winds has several requirements. First, accelerometer measurements need to be calibrated sufficiently. As already explained in Sect. 3.1.5, this requires the determination of a bias and scale factor for each direction. In a second step, satellite-induced artefacts such as thruster firings need to be eliminated from the calibrated accelerometer data since they perturb the measured accelerations. This can either be done by modelling the accelerations resulting from the thrusts or by removing the affected data. Then, radiation pressure accelerations are modelled, e.g., using the extended model presented in Sect. 4.4.3, and removed from the prepared accelerometer data

$$\boldsymbol{a}_{\mathrm{obs}} = \boldsymbol{a}_{\mathrm{cal}} - \boldsymbol{a}_{\mathrm{RP}}. \tag{6.1.3}$$

The so-called observed aerodynamic acceleration remains, which can be equated with the analytically modelled aerodynamic acceleration (Eq. (4.1.1)), which is the basis for the neutral density and wind estimation from both the direct and iterative algorithm according to Doornbos et al. (2010), which are briefly presented in the following.

#### Direct algorithm

Within the direct algorithm, considering only the x-component of the relation between the modelled and observed aerodynamic acceleration ($\boldsymbol{a}_{\mathrm{obs}} = [a_{\mathrm{obs,x}}, a_{\mathrm{obs,y}}, a_{\mathrm{obs,z}}]^T$) and solving it for the thermospheric neutral density yields

$$\rho = \frac{2\,m\,a_{\mathrm{obs,x}}}{A_{\mathrm{ref}} C_{\mathrm{a,x}} v_{\mathrm{r}}^2}. \tag{6.1.4}$$

The geometry of the direct neutral density and wind estimation is shown in Fig. 6.1. The wind velocity $v_{\mathrm{w,y}}$ can be obtained from aligning the direction of the initial relative velocity vector $\boldsymbol{v}_{\mathrm{r},0}$ with the observed drag acceleration $\boldsymbol{a}_{\mathrm{obs,D}}$ (see Fig. 6.1b)

$$v_{\mathrm{w,y}} = \frac{a_{\mathrm{obs,D,y}}}{a_{\mathrm{obs,D,x}}} v_{\mathrm{r},0,\mathrm{x}} - v_{\mathrm{r},0,\mathrm{y}}. \tag{6.1.5}$$

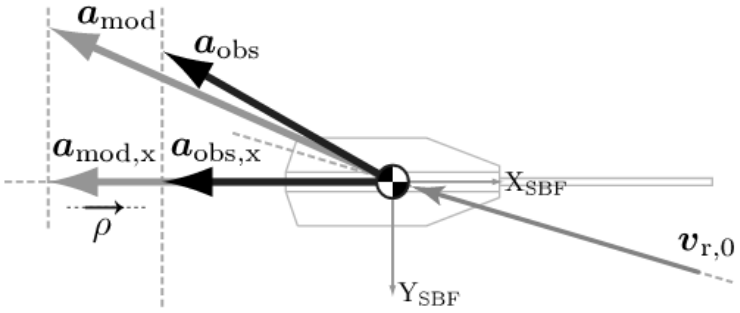
This is also known as dual-axis method in Sutton et al. (2007). The observed drag acceleration results from the difference between the observed aerodynamic acceleration and the modelled lift and side aerodynamic acceleration

$$\boldsymbol{a}_{\mathrm{obs,D}} = \boldsymbol{a}_{\mathrm{obs}} - \boldsymbol{a}_{\mathrm{mod,L}}, \tag{6.1.6}$$

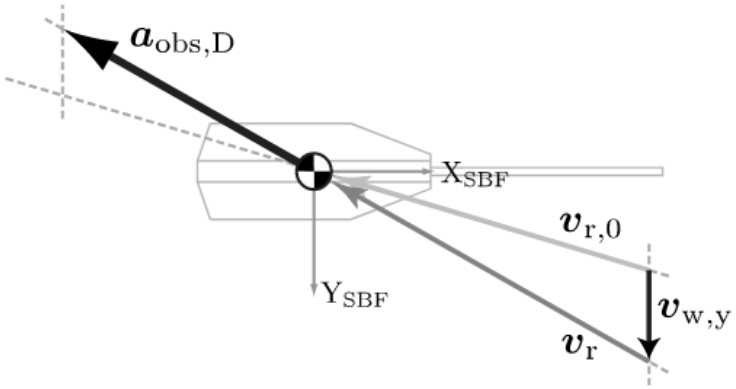
where the latter can be obtained from projecting the modelled aerodynamic acceleration into the direction of the initial relative velocity vector of the satellite $\boldsymbol{v}_{\mathrm{r},0}$

$$\boldsymbol{a}_{\mathrm{mod,L}} = \boldsymbol{a}_{\mathrm{mod}} - \boldsymbol{a}_{\mathrm{mod,D}} \tag{6.1.7}$$

$$= \boldsymbol{a}_{\mathrm{mod}} - (\boldsymbol{a}_{\mathrm{mod}} \cdot \hat{\boldsymbol{v}}_{\mathrm{r},0})\, \hat{\boldsymbol{v}}_{\mathrm{r},0}. \tag{6.1.8}$$




(a) Geometry of the direct neutral density estimation from Doornbos et al. (2010) (Fig. 3).




(b) Geometry of the direct wind estimation from Doornbos et al. (2010) (Fig. 4).

Figure 6.1: Geometry of the direct neutral density and wind estimation from Doornbos et al. (2010) (Fig. 3, 4), where $\boldsymbol{a}_{\mathrm{obs}}$ and $\boldsymbol{a}_{\mathrm{mod}}$ are the observed and modelled aerodynamic acceleration, respectively. $\boldsymbol{a}_{\mathrm{obs,D}}$ is the observed drag acceleration acting in the same direction as the satellite's relative velocity $\boldsymbol{v}_{\mathrm{r}}$. $\boldsymbol{v}_{\mathrm{r,0}}$ is the initial relative velocity. $X_{\mathrm{SBF}}$ and $Y_{\mathrm{SBF}}$ are the axes of the satellite body-fixed frame. $\rho$ denotes the neutral density and $\boldsymbol{v}_{\mathrm{w,y}}$ is the wind velocity vector. The angles are exaggerated for better visibility.

From the geometry, it becomes clear that with an increasing angle between the relative velocity and the $x$-axis of the satellite body-fixed frame, the wind velocity increases and the neutral density decreases. Consequently, the error depends on this angle, however, the attitude of the GRACE satellite varies only within 2°. In addition, the computation of the relative velocity considers the satellite's orbital velocity, the velocity of the co-rotating atmosphere and optionally the wind velocity, e.g., from HWM14. With the computation of the wind velocity (Eq. (6.1.5)), updating the relative velocity and accordingly the force coefficient and the neutral density becomes possible. Thus, Doornbos et al. (2010) also developed an iterative algorithm to overcome these limitations.

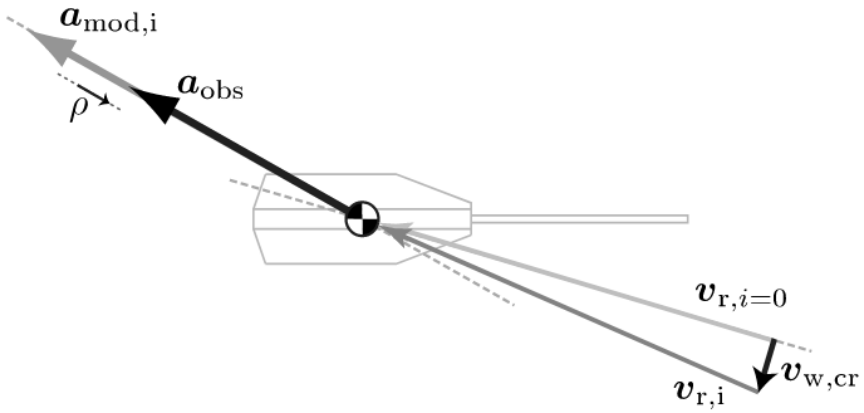
**Iterative algorithm**

This algorithm (Doornbos et al., 2010) aims at iteratively aligning the direction and the magnitude of the modelled and observed aerodynamic acceleration (see Fig. 6.2). In the first step, the direction of the aerodynamic acceleration is modified by rotating the relative velocity vector. The rotation is about the normalized local vertical direction $\hat{\boldsymbol{u}}_{\mathrm{up}}$, i.e., the anti-radial direction. Then, both the modelled and aerodynamic acceleration are updated according to

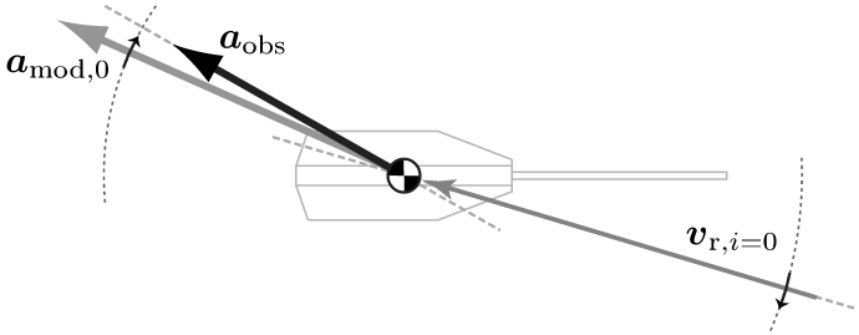
$$\boldsymbol{a}' = \boldsymbol{a} - (\boldsymbol{a} \cdot \hat{\boldsymbol{u}}_{\mathrm{up}})\hat{\boldsymbol{u}}_{\mathrm{up}}. \tag{6.1.9}$$

The initial guess of the relative velocity $\boldsymbol{v}_{\mathrm{r,i=0}}$ considers the satellite's orbital velocity $\boldsymbol{v}_{\mathrm{o}}$ and the velocity $\boldsymbol{v}_{\mathrm{c}}$ of the co-rotating atmosphere

$$\boldsymbol{v}_{\mathrm{r,i=0}} = \boldsymbol{v}_{\mathrm{o}} + \boldsymbol{v}_{\mathrm{c}}. \tag{6.1.10}$$




(a) Geometry of the iterative neutral density estimation from Doornbos et al. (2010) (Fig. 5a).




(b) Geometry of the iterative wind estimation from Doornbos et al. (2010) (Fig. 5b).

Figure 6.2: Geometry of the iterative neutral density and wind estimation from Doornbos et al. (2010) (Fig. 5), where $\boldsymbol{a}_{\mathrm{obs}}$ and $\boldsymbol{a}_{\mathrm{mod}}$ are the observed and modelled aerodynamic acceleration, respectively. The index 0 of the modelled acceleration denotes the initial guess and the index $i$ is the final adjusted acceleration after convergence of the iteration. Similarly, $\boldsymbol{v}_{\mathrm{r},0}$ or $\boldsymbol{v}_{\mathrm{r,i=0}}$ is the initial relative velocity vector of the satellite and $\boldsymbol{v}_{\mathrm{r,i}}$ is the velocity from the iterative estimation. $\rho$ denotes the final neutral density and $\boldsymbol{v}_{\mathrm{w,cr}}$ is the final wind velocity vector in cross-track direction from the iterative estimation. The angles are exaggerated for better visibility.

Including the modelled wind speed $\boldsymbol{v}_{\mathrm{w,mod}}$ is possible by projecting it on the in-track direction $\boldsymbol{v}_{\mathrm{w,it}}$ and on the rotation axis $\boldsymbol{v}_{\mathrm{w,up}}$ following

$$\boldsymbol{v}_{\mathrm{w,it}} = (\boldsymbol{v}_{\mathrm{w,mod}} \cdot \hat{\boldsymbol{v}}_{\mathrm{r}})\, \hat{\boldsymbol{v}}_{\mathrm{r}}, \tag{6.1.11}$$

$$\boldsymbol{v}_{\mathrm{w,up}} = (\boldsymbol{v}_{\mathrm{w,mod}} \cdot \hat{\boldsymbol{u}}_{\mathrm{up}})\, \hat{\boldsymbol{u}}_{\mathrm{up}}. \tag{6.1.12}$$

This computation needs to be updated in each iteration. Then, the residuals of the normalized modelled and observed aerodynamic acceleration are computed, where the latter can be replaced by the normalized force coefficient vector $\hat{\boldsymbol{C}}'$

$$\boldsymbol{d} = \hat{\boldsymbol{a}}'_{\mathrm{obs}} - \hat{\boldsymbol{a}}'_{\mathrm{mod}} = \hat{\boldsymbol{a}}'_{\mathrm{obs}} - \hat{\boldsymbol{C}}'_{\mathrm{a,i}}(\boldsymbol{v}_{\mathrm{r,i}}, ...). \tag{6.1.13}$$

This procedure is repeated until $d$ is below a predefined threshold, e.g., $10^{-7}\,\mathrm{m/s^2}$. The adjusted velocity vector $\hat{\boldsymbol{v}}_{\mathrm{adj,i}}$ of the current iteration is normalized and by definition orthogonal to the relative velocity and the rotation axis

$$\hat{\boldsymbol{v}}_{\mathrm{adj,i}} = \frac{\boldsymbol{v}_{\mathrm{r,i}} \times \hat{\boldsymbol{u}}_{\mathrm{up}}}{||\boldsymbol{v}_{\mathrm{r,i}} \times \hat{\boldsymbol{u}}_{\mathrm{up}}||}. \tag{6.1.14}$$

Then, a forward and a backward numerical differentiation are performed to adjust the direction. For that purpose, new relative velocity vectors

$$\boldsymbol{v}_{\mathrm{r}}^{+} = ||\boldsymbol{v}_{\mathrm{r,i}}|| \frac{\boldsymbol{v}_{\mathrm{r,i}} + \partial \hat{\boldsymbol{v}}_{\mathrm{adj,i}}}{||\boldsymbol{v}_{\mathrm{r,i}} + \partial \hat{\boldsymbol{v}}_{\mathrm{adj,i}}||}, \tag{6.1.15}$$

$$\boldsymbol{v}_{\mathrm{r}}^{-} = ||\boldsymbol{v}_{\mathrm{r,i}}|| \frac{\boldsymbol{v}_{\mathrm{r,i}} - \partial \hat{\boldsymbol{v}}_{\mathrm{adj,i}}}{||\boldsymbol{v}_{\mathrm{r,i}} - \partial \hat{\boldsymbol{v}}_{\mathrm{adj,i}}||} \tag{6.1.16}$$

are obtained. Based on these velocities, the modelled aerodynamic acceleration can be modified, which leads to the two residuals

$$\boldsymbol{d}^{+} = \hat{\boldsymbol{a}}'_{\mathrm{obs}} - \hat{\boldsymbol{C}}'_{\mathrm{a,i}} \left( \boldsymbol{v}_{\mathrm{r}}^{+}, ... \right), \tag{6.1.17}$$

$$\boldsymbol{d}^{-} = \hat{\boldsymbol{a}}'_{\mathrm{obs}} - \hat{\boldsymbol{C}}'_{\mathrm{a,i}} \left( \boldsymbol{v}_{\mathrm{r}}^{-}, ... \right). \tag{6.1.18}$$

With the difference between the velocity vectors

$$\Delta \boldsymbol{v}_{\mathrm{r}} = \boldsymbol{v}_{\mathrm{r}}^{+} - \boldsymbol{v}_{\mathrm{r}}^{-} \tag{6.1.19}$$

and the residual acceleration

$$\Delta d = ||\boldsymbol{d}^{+}|| - ||\boldsymbol{d}^{-}||, \tag{6.1.20}$$

the relative velocity can be updated for the next iteration by keeping its magnitude and changing its direction

$$\boldsymbol{v}_{\mathrm{r,i+1}} = ||\boldsymbol{v}_{\mathrm{r,i}}|| \frac{\boldsymbol{v}_{\mathrm{r,i}} - d \left( \Delta \boldsymbol{v}_{\mathrm{r}} / \Delta d \right)}{||\boldsymbol{v}_{\mathrm{r,i}} - d \left( \Delta \boldsymbol{v}_{\mathrm{r}} / \Delta d \right) ||}. \tag{6.1.21}$$

Then, Eq. 6.1.13 can be recomputed with the updated velocity. In case, the convergence criterion is reached, the neutral density and the crosswind velocity can be finally obtained from

$$\rho = \frac{2m||\boldsymbol{a}'_{\mathrm{obs}}||}{A_{\mathrm{ref}}||\boldsymbol{C}'_{\mathrm{a,i}}||v_{\mathrm{r,i}}^{2}}, \tag{6.1.22}$$

$$\boldsymbol{v}_{\mathrm{w,cr}} = \boldsymbol{v}_{\mathrm{r,i}} - \boldsymbol{v}_{\mathrm{r},0}. \tag{6.1.23}$$

**Scale factors from accelerometer-derived densities**

The neutral densities derived from accelerometer measurements can be further used to scale the neutral density from thermospheric models (see Sect. 2.2.3). The estimation of such scale factors also enables the comparison of the neutral density derived from other measurement techniques, such as from SLR data in Sect. 6.2, as shown in Zeitler et al. (2021), where the model density was obtained from NRLMSISE-00. Scale factors from accelerometer-derived densities have also been investigated in Doornbos (2012); Vielberg et al. (2018).

Dividing the neutral density $\rho$ resulting from the direct or iterative algorithm by the neutral density obtained from a model $\rho_{\mathrm{m}}$ yields the scale factor

$$f_{\mathrm{s,ACC}} = \frac{\rho}{\rho_{\mathrm{m}}}. \tag{6.1.24}$$

The scale factors can be computed for every time step, where accelerometer-derived densities are available. The model, which is NRLMSIS 2.0 in this thesis, is evaluated at the position of the satellite for the same time steps. Thus, scale factors for GRACE are obtained at a 10 s resolution.

### 6.1.3 Results

This section provides selected results from the thermospheric neutral density estimation based on accelerometer data from GRACE-A as an example for an inverse estimation using non-gravitational force models. After presenting the results of the neutral density for the total mission lifetime, the results are compared to accelerometer-based neutral density estimates processed by other institutions. This comparison is important to point out the impact of the processing method and underlying assumptions on the final neutral density estimates, however, it is not possible to make a statement about which data set is closest to the truth. A comparison in terms of scale factors derived from SLR data is performed later in Sect. 6.2.4.

Further comparisons between the accelerometer-derived neutral density and the neutral density obtained from other methods such as TLE data as well as comparisons to other missions are not performed here. For such comparisons, I refer to Bruinsma et al. (2022); Calabia et al. (2020); March et al. (2017); Emmert (2015). However, it should be mentioned here that a comparison to other missions requires further calibration of the data sets to account for inter-mission biases, i.e., biases between neutral density estimates from accelerometers on-board different satellites (Bruinsma et al., 2022).

It should also be mentioned that cross-wind velocities are a side product of the iterative neutral density estimation (see Sect. 6.1.2), which require precise cross-track radiation pressure force models and calibrated accelerometer data in addition to precise aerodynamic modelling. Nevertheless, large errors are known to occur especially during low solar activity (e.g., Doornbos, 2012), thus, I do not show cross-wind velocities here and focus instead on the results of the neutral density.

The neutral density derived from GRACE-A accelerometer measurements is presented in Fig. 6.3 for the mission lifetime w.r.t. the argument of latitude. Hence, one column in Fig. 6.3 corresponds to one orbital revolution and thus this illustration combines both spatial and temporal aspects. To obtain the neutral density along the GRACE-A orbit, I applied the direct algorithm as described in Sect. 6.1.2. For the computation of the radiation pressure acceleration within this estimation, the best force model from the validation with SLR (see Sect. 5.1.5) is applied (SRP 11000, ERP 13100, TRP 13000). In addition, the aerodynamic model as described in Sect. 4.1 is used with constituents and temperature data from NRLMSIS 2.0. The force models are evaluated at satellite positions from the reduced-dynamic GNV1B orbits. The gaps in the time series occur due to missing orbit, star camera and/or accelerometer data especially at the end of the mission lifetime.

From Fig. 6.3, it is clearly visible that the neutral density weakens within the first few years of the mission and reaches a minimum around 2008. During this solar minimum, the neutral density is below $6\times10^{-13}\,\mathrm{kg/m^3}$, which is approximately five times smaller than during solar maximum in 2003. In 2015, where the maximium of the solar cycle 24 is reached, the neutral density obtained from GRACE-A is above $5\times10^{-12}\,\mathrm{kg/m^3}$. Even though the solar activity was much higher during 2003 ($F_{10.7}$ index up to 250 sfu, see Fig. 6.3, top) than during 2015 ($F_{10.7}$ index around 150 sfu), the derived neutral density is larger in 2015 due to the lower satellite altitude near 400 km, which is 100 km below the satellite altitude during 2003 (see Fig. 6.3, top).

In addition to this temporal behaviour, spatial patterns are visible in Fig. 6.3. When the satellite is exposed to sunlight, the neutral density is more than twice as large as in umbra. These day-night variations cause neutral density changes along the argument of latitude, e.g., with a maximum at the descending equator during August 2002. However, already at the beginning of 2003 the pattern reversed such that the neutral density is minimal at the ascending equator due to the orbit dynamics.

Neutral densities are processed using the iterative algorithm as well (Fig. 6.3). Here, the settings, i.e., force modelling and background models, are the same as in the direct processing. Additionally, neutral density data sets have been produced by several other institutes also based on GRACE-A accelerometer data. Tab. 6.1 provides an overview of neutral density data sets derived from GRACE-A accelerometer measurements including their processing details (as far as available). Please note that the list is likely incomplete as only the most popular data sets are listed. All data sets have in common that they apply an inverse estimation using either the direct or iterative algorithm with their in-house accelerometer calibration and non-gravitational

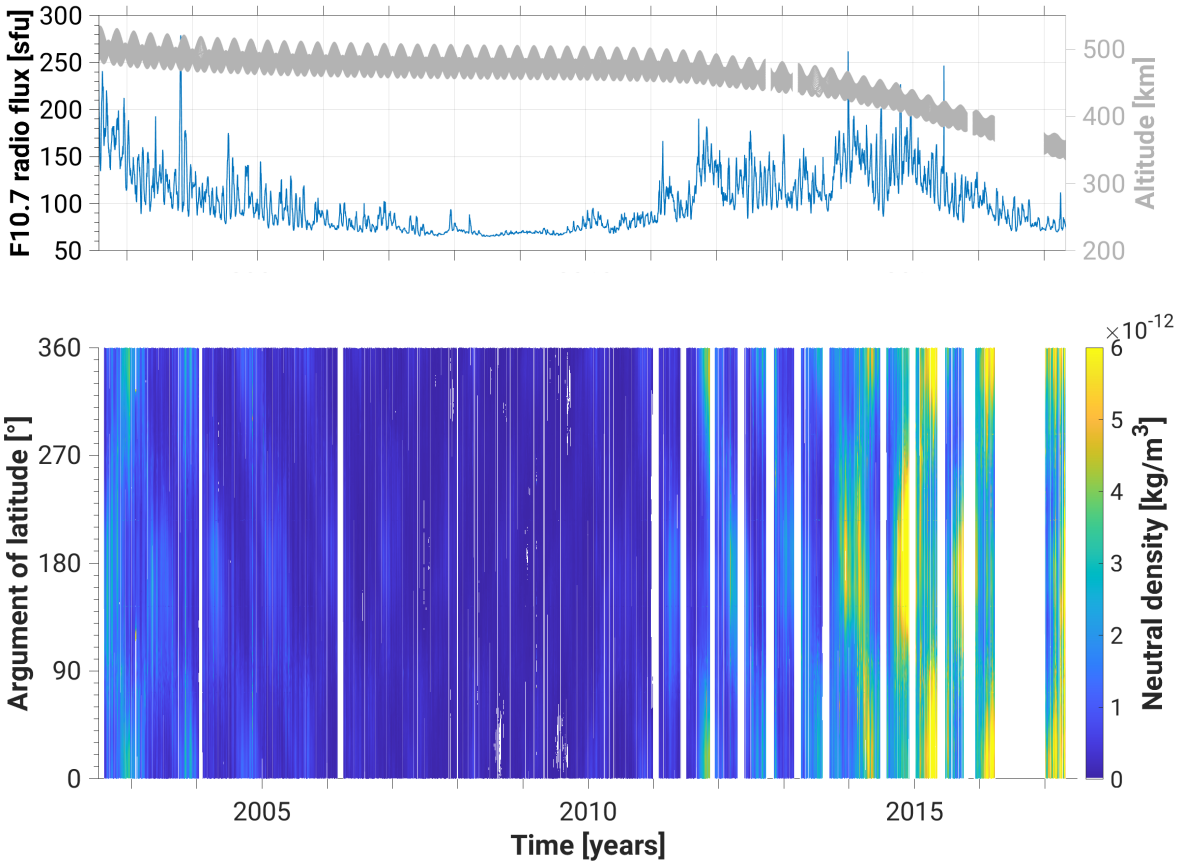



Figure 6.3: Top: F10.7 radio flux index and satellite altitude of GRACE-A during the mission lifetime. Bottom: Neutral density derived from GRACE-A accelerometer data during the mission lifetime. The neutral density estimation is performed with the direct algorithm as described in Sect. 6.1.2. For the computation of the radiation pressure acceleration, the best force model from the validation with SLR (see Sect. 5.1.5) is applied (SRP 11000, ERP 13100, TRP 13000). Gaps (white) in the time series occur due to missing orbit, star camera and/or accelerometer data.

force modelling. Already the calibrated accelerometer data are known to show large variations depending on the parametrization and calibration procedure (e.g., Vielberg et al., 2018; Klinger and Mayer-Gürr, 2016). Further, there can be large differences in the modelled non-gravitational forces as shown in Ch. 5. Consequently, the resulting neutral density estimates are not equal.

Table 6.1: Overview of various neutral density data sets derived from GRACE-A accelerometer data. $\boldsymbol{C}_\mathrm{a}$ and $\alpha$ denote the aerodynamic coefficient and energy accommodation coefficient, respectively.

| Name | Publication | Algorithm | Resolution | Macro-model | Aerodynamic force model | Radiation pressure force models | Accelerometer calibration |
|---|---|---|---|---|---|---|---|
| Direct | processed for this thesis (Vielberg, 2023) | direct | 10 s | panel | NRLMSIS2.0; no wind; $\alpha$ =0.93; $\boldsymbol{C}_\mathrm{a}$: Sentman (1961), Moe and Moe (2005) | SRP: TSI, phys. shadow; ERP: 1° CERES SYN1deg+ADMs; TRP: fitted heat-diffusive | daily biases, mission scales |
| Iterative | processed for this thesis (Vielberg, 2023) | iterative | 10 s | panel | same as above | same as above | same as above |
| IGG-RL01 | Vielberg et al. (2021) [1] | direct | 10 s | panel | same as above | SRP: as above for vis. & IR radiation; ERP: same as above TRP: instantaneous | same as above |
| TOLEOS | Siemes et al. (2023) [2] | iterative | 10 s | high-fidelity | NRLMSISE-00; HWM07; $\alpha$ =0.85; $\boldsymbol{C}_\mathrm{a}$: Monte Carlo (March et al., 2021) | SRP: solar const., phys. shadow ERP: monthly maps 2° resolution TRP: heat-diffusive | daily biases, mission scales, thermal correction |
| Graz | Krauss et al. (2020) [3] | iterative | 60 s | panel | NRLMSIS2.0; HWM14; $\alpha$ =0.90; $\boldsymbol{C}_\mathrm{a}$: Sentman (1961), Moe and Moe (2005) | SRP: TSI, phys. shadow, BRDF; ERP: 1° CERES SYN1deg, BRDF; TRP: instantaneous | daily biases, daily scale factor matrix |
| Mehta | Mehta et al. (2017) [4] | iterative | 5 s | high-fidelity | NRLMSISE-00, no wind, $\alpha$ altitude-dependent; $\boldsymbol{C}_\mathrm{a}$: Monte Carlo (Mehta et al., 2017) | SRP, ERP: standard; TRP: no | daily biases, daily scales |
| Sutton | Sutton (2008) [4] | iterative | 5 s | panel | TIE-GCM; no wind; $\alpha$ altitude-dependent; $\boldsymbol{C}_\mathrm{a}$: Sentman (1961), Moe and Moe (2005) | SRP, ERP: standard; TRP: no | daily biases, daily scales |

[1] `doi:10.1594/PANGAEA.931347`

[2] `http://thermosphere.tudelft.nl/page1.html`, last access: April 13, 2023

[3] `https://ftp.tugraz.at/outgoing/ITSG/satelliteOrbitProducts/operational/GRACE-1/neutralDensity/`, last access: April 13, 2023

[4] `http://tinyurl.com/densitysets`, last access: April 13, 2023

In the following, a comparison of these seven neutral density data sets is conducted. Therefore, three periods of different solar and geomagnetic conditions are selected exemplarily for further analyses:

- October 1-23, 2003, to represent high solar activity and quite geomagnetic conditions,
- Halloween storm during October 24-31, 2003, to represent high solar activity and a severe geomagnetic storm,
- January 12, 2008, to represent low solar activity and quite geomagnetic conditions.

Even though possible, low solar activity in combination with high geomagnetic activity is not considered here since these events are relatively rare and no further insights are expected from comparisons during such periods.

Fig. 6.4 shows the neutral density of the seven selected data sets for approximately one orbital revolution within each of the three periods. On October 12, 2003, which represents high solar activity and quite geomagnetic conditions, the neutral density varies between $0.1\times10^{-12}\,\mathrm{kg/m^3}$ and $1.2\times10^{-12}\,\mathrm{kg/m^3}$. Here, the day-night variation is clearly visible with a peak on the dayside at 17 h local solar time near the equator. The largest neutral density estimates result from the direct algorithm, which is used in the *direct* data set from this thesis as well as in *IGG-RL01*. The neutral densities resulting from these two data sets vary less than 1 %, since accelerometer calibration and aerodynamic remain unchanged. Processing differences occur in the radiation pressure modelling. In the *IGG-RL01* data, instantaneous thermal re-radiation has been applied and the solar radiation modelling considers both visible and infrared wavelengths, which turned out to be insufficient in the validation with SLR data (Sect. 5.1.5) and is therefore not considered in the *direct* data set in this thesis. The *direct* data additionally consider fitted heat-diffusive thermal re-radiation (see also Tab. 6.1). It can already be stated here that the radiation pressure modelling has a minor effect on the estimated neutral densities during high solar activity, where the aerodynamic signal is only five times larger than the radiation pressure signal (see also Fig. 5.1), i.e., the drag signal to noise ratio is small.

In addition to the *direct* data set, the *iterative* data set is processed with the same force modelling within the iterative algorithm (see Sect. 6.1.2). The neutral density resulting from the *iterative* data set is generally smaller (about 8 %). Strikingly, the neutral density shows various peaks, e.g., at 00:19 h or 00:27 h. However, these are not visible in any other neutral density estimates even though the remaining data sets are also based on the iterative algorithm. Consequently, the peaks are likely related to my own processing. Neutral density estimates from *TOLEOS* and *Sutton* agree well with each other and show only slight differences on the dayside. Both data sets agree well with the *iterative* neutral density between 00:50 h and 1:15 h, whereas the neutral density on the dayside shows variations of up to 20 %. The smallest neutral density reaching $0.1\times10^{-12}\,\mathrm{kg/m^3}$ on the nightside is from the *Graz* data set, which is close to the data from *Mehta* especially on the dayside. The neutral density from *Graz* is generally smoother due to the temporal resolution of 1 minute compared to 5-10 s within the remaining data sets.

As shown in Tab. 6.1, there are a variety of processing details such as the aerodynamic modelling, radiation pressure force modelling, accelerometer calibration or the macro-model, which differ between the neutral density versions. Thus, it is hardly impossible to assign the differences clearly to one of these aspects. However, computing the impact of changes in the measured and modelled accelerations on the neutral density reveals that changes in the accelerometer data and the aerodynamic modelling of, e.g., 5 %, are reflected 1:1 in the density. Thus, the accelerometer calibration as well as the aerodynamic coefficient, which reflects the gas-surface interactions, strongly impact the neutral density estimates (see e.g., March et al., 2019a; Bruinsma and Biancale, 2003). On the other hand, the impact of the radiation pressure force modelling on the neutral density strongly depends on the solar activity. During high solar activity in October 2003, changes of 15 % in the radiation pressure acceleration are necessary to impact the neutral density by 1 %. In comparison, during low solar activity radiation pressure variations of 15 % lead to changes of 5 % in the neutral density. Consequently, differences in the radiation pressure force modelling can

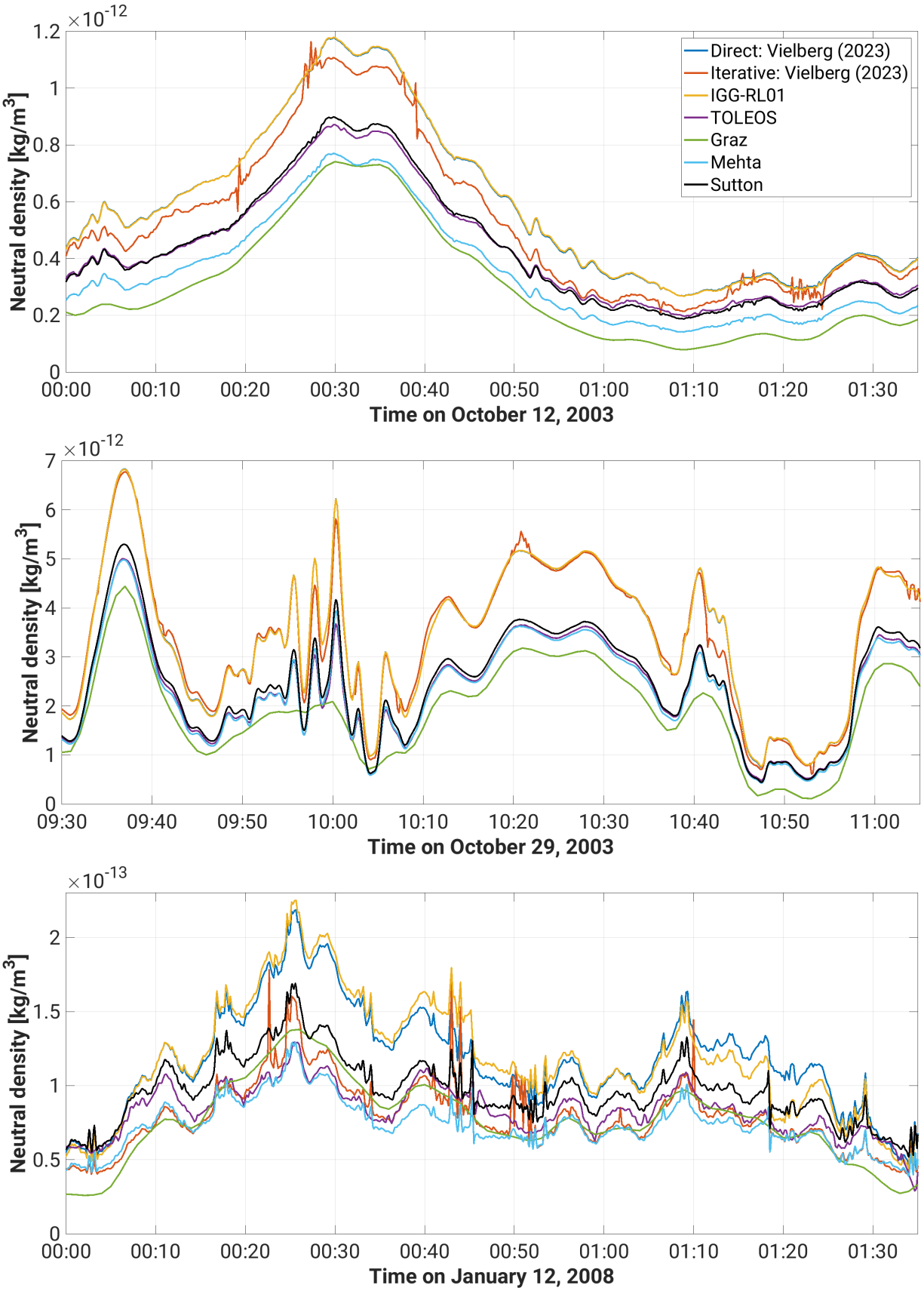



Figure 6.4: Neutral density processed by different institutions using GRACE-A accelerometer data. Three time series are exemplarily shown for approximately one orbital revolution during different solar and geomagnetic conditions. Top: October 12, 2003, high solar activity and quite geomagnetic conditions. Middle: October 29, 2003, high solar activity and severe geomagnetic storm. Bottom: January 12, 2008, low solar activity and quiet geomagnetic conditions. Time is given in GPS-time. An overview of the data sets is presented in Tab. 6.1.

be excluded from the cause of the density differences during October 12, 2003 in Fig. 6.4. Instead, differences in the aerodynamic modelling together with the high-fidelity satellite model and differences in the accelerometer calibration are most likely the reason for the varying neutral density estimates.

The second selected time period shows the neutral density also at high solar activity, however, during a severe geomagnetic storm. The so-called Halloween storm between 28-31 October, 2003, has been the strongest geomagnetic storm within this century so far, where the $Kp$ index reached the end of the scale with values of 9. Fig. 6.4 depicts the storm on October 29 between 9:30 h and 11:00 h. Here, the neutral density is about 10 times larger than during the previously analysed quite period with a maximum of nearly $7\times10^{-12}\,\mathrm{kg/m^3}$ at 9:37 h for the three data sets *direct*, *iterative* and *IGG-RL01*. Interestingly, the *direct* and *iterative* neutral density estimates show much smaller differences than during quite time, for which the reason remains unclear. Still, the variation between the data sets is large, e.g., the neutral density from *Graz* is only half the size of the *iterative* neutral density. As during the quite period, the neutral density estimates from *TOLEOS* and *Sutton* agree well with differences below 5 % and in addition the neutral density from *Mehta* fits the *TOLEOS* estimates nearly perfectly. Both *Mehta* and *TOLEOS* apply particle Monte Carlo simulations (Haghighat, 2020) on a high-fidelity macro-model to model the gas surface interaction. This innovative aerodynamic modelling in combination with the large drag signal to noise ratio during this period is most likely the reason for the good agreement between the data sets. Furthermore, the neutral density from *Graz* are the smallest during the Halloween storm. Due to the coarser temporal resolution of the *Graz* density, several peaks of the storm cannot be captured, which are visible in the remaining data sets.

In contrast to high solar activity, Fig. 6.4 (bottom) shows the neutral density during low solar activity on January 12, 2008, between 00:00 h and 1:35 h. First of all, it is noticeable that the neutral density is not only smaller with values below $2\times10^{-13}\,\mathrm{kg/m^3}$ but also less smooth. These small scale neutral density variations might be artefacts from the processing, since a small drag signal to noise ratio is disadvantageous to obtain good density estimates (e.g., Bruinsma et al., 2022). Similar to high solar activity, the largest neutral density results from the direct algorithm, which has been used in the *direct* and *IGG-RL01* data sets. However, the differences between both data sets of up to 5 % are larger than during high solar activity, since the neutral density is much more sensitive to changes in the radiation pressure modelling here. Changing the radiation pressure by 15 % leads to neutral density variations of 5 % here, thus, including the heat-diffusive thermal re-radiation within the *direct* data sets brings the neutral density closer to the remaining data sets. Interestingly, the *iterative* neutral density is now close to the solutions from *TOLEOS* and *Mehta*. Thus, detailed radiation pressure modelling seems much more beneficial than during low solar activity. At the same time, aerodynamic modelling has a smaller effect during this period also due to the large radiation pressure signal. Both *iterative* and *TOLEOS* data sets consider heat-diffusive thermal re-radiation.

In addition to the neutral density time series, where the analyses are limited to a 90-minute period, the data sets can be compared in terms of average density ratios for longer time periods. A density ratio is simply the neutral density from one data set divided by the neutral density of another data set averaged over a specific time span. For the three selected periods of different solar and geomagnetic conditions, Fig. 6.5 provides the density ratios of the data sets in terms of a matrix, where each entry results from dividing the neutral density from the data set assigned at the row by the one at the column. The density ratio shown here is the mean ratio during the three selected time spans. Generally, the density ratios vary between 0.6 and 1.8, which is quite a lot since one would expect that neutral densities obtained from the same measurement (here: accelerometer data) should be rather similar. During high solar activity and independent of the geomagnetic conditions, the largest agreement, i.e., density ratios of 1, can be found between both data sets using the direct algorithm (*direct* and *IGG-RL01*) as well as between *TOLEOS* and *Sutton*, even though their processing shows several differences (see Tab. 6.1). Good agreement is also found between *Mehta* and *Graz* with average density ratios of 0.97. The average density ratio between both *direct* and *IGG-RL01* w.r.t. the *iterative* solution is 0.93. The remaining average

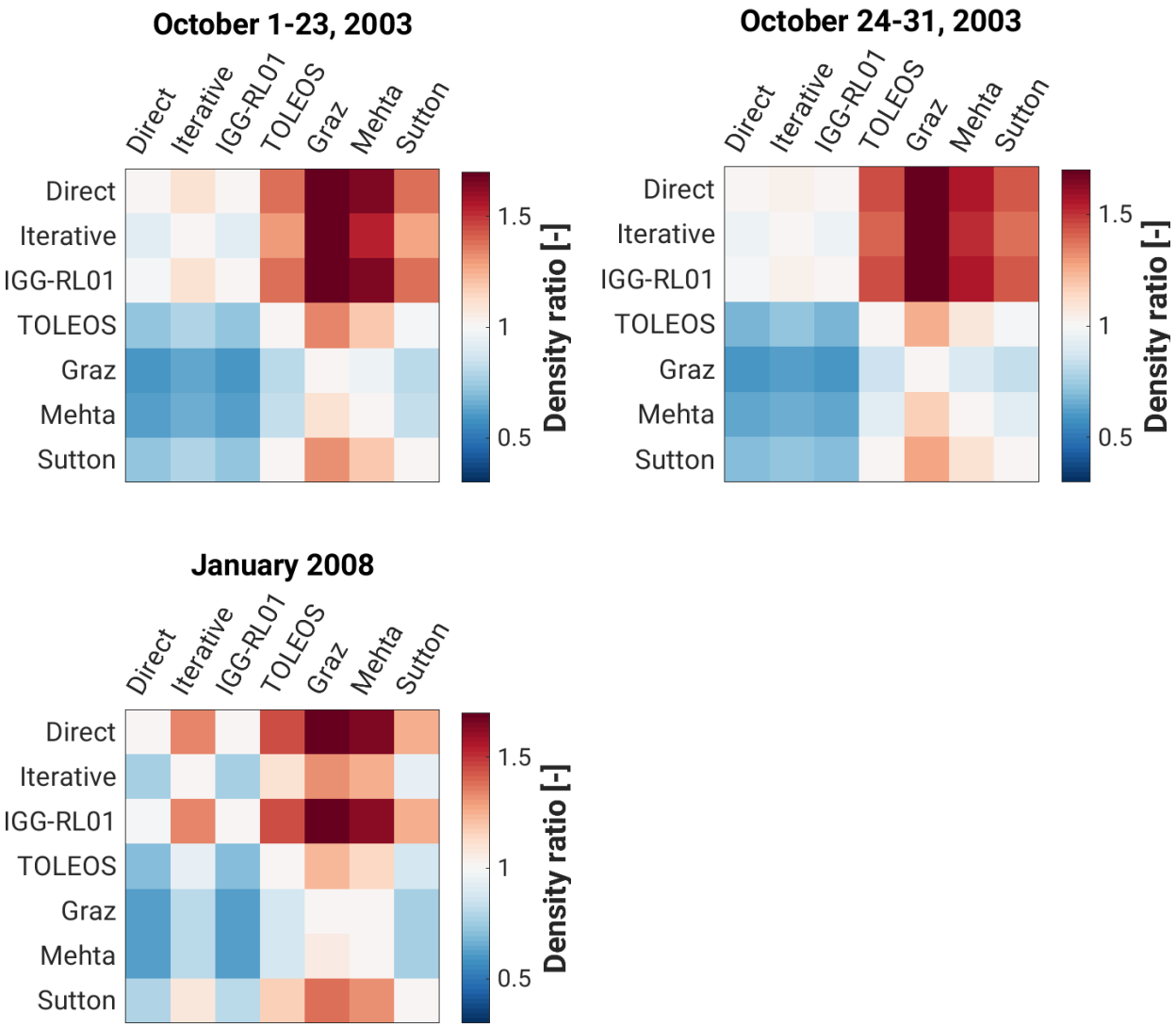



Figure 6.5: Ratios between neutral density data sets processed by different institutions using GRACE-A accelerometer data. The density ratios are averaged over the selected time period, which cover different solar and geomagnetic conditions. Top: October 1-23, 2003, high solar activity and quite geomagnetic conditions. Middle: October 24-29, 2003, high solar activity and severe geomagnetic storm. Bottom: January, 2008, low solar activity and quiet geomagnetic conditions. Each density ratio in the matrices is obtained from dividing the neutral density from the data set assigned at the row by the one assigned at the column. An overview of the data sets is presented in Tab. 6.1.

density ratios are above or below 1.1 and 0.9, respectively. The largest average density ratios of 1.82 occur between the *direct* data sets and *Graz*. This is related to the relatively small density from *Graz* (see also Fig. 6.4). Even though the algorithm is the same, the density ratios between *Graz* and *Sutton* as well as between *Graz* and the *iterative* data set are large with density ratios of 1.28 and 1.76, respectively.

During low solar activity, density ratios of 1 occur similarly between the *direct* and *IGG-RL01* data sets and additionally between *Mehta* and *Graz* densities. However, the density ratio between *TOLEOS* and *Sutton* decreased to 0.87. Instead, the *iterative* data set is now closest to *TOLEOS* and *Sutton* with density ratios of 0.94 and 1.08, respectively. As mentioned above, the radiation pressure modelling is highly relevant during low solar activity, thus it is not surprising that the

*iterative* and *TOLEOS* densities, which include heat-diffusive thermal re-radiation, agree well.

To conclude, the neutral densities derived from GRACE accelerometer measurements do not necessarily agree well. In terms of density ratios, values of 1.76 have been observed even though the processing algorithms agree (iterative density estimation, see Sect. 6.1.2). The reason for this is that the modelling details of the inverse estimation especially the aerodynamic modelling as well as the accelerometer calibration impact the density estimates directly independent of the solar and geomagnetic conditions. Additionally, during low solar activity, precise radiation pressure modelling is crucial. A good agreement (density ratios of 0.94) between the *iterative* densities and the *TOLEOS* data set has been observed during low solar activity.

The accelerometer-derived neutral density can be further used to scale the neutral density from empirical thermosphere models. The results are shown in Sect. 6.2.4.

## 6.2 Inverse estimation based on POD

Besides the accelerometer-derived in-situ neutral density, the neutral density can be obtained from a POD. Within a POD, precise models of the satellite dynamics, which include gravitational and non-gravitational force models, are fitted to accurate tracking measurements in an iterative procedure. Besides orbit-related parameters, it is possible to adjust parameters related to errors in the force modelling such as scale factors for the neutral density from models during a predefined time span. Consequently, the resulting neutral density scale factor is an integrated quantity, which can be used to scale the model density.

Such scale factors have already been derived in several studies, e.g., Doornbos et al. (2007); Panzetta et al. (2018); Zeitler et al. (2021). Doornbos et al. (2007) estimated scale factors from SLR tracking data of the ERS-2 satellite with a temporal resolution of 6 h to adjust the NRLMSISE-00 model. More recently, Panzetta et al. (2018) derived scale factors with the same resolution from SLR observations to the spherical ANDE-P satellite for four different empirical thermosphere models including NRLMSISE-00 and found that during the analysis period in 2009, where the solar activity was low, all models overestimate the neutral density. In Zeitler et al. (2021), scale factors for the neutral density from NRLMSISE-00 were derived from SLR range measurements of a variety of spherical satellites using two different software packages. Scale factors computed with GROOPS at IGG Bonn provided very similar results as the independent software package DOGS used at DGFI Munich. In addition, the accelerometer-derived scales from GRACE and CHAMP from IGG-RL01 (Vielberg et al., 2021) show correlations between 0.7 and 0.8 to SLR-derived scale factors after temporal averaging in Zeitler et al. (2021).

As already mentioned, a POD requires precise tracking measurements of the satellite's position. Within the validation of the non-gravitational force models in Ch. 5, scale factors for the neutral density from NRLMSIS 2.0 have already been co-estimated within a POD, where kinematic orbits were used in case of GRACE and SLR range measurements in the context of spherical satellites. However, the resulting scale factors were not further analysed since the focus was on the radiation pressure force model validation.

In this section, scale factors for the neutral density estimated within a POD using (1) SLR range measurements to spherical satellites and (2) kinematic orbits from GRACE are discussed. First, the parametrization is outlined in Sect. 6.2.1 before summarizing details of the conducted POD (Sect. 6.2.2). Before presenting the results, the comparability to scale factors from accelerometer data is discussed. Finally, scale factors for the NRLMSIS 2.0 obtained from both POD and accelerometer measurements are presented and compared in Sect. 6.2.4.

### 6.2.1 Parametrization

Within a POD various parameters are estimated depending on the used tracking data. In case SLR range measurements to spherical satellites are used as observations, the initial state and the station coordinates need to be estimated besides monthly range biases to compensate station- and satellite-related systematics (see also Tab. 5.8). Additionally, a scale factor for the modelled

radiation pressure acceleration is commonly co-estimated to absorb possible mismodelling especially due to the TRP (see also Sect. 5.2.1). The radiation pressure scale factor is estimated monthly for every satellite in this thesis. In addition, a scale factor of the modelled aerodynamic acceleration is introduced, which is usually interpreted as a correction for the neutral density from a model (here: NRLMSIS 2.0) required for the aerodynamic force modelling. Nevertheless, the scale factor also absorbs the mismodelling of the gas-surface interaction, which includes the area projected in flight direction, the satellite's mass, the satellite's relative velocity and the aerodynamic coefficient, of which the latter is the most critical one.

In this experiment, the aerodynamic scale factor is estimated daily for every selected spherical satellite. A lower temporal resolution would be beneficial to capture higher frequency variations of the thermosphere. Resolutions of up to six hours have been used in Panzetta et al. (2018), however, the variation of the estimated scale factors is relatively high and only a limited number of parameters can be estimated since observations are quite sparse. Thus, a daily resolution is chosen in this thesis. Empirical accelerations to parametrize the mismodelling of non-gravitational accelerations are not used here. The selection of remaining parameters varies with the purpose of the analysis. For example, Löcher and Kusche (2021) include the estimation of monthly gravity field coefficients. Bloßfeld et al. (2018) estimate gravity field coefficients together with Earth rotation parameters. Since such parameters are not of interest for this thesis, they are not co-estimated. An overview of the parameters estimated here together with their temporal resolution can be found in Tab. 5.8. The LAGEOS satellites are excluded from the analyses, since their orbital altitude of more than 5000 km is too high to detect sufficient aerodynamic signals.

In case of using kinematic orbits as observations within a POD, the parametrization is different. Again GRACE-A is selected for further analyses, however, this procedure is also suitable for other satellites. When validating the radiation pressure force models for GRACE in Sect. 5.1.5, daily initial states and hourly aerodynamic scale factors have been estimated. In this experiment, the same parametrization is applied. Consequently, the temporal resolution of the aerodynamic scale factor is much higher compared to SLR, where daily aerodynamic scale factors are estimated. Similar to SLR, the aerodynamic scale factor does not only reflect the mismodelled neutral density, since deficiencies in the gas-surface interaction modelling and cross-wind speeds are absorbed. Cross-winds are relevant at GRACE altitude as they reach up to several 100 m/s. With higher altitudes the effect decreases. Even though it would be beneficial to include a scale factor for the cross-wind velocities in the POD this appears challenging since errors in the neutral density, the gas surface interaction model and the wind speed are hardly separable.

Instead of estimating an aerodynamic scale factor, which is valid globally, a representation in terms of spherical harmonics would be beneficial to obtain a higher spatial resolution. However, the temporal resolution is already too sparse to realize such parametrization within a POD.

Independent of the choice of the observables, the selection of parameters as well as their temporal resolution can impact the estimates. This cannot be avoided and should be kept in mind when interpreting the results. In this thesis, the choice of the parameters relies on the experience from colleagues and mentioned literature. These aspects indicate once more that a joint estimation especially in case of GRACE should be investigated in the future.

### 6.2.2 Algorithm

The POD is an iterative procedure, where orbit parameters are adjusted to minimize the residuals. The POD based on SLR observations has been explained and applied in the context of the force model validation for spherical satellites, thus, please see Sect. 5.2.4 for details. The only difference is that the radiation pressure force model is kept fixed in this experiment. Since the validation in Sect. 5.2.4 did not clearly reveal which force model is the best choice, I apply the most advanced force model for spherical satellites: SRP model 1100 considering a physical shadow model and daily values of the TSI in combination with ERP model 1310, which accounts for outgoing fluxes from CERES SYN1deg on a 1° grid with ADMs. The aerodynamic model is the same as in Sect. 5.2.4 and considers the neutral density from NRLMSIS 2.0. The TRP acceleration is not modelled analytically. Instead a radiation pressure scale factor is included in the parametrization

(see Tab. 5.8). In addition, gravitational background models from Tab. 3.2 are applied. Generally, the method applied here is the same method as in Zeitler et al. (2021) with slightly different settings.

In case of GRACE, the POD has already been applied for the radiation pressure force model validation in Sect. 5.1.5. Here the same gravitational background models are applied as in the POD for spherical satellites. The non-gravitational force model applied here is the one, which yielded the smallest RMS in the validation with SLR observations (see Sect. 5.1.5): SRP model 11000 using daily TSI and a physical shadow function in combination with the ERP model 13100 using outgoing fluxes from hourly CERES SYN1deg data on a 1° grid with ADMs and the heat-conductive TRP model with fitted thermal diffusivity. Radiation pressure scale factors are not co-estimated. The aerodynamic model is the same as above. Consequently, scale factors for the NRLMSIS 2.0 are estimated.

### 6.2.3 Comparability to accelerometer-based results in terms of scale factors

Before presenting the results of the estimated scale factors, the comparability of POD-based and accelerometer-based scale factors is discussed. As already mentioned above, the estimated aerodynamic scale factors from both POD or accelerometer data are usually treated as thermospheric neutral density correction (e.g., Vielberg et al., 2018; Zeitler et al., 2021; Bruinsma et al., 2022), although they are strictly speaking a scale factor for the total modelled aerodynamic acceleration. The scale factors also depend on the selected force modelling as briefly shown in Sect. 5.1.5.

For POD-based scale factors from both SLR and GRACE, the applied gravitational force models are the same. Within the accelerometer-based approach, such gravitational force models are not required since the accelerometer only measures non-gravitational accelerations.

The non-gravitational force modelling for GRACE is the same for both the POD-based and accelerometer-based approach. For spherical satellites, the non-gravitational force modelling is generally different (see Sect. 5.2.1). However, the non-gravitational force models applied here are chosen to match the GRACE force modelling as closely as possible. Thus, the ERP and SRP models consider the same shadow function and radiation data. Only the TRP modelling for spherical satellites is neglected as already mentioned before.

Besides the force modelling, there are differences in the temporal resolution of POD and accelerometer-derived scale factors. The POD-based scale factors are integrated quantities, i.e., the temporal resolution is limited. In case of SLR satellites, the aerodynamic scale factor is estimated daily. The POD-based aerodynamic scale factor for GRACE has a temporal resolution of 1h. The reason for these differences is the chosen parametrization, which should be carefully selected in a POD to avoid high correlations between the parameters (see Sect. 6.2.1). In contrast, the accelerometer-based scale factors are based on in-situ neutral densities, which have a higher temporal resolution of here 10 s. In order to compare the scale factors from both POD and accelerometer data, temporally averaging of accelerometer-based scale factors is helpful.

### 6.2.4 Comparison of scale factors

Figure 6.6 shows the aerodynamic scale factors for the NRLMSIS 2.0 derived from different methods during the lifetime of the GRACE mission (August 2002 - June 2017). From a POD, scale factors for the spherical satellites Larets, Stella, Starlette and Ajisai are presented, which are filtered with a 10-day moving average to reduce the noise. In addition, scale factors for GRACE-A are estimated within a POD at a 1h resolution. Since for GRACE-A, accelerometer-derived neutral densities are available, scale factors for the NRLMSIS 2.0 are derived from TOLEOS neutral densities as well as from neutral densities computed within this thesis from both the direct and iterative algorithm. For better comparability, the results for GRACE from both POD and accelerometer are averaged over one day before applying a 10-day moving average. For better visibility, the resulting time series are shifted by +1. A similar figure has been presented in Zeitler et al. (2021) for scale factors of the NRLMSISE-00. The recent TLE2021 data set (Emmert et al., 2021) is not included here as it shows the scale factors for NRLMSISE-00 instead of NRLMSIS 2.0 even though a comparison to data from a large data base would be interesting.

Beginning with the scale factors from the spherical satellites, the results of Larets, Stella and Starlette agree very well. During solar maximum in 2003, the scale factors are quite large with values up to 1.7, i.e., the model strongly underestimates the neutral density. With decreasing solar activity, the scale factors show less variations and are close to one especially during 2006 and 2007. During solar minimum in 2008, scale factors are slightly below one, i.e., the model slightly overestimates the neutral density. This overestimation is slightly larger for Larets and Stella than for Starlette, which is likely related to the elliptical orbit of the Starlette leading to larger variations in the scale factor. From 2010 onwards, the scale factors increase until the solar maximum in 2015, where scale factors of 1.9 are reached. Generally, the scale factors of these three spherical satellites agree well independent of the solar conditions. The Pearson correlation coefficient between the scale factors of Larets and Stella reach 0.89, whereas the correlations of scale factors from Larets and Stella w.r.t. Starlette are smaller with 0.71 and 0.77, respectively.

For Ajisai, the time series of the scale factors looks very different especially during low solar activity. This is most likely related to the high altitude of Ajisai of 1500 km and its large area to mass ratio. Since the NRLMSIS 2.0 model is designed to evaluate the neutral density until the exobase (Emmert et al., 2020), the altitude of Ajisai might be too high to produce reliable outputs. During high solar activity the satellite experiences a relatively large aerodynamic signal and the scale factors usually fit well to the results from Larets, Stella and Starlette except during the strong oscillations of the scale factor of Ajisai beginning in March every year. The reason for this oscillation is not clear. As the solar activity decreases, the scale factor of Ajisai varies between 0.4 and 2.4 and does not fit the other scale factors at all. This is likely related to the satellite altitude. Since the neutral density is generally much smaller during these periods, the upper boundary of the thermosphere decreases. Consequently, it is questionable, if the scale factor at 1500 km altitude can still be interpreted as a neutral density correction at the altitude of Ajisai during solar minimum. Moreover, the large area to mass ratio might matter.

Fig. 6.6 additionally presents the scale factors for GRACE (1) from POD and (2) from accelerometer data. For the latter, the neutral densities from TOLEOS as well as the neutral densities from both the direct and iterative algorithm processed within this thesis are used to compute scale factors for the NRLMSIS 2.0 neutral density. The gaps in the resulting time series are usually due to missing accelerometer data and partly due to mission star camera or orbit data. Besides these gaps, the scale factors from POD and accelerometer have in common that they both follow the course of the solar cycle. The TOLEOS-based scale factors fit the POD-based scale factors nicely especially until 2011, where the quality of the accelerometer data started decreasing. Before 2011, the correlation between TOLEOS and POD scale factors is large with 0.91. The overall correlation is 0.80. The accelerometer-based scale factors from the direct and iterative approaches show a good agreement among themselves (correlation coefficient of 0.89). Especially the scale factor time series from the iterative density estimation is more noisy and contains a few outliers, which is likely related to the estimation procedure in combination with the accelerometer calibration. The accelerometer calibration as well as the force modelling are the reason for the differences between the scale factors from this thesis and TOLEOS. Since their accelerometer calibration is constrained to the along-track axis, the resulting density and also the scale factors are smoother.

Interestingly, the scale factors for GRACE are generally smaller than for the spherical satellites. During low solar activity, the scale factors obtained from GRACE are well below 1 with values around 0.7. This underestimation of the density is independent of the applied method. Thus, it is likely related to the low satellite altitude, i.e., at higher altitudes the density fits the observations better during solar minimum. In contrast, the scale factors during high solar activity are generally larger for the satellites at high altitudes than for GRACE. Consequently, the variation of the scale factor is nearly the same independent of the altitude, however, an altitude-dependent bias can be observed between the scale factor time series from SLR and GRACE.

In summary, the scale factors obtained from POD and accelerometry agree well (correlation of up to 0.9). POD-based scale factors cannot only be obtained for spherical satellites, but also for satellites with a panel model. Since this requires accurate force models instead of calibrated accelerometer measurements, the POD-derived scale factors show generally less outliers. Differences

in the accelerometer-based estimates can be explained by differently calibrated accelerations and the use of different non-gravitational force modelling. Consequently, the aerodynamic scale factors are not independent of the chosen force model. Generally, NRLMSIS 2.0 overestimates the neutral density during solar minimum and overestimations are likely during high solar activity, which was also found by Doornbos (2012); Zeitler et al. (2021) or Bruinsma et al. (2022). Finally, an altitude-dependency of the scale factor can be observed leading to increased overestimations of the neutral density at GRACE-altitude.

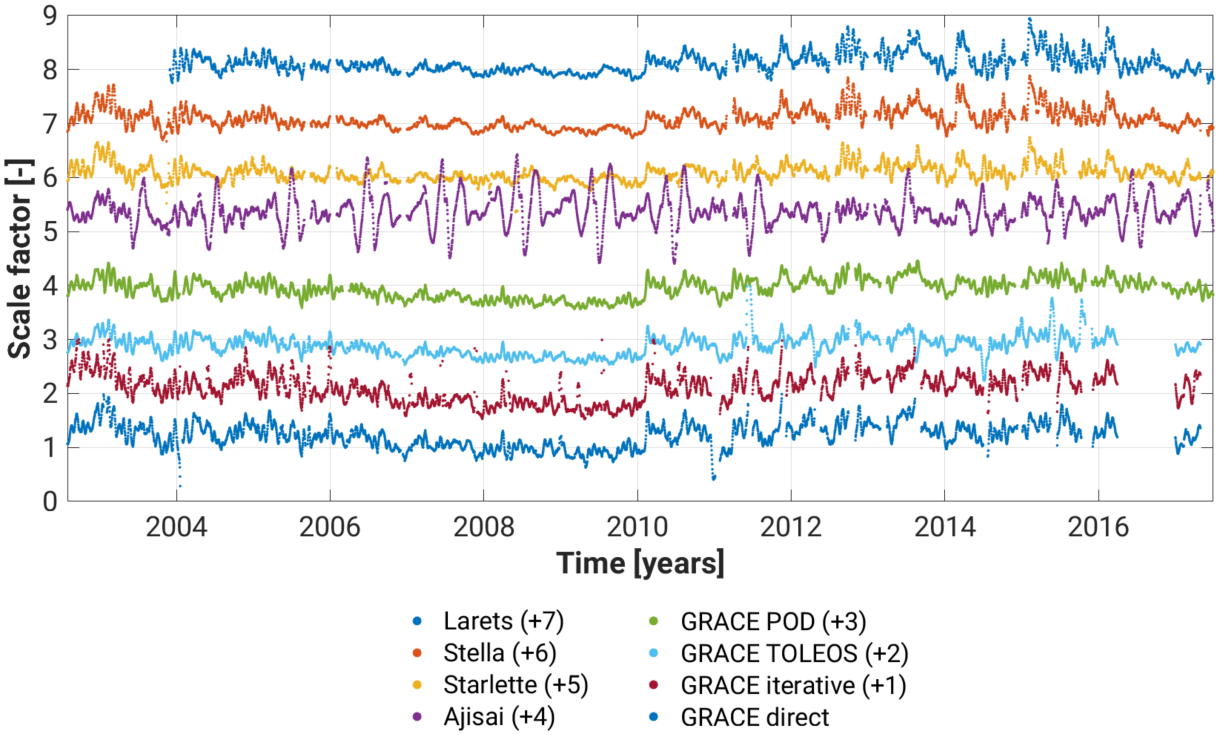



Figure 6.6: Scale factors for the neutral density from NRLMSIS 2.0 during the lifetime of the GRACE mission. The scale factors are derived from three different methods and filtered with a 10-day moving average filter. For the spherical satellites Larets, Starlette, Stella and Ajisai, the scale factors are coestimated within a POD. The GRACE-POD solution shows the scale factors obtained from a POD with kinematic orbits as observations. The three remaining time series are derived from the neutral density from GRACE accelerometer data by dividing these by the NRLMSIS 2.0 neutral density before averaging the resulting scale factors for each day and applying the same 10-day moving average filter as for the remaining time series. Gaps in the time series occur due to missing orbit, star camera and/or accelerometer data. Please note that the time series are shifted by +1 for better visibility.

# Chapter 7

# Inverse estimation: Earth's energy imbalance

A second application of the inverse estimation in the context of non-gravitational force modelling is the estimation of radiation-related parameters. Remaining biases in radiation data sets and the satellite's material introduce systematic errors in the radiation pressure force models. This chapter aims to reduce these errors by solving for corrections of the radiation-related data sets.

As for the neutral density estimation, this inverse estimation is tested for GRACE first by considering modelled and measured non-gravitational accelerations and attempting to solve for selected parameters to correct the radiation data sets and the satellite's material. In the second part of this chapter, scale factors for the radiation pressure force models are estimated within a POD. Their interpretation as a correction for radiation data sets is outlined and the comparability to the results from GRACE is discussed afterwards. In this context, attempts to link estimated radiation-related parameters to EEI are made.

## 7.1 Inverse estimation based on accelerometer data

Relating accelerometer measurements to EEI has already been investigated in earlier studies. During the 1970s, measurements from the CACTUS accelerometer on-board the almost spherical CASTOR satellite have been successfully used to obtain an annual mean Earth radiation budget in Boudon (1986). This concept is based on the conversion from non-gravitational accelerations to fluxes and requires accelerometer measurements on-board a (nearly) spherical satellite. More recently, the method has been taken up again by Hakuba et al. (2018), who propose a spherical satellite mission with an improved accelerometer and a highly reflective or perfectly absorbing surface, in order to contribute to accurate EEI estimates.

The first attempt to estimate radiation-related parameters from accelerometer data of a non-spherical satellite has been performed in Vielberg and Kusche (2020), where extended solar and Earth radiation pressure force models are used in an inverse approach. Various combinations of possible systematic errors have been evaluated in terms of rank deficiency and condition numbers. It turned out that the estimability depends more on the parametrization of the radiation source-related parameters than on the material-related parameters. The parametrization with the smallest condition number has been selected for the inverse estimation. Consequently, corrections for material coefficients and CERES fluxes over land and ocean have been estimated using one year of GRACE-A accelerometer measurements. Correlation analysis of the estimated parameters revealed a strong correlation (57 %) of nadir visible material coefficients and the Earth's outgoing shortwave radiation. The results were encouraging that certain physical radiation pressure model parameters could indeed be determined from satellite accelerometry. This section is basically an extension of the study from Vielberg and Kusche (2020).

### 7.1.1 Parametrization

Similar to the neutral density estimation, the inverse estimation here is based on modelled and measured accelerometer measurements. Within the radiation pressure force modelling, several parameters are related to the radiation reaching the satellite. These include the incoming solar radiation, the Earth's outgoing shortwave and longwave radiation together with the ADMs, and the satellite's thermo-optical material properties.

The solar radiation varies less than 0.3 % over the course of the solar cycle and is generally well known with an uncertainty of $0.13\,\mathrm{W/m^2}$. Thus, estimating a correction for TSI is not aimed here. However, the outgoing radiation of the Earth, which is taken from CERES in the ERP and TRP modelling, contain biases (see Sect. 2.3.4) limiting the accuracy of the important climate variable EEI to quantify global warming. Thus, there is a need to adequately correct the remaining biases in the utilized CERES data. Additionally, the thermo-optical material properties are not well known, which impacts the SRP, ERP and TRP force modelling. Thus, further improving the precise non-gravitational force models requires the correction of such parameters.

The observation equation (see Eq. (6.1.2))

$$\boldsymbol{a}_{\mathrm{cal}} = \boldsymbol{a}_{\mathrm{aero}} + \boldsymbol{a}_{\mathrm{RP}} + \boldsymbol{a}_{\mathrm{sat}} + \epsilon$$

relates the calibrated non-gravitational accelerometer measurements to the radiation pressure force model. For the neutral density estimation, a stable along-track calibration of the accelerometer is required, whereas the inverse estimation of parameters related to Earth radiation data sets requires a stable radial component.

Even though a joint estimation of calibration parameters and radiation-related parameters would be desirable, the effort of finding such stable parametrization is not expended in this thesis. Instead an iterative stepwise procedure is performed, i.e., the accelerometer is calibrated first and the estimation of radiation-related parameters is performed afterwards.

There are multiple options to parametrize the estimation of radiation-related parameters. Since radiation data sets as well as thermo-optical material properties already exist even though with limited accuracy, it makes sense to estimate corrections for these data, e.g., in terms of scale factors or biases. For the correction of the CERES fluxes, a separation between longwave and shortwave fluxes is suggested. Due to the long-term difference between the CERES SYN1deg and EBAF data of $1.5\,\mathrm{W/m^2}$ for the longwave and $2\,\mathrm{W/m^2}$ for the shortwave fluxes (Loeb et al., 2018), the shortwave correction is expected to be larger. This is in line with the findings from the calibration between CERES and other radiometer missions (Qiu et al., 2012), where biases in short-wave fluxes were found to be generally larger. Considering the magnitude of the fluxes, which is more than twice as large for longwave than for shortwave fluxes with $239\,\mathrm{W/m^2}$ and $100\,\mathrm{W/m^2}$, respectively, according to the global annual mean from Wild et al. (2015), estimating a correction for the shortwave fluxes appears more promising.

The most simple parametrization of CERES corrections is a global scale factor. The temporal resolution of such scale factors should be long enough to ensure a global coverage of the satellite accelerometer data, e.g., annual or monthly. As depicted in Fig. 2.9, the differences between CERES SYN1deg and EBAF shortwave data differ between land and ocean such that the estimation of a separate scale factor for each area is desirable. This has also been part of the parametrization with the smallest condition number in Vielberg and Kusche (2020). An even finer spatial resolution according to different surface and cloud conditions would enable to solve for errors in the ADMs. However, this would increase the number of parameters drastically such that this is not considered in this experiment. A parametrization of CERES corrections in terms of a spherical harmonic representation turned out to be too complex as well (Vielberg and Kusche, 2020). Moreover, a separate scale factor for the polar regions above 60° and the equatorial regions is expected to be beneficial, since the difference between shortwave CERES SYN1deg and EBAF data are especially large in the polar regions.

In Vielberg and Kusche (2020), different parametrizations of a correction for the thermo-optical material properties have been tested. The estimation of biases turned out to be more suitable than the estimation of time-dependent as well as angular-dependent corrections.

When estimating biases for the thermo-optical properties together with scale factors of radiation fluxes, the separability of these corrections needs to be guaranteed. Vielberg and Kusche (2020) found a correlation of 57 % between errors of the visible material coefficient of the nadir panel and the Earth's outgoing shortwave radiation. Such correlations cannot be avoided, but constraining the thermo-optical material coefficients of similar panels might stabilize the parametrization.

In order to avoid that errors in the mismodelling of the remaining non-gravitational forces are absorbed in the corrections for the CERES data or thermo-optical material coefficients, Vielberg and Kusche (2020) estimated an additional scale factor. Alternatively, the aerodynamic scale factors interpreted as neutral density correction from the previous chapter can be applied beforehand to minimize the error of the aerodynamic model.

### 7.1.2 Algorithm

The estimation of selected radiation-related parameters is performed within a least squares adjustment. The observation equation relates the calibrated accelerometer measurement to modelled non-gravitational accelerations. Depending on the parametrization, the observation equation varies slightly. In Vielberg and Kusche, 2020, we focussed on the estimation of thermo-optical properties, which occur in the solar and Earth radiation pressure accelerations, as well as corrections for the Earth's outgoing radiation. Thus, the observation equation $l$ contains the observed radiation pressure acceleration resulting from the subtraction of the modelled aerodynamic acceleration $\boldsymbol{a}_{\text{aero}}$ from calibrated accelerometer measurements $\boldsymbol{a}_{\text{cal}}$

$$l = \boldsymbol{a}_{\text{cal}} - \boldsymbol{a}_{\text{aero}}. \tag{7.1.1}$$

The calibration commonly considers biases and scale factors, which need to be estimated beforehand. To avoid the impact of satellite-induced accelerations, the thruster firings are eliminated from the calibrated accelerometer measurements as in Vielberg and Kusche (2020).

Then, the derivatives of the analytical formulations of the SRP and ERP accelerations with respect to the parameters are computed to construct the design matrix. Here, the derivatives are obtained analytically and are provided in App. C.

Ideally, the uncertainty of the calibrated accelerometer measurements and the modelled non-gravitational forces would be considered in inverse estimation by building a realistic variance-covariance matrix. However, finding a suitable weighting is difficult. Weighting the data based on the measurement accuracy of the accelerometer would lead to an extreme down-weighting of the cross-track acceleration making the system of equations unstable. Further considering possible errors introduced with the accelerometer calibration appears challenging. Additionally, the uncertainty of modelled forces should be considered when building a realistic variance-covariance matrix. This requires a variance propagation of the force modelling, which is not performed in this thesis. Thus, similar to Vielberg and Kusche (2020) equal weighting is assumed here, which should be revised in the future.

In the next step, the normal equation matrix can be computed. Optionally, constraints between specific parameters can be considered by extending the normal equation matrix with restrictions, e.g., corrections for the thermo-optical material coefficients of the front and rear panel should be equal. Moreover, the relation that the reflection and absorption coefficients should sum up to one could be added as a constrain. Finally, the parameters are obtained from the least squares adjustment. For details on the least squares adjustment please see Niemeier (2008).

Variations of this algorithm are generally possible. In this thesis, the algorithm is extended by additionally considering the thermal re-radiation pressure. Since the thermal diffusivity has been adjusted beforehand (see Sect. 5.1.5), the derivation of TRP acceleration w.r.t. the radiation-related parameters is omitted here. Instead, the fitted TRP acceleration $\boldsymbol{a}_{\text{TRP}}$ is considered within the observation equation

$$l = \boldsymbol{a}_{\text{cal}} - \boldsymbol{a}_{\text{aero}} - \boldsymbol{a}_{\text{TRP}}. \tag{7.1.2}$$

Instead, of using the data along all three axes, the adjustment of the radial direction only is expected to be beneficial for the adjustment of Earth radiation data sets.

### 7.1.3 Results

From the differences in the CERES SYN1deg and EBAF data, average biases of $1.5\,\mathrm{W/m^2}$ and $2\,\mathrm{W/m^2}$ in the longwave and shortwave fluxes, respectively, are known (Loeb et al., 2018). Thus, when aiming to correct CERES SYN1deg data within the inverse estimation, biases of at least $1\,\mathrm{W/m^2}$ need to be detected. For the GRACE-A satellite, the impact of $1\,\mathrm{W/m^2}$ changes in the Earth's outgoing radiation data on the acceleration is tested for January 2008. The visible ERP acceleration shows the largest changes of 0.8 %. In comparison, the infrared ERP acceleration changes only 0.5 %, since the longwave flux is generally larger than the shortwave flux. The total ERP acceleration changes by 0.6 %, when adding $1\,\mathrm{W/m^2}$ on both longwave and shortwave fluxes. Finally, the impact on the total non-gravitational acceleration is slightly below 0.1 %.

Detecting such small changes within a least squares adjustment using modelled and measured non-gravitational accelerations appears challenging. Thus, well-calibrated accelerometer measurements are essential. Since errors in the CERES data are expected to have a particular effect on the radial acceleration, a precisely calibrated radial accelerometer measurement is required. However, the inspection of the radial accelerometer biases from the calibration presented in Sect. 3.1.5, reveals that the radial biases contain systematics. The systematic oscillation has a period of about four months and its magnitude varies with the solar activity. Calibrating the accelerometer data using these radial biases would introduce artificial trends in the radial measurements, which complicates the estimation of radiation-related parameters.

To overcome the systematics in the radial biases, the calibration needs to be modified. In the following, I aim to assess how a stable radial accelerometer calibration can be reached.

In the validation of the forward force modelling for GRACE (Sect. 5.1.5), it turned out that increasing the temporal resolution of the estimated biases reduces the SLR residuals. Inspecting the estimated biases (not shown here) from this procedure revealed that the systematics in the radial component are eliminated and only noise remains. Therefore, hourly biases are estimated for the whole mission lifetime with the same procedure and the resulting biases are presented in Fig. 7.1 in red. The noise in along-track and radial biases is generally larger than in the previous calibration (Fig. 3.5). However, with increasing temporal resolution of the biases the systematic oscillations in the radial direction vanished. The reason for this is not clear at the moment. I suspect that temporal aliasing can play a role here, however, this has not been reported before in the context of accelerometer calibration and, thus, further analyses are required in the future. It should be mentioned that the calibration here does not consider a scale factor. For better comparability with the previous calibration, the biases estimated with the assumption of constant scale factors (along-track 0.94, cross-track 0.91, radial 0.93) are also shown in Fig. 7.1 in blue. The noise in the biases from this solution is slightly larger in the along-track and radial directions, which are known to be correlated. Interestingly, additional offsets between the two bias solutions can be observed in all directions. Even though this offset is smallest in the radial direction, it reaches an average value of $0.5 \times 10^{-7}\,\mathrm{m/s^2}$, which is nearly 10 % of the bias itself. Consequently, this offset maps onto the calibrated accelerations.

A comparison of the calibrated accelerations between 5-8 a.m. on January 1, 2008, is presented in Fig. 7.2. Besides the accelerations calibrated with hourly biases, the previous solution from the three-step procedure resulting in daily biases and constant scales (Sect. 3.1.5) is shown and assigned as *Uni Bonn*. For comparison, the calibrated acceleration from *TU Delft* (Siemes et al., 2023) is also presented, where daily biases and constant scales have also been obtained from such three-step procedure. The advantage of the three-step procedure is that the along-track and cross-track directions are well calibrated, which is important for the estimation of thermospheric densities. To improve the along-track component for this purpose, Siemes et al. (2023) make use of the correlation between along-track and radial biases by constraining the radial biases. This constrain led to nearly smooth radial biases of around $0.5 \times 10^{-6}\,\mathrm{m/s^2}$ (see Fig. 5 therein). With this constrain and the consideration of a temperature correction, the *TU Delft* calibration differs from the *Uni Bonn* solution.

Comparing the resulting calibrated radial accelerations to the modelled ones shows that the calibrated accelerations from *TU Delft* fit the modelled accelerations very well, whereas the re-

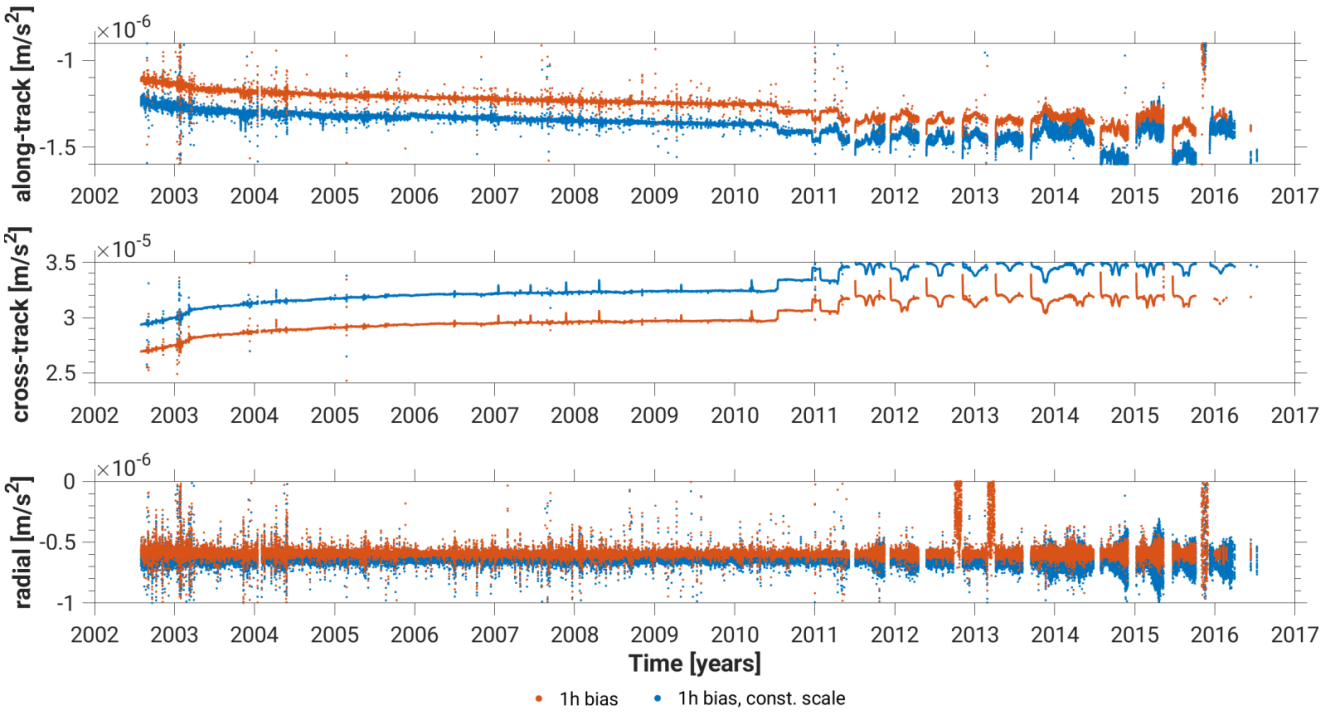



Figure 7.1: Hourly accelerometer biases in the along-track, cross-track and radial directions for GRACE-A estimated within a POD for the lifetime of the mission. Red: Scale factors are not considered in this parametrization. Blue: For better comparability with the calibration in Sect. 3.1.5, the estimation of hourly biases is repeated with the same constant scale factors of 0.94 (along-track), 0.91 (cross-track) and 0.93 (radial).

maining solutions show biases of more than 40 nm/s$^2$. Even though my own calibration does not consider a temperature correction, the differences cannot be assigned to this consideration only as they are at the order of $-6 \times 10^{-9}$ m/s$^2$ for the radial component. Wöske (2020) observed remaining biases between modelled and calibrated accelerations from a POD as well. He explains this in terms of orbit mechanics, as the radial acceleration has a smaller effect on the orbital energy than the along-track acceleration, which makes the determination of radial biases more difficult. To overcome remaining radial biases after the POD-base calibration, Wöske (2020) performs a second calibration by adjusting the (pre)calibrated to modelled accelerations. Nevertheless, it is remains unclear, why the calibration from *TU Delft*, which is also based on a POD does not show such biases during the selected period.

As already mentioned, the disadvantage of the three-step approach with this parametrization are the remaining systematics in the radial biases. Applying constraints is one option to avoid such systematics.

Another aspect that should be discussed is the suitability of the calibrated accelerations for a POD. Applying the accelerations calibrated with the biases from the three-step procedure within a POD turned out to lead to large residuals of on average above 4 cm during 2008 (Sect. 5.1.5). In contrast, applying accelerations calibrated with hourly biases within a POD yields average residuals of only 1.85 cm during the same period. However, the calibrated accelerations with hourly biases still contain a bias w.r.t. modelled accelerations as discussed above.

To conclude, the calibration of the accelerometer measurements still has some inconsistencies. In terms of residuals from one year POD, hourly biases yield the best calibration and systematic oscillations in the radial biases can be avoided. However, a calibration leading to small residuals within a POD does not necessarily fit the modelled radial accelerations well. Such remaining biases might be corrected by adjusting the calibrated to modelled accelerations. On the other hand, applying the biases from a three-step procedure yields larger residuals in a POD. At the

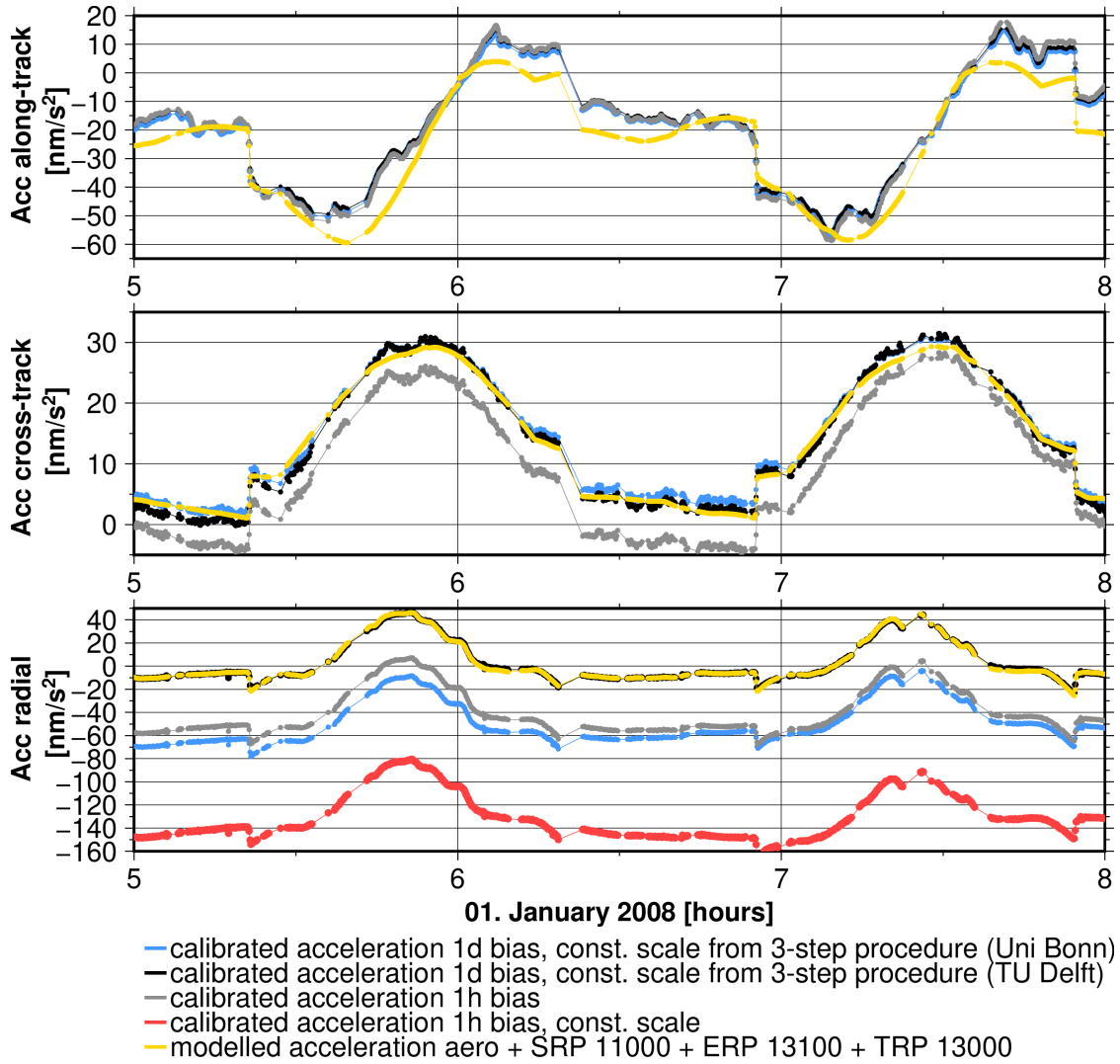



Figure 7.2: Differently calibrated accelerations in the along-track, cross-track and radial directions for GRACE-A in the SRF during 3 hours (5-8 a.m.) on January 1, 2008. The solutions in blue and black have been obtained within a three-step procedure at *Uni Bonn* (Vielberg et al., 2018) and *TU Delft* (Siemes et al., 2023), respectively, and have already been applied in the thermospheric density estimation. Grey and red shows the accelerations calibrated with hourly biases directly within a POD without scale factor and with the same constant scale factor as in the *Uni Bonn* variant, respectively. The calibrated accelerations with hourly bias and constant scale factor are only shown in the radial direction, since the offset in the other directions is too large. For comparability, the acceleration from the best model according to the validation with SLR is shown as well.

same time, well-calibrated along-track accelerations can be obtained, but systematics in the radial biases remain. Constraints allow to obtain smooth radial biases. Further experiments are required to sort the effect of remaining biases in the radial component to the method of calibration, the parametrization, the constraints and the temperature correction.

Consequently, the aim of obtaining perfectly calibrated accelerations, especially in the radial component cannot be reached at the moment. The problem is not necessarily the accuracy of the accelerometer, but the inconsistencies of the accelerometer calibration. Further effort is required, to overcome such inconsistencies in the calibration and to clear up the question, whether differently calibrated accelerometer data should exist for different applications.

Besides well-calibrated accelerometer measurements, precise non-gravitational force models are

essential for the success of the inverse estimation. Since the aerodynamic model applied in this thesis is rather conservative, scale factors from the previous chapter are considered. Here, I apply the aerodynamic scale factor from the POD because it accounts - strictly speaking - not only for a density correction, but for the total aerodynamic mismodelling. The 10-day averaged scale factor is interpolated to fit the temporal resolution of the accelerometer measurements of 10 s. Furthermore, the best radiation pressure force model in terms of SLR residuals is selected here.

Radiation pressure model parameters are estimated within a least squares adjustment using data from GRACE-A. Instead of employing the year 2010 as in Vielberg and Kusche (2020), the year 2008 is selected here due to the low aerodynamic signal. For this experiment, the calibration parameters from the POD with hourly biases are applied. To avoid the impact of thruster firings, data 30 s before and after each thrust are not considered. As discussed above, equal weighting is assumed here.

According to the condition number of the parametrization, Vielberg and Kusche (2020) found that the best-conditioned parametrization accounts for scale factors for the radiation pressure accelerations in the three directions, biases for the specular visible material coefficients, and multiplicative corrections for longwave and shortwave flux over land and over ocean. In addition, an error in the derivative w.r.t. longwave fluxes has been corrected. The same parametrization is used here and the least squares adjustment is performed using the calibrated and modelled forces described above. The condition number of this parametrization is $4.5\times10^{-5}$. The resulting parameters and their formal errors are presented in the left Tab. 7.1. Generally, the estimated parameters are

Table 7.1: Estimated unit-less radiation-related parameters and their formal errors. Accelerometer data calibrated with hourly biases from POD are used as well as the best force model in terms of SLR residuals. Left: The same parametrization as in Vielberg and Kusche (2020) is applied including scale factors $S$ for each direction, multiplicative corrections of the CERES SYN1deg shortwave and longwave fluxes over ocean and over land, and offsets of the visible thermo-optical material coefficients. Right: A modified parametrization is tested including biases in all directions, multiplicative corrections of the CERES SYN1deg above and below ±60° latitude, and offsets of the visible thermo-optical material coefficients.

| Parameter | $\tilde{x}$ | $\sigma_{\tilde{x}}$ |
|---|---|---|
| $S_{\mathrm{x}}$ | -15.79 | 0.10 |
| $S_{\mathrm{y}}$ | -0.18 | 0.11 |
| $S_{\mathrm{z}}$ | 7.89 | 0.05 |
| $\epsilon_{\text{FSW ocean}}$ | 5.41 | 0.19 |
| $\epsilon_{\text{FSW land}}$ | 4.79 | 0.15 |
| $\epsilon_{\text{FLW ocean}}$ | -4.73 | 0.20 |
| $\epsilon_{\text{FLW land}}$ | -0.99 | 0.11 |
| $\epsilon_{\text{csvis front}}$ | 43.44 | 0.26 |
| $\epsilon_{\text{csvis rear}}$ | -27.41 | 0.29 |
| $\epsilon_{\text{csvis starboard out}}$ | -1.64 | 0.14 |
| $\epsilon_{\text{csvis starboard in}}$ | -150.49 | 2.63 |
| $\epsilon_{\text{csvis port out}}$ | -7.14 | 0.14 |
| $\epsilon_{\text{csvis port in}}$ | -89.40 | 2.77 |
| $\epsilon_{\text{csvis nadir}}$ | -16.48 | 0.17 |
| $\epsilon_{\text{csvis zenith}}$ | -15.06 | 0.30 |

| Parameter | $\tilde{x}$ | $\sigma_{\tilde{x}}$ |
|---|---|---|
| $b_{\mathrm{x}}$ | $3.35\times10^{-8}$ | $1.60\times10^{-9}$ |
| $b_{\mathrm{y}}$ | $-1.71\times10^{-8}$ | $1.61\times10^{-9}$ |
| $b_{\mathrm{z}}$ | $-7.96\times10^{-8}$ | $1.65\times10^{-9}$ |
| $\epsilon_{\text{FSW equator}}$ | 3.29 | 0.14 |
| $\epsilon_{\text{FSW pole}}$ | -9.61 | 0.17 |
| $\epsilon_{\text{FLW equator}}$ | 3.93 | 0.11 |
| $\epsilon_{\text{FLW pole}}$ | -12.50 | 0.19 |
| $\epsilon_{\text{csvis front}}$ | 6.20 | 0.12 |
| $\epsilon_{\text{csvis rear}}$ | 6.20 | 0.12 |
| $\epsilon_{\text{csvis starboard out}}$ | 14.05 | 0.12 |
| $\epsilon_{\text{csvis port out}}$ | 5.97 | 0.12 |
| $\epsilon_{\text{csvis nadir}}$ | 45.38 | 0.07 |
| $\epsilon_{\text{csvis zenith}}$ | 14.28 | 0.05 |

much larger than expected. Scale factors between calibrated and modelled data should be close to 1, which is not the case. Moreover, the estimated scale factors for the CERES SYN1deg data are quite large. These corrections also indicate the correction over ocean is larger than over land. From the inspection of the differences between CERES SYN1deg and EBAF fluxes in Fig. 2.9, it should ideally be vice versa. In addition, the estimated material corrections should be below 1, which is

not the case. This indicates that the applied parametrization is not optimal.

From the comparison of calibrated and modelled accelerations, it became clear that the estimation of biases seems more reasonable than the estimation of scale factors. Besides, separating the CERES SYN1deg corrections for latitudes above and below ±60° might be more adequate. Additionally, the correction of the thermo-optical material coefficients were found to be correlated in Vielberg and Kusche (2020). Corrections for panels with similar material should ideally be constrained. Especially corrections for front and rear panels, which experienced similar conditions, since the satellites have been turned (and switched) after a few years in orbit. Furthermore, the visible material coefficient of the inner port and starboard might better be excluded from the estimation, since unmodelled self-shadowing effects are expected to impact the estimation of these parameters.

Therefore, the parametrization is updated with the above suggestions and the inverse estimation is performed again, where the remaining settings are the same. The condition number of this parametrization turned out to be smaller with $-5.5\times10^{-7}$. The estimated parameters and the formal errors are presented in the right of Tab. 7.1. The resulting parameters still appear too large. However, the magnitude of the estimated corrections for the CERES SYN1deg data is consistent with the expectation that they are larger over the poles than near the equator.

In both experiments, the formal errors, which are generally too optimistic, appear to be too small as well. To obtain more realistic errors, a fully populated variance-covariance matrix should be included in the estimation. This is expected to also significantly improve the estimated parameters in the future.

Additionally, differently calibrated accelerations are tested in the experiment above. As expected, this leads to large differences in the estimated biases. However, the changes in the radiation-related parameters is below 0.5 %. Thus, well-calibrated accelerometer measurements should still be aimed, but finding a stable parametrization is even more demanding.

To conclude, the inverse estimation confirms that the errors of CERES SYN1deg data are especially large at the poles. Improvements of the inverse modelling are definitely necessary. This includes not only obtaining well-calibrated (radial) accelerometer measurements, but also efforts to optimize the parametrization especially by introducing suitable weighting.

## 7.2 Inverse estimation based on SLR data

To account for the mismodelling of radiation pressure force models, scale factors are commonly co-estimated within the POD of spherical SLR satellites. Here, such scale factors are estimated for spherical satellites at altitudes below 1500 km and their suitability to correct existing radiation data sets is assessed.

### 7.2.1 Parametrization

Different possibilities exist to parametrize the scale factor for the radiation pressure, which is also known as radiation pressure coefficient. Whereas Löcher and Kusche (2021) estimate monthly scale factors for the SRP acceleration, Bloßfeld et al. (2018) parametrize the radiation pressure mismodelling by accounting for both SRP and ERP scale factors every 7 to 15 days depending on the period of estimation. In contrast, Sośnica et al. (2015) estimate once-per-revolution empirical accelerations in the along-track direction to account for the radiation pressure mismodelling.

In this thesis, the modelled radiation pressure is first scaled by a monthly factor for every satellite. Here, the modelled radiation pressure includes the SRP and ERP modelling. This parametrization is the same as in the previously performed POD. Within the POD other parameters such as the initial state vector, station coordinates, range biases and aerodynamic scale factors are estimated according to Tab. 5.8.

Another parametrization is the separate estimation of SRP and ERP scale factors. To avoid a high correlation between the parameters, it makes sense to estimate the SRP scale factor per satellite, whereas the ERP scale factor is estimated globally. The temporal resolution to allow for

the estimation of a global ERP scale factor should be large enough to guarantee a global coverage of the observations. Thus, a monthly temporal resolution is suggested. The remaining parameters are the same as in the first experiment. In case, correlations between SRP and ERP scale factors are too large, the SRP scale factors could be fixed to a long-term mean.

Since the thermal re-radiation is not modelled here, the radiation pressure scale factors absorb its mismodelling as well. With this in mind, the interpretation of the radiation pressure scale factor as correction for existing radiation data sets is expected to be too pessimistic.

Different from the estimation of aerodynamic scale factors, the experiments here are not conducted for GRACE, since a radiation pressure scale factor is usually not co-estimated within the POD of satellites from this mission.

### 7.2.2 Algorithm

The POD applied here is basically the same as within the estimation of the POD-based scale factors of the neutral density for spherical satellites in the previous chapter. Again, the SRP force model considers the physical shadow model and daily TSI. As a reminder, the ERP force model accounts for outgoing fluxes from CERES SYN1deg data on a 1° grid with ADMs and TRP is not modelled. The aerodynamic model again considers the thermospheric density from NRLMSIS 2.0 and an aerodynamic scale factor is co-estimated daily. For further details of the POD estimation, I refer to Sects. 5.2.4 and 6.2.2.

### 7.2.3 Results

First, the impact of changes of $1\,\mathrm{W/m^2}$ in the Earth's outgoing longwave and shortwave fluxes on the acceleration of spherical satellites is assessed (Tab. 7.2). The four spherical satellites selected

Table 7.2: Impact of changes of $1\,\mathrm{W/m^2}$ in the Earth's outgoing longwave and shortwave CERES SYN1deg fluxes on the acceleration of four SLR satellites during January 2008.

| | ERP vis | ERP ir | ERP total | total non-gravitational |
|---|---|---|---|---|
| Starlette | 0.9 % | 0.4 % | 0.6 % | -0.2 % |
| Stella | 0.9 % | 0.4 % | 0.6 % | $\leq$ 0.01 % |
| Ajisai | 0.9 % | 0.4 % | 0.6 % | -0.7 % |
| Larets | 0.8 % | 0.4 % | 0.6 % | -0.03 % |

here orbit below 1500 km. Generally, the impact of the flux changes on the acceleration is below 1 % for all satellites. The visible ERP acceleration changes at most 0.9 %, which is about twice as much as the infrared ERP acceleration. This can be explained by the smaller magnitude of the shortwave fluxes. The impact of the $1\,\mathrm{W/m^2}$ flux changes on the infrared and total ERP acceleration is 0.4 % and 0.6 %, respectively, for all satellites. The total non-gravitational acceleration remains almost unchanged for Stella. With changes of 0.7 % in the total non-gravitational acceleration, Ajisai seems to be the most promising candidate to detect variations in the radiation data sets. The reason why changes in the radiation data sets are most visible for Ajisai is because of its large area to mass ratio.

The results of the first experiment are presented in Fig. 7.3. The monthly radiation pressure scale factors for the four satellites are shown for the period August 2002 to May 2017, which corresponds the lifetime of the GRACE mission and covers nearly two solar cycles. It is clearly visible that the radiation pressure scale factor for Starlette and Stella with an average value of 1.13 and 1.14, respectively, is larger than for Ajisai and Larets, where the average radiation pressure coefficient is 1. During low solar activity, the variations of the radiation pressure scale factor are small. Before 2005 and after 2011 the variations increase for all satellites except Ajisai. The correlation of the radiation pressure scale factor with the aerodynamic scale factor is below 5 % for Ajisai, whereas it is largest for Larets with 19 %. Thus, the correlation decreases with higher altitude.

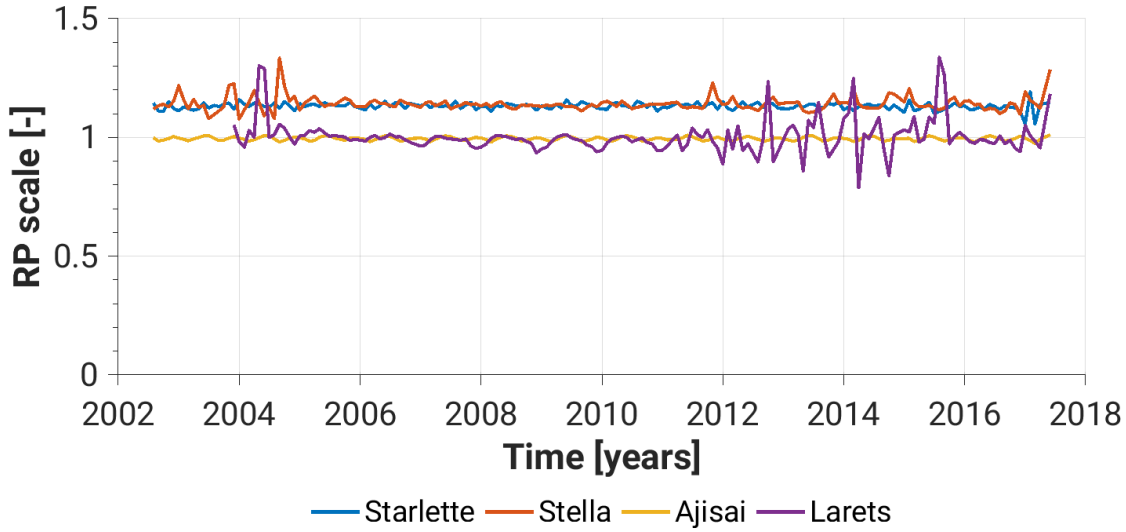
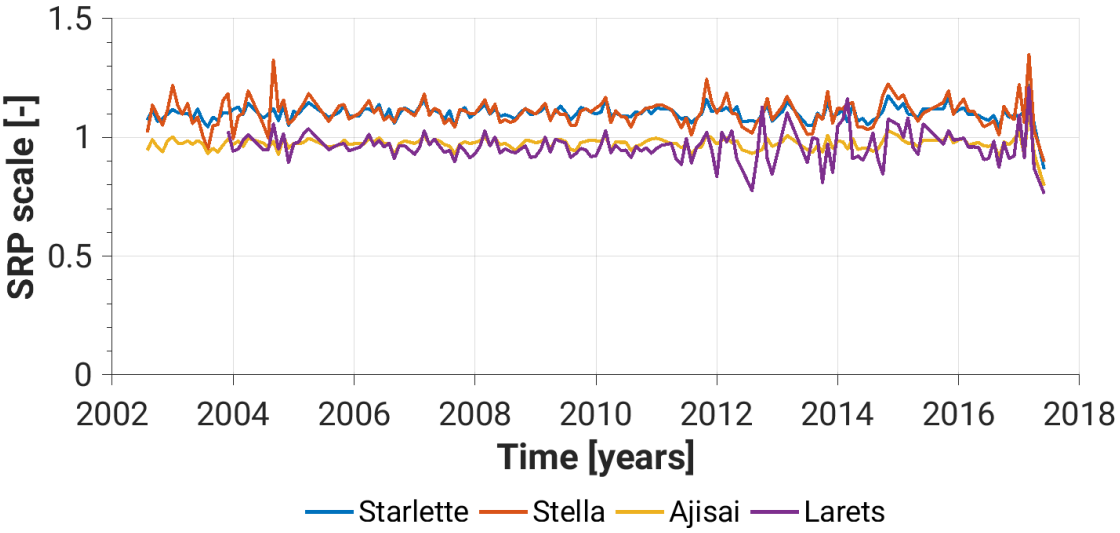



Figure 7.3: Monthly radiation pressure scale factor for four spherical SLR satellites estimated within a POD between August 2002 and May 2017. Mean values: 1.13 (Starlette), 1.14 (Stella), 0.99 (Ajisai), 1.00 (Larets).

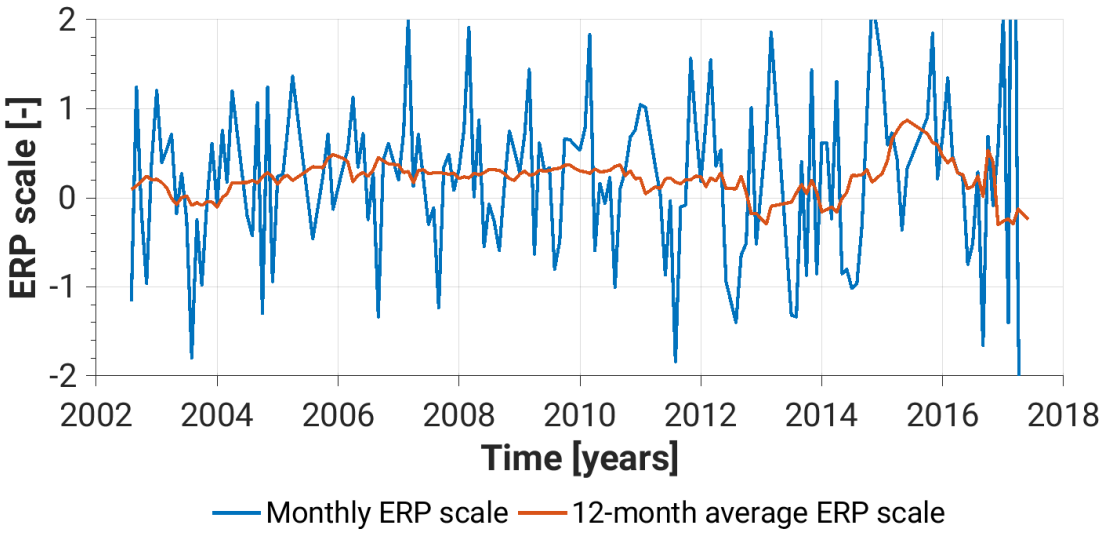
Taking a closer look at the variations of the scale factor for Ajisai reveals a cyclic behaviour of twice per year. The peak-to-peak amplitude is 3.6 % of the average radiation pressure scale factor. Converting these variations to corrections of the applied CERES SYN1deg data with the help of Tab. 7.2 reveals that the fluxes are wrong by 2.52 $\mathrm{W/m^2}$ on average. This fits remarkably well with the average biases of longwave and shortwave fluxes of 1.5 and 2 $\mathrm{W/m^2}$, respectively, between CERES SYN1deg and EBAF data. Nevertheless, this interpretation must be viewed with some caution. Although the TRP acceleration for Ajisai is expected to be relatively small due to its highly reflective surface, the unmodelled TRP acceleration affects the radiation pressure scale factor estimates. At the same time the scale factor absorbs the mismodelling of the ERP and SRP acceleration.

Another parametrization is tested for the four spherical satellites as well. The monthly estimated solar radiation pressure scale factor for every satellite as well as the monthly global scale factor for the Earth radiation pressure are presented in Fig. 7.4. Generally, the SRP scale factor shows a similar behaviour as the radiation pressure scale factor from the previous experiment, although the time series are not as smooth during low solar activity. The ERP scale factor is estimated globally, i.e., monthly for all satellites at once. The time series shows large oscillations between -2 and 2. Furthermore, Pearson's linear correlation coefficient is computed between the global ERP scale factor and the SRP scale factor of every satellite. The results show correlations of 86 % for Starlette and Stella, 97 % for Ajisai and 65 % for Larets. Such high correlations reveal that ERP scale factor and SRP scale factors are hardly separable.

To avoid the correlation between ERP and SRP scale factors, another parametrization is tested. Here, the SRP scale factor is kept fixed to the long-term radiation pressure coefficient $C_r$ from (Sośnica et al., 2015) and a global ERP scale factor is estimated with the observations to all four satellites. The resulting ERP scale factor is presented in Fig. 7.5. The monthly ERP scale factor varies roughly between 0.6 and 1.6 with an average value of 1.15. It shows a clear annual oscillation. The reason for this is likely related to the orientation of the satellites towards the Sun. Additionally, the ERP scale factor shows a correlation of 43 % with monthly global average CERES SYN1deg net flux. Experimentally, the mean ERP scale factor of 1.15 is converted to correction of the applied CERES SYN1deg fluxes by assuming that a 0.7 % deviation of the scale factor from 1 is equal to changes of 1 $\mathrm{W/m^2}$ according to Tab. 7.2. This results in a correction of the fluxes of 21 $\mathrm{W/m^2}$. As this appears quite large, I conclude that relating corrections of the radiation data sets directly to the ERP scale factors remains challenging.




(a) Solar radiation pressure scale factor per satellite.




(b) Global Earth radiation pressure scale factor.

Figure 7.4: Monthly solar radiation pressure scale factor for four spherical SLR satellites estimated within a POD between August 2002 and May 2017 (top) with mean values of 1.10 (Starlette), 1.10 (Stella), 0.97 (Ajisai), 0.96 (Larets). Estimated global Earth radiation pressure scale factor (bottom) with a monthly resolution (mean value of 0.19) as well as its 12-month moving average.

In summary, the estimation of radiation related parameters for spherical satellites and their interpretation as a correction of existing radiation data has been tested. Interpreting the RP scale factor as a correction of CERES SYN1deg fluxes seems very promising for Ajisai as it reveals that the fluxes need to be corrected by 2.52 $\mathrm{W/m^2}$ on average. A separation between ERP and SRP scale factors is not possible due to high correlations of up to 97 %. Fixing the SRP scale factors and estimating a global ERP scale factor reveals a clear annual signal, which shows a correlation of 43 % to monthly global CERES SYN1deg net fluxes. Further research especially on Ajisai is required to separate the estimated scale factors from the impact of the unmodelled TRP acceleration and remaining radiation pressure mismodelling.

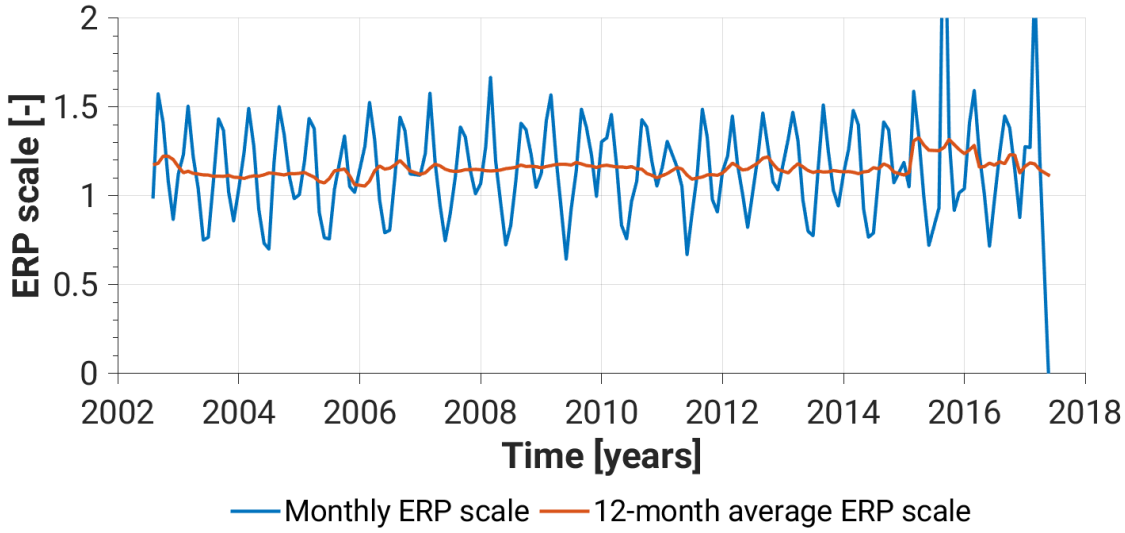



Figure 7.5: Monthly global Earth radiation pressure scale factor (blue) estimated within a POD of four spherical satellites with observations between August 2002 and May 2017. Its 12-month moving average is shown in red. Mean value: 1.15.

## 7.3 Comparability of the results from GRACE and SLR

The estimated parameters from both GRACE accelerometry and POD of SLR satellites have in common that they are integrated quantities. The temporal resolution of radiation pressure coefficients from SLR is monthly, whereas for GRACE attempts to estimate yearly corrections for radiation-related parameters have been made.

The estimation of radiation pressure scale factors from SLR is more stable in terms of correlations than the accelerometery-based adjustments. In case of finding a stable parametrization for GRACE in the future, the temporal resolution of the parameters might be increased towards a monthly resolution as well. Moreover, strong correlations between estimated parameters impact the estimation in both scenarios. The SLR-derived ERP and SRP scale factors are highly correlated and for GRACE correlations between the estimated corrections for the thermo-optical material properties occur. Further research is needed on how constraints can be formulated to reduce such correlations.

For SLR, the radiation pressure scale factor absorbs the mismodelling in the total radiation pressure force model especially the unmodelled TRP acceleration. This is not the case for GRACE, where material correction as well as overall scale factors between modelled and calibrated non-gravitational accelerations are co-estimated.

The SLR-derived radiation pressure scale factors do not distinguish between longwave and shortwave effects, whereas this is aimed with the experiments conduced for GRACE. Although the separation of longwave and shortwave corrections increases the number of parameters, it is worth testing such parametrization within the SLR estimation in the future.

In both experiments, the uncertainty of the force modelling is not accounted for within the parameter estimation. This should ideally be revised in the future by building full variance-covariance matrices and conducting error-propagations of the modelled forces.

In summary, both approaches have their advantages and disadvantages. Further research is needed to improve the estimation of radiation-related parameters and to contribute to a geodetic EEI in the future.

# Chapter 8

# Conclusion

This thesis addressed the improvement of non-gravitational satellite force models with a focus on radiation pressure force modelling. In a first step, systematics in the analytical formulations have been detected and suggestions to extend the radiation pressure models have been made. The forward model extensions have been applied to GRACE as well as to spherical SLR satellites and have been carefully validated. In a second step, the extended radiation pressure force models have been used in inverse estimations to improve on the remaining inconsistencies.

The findings from this thesis contribute to meeting the increasing demands for precise non-gravitational force models, e.g., in the context of the determination of precise orbits or the estimation neutral densities. Furthermore, the suggested inverse estimation provides a tool to estimate radiation-related parameters with the availability of improved calibrated accelerometer measurements in the near future.

## 8.1 Conclusions

**Extended radiation pressure force modelling**

Within the analytical radiation pressure force models, several inconsistencies between currently available concepts and measurements, and the parametrization of existing forward radiation pressure force models have been detected. Both SRP and ERP accelerations consider the reflection and absorption of the radiation at the satellite's surface. This requires the availability of thermo-optical material properties, which are - if available - inaccurate by a few percent and are the largest source of errors in the radiation pressure force modelling. Additionally, only few experiments analysed the degradation of the material in space, which introduces further errors. For GRACE, the thermo-optical material coefficients are provided for shortwave and longwave radiation. This allows for considering the radiation at different wavelengths, not only for the Earth's outgoing radiation, but also for different parts of the solar spectrum, which is usually omitted. To account for additional wavelengths, an interpolated macro-model is suggested, however, the variation of the reflection properties over the entire spectrum are unknown. Furthermore, accounting for the anisotropic reflection of radiation at the satellite's surface is expected to improve the radiation pressure force models. Even though modelling the anisotropy is challenging as it requires detailed material information, a first step in this direction is tested here by apply BRDFs developed by Wetterer et al. (2014).

In the SRP modelling, purely geometrical shadow models usually account for eclipse periods. Neglecting the refraction and scattering processes of the sunlight in the Earth's atmosphere can shorten the satellite's penumbra transition by a few minutes depending on the orbit. Thus, the use of physical shadow models is recommended (Robertson et al., 2015). Then, the incoming solar radiation is usually considered by assuming the solar constant. Within the solar cycle, the solar radiation varies about 1 % at the position of the Earth and the consideration of daily measurements of the TSI is suggested.

The ERP acceleration is often modelled following Knocke et al. (1988), where the Earth's foot-

print is discretized with few segments, e.g., 19. Since the outgoing radiation of the Earth shows large variations locally, a higher spatial resolution of 1° in longitude and latitude is suggested. Another aspect is the parametrization of the Earth's outgoing radiation. The Knocke model considers monthly averages of long-term albedo and emission data. With the availability of measured fluxes at TOA of the Earth's outgoing radiation from the CERES project, the outgoing radiation can be used directly and I suggest to reformulate the analytical equation to avoid inconsistencies in the application of the radiation data. The CERES SYN1deg data are available hourly, which allows for a more detailed ERP modelling. However, biases of a few $W/m^2$ in the CERES SYN1deg fluxes introduce errors in the forward-modelled ERP acceleration, which can currently not be avoided. Within the processing of the CERES data, the measured radiation is converted to fluxes by applying empirical ADMs (Su et al., 2015a; Su et al., 2015b). In turn, when computing the radiation at the position of a satellite, the fluxes need to be back-converted, which has been suggested first in Vielberg and Kusche, 2020. Here, the ERBE ADMs are applied.

Models of the re-radiation of the absorbed heat at the satellite's surface are often neglected in the radiation pressure force modelling, even though the resulting acceleration is at the same order of magnitude as the ERP acceleration for LEO satellites. Instantaneous re-radiation is a simplistic way to account for this effect. More advanced approaches consider transient heat-conductive re-radiation (Wöske et al., 2019).

Satellite-induced effects, which can cause large spikes in the accelerations, are rarely considered in non-gravitational force models. Precise models should at least account for thruster firings, and if possible, antenna thrust and electromagnetic accelerations.

Based on the suggested force model extensions, an extended radiation pressure force model has been formulated. It considers a physical shadow function, daily TSI with wavelength-dependency, hourly outgoing radiation data from CERES SYN1deg with the consideration of ADMs on a 1° grid, and heat-conductive thermal re-radiation.

**Validation of radiation pressure force model extensions**

The suggested force model extensions can be applied to all missions with available satellite geometry and thermo-optical material properties. In this thesis, the radiation pressure force model extensions have been applied to GRACE and to spherical SLR satellites. For GRACE, the SRP is the largest radiation pressure acceleration with up to $60\,nm/s^2$ in the radial direction during January 1, 2008. The variations of the suggested extensions are small (below $5\,nm/s^2$), except the consideration of the anisotropic reflection at the satellite, causing variations of up to $20\,nm/s^2$ shortly before and after the eclipse periods. The ERP acceleration is largest in the radial direction and the force model extensions show large variations. When applying the model by Knocke et al., 1988, the radial ERP acceleration reaches up to -65 $nm/s^2$, however, the extended model results in a smaller magnitude of -35 $nm/s^2$. The TRP acceleration reaches about $10\,nm/s^2$ and the force model extensions cause phase shifts and variations with a magnitude of up to 40 %.

A comparison to accelerometer measurements reveals that increasing the discretization of the Earth's footprint brings the modelled accelerations closer to the measurements with an RMSD reduction of up to 40 % depending on the applied calibration. Further, including a heat-conductive TRP model decreases the RMSD reduction by 28 %.

Since the accelerometer calibration strongly impacts the comparison, an independent validation is performed. Here, the force model extensions are applied within a POD and the residuals to SLR ranges are used as a quality measure. For GRACE, the validation revealed that the choice of the radiation pressure force model leads to variations in the average SLR residuals of the year 2008 of more than 2 cm. The largest improvements of 47 % and 24 % in terms of SLR residuals are achieved by discretizing the Earth's footprint on a 1° grid and by introducing heat-conductive TRP, respectively. Fitted thermal diffusivity has been found to decrease the SLR residuals by 36% compared to using instantaneous re-radiation. Furthermore, the selection of the radiation data impacts the residuals by 11 % and reveals that the CERES processing has a significant effect on the radiation pressure force model. Moreover, it turned out that including BRDFs increases the RMS

by more than 2 mm. Finally, the model with the smallest residuals of 2.31 cm applied daily TSI, the physical shadow function, outgoing fluxes from CERES SYN1deg on a 1° grid and a fitted heat-conductive TRP model. This differs from the suggested extended model as wavelength-dependent SRP is not considered and the thermal diffusivity has been scaled.

Radiation pressure force model extensions have also been applied on six selected SLR satellites at 700-1500 km altitude. The validation of the Earth and solar radiation pressure force models within a POD revealed that the RMS during the year 2008 decreases by up to 1 mm, i.e., the impact of the force model extensions is smaller than for GRACE mainly due to the higher altitude. Especially the choice of the radiation data decreased the SLR residuals. The TRP accelerations have not been modelled here due to complex spin behaviours. Instead, a radiation pressure scale factor has been co-estimated within the validation, however, this should ideally be revised in the future.

**Inverse estimation**

The radiation pressure force models can be used in inverse estimations, where the adjustment of modelled and measured non-gravitational accelerations in a least squares sense allows to solve for selected parameters. Since a joint estimation of several parameters at once, such as accelerometer calibration parameters, thermospheric neutral density, cross-wind speed, corrections for thermo-optical material coefficients, and corrections for radiation data, would require extensive numerical testing, two examples were selected in this thesis for an iterative stepwise procedure.

The first application was the estimation of the thermospheric neutral density. For GRACE, accelerometer-derived densities were obtained at a 10 s resolution following Doornbos (2012). Since this algorithm is not new, a variety of results exist with slightly different processing. Differences between the data sets were found to be large with up to 76 % during high solar activity, which is related to differently calibrated and modelled accelerations. Especially during low solar activity, good agreement was found between the recently published thermospheric neutral density data set (Siemes et al., 2023) and the density obtained within this thesis using the best extended radiation pressure force model in terms of smallest SLR residuals. The accelerometer-derived thermospheric neutral density can be used to scale a model density. Furthermore, aerodynamic scale factors, which can be interpreted as scale factors of the applied empirical density model (here: NRLMSIS 2.0), have been obtained within a POD for six spherical SLR satellites as well as for GRACE. Good correlations of 90 % were found for scale factors from POD and accelerometery. An overestimation of the NRLMSIS 2.0 thermospheric neutral density during solar minimum has also been observed as well as an altitude-dependency of the scale factors.

In a second example, the goal was the estimation of radiation-related parameters. Especially a correction for the Earth's radiation data sets was intended to pave the way to a geodetic EEI estimate. Since the Earth's radiation impacts mainly the radial acceleration of the satellite, this inverse estimation for GRACE required perfectly calibrated radial accelerometer measurements. However, it turned out that the calibrated accelerations contained systematic oscillations in the radial direction. Further testing revealed that these systematics disappear with increasing temporal resolution (hourly instead of daily) of the biases. The reason for this remained unclear, but aliasing effects might play a role here, which should be further investigated in the future. Moreover, biases between differently calibrated radial accelerations have been observed, which is not only related to the parametrization, but also likely related to the orbit dynamics. This complicated the estimation of calibration parameters in the radial direction. The quality of the accelerometer calibration especially in the radial direction limits the estimation of radiation-related parameters. At the same time, finding a stable parametrization remains challenging. Nevertheless, it could be confirmed that errors in the applied radiation data are larger in the polar regions than near the equator.

Within the POD for spherical satellites, scale factors of the radiation pressure are commonly co-estimated. Here, different parametrizations of the radiation pressure scale factor have been tested for four SLR satellites below 1500 km altitude and their interpretation as a correction for existing radiation data sets is assessed. The results show that Ajisai is a good candidate for this

purpose due to its large area to mass ratio and its highly reflective surface. The first results in this direction reveal that the CERES SYN1deg fluxes need to be corrected by 2.52 $W/m^2$, however, further research is required to separate this effect from remaining radiation pressure mismodelling.

## 8.2 Recommendations

With the end of this thesis, the limit of improving radiation pressure force models is not yet reached. Further suggestions to extend the forward and inverse modelling are summarized in the following, which will benefit applications such as POD, thermospheric neutral density estimation, and the estimation of a geodetic EEI in the future.

**Forward modelling**

Within the ERP modelling, the Earth's outgoing radiation reaching the satellite is required. I found that ADMs should be applied for the back-projection of the CERES fluxes to the position of the satellite. Nevertheless, only previous ADMs are available nowadays, which are known to introduce errors. For CERES TOA fluxes, the error due to radiance-to-flux conversion is 10 $W/m^2$ for shortwave and 3-5 $W/m^2$ for longwave fluxes (Loeb et al., 2007). Thus, the availability of state-of-the-art ADMs is desired to reduce systematics in the ERP modelling in the future.

CERES fluxes are available since March 2000 until today with a latency of six months. For earlier computations of the ERP acceleration, radiation data from the DEEP-C data set (Liu and Allan, 2020) can be used as they contain reconstructed radiation data until 1985 on a 0.7° grid. In the future, the CERES project will be continued with Libera (Pilewskie et al., 2023), which contains an additional near IR channel. Furthermore, the FORUM mission will measure the Earth's outgoing far IR radiation (Pachot et al., 2020). Both missions are planned to launch in 2027. The availability of the radiation at additional wavelengths also paves the way for a wavelength-dependent radiation pressure model.

The radiation reaching the satellite is partly absorbed and reflected. Modelling these effects requires precise thermo-optical material properties; ideally at different wavelengths. However, the accuracy of the provided thermo-optical material properties is currently insufficient as they are known to vary by several percent and the wavelengths at which they are valid are not clearly defined. There is a high demand for precise thermo-optical properties from the science community as this will benefit a variety of satellite applications such as POD, lifetime prediction, and thermospheric neutral density estimation. To improve the modelling of the anisotropic reflection, extensive testing of the reflection properties of the satellite's material is required to develop suitable BRDFs. This means that detailed measurements of the material properties should be conducted at least before launch.

Besides taking the effort to provide improved information on the satellite's thermo-optical material properties, the manufacturers are kindly asked to publish information on the material's thickness and thermal diffusivity. This would help to further improve the TRP modelling. Even though modelling the satellite's interior temperature behaviour might be challenging and requires further information on the satellite's inner construction, it would be beneficial to model the heat exchange between different panels. Additionally, measurements of the satellite's surface temperature, e.g., from the CESS sensors, would help to validated the thermal modelling. The possibility of continuos and open-access temperature measurements from the satellite's surface should be addressed in the future, since this would ideally replace the complex temperature modelling.

Radiation pressure force models can also be extended by applying finite element models. In this thesis, the radiation pressure force models have been applied on simply shaped satellites with available macro-models. When applying the force modelling on satellites with more complex shapes, the consideration of finite element models is inevitable. Even though the runtime increases, this allows for the modelling of multiple reflections and self-shadowing effects, which is among others important for GNSS satellites. Additionally, the antenna thrust should be accounted for in the precise non-gravitational force model of such satellites.

**Inverse modelling**

To further the inverse estimations with non-gravitational force models, progress in the accelerometer calibration as well as in the aerodynamic force modelling is required. To improve the accelerometer calibration, further studies should figure out why increasing the temporal resolution of the biases avoids such systematics in the radial direction and if aliasing plays a role here. Since different applications require different calibration parameters, the question remains, if a standard calibration model could be defined. It should be addressed, whether it makes sense to revise the parametrization of the calibration in the future.

Besides, future missions will carry improved accelerometers. The MAGIC mission, which is planned to continue the GRACE-FO measurements after 2028, might already carry next generation accelerometers (Daras et al., 2023). Furthermore, the technology of cold-atom interferometer accelerometry is currently investigated (Carraz et al., 2014; Siemes et al., 2022). Here, the benefit is that such instruments do not require such careful calibration as it is the case for classical space-borne accelerometers. This will be a key advantage to improve the inverse estimations.

The aerodynamic model used in this thesis is rather conservative. In case the along-track component is included in the inverse estimation, which is especially relevant for the estimation of the thermospheric neutral density, the gas surface interaction model should be updated. This can be done by simulating the particle flow with Monte Carlo simulations that consider quasi-specular reflections (Mehta et al., 2014; Walker et al., 2014). The accommodation coefficient should be revised as well to account for its altitude-dependency (Walker et al., 2014; Bernstein and Pilinski, 2022). Additionally, the wind velocities from empirical models and the satellite's surface temperature from the TRP modelling can be included in the aerodynamic force model. For the improvement of the aerodynamic force model, future satellite missions should carry spectrometers to obtain direct measurements of the thermospheric neutral density and its composition.

An accurately modelled thermospheric neutral density might not only aid atmospheric studies of past events, but also future predictions. Artificial intelligence has already been applied to forecast the thermospheric neutral density (Forootan et al., 2019; Packbier, 2021), geomagnetic storms (Camporeale, 2019; Tasistro-Hart et al., 2021; Ren et al., 2023) and other atmospheric quantities, such as the electron density (Smirnov et al., 2023). These forecasts are not only expected to be beneficial for detecting and understanding anomalies between forecasts and observations at short time scales up to a few days, but also for future mission planning.

Within the estimation of radiation-related parameters from accelerometry, finding a stable parametrization turned out to be difficult. This issue should be further addressed after including a full variance-covariance matrix in the estimation. Therefore, a careful variance propagation of the force modelling errors is required. Additionally, a suitable weighting of calibrated accelerometer measurements should be considered. Further research is needed to figure out how constraints can help to stabilize the solution and how correlations between estimated parameters can be reduced. These modifications are expected to be beneficial for finding a stable adjustment of radiation-related parameters.

Estimated corrections of the radiation data sets will benefit state-of-the-art climate models. Recently, significant progress has been made to reduce discrepancies between observed and modelled fluxes (Wild, 2020). Correcting existing radiation data might further reduce remaining differences, e.g., by assimilating obtained net fluxes into existing models. Moreover, the sensitivity of climate models w.r.t. differences in observed EEI might be further investigated. In this context, experiments with single-column models might also be helpful.

Based on the findings from the radiation pressure scale factors for different SLR satellites from a POD, recommendations for future missions to solve for a geodetic EEI can be made. A satellite with large area to mass ratio at altitudes, where the atmospheric drag is negligible, would be beneficial. Additionally, a highly reflective (mirror-like) surface would decrease the impact of the unmodelled thermal re-radiation.

Furthermore, a space-borne accelerometer on-board a spherical satellite with the above characteristics is expected to be a good candidate to bring the two approaches together. This goes

into the direction of the suggested mission concept by Hakuba et al. (2018). They investigated the relation between the measured radial non-gravitational acceleration and the net flux at TOA and concluded that improved accelerometry on-board a perfectly absorbing or reflecting spherical satellite will allow for the estimation of an independent EEI. In this context, the usage of cold-atom interferometry accelerometers seems promising, since no calibration is required.

The suggested improvements and concepts are promising to pave the way towards a geodetic EEI. These future results are expected to complement current EEI estimates, which is beneficial to provide the society with validated data of the current state of global warming.

# Appendix A

# Coordinate transformation: ECEF to CRF

A TRF sometimes also referred to as ECEF, such as the ITRF 2014 (Altamimi et al., 2016), is originated at the mass centre of the Earth and follows the Earth's rotation. It is realized by combining several space geodetic measurement techniques: VLBI, SLR, GNSS, and DORIS. The (geocentric) CRF is also located in the mass centre of the Earth, however, it is fixed with respect to space. According to Petit and Luzum (2010) (Eq. (5.1)), the rotation between the ECEF and the CRF reads

$$\boldsymbol{r}_{\mathrm{CRF}} = \boldsymbol{Q}(t)\boldsymbol{R}(t)\boldsymbol{W}(t)\boldsymbol{r}_{\mathrm{ECEF}}. \tag{A.0.1}$$

In dependency of the time $t$, it considers the Earth's precession and nutation $\boldsymbol{Q}$, the Earth's rotation $\boldsymbol{R}$, and the polar motion $\boldsymbol{W}$. In this thesis, the software routines from the International Astronomical Union (IAU)'s SOFA collection [1] (Board, 2021) were used to obtain the rotation matrix between these two reference frames, e.g., to transform the magnetic potential to the CRF in Sect. 4.3.

Note that there are two options to obtain the rotation matrix according to IERS conventions (Petit and Luzum, 2010). Matrices $\boldsymbol{R}$ and $\boldsymbol{Q}$ in Eq. (A.0.1) can be obtained from two procedures depending on the realization of the intermediate celestial reference system. On the one hand, which is the classic approach, its $z$-axis is the Celestial Intermediate Pole (CIP) and its $x$-axis the equinox. In the modern procedure, the systems' $z$-axis is the CIP as well, but its $x$-axis is the Celestial Intermediate Origin (CIO) (Petit and Luzum, 2010). Here, the modern approach is applied.

[1] Copyright © International Astronomical Union Standards of Fundamental Astronomy `http://www.iausofa.org`

# Appendix B

# Simulation of star camera data

Radiation pressure accelerations are generally computed in the CRF, however, for interpreting the results the SRF is more suitable. For satellites equipped with star cameras, the quaternions can be used to build the rotation matrix from CRF to SRF. Spherical satellites are usually not equipped with star cameras, thus, the quaternions defining the satellite fixed coordinate system need to be simulated from orbital positions and velocities.

There exist two different methods to simulate the star camera data, which are described below following the formulation in the GROOPS version at IGG. On the one hand, one can choose the velocity vector as along-track direction, then compute the cross-track direction by applying the cross-product of the velocity vector $\boldsymbol{v}$ and the vector $\boldsymbol{x}$ pointing from the Earth's centre to the satellite. Then, the radial direction, which does not match the direction towards the Earth in case of an elliptical orbit, can be obtained from the cross-product of the along-track and cross-track directions.

$$\boldsymbol{x}_{\text{srf}} = \boldsymbol{v} \tag{B.0.1}$$

$$\boldsymbol{y}_{\text{srf}} = \boldsymbol{v} \times \boldsymbol{x} \tag{B.0.2}$$

$$\boldsymbol{z}_{\text{srf}} = \boldsymbol{x}_{\text{srf}} \times \boldsymbol{y}_{\text{srf}} \tag{B.0.3}$$

On the other hand, simulate star camera data can be simulated such that the radial direction points exactly towards the Earth's centre. However, then the along-track direction does not exactly match the velocity direction in case of an elliptical orbit. Here, the radial direction is simply the negative $\boldsymbol{x}$ vector. The cross-track direction is the same as in the upper case. And the along-track direction can be obtained from the cross-product of the cross-track and radial directions.

$$\boldsymbol{x}_{\text{srf}} = \boldsymbol{y}_{\text{srf}} \times \boldsymbol{z}_{\text{srf}} \tag{B.0.4}$$

$$\boldsymbol{y}_{\text{srf}} = \boldsymbol{v} \times \boldsymbol{x} \tag{B.0.5}$$

$$\boldsymbol{z}_{\text{srf}} = -\boldsymbol{x} \tag{B.0.6}$$

Since GRACE has a nearly circular orbit with an eccentricity of $e < 0.005$, the results of both methods do not differ beyond the numerical accuracy.

# Appendix C

# Derivatives of analytical radiation pressure equations

In the following, the derivatives of the analytical formulations of the ERP and SRP w.r.t. selected parameters are provided. The parameters according to Ch. 7 are (1) a bias correction of the visible material coefficient and (2) a scale factor correction of the outgoing longwave and shortwave fluxes, respectively. Generally, the derivatives are computed in the SRF and are then transformed to the CRF.

The derivative of the RP w.r.t. the error of the visible material coefficient, which is parametrized as $\epsilon_{c_{s_{\text{vis}}}} + c_{s_{\text{vis}}}$ for one panel reads

$$\begin{aligned}\frac{\partial f}{\partial \epsilon_{c_{s_{\text{vis}}}}} =& \frac{\partial \boldsymbol{a}_{\text{SRP}}}{\partial \epsilon_{c_{s_{\text{vis}}}}} + \frac{\partial \boldsymbol{a}_{\text{ERP}}}{\partial \epsilon_{c_{s_{\text{vis}}}}} \\ =& \frac{A}{m} \cos(\gamma)\, \nu \left(0.5 \left[-c_{s_{\text{vis}}} \boldsymbol{s}^{\odot} - 2c_{s_{\text{vis}}} \cos(\gamma) \boldsymbol{n}\right]\right) P_{\odot} \\ &+ \frac{A}{m} \sum_j \cos(\gamma_j) \left[-c_{s_{\text{vis}}} \boldsymbol{s}_j^{\oplus} - 2c_{s_{\text{vis}}} \cos(\gamma_j)\, \boldsymbol{n}\right] \left(F_{\text{SW,j}} R_{\text{SW,j}}\right) \frac{\cos(\alpha_j)\, \Delta\omega_j}{\pi c r_{\text{Sat},j}^2}.\end{aligned} \tag{C.0.1}$$

Here, $A$ denotes the area of the panel and $m$ is the mass of the spacecraft. $\gamma$ is the angle between the incident radiation of Sun $\boldsymbol{s}^{\odot}$ or Earth $\boldsymbol{s}^{\oplus}$ and the normal vector $\boldsymbol{n}$ of the surface panel. The shadow function is denoted with $\nu$ and the radiation pressure of the Sun is accounted for with $P_{\odot}$ according to Eq. (4.2.12). Within the derivative of the ERP acceleration w.r.t. the material correction, a summation of the radiation pressure over the Earth's footprint is required, which can be discretized using $j$ segments with surface area $\Delta\omega_j$. $r_{\text{Sat},j}$ denotes the distance between the surface element and the satellite and $c$ is the speed of light. The outgoing shortwave radiation of a segment under consideration of the ADMs is accounted for by $F_{\text{SW,j}} R_{\text{SW,j}}$.

The derivative of the RP w.r.t. a scale factor of the fluxes are provided here exemplarily for the shortwave flux. The scale factor can be parametrized as a separate correction over ocean and land, which is formulated as $\left[\epsilon_{F_{\text{SW}_\text{o}}} O(\lambda,\phi) + \epsilon_{F_{\text{SW}_\text{l}}} (1 - O(\lambda,\phi))\right] F_{\text{SW}}$ with the ocean function $O(\lambda,\phi)$ depending on longitude $\lambda$ and latitude $\phi$.Following this, the derivative of the RP w.r.t. a multiplicative correction over the oceans $\epsilon_{F_{\text{SW}_\text{o}}}$ reads

$$\begin{aligned}\frac{\partial f}{\partial \epsilon_{F_{\text{SW}_\text{o}}}} =& \frac{\partial \boldsymbol{a}_{\text{ERP}}}{\partial \epsilon_{F_{\text{SW}_\text{o}}}} \\ =& \frac{A}{m} \sum_j \cos(\gamma_j)\, \boldsymbol{c}_R^{\oplus} \left(O(\lambda,\phi) F_{\text{SW,j}} R_{\text{SW,j}}\right) \frac{\cos(\alpha_j)\, \Delta\omega_j}{\pi c r_{\text{Sat},j}^2}.\end{aligned} \tag{C.0.2}$$

Here, $\boldsymbol{c}_R^{\oplus}$ is the radiation pressure coefficient from Eq. (4.2.21). Similarly, the derivative of the RP

can be formulated w.r.t. a multiplicative correction over land $\epsilon_{F_{\mathrm{SW_l}}}$ as

$$\begin{aligned}\frac{\partial f}{\partial \epsilon_{F_{\mathrm{SW_l}}}} =& \frac{\partial \boldsymbol{a}_{\mathrm{ERP}}}{\partial \epsilon_{F_{\mathrm{SW_l}}}} \\ =& \frac{A}{m} \sum_j \cos\left(\gamma_j\right) \boldsymbol{c}_R^{\oplus} \left((1 - O(\lambda, \phi)) F_{\mathrm{SW,j}} R_{\mathrm{SW,j}}\right) \frac{\cos\left(\alpha_j\right) \Delta\omega_j}{\pi c r_{\mathrm{Sat},j}^2}.\end{aligned} \tag{C.0.3}$$

On the other hand, the flux corrections can be separated for equatorial and polar regions, where the latitudinal border is set to $\pm 60°$, which is considered here by limiting the number of segments to a specific latitude. In this case, the derivative can be written as

$$\begin{aligned}\frac{\partial f}{\partial \epsilon_{F_{\mathrm{SW_{e/p}}}}} =& \frac{\partial \boldsymbol{a}_{\mathrm{ERP}}}{\partial \epsilon_{F_{\mathrm{SW_{e/p}}}}} \\ =& \frac{A}{m} \sum_{j_{e/p}} \cos\left(\gamma_j\right) \boldsymbol{c}_R^{\oplus} \left(F_{\mathrm{SW,j}} R_{\mathrm{SW,j}}\right) \frac{\cos\left(\alpha_j\right) \Delta\omega_j}{\pi c r_{\mathrm{Sat},j}^2}.\end{aligned} \tag{C.0.4}$$

When applying this equation for the equatorial regions, only segments between $-60°$ and $60°$ latitude are considered. Accordingly, the derivative of the RP w.r.t. a multiplicative correction in polar regions considers segments above $60°$ and below $-60°$, respectively.

# List of Figures


1.1 Variation of modelled non-gravitational accelerations with altitude . . . . . 2
1.2 Thermospheric neutral density from four different models . . . . . 6
1.3 Flow chart of inverse estimations . . . . . 8
1.4 Workflow of this thesis . . . . . 11

2.1 Vertical profiles of temperature, thermospheric neutral density, and composition. . . 16
2.2 Time series of solar and geomagnetic indices . . . . . 17
2.3 Inverse square law . . . . . 19
2.4 Spectral irradiance of Sun . . . . . 20
2.5 Total solar irradiance . . . . . 21
2.6 Incoming solar radiation . . . . . 21
2.7 Earth's spectral irradiance . . . . . 22
2.8 Energy budget of the Earth . . . . . 23
2.9 CERES fluxes at TOA . . . . . 25

3.1 Internal instrument overview of a GRACE satellite . . . . . 30
3.2 Satellite-body fixed frames . . . . . 32
3.3 LEO satellite missions with space-borne accelerometers . . . . . 33
3.4 Comparison of temperature and raw accelerometer measurements for GRACE-A . . 35
3.5 Accelerometer bias estimated within a POD using a three-step approach . . . . . 38
3.6 SLR satellites . . . . . 40

4.1 Mass of GRACE during the mission lifetime . . . . . 46
4.2 Specular and diffuse reflection and absorption of incoming photons on a flat surface . 48
4.3 Geometry of a BRDF . . . . . 52
4.4 Geometrical sketch of a shadow function . . . . . 55
4.5 Shadow functions during penumbra transition . . . . . 57
4.6 ERP geometry . . . . . 60
4.7 Geometry of ADMs . . . . . 63
4.8 Land cover map . . . . . 65

5.1 Aerodynamic vs. radiation pressure acceleration . . . . . 78
5.2 Norm of radiation pressure accelerations during 2008 . . . . . 79
5.3 Modelled SRP accelerations acting on GRACE-A . . . . . 81
5.4 Ground track of GRACE-A . . . . . 82
5.5 Mean differences and RMSDs between different SRP extensions . . . . . 83
5.6 CERES SYN1deg data on January 1, 2010, at 6 a.m. . . . . 83
5.7 Modelled ERP accelerations acting on GRACE-A . . . . . 85
5.8 Mean differences and RMSDs between different ERP extensions . . . . . 86
5.9 Modelled TRP accelerations acting on GRACE-A . . . . . 88
5.10 Mean differences and RMSDs between different TRP extensions . . . . . 89
5.11 Modelled and calibrated non-gravitational accelerations of GRACE-A . . . . . 90
5.12 Mean differences, RMSDs and RMSDs reduction between modelled and calibrated accelerations of GRACE-A . . . . . 92

5.13 Best non-gravitational force model for GRACE-A . . . . . 97
5.14 Radiation pressure accelerations for Starlette . . . . . 102
5.15 Radiation pressure coefficient . . . . . 105

6.1 Geometry of direct neutral density and wind estimation . . . . . 110
6.2 Geometry of iterative neutral density and wind estimation . . . . . 111
6.3 Neutral density from GRACE-A accelerometer data . . . . . 114
6.4 Comparison of different GRACE-A neutral density data sets derived from accelerometer data . . . . . 117
6.5 Comparison of different GRACE-A neutral density data sets derived from accelerometer data in terms of density ratios . . . . . 119
6.6 Scale factors for NRLMSIS 2.0 during GRACE lifetime . . . . . 124

7.1 Hourly accelerometer biases . . . . . 129
7.2 Differently calibrated accelerations . . . . . 130
7.3 Radiation pressure scale factor . . . . . 134
7.4 Solar and Earth radiation pressure scale factors . . . . . 135
7.5 Global Earth radiation pressure scale factor . . . . . 136

# List of Tables

2.1 Earth energy imbalance estimates . . . . . 23

3.1 GRACE macro-model . . . . . 33
3.2 Geophysical background models . . . . . 38
3.3 Overview of SLR missions . . . . . 40

4.1 Assumptions of wavelength-dependent material coefficients for GRACE . . . . . 50
4.2 Coefficients of the SOLAARS-CF shadow function . . . . . 56
4.3 Assumptions for TRP modelling . . . . . 69

5.1 Overview of the five-digit code of different SRP model extensions. . . . . 80
5.2 Overview of the five-digit code of different ERP model extensions. . . . . 84
5.3 Overview of the five-digit code of different TRP model extensions. . . . . 86
5.4 Data and models used in SLR processing . . . . . 94
5.5 RMS of the residuals between SLR and dynamic orbits. . . . . 95
5.6 RMS of the residuals between SLR and dynamic and kinematic orbits. . . . . 98
5.7 Non-gravitational accelerations acting on the spherical SLR satellites . . . . . 99
5.8 Parameter set for POD . . . . . 103
5.9 RMS of the residuals between SLR observations and estimated dynamic orbit. . . . . 104

6.1 Overview of different GRACE-A neutral density data sets derived from accelerometer data. . . . . 115

7.1 Estimated radiation-related parameters. . . . . 131
7.2 Impact of changes in the fluxes on the satellite's acceleration . . . . . 133

# Bibliography


Abrykosov, P., R. Pail, T. Gruber, N. Zahzam, A. Bresson, E. Hardy, B. Christophe, Y. Bidel, O. Carraz, and C. Siemes. "Impact of a novel hybrid accelerometer on satellite gravimetry performance." In: *Advances in Space Research* 63.10 (2019), pp. 3235–3248. ISSN: 0273-1177. DOI: 10.1016/j.asr.2019.01.034.

Adhya, S. "Thermal re-radiation modelling for the precise prediction and determination of spacecraft orbits." PhD thesis. University of London, 2005.

Adhya, S., A. Sibthorpe, M. Ziebart, and P. Cross. "Oblate earth eclipse state algorithm for low-Earth-orbiting satellites." In: *Journal of Spacecraft and Rockets* 41.1 (2004), pp. 157–159. ISSN: 0022-4650, 1533-6794. DOI: 10.2514/1.1485.

Afonso, G., F. Barlier, C. Berger, F. Mignard, and J. J. Walch. "Reassessment of the charge and neutral drag of LAGEOS and its geophysical implications." In: *Journal of Geophysical Research: Solid Earth* 90.B11 (1985), pp. 9381–9398. ISSN: 2156-2202. DOI: 10.1029/JB090iB11p09381.

Alken, P. et al. "International Geomagnetic Reference Field: the thirteenth generation." In: *Earth, Planets and Space* 73.1 (2021), p. 49. ISSN: 1880-5981. DOI: 10.1186/s40623-020-01288-x.

Altamimi, Z., P. Rebischung, L. Métivier, and X. Collilieux. "ITRF2014: A new release of the International Terrestrial Reference Frame modeling nonlinear station motions: ITRF2014." In: *Journal of Geophysical Research: Solid Earth* 121.8 (2016), pp. 6109–6131. ISSN: 21699313. DOI: 10.1002/2016JB013098.

Andrés, J. I., R. Noomen, G. Bianco, D. G. Currie, and T. Otsubo. "Spin axis behavior of the LAGEOS satellites." In: *Journal of Geophysical Research: Solid Earth* 109.B6 (2004). ISSN: 2156-2202. DOI: 10.1029/2003JB002692.

Andrés, J. I., R. Noomen, and S. Vecellio None. "Numerical simulation of the LAGEOS thermal behavior and thermal accelerations." In: *Journal of Geophysical Research: Solid Earth* 111.B9 (2006). ISSN: 2156-2202. DOI: 10.1029/2005JB003928.

Antreasian, P. G. and G. W. Rosborough. "Prediction of radiant energy forces on the TOPEX/-POSEIDON spacecraft." In: *Journal of Spacecraft and Rockets* 29.1 (1992), pp. 81–90. ISSN: 0022-4650, 1533-6794. DOI: 10.2514/3.26317.

Arnold, D., M. Meindl, G. Beutler, R. Dach, S. Schaer, S. Lutz, L. Prange, K. Sośnica, L. Mervart, and A. Jäggi. "CODE's new solar radiation pressure model for GNSS orbit determination." In: *Journal of Geodesy* 89.8 (2015), pp. 775–791. ISSN: 1432-1394. DOI: 10.1007/s00190-015-0814-4.

Arnold, D. and A. Jäggi. *AIUB GRACE kinematic orbits, release 01*. Bern, Switzerland: Astronomical Institute University of Bern (AIUB), 2020.

Arnold, D., O. Montenbruck, S. Hackel, and K. Sośnica. "Satellite laser ranging to low Earth orbiters: orbit and network validation." In: *Journal of Geodesy* 93.11 (2019), pp. 2315–2334. ISSN: 1432-1394. DOI: 10.1007/s00190-018-1140-4.

Aschenneller, S. "Linking Top-Of-Atmosphere Radiation Imbalance with Observed Variations in Ocean Heat Content." MA thesis. Bonn, Germany: University of Bonn, 2021.

Ashikhmin, M. and S. Premože. *Distribution-based BRDFs*. Technical Report. University of Utah, 2007.

Ashikhmin, M. and P. Shirley. "An anisotropic phong BRDF model." In: *Journal of Graphics Tools* 5.2 (2000), pp. 25–32. DOI: 10.1080/10867651.2000.10487522.

Bandikova, T., C. McCullough, G. L. Kruizinga, H. Save, and B. Christophe. "GRACE accelerometer data transplant." In: *Advances in Space Research* 64.3 (2019), pp. 623–644. ISSN: 0273-1177. DOI: 10.1016/j.asr.2019.05.021.

Bartels, J. "The standardized index, Ks, and the planetary index, Kp." In: *IATME Bull. 12b* 97.2010 (1949), p. 2021.

Behzadpour, S., T. Mayer-Gürr, and S. Krauss. "GRACE Follow-On Accelerometer Data Recovery." In: *Journal of Geophysical Research: Solid Earth* 126.5 (2021), e2020JB021297. ISSN: 2169-9356. DOI: 10.1029/2020JB021297.

Bernstein, V. and M. Pilinski. "Drag Coefficient Constraints for Space Weather Observations in the Upper Thermosphere." In: *Space Weather* 20.5 (2022), e2021SW002977. ISSN: 1542-7390. DOI: 10.1029/2021SW002977.

Bertotti, B. and L. Iess. "The rotation of LAGEOS." In: *Journal of Geophysical Research* 96.B2 (1991), p. 2431. ISSN: 0148-0227. DOI: 10.1029/90JB01949.

Bettadpur, S. "Gravity recovery and climate experiment: product specification document." In: *Tech. Rep. GRACE 327-720. Center for Space Research, The University of Texas at Austin* (2012).

Bettadpur, S. "Recommendation for a-priori bias & scale parameters for Level-1B ACC data (version 2)." In: *GRACE TN-02. Center for Space Research, The University of Texas at Austin* (2009).

Bezděk, A. "Calibration of accelerometers aboard GRACE satellites by comparison with POD-based nongravitational accelerations." In: *Journal of Geodynamics* 50.5 (2010), pp. 410–423. DOI: http://dx.doi.org/10.1016/j.jog.2010.05.001.

Bhattarai, S., M. Ziebart, T. Springer, F. Gonzalez, and G. Tobias. "High-precision physics-based radiation force models for the Galileo spacecraft." In: *Advances in Space Research* 69.12 (2022), pp. 4141–4154. DOI: 10.1016/j.asr.2022.04.003.

Blinn, J. F. "Models of light reflection for computer synthesized pictures." In: *Proceedings of the 4th annual conference on Computer graphics and interactive techniques*. 1977, p. 7.

Bloßfeld, M., H. Müller, M. Gerstl, V. Štefka, J. Bouman, F. Göttl, and M. Horwath. "Second-degree Stokes coefficients from multi-satellite SLR." In: *Journal of Geodesy* 89.9 (2015), pp. 857–871. ISSN: 1432-1394. DOI: 10.1007/s00190-015-0819-z.

Bloßfeld, M., S. Rudenko, A. Kehm, N. Panafidina, H. Müller, D. Angermann, U. Hugentobler, and M. Seitz. "Consistent estimation of geodetic parameters from SLR satellite constellation measurements." In: *Journal of Geodesy* 92.9 (2018), pp. 1003–1021. ISSN: 0949-7714, 1432-1394. DOI: 10.1007/s00190-018-1166-7.

Board, I. S. *IAU SOFA Software Collection*. 2021.

Börger, L. "Application of realistic ray-tracing algorithms in non-gravitational force modeling." MA thesis. Bonn, Germany: University of Bonn, 2021.

Bottke, W. F., D. Vokrouhlický, D. P. Rubincam, and D. Nesvorný. "The Yarkovsky and Yorp effects: Implications for asteroid dynamics." In: *Annual Review of Earth and Planetary Sciences* 34.1 (2006), pp. 157–191. DOI: 10.1146/annurev.earth.34.031405.125154.

Boudon, Y. "Measurement of the Radiation Pressures by Accelerometry: A New Way to the Determination of the Earth Radiation Budget. Result Obtained with Castor/Cactus Experiment." In: *Current Issues in Climate Research: Proceedings of the EC Climatology Programme Symposium, Sophia Antipolis, France, 2–5 October 1984*. Ed. by A. Ghazi and R. Fantechi. Dordrecht: Springer Netherlands, 1986, pp. 341–352. ISBN: 978-94-009-5494-6. DOI: 10.1007/978-94-009-5494-6_32.

Bowman, B., W. K. Tobiska, F. Marcos, C. Huang, C. Lin, and W. Burke. "A new empirical thermospheric density model JB2008 using new solar and geomagnetic indices." In: *AIAA/AAS Astrodynamics specialist conference and exhibit*. AIAA/AAS Astrodynamics Specialist Conference. Honolulu, Hawaii: American Institute of Aeronautics and Astronautics, 2008, p. 6438.

Boy, J.-P., L. Longuevergne, F. Boudin, T. Jacob, F. Lyard, M. Llubes, N. Florsch, and M.-F. Esnoult. "Modelling atmospheric and induced non-tidal oceanic loading contributions to surface gravity and tilt measurements." In: *Journal of Geodynamics*. New Challenges in Earth's Dynam-

ics - Proceedings of the 16th International Symposium on Earth Tides 48.3 (2009), pp. 182–188. ISSN: 0264-3707. DOI: 10.1016/j.jog.2009.09.022.

Bruinsma, S., D. Tamagnan, and R. Biancale. "Atmospheric densities derived from CHAMP/STAR accelerometer observations." In: *Planetary and Space Science* 52.4 (2004), pp. 297–312. DOI: 10.1016/j.pss.2003.11.004.

Bruinsma, S., E. Doornbos, and B. Bowman. "Validation of GOCE densities and evaluation of thermosphere models." In: *Advances in Space Research* 54.4 (2014), pp. 576–585. ISSN: 02731177. DOI: 10.1016/j.asr.2014.04.008.

Bruinsma, S. and R. Biancale. "Total Densities Derived from Accelerometer Data." In: *Journal of Spacecraft and Rockets* 40.2 (2003), pp. 230–236. ISSN: 0022-4650, 1533-6794. DOI: 10.2514/2.3937.

Bruinsma, S. and C. Boniface. "The operational and research DTM-2020 thermosphere models." In: *Journal of Space Weather and Space Climate* 11 (2021), p. 47. ISSN: 2115-7251. DOI: 10.1051/swsc/2021032.

Bruinsma, S., J. M. Forbes, R. S. Nerem, and X. Zhang. "Thermosphere density response to the 20–21 November 2003 solar and geomagnetic storm from CHAMP and GRACE accelerometer data." In: *Journal of Geophysical Research: Space Physics* 111.A6 (2006).

Bruinsma, S., C. Siemes, J. T. Emmert, and M. G. Mlynczak. "Description and comparison of 21st century thermosphere data." In: *Advances in Space Research* (2022). ISSN: 0273-1177. DOI: 10.1016/j.asr.2022.09.038.

Bury, G., R. Zajdel, and K. Sośnica. "Accounting for perturbing forces acting on Galileo using a box-wing model." In: *GPS Solutions* 23.3 (2019), p. 74. ISSN: 1521-1886. DOI: 10.1007/s10291-019-0860-0.

Calabia, A., G. Tang, and S. Jin. "Assessment of new thermospheric mass density model using NRLMSISE-00 model, GRACE, Swarm-C, and APOD observations." In: *Journal of atmospheric and solar-terrestrial physics* 199 (2020), p. 105207. ISSN: 1364-6826. DOI: 10.1016/j.jastp.2020.105207.

Calabia, A., S. Jin, and R. Tenzer. "A new GPS-based calibration of GRACE accelerometers using the arc-to-chord threshold uncovered sinusoidal disturbing signal." In: *Aerospace science and technology* 45 (2015), pp. 265–271. ISSN: 12709638. DOI: 10.1016/j.ast.2015.05.013.

Camporeale, E. "The Challenge of Machine Learning in Space Weather: Nowcasting and Forecasting." In: *Space Weather* 17.8 (2019), pp. 1166–1207. ISSN: 1542-7390. DOI: 10.1029/2018SW002061.

Carraz, O., C. Siemes, L. Massotti, R. Haagmans, and P. Silvestrin. "A Spaceborne Gravity Gradiometer Concept Based on Cold Atom Interferometers for Measuring Earth's Gravity Field." In: *Microgravity science and technology* 26.3 (2014), pp. 139–145. DOI: 10.1007/s12217-014-9385-x.

Carrere, L., F. Lyard, M. Cancet, and A. Guillot. "FES 2014, a new tidal model on the global ocean with enhanced accuracy in shallow seas and in the Arctic region." In: *Geophysical Research Abstracts*. EGU General Assembly 2015, Vienna, Austria. Vol. 17. 2015, p. 5481.

Case, K., G. Kruizinga, and S.-C. Wu. "GRACE Level 1B data product user handbook." In: *Tech. Rep. JPL D-22027. Jet Propulsion Laboratory* (2010).

Ceniceros, A., D. E. Gaylor, J. Anderso, E. Pinon III, P. Dao, and R. Rast. *Comparison of BRDF Predicted and Observed Light Curves of GEO Satellites*. Tucson, United States: University of Arizona, 2015.

*CERES_SYN1deg_Ed4A Data Quality Summary (10/3/2017)*. Atmospheric Science Data Center, 2017.

Cerri, L., J. P. Berthias, W. I. Bertiger, B. J. Haines, F. G. Lemoine, F. Mercier, J. C. Ries, P. Willis, N. P. Zelensky, and M. Ziebart. "Precision orbit determination standards for the Jason series of altimeter missions." In: *Marine Geodesy* 33 (2010), pp. 379–418. ISSN: 0149-0419. DOI: 10.1080/01490419.2010.488966.

Chelton, D. B., J. C. Ries, B. J. Haines, L.-L. Fu, and P. S. Callahan. "Satellite Altimetry." In: *International Geophysics*. Ed. by L.-L. Fu and A. Cazenave. Vol. 69. Satellite Altimetry and Earth Sciences. Academic Press, 2001, pp. 1–131. DOI: 10.1016/S0074-6142(01)80146-7.

Christophe, B., D. Boulanger, B. Foulon, P.-A. Huynh, V. Lebat, F. Liorzou, and E. Perrot. "A new generation of ultra-sensitive electrostatic accelerometers for GRACE Follow-on and towards the next generation gravity missions." In: *Acta Astronautica* 117 (2015), pp. 1–7. ISSN: 0094-5765. DOI: 10.1016/j.actaastro.2015.06.021.

Christophe, B., B. Foulon, F. Liorzou, V. Lebat, D. Boulanger, P.-A. Huynh, N. Zahzam, Y. Bidel, and A. Bresson. "Status of Development of the Future Accelerometers for Next Generation Gravity Missions." In: *International Symposium on Advancing Geodesy in a Changing World*. International Association of Geodesy Symposia 149. Ed. by J. T. Freymueller and L. Sánchez. Springer, Berlin, Heidelberg, 2018, pp. 1–5. DOI: 10.1007/1345_2018_42.

Ciufolini, I., R. A. Matzner, J. C. Feng, A. Paolozzi, D. P. Rubincam, E. C. Pavlis, J. C. Ries, G. Sindoni, and C. Paris. "A new laser-ranged satellite for General Relativity and space geodesy: IV. Thermal drag and the LARES 2 space experiment." In: *The European Physical Journal Plus* 133.8 (2018), p. 333. ISSN: 2190-5444. DOI: 10.1140/epjp/i2018-12174-y. arXiv: 1911.05016.

Cook, G. "Satellite drag coefficients." In: *Planetary and Space Science* 13.10 (1965), pp. 929–946. ISSN: 0032-0633. DOI: 10.1016/0032-0633(65)90150-9.

Cook, R. L. and K. E. Torrance. "A reflectance model for computer graphics." In: *Acm transactions on graphics (tog)* 1.1 (1982), pp. 7–24. DOI: 10.1145/357290.357293.

Corbin, A. and J. Kusche. "Improving the estimation of thermospheric neutral density via two-step assimilation of in situ neutral density into a numerical model." In: *Earth, Planets and Space* 74.1 (2022), p. 183. ISSN: 1880-5981. DOI: 10.1186/s40623-022-01733-z.

Dahle, C., F. Flechtner, M. Murböck, G. Michalak, K. Neumayer, O. Abrykosov, A. Reinhold, R. König, and D. G. Publikationen aller GRACE-unterstützten Projekte. "GRACE-FO D-103919 (Gravity Recovery and Climate Experiment Follow-On): GFZ Level-2 Processing Standards Document for Level-2 Product Release 06 (Rev. 1.0, June 3, 2019)." In: *Potsdam: GFZ German Research Centre for Geosciences* (2019). DOI: 10.2312/GFZ.b103-19098.

Dahle, C., M. Murböck, F. Flechtner, H. Dobslaw, G. Michalak, K. H. Neumayer, O. Abrykosov, A. Reinhold, R. König, R. Sulzbach, and C. Förste. "The GFZ GRACE RL06 Monthly Gravity Field Time Series: Processing Details and Quality Assessment." In: *Remote Sensing* 11.18 (2019), p. 2116. ISSN: 2072-4292. DOI: 10.3390/rs11182116.

Dahle, C., R. Biancale, and F. Flechtner. "Alternative processing of GRACE gravity field products to overcome present gaps in accelerometer data." In: *GRACE Science Team Meeting, Austin, USA*. 2011.

Daras, I., L. Tsaoussi, G. March, L. Massotti, B. C. Dominguez, and O. Carraz. "ESA/NASA Mass change And Geosciences International Constellation (MAGIC) mission concept – science and application prospects." In: EGU General Assembly 2023, Vienna, Austria. EGU23-13535. 2023. DOI: 10.5194/egusphere-egu23-13535.

Darugna, F., P. Steigenberger, O. Montenbruck, and S. Casotto. "Ray-tracing solar radiation pressure modeling for QZS-1." In: *Advances in Space Research* 62.4 (2018), pp. 935–943. ISSN: 02731177. DOI: 10.1016/j.asr.2018.05.036.

Deo, S. and B. Kushvah. "Yarkovsky effect and solar radiation pressure on the orbital dynamics of the asteroid (101955) Bennu." In: *Astronomy and Computing* 20 (2017), pp. 97–104. ISSN: 22131337. DOI: 10.1016/j.ascom.2017.07.002.

Desai, S. D. "Observing the pole tide with satellite altimetry." In: *Journal of Geophysical Research: Oceans* 107.C11 (2002), pp. 7-1-7–13. ISSN: 2156-2202. DOI: 10.1029/2001JC001224.

Dewitte, S. and N. Clerbaux. "Measurement of the Earth radiation budget at the top of atmosphere – A review." In: *Remote Sensing* 9.11 (2017), p. 1143. DOI: 10.3390/rs9111143.

Dieng, H. B., H. Palanisamy, A. Cazenave, B. Meyssignac, and K. von Schuckmann. "The Sea Level Budget Since 2003: Inference on the Deep Ocean Heat Content." In: *Surveys in Geophysics* 36.2 (2015), pp. 209–229. ISSN: 1573-0956. DOI: 10.1007/s10712-015-9314-6.

Dobslaw, H., I. Bergmann-Wolf, R. Dill, L. Poropat, M. Thomas, C. Dahle, S. Esselborn, R. König, and F. Flechtner. "A new high-resolution model of non-tidal atmosphere and ocean mass variability for de-aliasing of satellite gravity observations: AOD1B RL06." In: *Geophysical Journal International* 211.1 (2017), pp. 263–269. ISSN: 0956-540X, 1365-246X. DOI: 10.1093/gji/ggx302.

Doelling, D. R., M. Sun, L. T. Nguyen, M. L. Nordeen, C. O. Haney, D. F. Keyes, and P. E. Mlynczak. "Advances in geostationary-derived longwave fluxes for the CERES synoptic (SYN1deg) product." In: *Journal of Atmospheric and Oceanic Technology* 33.3 (2016), pp. 503–521. ISSN: 0739-0572, 1520-0426. DOI: 10.1175/JTECH-D-15-0147.1.

Doll, B. and W. Pitz. "Grober Sonnen- oder Erdsensor für einen Satelliten sowie Verfahren zur groben Positionsbestimmung von Sonne oder Erde an Bord eines Satelliten." German pat. 19709351C2. Dornier GmbH. Jan. 21, 1999. Expired - Fee Related.

Döll, P., H. M. M. Hasan, K. Schulze, H. Gerdener, L. Börger, S. Shadkam, S. Ackermann, S.-M. Hosseini-Moghari, H. Müller Schmied, A. Güntner, and J. Kusche. "Multi-variable parameter estimation for a global hydrological model: Comparison and evaluation of three ensemble-based calibration methods for the Mississippi River basin." In: *Hydrology and Earth System Sciences Discussions* (2023), pp. 1–54. DOI: 10.5194/hess-2023-18.

Doornbos, E., S. Bruinsma, B. Fritsche, P. Visser, J. Van Den IJssel, J. T. Encarnacao, and M. Kern. "Air density and wind retrieval using GOCE data." In: *ESA Living Planet Symposium*. Vol. 722. 2013, p. 7.

Doornbos, E., M. Forster, B. Fritsche, T. van Helleputte, J. van den IJssel, G. Koppenwallner, H. Lühr, D. Rees, and P. Visser. "ESTEC Contract 21022/07/NL/HE Air Density Models Derived from Multi-Satellite Drag Observations - Final Report." In: *DEOS/Delft Univ. of Technology Scientific TR* 1 (2009), pp. 7–39.

Doornbos, E. "Thermospheric density and wind determination from satellite dynamics." In: *Springer Science & Business Media, Berlin* (2012). ISSN: 2190-5053. DOI: 10.1007/978-3-642-25129-0.

Doornbos, E., J. V. Den Ijssel, H. Lühr, M. Förster, and G. Koppenwallner. "Neutral density and crosswind determination from arbitrarily oriented multiaxis accelerometers on satellites." In: *Journal of Spacecraft and Rockets* 47.4 (2010), pp. 580–589. DOI: 10.2514/1.48114.

Doornbos, E., H. Klinkrad, R. Scharroo, and P. Visser. "Thermosphere density calibration in the orbit determination of ERS-2 and Envisat." In: *Envisat Symposium 2007*. 23–27 April 2007 (ESA SP-636, July 2007). Montreux, Switzerland, 2007, p. 5.

Doornbos, E., H. Klinkrad, and P. Visser. "Use of two-line element data for thermosphere neutral density model calibration." In: *Advances in Space Research* 41.7 (2008), pp. 1115–1122. ISSN: 02731177. DOI: 10.1016/j.asr.2006.12.025.

Drinkwater, M. R., R. Haagmans, D. Muzi, A. Popescu, R. Floberghagen, M. Kern, and M. Fehringer. "The GOCE gravity mission: ESA's first core Earth explorer." In: *Proceedings of the 3rd international GOCE user workshop*. Citeseer. 2006, pp. 6–8.

Drob, D. P., J. T. Emmert, J. W. Meriwether, J. J. Makela, E. Doornbos, M. Conde, G. Hernandez, J. Noto, K. A. Zawdie, S. E. McDonald, J. D. Huba, and J. H. Klenzing. "An update to the Horizontal Wind Model (HWM): The quiet time thermosphere." In: *Earth and Space Science* 2.7 (2015), pp. 301–319. ISSN: 2333-5084. DOI: 10.1002/2014EA000089.

Dudok de Wit, T., S. Bruinsma, and K. Shibasaki. "Synoptic radio observations as proxies for upper atmosphere modelling." In: *Journal of Space Weather and Space Climate* 4 (2014), A06.

Eanes, R. . J., R. S. Nerem, P. A. M. Abusali, W. Bamford, K. Key, J. C. Ries, and B. E. Schutz. "GLONASS Orbit Determination at the Center for Space Research." In: Proceedings of the International GLONASS Exper- Iment (IGEX-98) Workshop, IGS, Jet Propulsion Laboratory. 2000.

Elsner, N. *Grundlagen der technischen Thermodynamik*. Akademie-Verlag Berlin, 1988.

Emmert, J. T. "Thermospheric mass density: A review." In: *Advances in Space Research* 56.5 (2015), pp. 773–824. ISSN: 02731177. DOI: 10.1016/j.asr.2015.05.038.

Emmert, J. T., M. S. Dhadly, and A. M. Segerman. "A Globally Averaged Thermospheric Density Data Set Derived From Two-Line Orbital Element Sets and Special Perturbations State Vectors."

In: *Journal of Geophysical Research: Space Physics* 126.8 (2021). ISSN: 2169-9380, 2169-9402. DOI: 10.1029/2021JA029455.

Emmert, J. T., D. P. Drob, J. M. Picone, D. E. Siskind, M. Jones, M. G. Mlynczak, P. F. Bernath, X. Chu, E. Doornbos, B. Funke, L. P. Goncharenko, M. E. Hervig, M. J. Schwartz, P. E. Sheese, F. Vargas, B. P. Williams, and T. Yuan. "NRLMSIS 2.0: A whole-atmosphere empirical model of temperature and neutral species densities." In: *Earth and Space Science* 8 (2020), e2020EA001321. ISSN: 2333-5084. DOI: 10.1029/2020EA001321.

Emmert, J. T., J. M. Picone, J. L. Lean, and S. H. Knowles. "Global change in the thermosphere: Compelling evidence of a secular decrease in density." In: *Journal of Geophysical Research: Space Physics* 109.A2 (2004). ISSN: 2156-2202. DOI: 10.1029/2003JA010176.

Ermolli, I., K. Matthes, T. Dudok de Wit, N. A. Krivova, K. Tourpali, M. Weber, Y. C. Unruh, L. Gray, U. Langematz, P. Pilewskie, et al. "Recent variability of the solar spectral irradiance and its impact on climate modelling." In: *Atmospheric Chemistry and Physics* 13.8 (2013), pp. 3945–3977.

Fahnestock, E., R. Park, D.-N. Yuan, and A. Konopliv. "Spacecraft Thermal and Optical Modeling Impacts on Estimation Of the GRAIL Lunar Gravity Field." In: AIAA/AAS Astrodynamics Specialist Conference 2012. 2012. ISBN: 978-1-62410-182-3. DOI: 10.2514/6.2012-4428.

Falck, C., S. Reißland, K. Snopek, and F.-H. Massmann. "Satellite data reception at Ny-Ålesund, Spitsbergen: From CHAMP to GRACE Follow-On." In: *zfv – Zeitschrift für Geodäsie, Geoinformation und Landmanagement* 2020 (2020), pp. 111–117. ISSN: 1618-8950. DOI: 10.12902/zfv-0290-2020.

Fliegel, H. F., T. E. Gallini, and E. R. Swift. "Global positioning system radiation force model for geodetic applications." In: *Journal of Geophysical Research: Solid Earth* 97.B1 (1992), pp. 559–568. ISSN: 2156-2202. DOI: 10.1029/91JB02564.

Fliegel, H. F. and T. E. Gallini. "Solar force modeling of block IIR Global Positioning System satellites." In: *Journal of Spacecraft and Rockets* 33.6 (1996), pp. 863–866. ISSN: 0022-4650, 1533-6794. DOI: 10.2514/3.26851.

Floberghagen, R., M. Fehringer, D. Lamarre, D. Muzi, B. Frommknecht, C. Steiger, J. Piñeiro, and A. da Costa. "Mission design, operation and exploitation of the gravity field and steady-state ocean circulation explorer mission." In: *Journal of Geodesy* 85.11 (2011), pp. 749–758. DOI: 10.1007/s00190-011-0498-3.

Floberghagen, R., P. Visser, and F. Weischede. "Lunar albedo force modeling and its effect on low lunar orbit and gravity field determination." In: *Advances in Space Research*. Satellite Dynamics, Orbit Analysis and Combination of Space Techniques 23.4 (1999), pp. 733–738. ISSN: 0273-1177. DOI: 10.1016/S0273-1177(99)00155-6.

Flury, J., S. Bettadpur, and B. D. Tapley. "Precise accelerometry onboard the GRACE gravity field satellite mission." In: *Advances in Space Research* 42.8 (2008), pp. 1414–1423. ISSN: 02731177. DOI: 10.1016/j.asr.2008.05.004.

Folkner, W. M., J. G. Williams, and D. H. Boggs. "The planetary and lunar ephemeris DE 421." In: *JPL IOM 343R-08-003* (2008).

Forootan, E., S. Farzaneh, C. Lück, and K. Vielberg. "Estimating and predicting corrections for empirical thermospheric models." In: *Geophysical Journal International* 218.1 (2019), pp. 479–493. ISSN: 0956-540X, 1365-246X. DOI: 10.1093/gji/ggz163.

Forootan, E., M. Kosary, S. Farzaneh, T. Kodikara, K. Vielberg, I. Fernandez-Gomez, C. Borries, and M. Schumacher. "Forecasting global and multi-level thermospheric neutral density and ionospheric electron content by tuning models against satellite-based accelerometer measurements." In: *Scientific Reports* 12.1 (2022), p. 2095. ISSN: 2045-2322. DOI: 10.1038/s41598-022-05952-y.

Förstner, W. "Ein Verfahren zur Schätzung von Varianz- und Kovarianzkomponenten." In: *Allgemeine Vermessungsnachrichten* (11–12) (1979), pp. 446–453.

Friedl, M. and D. Sulla-Menashe. *MCD12C1 MODIS/Terra+Aqua Land Cover Type Yearly L3 Global 0.05Deg CMG V006 (Data set)*. 2015. DOI: 10.5067/MODIS/MCD12C1.006.

Friis-Christensen, E., H. Lühr, D. Knudsen, and R. Haagmans. "Swarm – An Earth Observation Mission investigating Geospace." In: *Advances in Space Research* 41.1 (2008), pp. 210–216. ISSN: 02731177. DOI: 10.1016/j.asr.2006.10.008.

Frommknecht, B. "Integrated sensor analysis of the GRACE mission." PhD thesis. Universität München, 2007.

Girardin, V. E. J. "Impact of non-gravitational forces on GPS-based precise orbit determination of low Earth orbiters." MA thesis. Delft University of Technology, 2016.

Glaser, S., M. Fritsche, K. Sośnica, C. J. Rodríguez-Solano, K. Wang, R. Dach, U. Hugentobler, M. Rothacher, and R. Dietrich. "A consistent combination of GNSS and SLR with minimum constraints." In: *Journal of Geodesy* 89.12 (2015), pp. 1165–1180. ISSN: 1432-1394. DOI: 10.1007/s00190-015-0842-0.

Glaser, S., G. Michalak, B. Männel, R. König, K. H. Neumayer, and H. Schuh. "Reference system origin and scale realization within the future GNSS constellation "Kepler"." In: *Journal of Geodesy* 94.12 (2020), p. 117. ISSN: 1432-1394. DOI: 10.1007/s00190-020-01441-0.

Goode, P. R., E. Pallé, A. Shoumko, S. Shoumko, P. Montañes-Rodriguez, and S. E. Koonin. "Earth's Albedo 1998–2017 as Measured From Earthshine." In: *Geophysical Research Letters* 48.17 (2021), e2021GL094888. ISSN: 1944-8007. DOI: 10.1029/2021GL094888.

Hackel, S., O. Montenbruck, P. Steigenberger, U. Balss, C. Gisinger, and M. Eineder. "Model improvements and validation of TerraSAR-X precise orbit determination." In: *Journal of Geodesy* 91.5 (2017), pp. 547–562. ISSN: 1432-1394. DOI: 10.1007/s00190-016-0982-x.

Haghighat, A. *Monte Carlo Methods for Particle Transport*. CRC Press, 2020. 311 pp. ISBN: 978-0-429-58410-7. Google Books: O_zyDwAAQBAJ.

Hakuba, M. Z., T. Frederikse, and F. W. Landerer. "Earth's Energy Imbalance From the Ocean Perspective (2005–2019)." In: *Geophysical Research Letters* 48.16 (2021), e2021GL093624. ISSN: 1944-8007. DOI: 10.1029/2021GL093624.

Hakuba, M. Z., G. L. Stephens, B. Christophe, A. E. Nash, B. Foulon, S. V. Bettadpur, B. D. Tapley, and F. H. Webb. "Earth's energy imbalance measured from space." In: *IEEE Transactions on Geoscience and Remote Sensing* (2018), pp. 1–14. ISSN: 0196-2892. DOI: 10.1109/TGRS.2018.2851976.

Hattori, A. and T. Otsubo. "Time-varying solar radiation pressure on Ajisai in comparison with LAGEOS satellites." In: *Advances in Space Research* 63.1 (2019), pp. 63–72. ISSN: 0273-1177. DOI: 10.1016/j.asr.2018.08.010.

Hauschild, A., O. Montenbruck, P. Steigenberger, I. Martini, and I. Fernandez-Hernandez. "Orbit determination of Sentinel-6A using the Galileo high accuracy service test signal." In: *GPS Solutions* 26.4 (2022), p. 120. ISSN: 1521-1886. DOI: 10.1007/s10291-022-01312-5.

Hedin, A. E., J. E. Salah, J. V. Evans, C. A. Reber, G. P. Newton, N. W. Spencer, D. C. Kayser, D. Alcayde, P. Bauer, L. Cogger, et al. "A global thermospheric model based on mass spectrometer and incoherent scatter data MSIS, 1. N2 density and temperature." In: *Journal of Geophysical Research* 82.16 (1977), pp. 2139–2147. DOI: 10.1029/JA082i016p02139.

Heinzel, G., B. Sheard, N. Brause, K. Danzmann, M. Dehne, O. Gerberding, C. Mahrdt, V. Müller, D. Schütze, G. Stede, W. Klipstein, W. Folkner, R. Spero, K. Nicklaus, P. Gath, and D. Shaddock. "Laser ranging interferometer for GRACE follow-on." In: *International Conference on Space Optics — ICSO 2012*. International Conference on Space Optics — ICSO 2012. Vol. 10564. SPIE, 2017, pp. 517–526. DOI: 10.1117/12.2309099.

Herman, J., A. Davis, K. B. Chin, M. Kinzler, S. Scholz, and M. Steinhoff. "Life with a weak Heart; Prolonging the Grace Mission despite degraded Batteries." In: *In: 12th International Conference on Space Operations (SpaceOps 2012), 11-15. Juni 2012, Stockhom, Schweden* (2012).

Hersbach, H. et al. "The ERA5 global reanalysis." In: *Quarterly Journal of the Royal Meteorological Society* 146.730 (2020), pp. 1999–2049. ISSN: 1477-870X. DOI: 10.1002/qj.3803.

Hofmann-Wellenhof, B. and H. Moritz. *Physical geodesy*. Springer Science & Business Media, 2006.

Hu, X. and X. Shi. "Thermophysical Characterization of Cyclic Frost Formation in the Subsurface and Nominal Water Activity on Comets: Case Study of 67P/Churyumov-Gerasimenko." In: *The*

*Astrophysical Journal* 910.1 (2021), p. 10. ISSN: 0004-637X, 1538-4357. DOI: 10.3847/1538-4357/abddbf.

Hubaux, C., A. Lemaître, N. Delsate, and T. Carletti. "Symplectic integration of space debris motion considering several Earth's shadowing models." In: *Advances in Space Research* 49.10 (2012), pp. 1472–1486. ISSN: 02731177. DOI: 10.1016/j.asr.2012.02.009. arXiv: 1201.5274.

Ince, E. S., F. Barthelmes, S. Reißland, K. Elger, C. Förste, F. Flechtner, and H. Schuh. "ICGEM – 15 years of successful collection and distribution of global gravitational models, associated services, and future plans." In: *Earth System Science Data* 11.2 (2019), pp. 647–674. ISSN: 1866-3508. DOI: 10.5194/essd-11-647-2019.

IPCC. *Synthesis Report of the IPCC Sixth Assessment Report (AR6)*. 2023.

Johnson, G. C., J. M. Lyman, and N. G. Loeb. "Improving estimates of Earth's energy imbalance." In: *Nature Climate Change* 6.7 (2016), pp. 639–640. ISSN: 1758-6798. DOI: 10.1038/nclimate3043.

Kato, S., F. G. Rose, D. A. Rutan, T. J. Thorsen, N. G. Loeb, D. R. Doelling, X. Huang, W. L. Smith, W. Su, and S.-H. Ham. "Surface Irradiances of Edition 4.0 Clouds and the Earth's Radiant Energy System (CERES) Energy Balanced and Filled (EBAF) Data Product." In: *Journal of Climate* 31.11 (2018), pp. 4501–4527. ISSN: 0894-8755, 1520-0442. DOI: 10.1175/JCLI-D-17-0523.1.

Kenneally, P. W. and H. Schaub. "Spacecraft Radiation Pressure Using Complex Bidirectional-Reflectance Distribution Functions On Graphics Processing Unit." In: *AAS Spaceflight Mechanics Meeting* (2019), pp. 1631–1650.

Kenneally, P. and H. Schaub. "Parallel spacecraft solar radiation pressure modeling using ray-tracing on graphic processing unit." In: *68th International Astronautical Congress*. Vol. C1. Adelaide, Australia, 2017, p. 11.

Kenneally, P. W. "High Geometric Fidelity Solar Radiation Pressure Modeling via Graphics Processing Unit." MA thesis. Department of Aerospace Engineering Sciences, University of Colorado, US, 2016.

Kim, J. "Simulation study of a low-low satellite-to-satellite tracking mission." PhD thesis. University of Texas at Austin, 2000.

Kim, J. and B. D. Tapley. "Error analysis of a low-low satellite-to-satellite tracking mission." In: *Journal of Guidance, Control, and Dynamics* 25.6 (2002), pp. 1100–1106.

Kim, J. and B. D. Tapley. "Estimation of non-gravitational acceleration difference between two co-orbiting satellites using single accelerometer data." In: *Journal of Geodesy* 89.6 (2015), pp. 537–550.

Kirchhoff, G. "Ueber das Verhältniss zwischen dem Emissionsvermögen und dem Absorptionsvermögen der Körper für Wärme und Licht." In: *Annalen der Physik* 185.2 (1860), pp. 275–301. ISSN: 1521-3889. DOI: 10.1002/andp.18601850205.

Kirpichnikov, S. N. "Accurate calculation of the motion of artificial moon satellites, including solar and lunar radiation pressure." In: *Soviet Astronomy* 12.3 (1968).

Klinger, B. and T. Mayer-Gürr. "The role of accelerometer data calibration within GRACE gravity field recovery: Results from ITSG-Grace2016." In: *Advances in Space Research* 58.9 (2016), pp. 1597–1609.

Knocke, P. C., J. C. Ries, and B. D. Tapley. "Earth radiation pressure effects on satellites." In: *Proceedings of the AIAA/AAS Astrodynamics Conference*. AIAA 88-4292. Minneapolis, USA, 1988, pp. 577–586.

Knocke, P. C. "Earth radiation pressure effects on satellites." University of Texas at Austin, 1989.

Konopliv, A. S., R. S. Park, D.-N. Yuan, S. W. Asmar, M. M. Watkins, J. G. Williams, E. Fahnestock, G. Kruizinga, M. Paik, D. Strekalov, N. Harvey, D. E. Smith, and M. T. Zuber. "The JPL lunar gravity field to spherical harmonic degree 660 from the GRAIL Primary Mission." In: *Journal of Geophysical Research: Planets* 118.7 (2013), pp. 1415–1434. ISSN: 2169-9100. DOI: 10.1002/jgre.20097.

Kopp, G. and J. L. Lean. "A new, lower value of total solar irradiance: Evidence and climate significance." In: *Geophysical Research Letters* 38.1 (2011). ISSN: 1944-8007. DOI: 10.1029/2010GL045777.

Koppenwallner, G. "Energy accommodation coefficient and momentum transfer modeling." In: *Hyperschall Technologie Göttingen GmbH TN-08-11, Katlenburg Lindau, Germany* (2009).

Krauss, S., S. Behzadpour, M. Temmer, and C. Lhotka. "Exploring Thermospheric Variations Triggered by Severe Geomagnetic Storm on 26 August 2018 Using GRACE Follow-On Data." In: *Journal of Geophysical Research: Space Physics* 125.5 (2020), e2019JA027731. ISSN: 2169-9402. DOI: 10.1029/2019JA027731.

Krauss, S., M. Pfleger, and H. Lammer. "Satellite-based analysis of thermosphere response to extreme solar flares." In: *Annales Geophysicae* 32.10 (2014), pp. 1305–1309. ISSN: 1432-0576. DOI: 10.5194/angeo-32-1305-2014.

Kucharski, D., H.-C. Lim, G. Kirchner, and J.-Y. Hwang. "Spin parameters of LAGEOS-1 and LAGEOS-2 spectrally determined from Satellite Laser Ranging data." In: *Advances in Space Research* 52.7 (2013), pp. 1332–1338. ISSN: 0273-1177. DOI: 10.1016/j.asr.2013.07.007.

Kvas, A., S. Behzadpour, M. Ellmer, B. Klinger, S. Strasser, N. Zehentner, and T. Mayer-Gürr. "ITSG-Grace2018: Overview and Evaluation of a New GRACE-Only Gravity Field Time Series." In: *Journal of Geophysical Research: Solid Earth* 124.8 (2019), pp. 9332–9344. ISSN: 2169-9356. DOI: 10.1029/2019JB017415.

Kvas, A., T. Mayer-Gürr, S. Krauss, J. M. Brockmann, T. Schubert, W.-D. Schuh, R. Pail, T. Gruber, A. Jäggi, and U. Meyer. "The satellite-only gravity field model GOCO06s." In: *GFZ Data Services* (2019). DOI: 10.5880/ICGEM.2019.002.

Landerer, F., F. Flechtner, H. Save, and C. Dahle. *GRACE Follow-On science data system newsletter report: Apri-Jun 2022 (No. 21)*. 2022.

Landerer, F. W. and S. S. Cooley. *Gravity Recovery and Climate Experiment Follow-on (GRACE-FO) Level-3 Data Product User Handbook*. GRACE D-103133. JPL, California Institute of Technology, NASA, 2021.

Landerer, F. W. et al. "Extending the Global Mass Change Data Record: GRACE Follow-On Instrument and Science Data Performance." In: *Geophysical Research Letters* 47.12 (2020), e2020GL088306. ISSN: 1944-8007. DOI: 10.1029/2020GL088306.

Laštovička, J., S. C. Solomon, and L. Qian. "Trends in the Neutral and Ionized Upper Atmosphere." In: *Space Science Reviews* 168.1-4 (2012), pp. 113–145. ISSN: 0038-6308, 1572-9672. DOI: 10.1007/s11214-011-9799-3.

Laundal, K. M. and A. D. Richmond. "Magnetic Coordinate Systems." In: *Space Science Reviews* 206.1-4 (2017), pp. 27–59. ISSN: 0038-6308, 1572-9672. DOI: 10.1007/s11214-016-0275-y.

Lemoine, F. G., S. Goossens, T. J. Sabaka, J. B. Nicholas, E. Mazarico, D. D. Rowlands, B. D. Loomis, D. S. Chinn, D. S. Caprette, G. A. Neumann, D. E. Smith, and M. T. Zuber. "High-degree gravity models from GRAIL primary mission data." In: *Journal of Geophysical Research: Planets* 118.8 (2013), pp. 1676–1698. ISSN: 2169-9097, 2169-9100. DOI: 10.1002/jgre.20118.

Li, R. and J. Lei. "Responses of Thermospheric Mass Densities to the October 2016 and September 2017 Geomagnetic Storms Revealed From Multiple Satellite Observations." In: *Journal of Geophysical Research: Space Physics* 126.1 (2021), e2020JA028534. ISSN: 2169-9402. DOI: 10.1029/2020JA028534.

Li, Z., M. Ziebart, S. Bhattarai, and D. Harrison. "A shadow function model based on perspective projection and atmospheric effect for satellites in eclipse." In: *Advances in Space Research* (2018). ISSN: 02731177. DOI: 10.1016/j.asr.2018.10.027.

Li, Z., M. Ziebart, S. Grey, and S. Bhattarai. "Earth Radiation Pressure Modeling for BDS IGSO satellite." In: *China Satellite Navigation Conference 2017 Proceedings*. China Satellite Navigation Conference (CSNC) 2017, 2017, p. 10.

Linares, R., J. Crassidis, M. Jah, and H. Kim. "Astrometric and Photometric Data Fusion for Resident Space Object Orbit, Attitude, and Shape Determination Via Multiple-Model Adaptive Estimation." In: American Institute of Aeronautics and Astronautics, 2010. ISBN: 978-1-60086-962-4. DOI: 10.2514/6.2010-8341.

List, M., S. Bremer, B. Rievers, and H. Selig. "Modelling of Solar Radiation Pressure Effects: Parameter Analysis for the MICROSCOPE Mission." In: *International Journal of Aerospace Engineering* 2015 (2015), p. 14. DOI: 10.1155/2015/928206.

Liu, C. and R. Allan. *Reconstructions of the radiation fluxes at the top of the atmosphere and net surface energy flux over 1985-2017 - DEEP-C Version 4.0*. University of Reading, 2020. DOI: 10.17864/1947.271.

Liu, H. and H. Lühr. "Strong disturbance of the upper thermospheric density due to magnetic storms: CHAMP observations." In: *Journal of Geophysical Research: Space Physics* 110.A9 (2005).

Liu, H.-L., C. G. Bardeen, B. T. Foster, P. Lauritzen, J. Liu, G. Lu, D. R. Marsh, A. Maute, J. M. McInerney, N. M. Pedatella, L. Qian, A. D. Richmond, R. G. Roble, S. C. Solomon, F. M. Vitt, and W. Wang. "Development and Validation of the Whole Atmosphere Community Climate Model With Thermosphere and Ionosphere Extension (WACCM-X 2.0)." In: *Journal of Advances in Modeling Earth Systems* 10.2 (2018), pp. 381–402. ISSN: 1942-2466. DOI: 10.1002/2017MS001232.

Liu, H., E. Doornbos, and J. Nakashima. "Thermospheric wind observed by GOCE: Wind jets and seasonal variations." In: *Journal of Geophysical Research: Space Physics* 121.7 (2016), pp. 6901–6913. ISSN: 2169-9402. DOI: 10.1002/2016JA022938.

Löcher, A. "Möglichkeiten der Nutzung kinematischer Satellitenbahnen zur Bestimmung des Gravitationsfeldes der Erde." PhD thesis. Institut für Geodäsie und Geoinformation (IGG) der Rheinischen Friedrich-Wilhelms-Universität Bonn, 2011.

Löcher, A. and J. Kusche. "A hybrid approach for recovering high-resolution temporal gravity fields from satellite laser ranging." In: *Journal of Geodesy* 95.6 (2021). ISSN: 1432-1394. DOI: 10.1007/s00190-020-01460-x.

Löcher, A. and J. Kusche. "Assessment of the impact of one-way laser ranging on orbit determination of the Lunar Reconnaissance Orbiter." In: *Journal of Geodesy* 93.11 (2019), pp. 2421–2428. ISSN: 1432-1394. DOI: 10.1007/s00190-018-1200-9.

Löcher, A. and J. Kusche. "Precise orbits of the Lunar Reconnaissance Orbiter from radiometric tracking data." In: *Journal of Geodesy* 92.9 (2018), pp. 989–1001. ISSN: 0949-7714, 1432-1394. DOI: 10.1007/s00190-018-1124-4.

Loeb, N. G., D. R. Doelling, H. Wang, W. Su, C. Nguyen, J. G. Corbett, L. Liang, C. Mitrescu, F. G. Rose, and S. Kato. "Clouds and the Earth's Radiant Energy System (CERES) Energy Balanced and Filled (EBAF) Top-of-Atmosphere (TOA) Edition-4.0 data product." In: *Journal of Climate* 31.2 (2018), pp. 895–918. DOI: 10.1175/JCLI-D-17-0208.1.

Loeb, N. G., B. A. Wielicki, D. R. Doelling, G. L. Smith, D. F. Keyes, S. Kato, N. Manalo-Smith, and T. Wong. "Toward optimal closure of the Earth's top-of-atmosphere radiation budget." In: *Journal of Climate* 22.3 (2009), pp. 748–766. DOI: 10:1175/2008JCLI2637.1.

Loeb, N. G., G. C. Johnson, T. J. Thorsen, J. M. Lyman, F. G. Rose, and S. Kato. "Satellite and Ocean Data Reveal Marked Increase in Earth's Heating Rate." In: *Geophysical Research Letters* 48.13 (2021), e2021GL093047. ISSN: 1944-8007. DOI: 10.1029/2021GL093047.

Loeb, N. G., S. Kato, K. Loukachine, N. Manalo-Smith, and D. R. Doelling. "Angular Distribution Models for Top-of-Atmosphere Radiative Flux Estimation from the Clouds and the Earth's Radiant Energy System Instrument on the *Terra* Satellite. Part II: Validation." In: *Journal of Atmospheric and Oceanic Technology* 24.4 (2007), pp. 564–584. ISSN: 0739-0572, 1520-0426. DOI: 10.1175/JTECH1983.1.

Loeb, N. G., S. Kato, and B. A. Wielicki. "Defining Top-of-the-Atmosphere Flux Reference Level for Earth Radiation Budget Studies." In: *Journal of Climate* 15.22 (2002), pp. 3301–3309. ISSN: 0894-8755, 1520-0442. DOI: 10.1175/1520-0442(2002)015<3301:DTOTAF>2.0.CO;2.

Lucchesi, D. M. "Reassessment of the error modelling of non-gravitational perturbations on LAGEOS II and their impact in the Lense–Thirring derivation—Part II." In: *Planetary and Space Science* 50.10 (2002), pp. 1067–1100. ISSN: 0032-0633. DOI: 10.1016/S0032-0633(02)00052-1.

Lück, C. "Large-scale mass redistribution in the Earth system from synergistic use of Swarm data." PhD thesis. Bonn, Germany: Universitäts- und Landesbibliothek Bonn, 2022.

Lück, C., J. Kusche, R. Rietbroek, and A. Löcher. "Time-variable gravity fields and ocean mass change from 37 months of kinematic Swarm orbits." In: *Solid Earth* 9.2 (2018), p. 323. DOI: 10.5194/se-9-323-2018.

Mao, X., D. Arnold, V. Girardin, A. Villiger, and A. Jäggi. "Dynamic GPS-based LEO orbit determination with 1 cm precision using the Bernese GNSS Software." In: *Advances in Space Research* 67.2 (2021), pp. 788–805. ISSN: 0273-1177. DOI: 10.1016/j.asr.2020.10.012.

March, G. "Consistent thermosphere density and wind data from satellite observations: A study of satellite aerodynamics and thermospheric products." PhD thesis. Delft University of Technology, 2020.

March, G., E. N. Doornbos, and P. N. A. M. Visser. "High-fidelity geometry models for improving the consistency of CHAMP, GRACE, GOCE and Swarm thermospheric density data sets." In: *Advances in Space Research* 63.1 (2019), pp. 213–238. ISSN: 0273-1177. DOI: 10.1016/j.asr.2018.07.009.

March, G., T. Visser, P. Visser, and E. Doornbos. "CHAMP and GOCE thermospheric wind characterization with improved gas-surface interactions modelling." In: *Advances in Space Research* 64.6 (2019), pp. 1225–1242. ISSN: 02731177. DOI: 10.1016/j.asr.2019.06.023.

March, G., E. Doornbos, and P. Visser. "CHAMP, GRACE, GOCE and Swarm Thermosphere Density Data with Improved Aerodynamic and Geometry Modelling." In: *4th Swarm Science Meeting & Geodetic Missions Workshop.* (2017).

March, G., J. van den IJssel, C. Siemes, P. N. A. M. Visser, E. N. Doornbos, and M. Pilinski. "Gas-surface interactions modelling influence on satellite aerodynamics and thermosphere mass density." In: *Journal of Space Weather and Space Climate* 11 (2021), p. 54. ISSN: 2115-7251. DOI: 10.1051/swsc/2021035.

Marr, J. M. and F. P. Wilkin. "A better presentation of Planck's radiation law." In: *American Journal of Physics* 80.5 (2012), pp. 399–405. ISSN: 0002-9505. DOI: 10.1119/1.3696974.

Marshall, J. A., S. B. Luthcke, P. G. Antreasian, and G. W. Rosborough. *Modeling radiation forces acting on Topex/Poseidon for precision orbit determination.* Technical Memorandum 92B00089. Greenbelt, Maryland: NASA-Goddard Space Flight Center, 1992, pp. 99–105.

Marti, F., A. Blazquez, B. Meyssignac, M. Ablain, A. Barnoud, R. Fraudeau, R. Jugier, J. Chenal, G. Larnicol, J. Pfeffer, M. Restano, and J. Benveniste. "Monitoring the ocean heat content change and the Earth energy imbalance from space altimetry and space gravimetry." In: *Earth System Science Data* 14.1 (2022), pp. 229–249. ISSN: 1866-3508. DOI: 10.5194/essd-14-229-2022.

Martin, C. F. and D. P. Rubincam. "Effects of Earth albedo on the LAGEOS I satellite." In: *Journal of Geophysical Research: Solid Earth* 101.B2 (1996), pp. 3215–3226. ISSN: 2156-2202. DOI: 10.1029/95JB02810.

Matzka, J., C. Stolle, Y. Yamazaki, O. Bronkalla, and A. Morschhauser. "The Geomagnetic Kp Index and Derived Indices of Geomagnetic Activity." In: *Space Weather* 19.5 (2021), e2020SW002641. ISSN: 1542-7390. DOI: 10.1029/2020SW002641.

Matzka, J., O. Bronkalla, K. Tornow, K. Elger, and C. Stolle. *Geomagnetic Kp index.* Version 1.0. GFZ Data Services, 2021. DOI: 10.5880/KP.0001.

Mayaud, P.-N. "Derivation, meaning, and use of geomagnetic indices." In: *Washington DC American Geophysical Union Geophysical Monograph Series* 22 (1980).

Mayer-Gürr, T. "Gravitationsfeldbestimmung aus der Analyse kurzer Bahnbögen am Beispiel der Satellitenmissionen CHAMP und GRACE." PhD thesis. Bonn, Germany: Institut für Geodäsie und Geoinformation (IGG) der Rheinischen Friedrich-Wilhelms-Universität Bonn, 2006.

Mazarico, E., M. T. Zuber, F. G. Lemoine, and D. E. Smith. "Effects of self-shadowing on non-conservative force modeling for Mars-orbiting spacecraft." In: *Journal of Spacecraft and Rockets* 46.3 (2009), pp. 662–669. ISSN: 0022-4650, 1533-6794. DOI: 10.2514/1.41679.

McCarthy, J. J. and T. V. Martin. "A computer efficient model of Earth albedo satellite effects." In: *Planetary Sciences Department Report 012* 77 (1977).

McCullough, C., N. Harvey, H. Save, and T. Bandikova. *Description of calibrated GRACE-FO accelerometer data products (ACT)*. Level-1 Product Version 04 JPL D-103863. JPL, California Institute of Technology, NASA, 2019.

McGirr, R., P. Tregoning, S. Allgeyer, H. McQueen, and A. Purcell. "Mitigation of thermal noise in GRACE accelerometer observations." In: *Advances in Space Research* 69.1 (2022), pp. 386–401. ISSN: 0273-1177. DOI: 10.1016/j.asr.2021.10.055.

McMahon, J. and D. J. Scheeres. "General Solar Radiation Pressure Model for Global Positioning System Orbit Determination." In: *Journal of guidance, control, and dynamics* 37.1 (2014), pp. 325–330. DOI: 10.2514/1.61113.

McMahon, J. W. and D. J. Scheeres. "New Solar Radiation Pressure Force Model for Navigation." In: *Journal of Guidance, Control, and Dynamics* (2012). DOI: 10.2514/1.48434.

Mehta, P. M. and R. Linares. "A new transformative framework for data assimilation and calibration of physical ionosphere-thermosphere models." In: *Space Weather* 16 (2018), pp. 1086–1100.

Mehta, P. M., A. Walker, C. A. McLaughlin, and J. Koller. "Comparing Physical Drag Coefficients Computed Using Different Gas–Surface Interaction Models." In: *Journal of Spacecraft and Rockets* (2014). DOI: 10.2514/1.A32566.

Mehta, P. M., A. C. Walker, E. K. Sutton, and H. C. Godinez. "New density estimates derived using accelerometers on board the CHAMP and GRACE satellites." In: *Space Weather* 15.4 (2017), pp. 558–576. ISSN: 1542-7390. DOI: 10.1002/2016SW001562.

Meindl, M., G. Beutler, D. Thaller, R. Dach, and A. Jäggi. "Geocenter coordinates estimated from GNSS data as viewed by perturbation theory." In: *Advances in Space Research* 51.7 (2013), pp. 1047–1064. ISSN: 0273-1177. DOI: 10.1016/j.asr.2012.10.026.

Mendes, V. B. and E. C. Pavlis. "High-accuracy zenith delay prediction at optical wavelengths." In: *Geophysical Research Letters* 31.14 (2004). ISSN: 1944-8007. DOI: 10.1029/2004GL020308.

Métris, G., D. Vokrouhlický, J. C. Ries, and R. J. Eanes. "Nongravitational effects and the LAGEOS eccentricity excitations." In: *Journal of Geophysical Research: Solid Earth* 102.B2 (1997), pp. 2711–2729. ISSN: 2156-2202. DOI: 10.1029/96JB03186.

Meyssignac, B. et al. "Measuring global ocean heat content to estimate the Earth energy imbalance." In: *Frontiers in Marine Science* 6.432 (2019). DOI: 10.3389/fmars.2019.00432.

Milani, A., A. M. Nobill, and P. Farinella. *Non-gravitational perturbations and satellite geodesy*. Bristol: Adam Hilger Ltd., 1987.

Moe, K., M. M. Moe, and C. J. Rice. "Simultaneous analysis of multi-instrument satellite measurements of atmospheric density." In: *Journal of Spacecraft and Rockets* 41.5 (2004), pp. 849–853.

Moe, K. and M. M. Moe. "Gas-surface interactions and satellite drag coefficients." In: *Planetary and Space Science* 53.8 (2005), pp. 793–801. ISSN: 0032-0633. DOI: 10.1016/j.pss.2005.03.005.

Montenbruck, O. and E. Gill. *Satellite orbits: models, methods and applications*. Springer Science & Business Media, 2012. ISBN: 978-3-642-58351-3.

Montenbruck, O., S. Hackel, and A. Jäggi. "Precise orbit determination of the Sentinel-3A altimetry satellite using ambiguity-fixed GPS carrier phase observations." In: *Journal of Geodesy* 92.7 (2018), pp. 711–726. ISSN: 1432-1394. DOI: 10.1007/s00190-017-1090-2.

Montenbruck, O., S. Hackel, J. van den Ijssel, and D. Arnold. "Reduced dynamic and kinematic precise orbit determination for the Swarm mission from 4 years of GPS tracking." In: *GPS Solutions* 22.3 (2018). ISSN: 1080-5370, 1521-1886. DOI: 10.1007/s10291-018-0746-6.

Montenbruck, O., P. Steigenberger, and F. Darugna. "Semi-analytical solar radiation pressure modeling for QZS-1 orbit-normal and yaw-steering attitude." In: *Advances in Space Research* 59.8 (2017), pp. 2088–2100. ISSN: 02731177. DOI: 10.1016/j.asr.2017.01.036.

Montenbruck, O., P. Steigenberger, and U. Hugentobler. "Enhanced solar radiation pressure modeling for Galileo satellites." In: *Journal of Geodesy* 89.3 (2015), pp. 283–297. DOI: 10.1007/s00190-014-0774-0.

NASA/LARC/SD/ASDC. *CERES and GEO-Enhanced TOA, Within-Atmosphere and Surface Fluxes, Clouds and Aerosols 1-Hourly Terra-Aqua Edition4A [Data set]*. NASA Langley Atmospheric Science Data Center DAAC, 2017.

Nicodemus, F. E., J. C. Richmond, J. J. Hsia, I. W. Ginsberg, and T. Limperis. *Geometrical considerations and nomenclature for reflectance*. NBS MONO 160. Gaithersburg, MD: National Bureau of Standards, 1977. DOI: 10.6028/NBS.MONO.160.

Niemeier, W. *Ausgleichungsrechnung: Statistische Auswertemethoden*. Walter de Gruyter, 2008.

Nimier-David, M., D. Vicini, T. Zeltner, and J. Wenzel. "Mitsuba 2: A Retargetable Forward and Inverse Renderer." In: *Transactions on Graphics (Proceedings of SIGGRAPH Asia)* 38.6 (2019). DOI: 10.1145/3355089.3356498.

Otsubo, T. and G. M. Appleby. "System-dependent center-of-mass correction for spherical geodetic satellites." In: *Journal of Geophysical Research: Solid Earth* 108.B4 (2003). ISSN: 2156-2202. DOI: 10.1029/2002JB002209.

Pachot, C., B. Carnicero Dominguez, H. Oetjen, B. Sierk, F. Mariani, S. Riel, G. Rodrigues, M. Copano, A. Martínez Carou, L. Palchetti, M. Lippa, P. Giaccari, C. Mastrandrea, G. Perron, C. Keim, and M. Kolm. "The infrared Fourier transform spectrometer and the infrared imager instrument concepts for the FORUM mission, ESA's 9th Earth Explorer." In: *Sensors, Systems, and Next-Generation Satellites XXIV*. Sensors, Systems, and Next-Generation Satellites XXIV. Ed. by S. P. Neeck, T. Kimura, and A. Hélière. Online Only, United Kingdom: SPIE, 2020, p. 9. ISBN: 978-1-5106-3873-0. DOI: 10.1117/12.2570867.

Packbier, C. "Reconstructing the global density of the thermosphere from satellite observations using deep learning." MA thesis. Bonn, Germany: University of Bonn, 2021.

Panzetta, F., M. Bloßfeld, E. Erdogan, S. Rudenko, M. Schmidt, and H. Müller. "Towards thermospheric density estimation from SLR observations of LEO satellites: a case study with ANDE-Pollux satellite." In: *Journal of Geodesy* (2018). ISSN: 0949-7714, 1432-1394. DOI: 10.1007/s00190-018-1165-8.

Pearlman, M., D. Arnold, M. Davis, F. Barlier, R. Biancale, V. Vasiliev, I. Ciufolini, A. Paolozzi, E. C. Pavlis, K. Sośnica, and M. Bloßfeld. "Laser geodetic satellites: a high-accuracy scientific tool." In: *Journal of Geodesy* (2019). ISSN: 1432-1394. DOI: 10.1007/s00190-019-01228-y.

Pearlman, M. R., C. E. Noll, E. C. Pavlis, F. G. Lemoine, L. Combrink, J. J. Degnan, G. Kirchner, and U. Schreiber. "The ILRS: approaching 20 years and planning for the future." In: *Journal of Geodesy* 93.11 (2019), pp. 2161–2180. ISSN: 1432-1394. DOI: 10.1007/s00190-019-01241-1.

Peter, H., A. Jäggi, J. Fernández, D. Escobar, F. Ayuga, D. Arnold, M. Wermuth, S. Hackel, M. Otten, W. Simons, P. Visser, U. Hugentobler, and P. Féménias. "Sentinel-1A – First precise orbit determination results." In: *Advances in Space Research* 60.5 (2017), pp. 879–892. ISSN: 0273-1177. DOI: 10.1016/j.asr.2017.05.034.

Peterseim, N., J. Flury, and A. Schlicht. "Magnetic torquer induced disturbing signals within GRACE accelerometer data." In: *Advances in Space Research* 49.9 (2012), pp. 1388–1394. ISSN: 02731177. DOI: 10.1016/j.asr.2012.02.013.

Petit, G. and B. Luzum. *IERS conventions (2010)*. DTIC Document, 2010.

Petty, G. W. *A first course in atmospheric radiation*. Sundog Pub, 2006. ISBN: 0-9729033-1-3.

Pharr, M., W. Jakob, and G. Humphreys. *Physically Based Rendering: From Theory to Implementation*. Morgan Kaufmann, 2016.

Phong, B. T. "Illumination for computer generated pictures." In: *Communications of the ACM* 18.6 (1975), pp. 311–317. ISSN: 0001-0782, 1557-7317. DOI: 10.1145/360825.360839.

Picone, J. M., J. T. Emmert, and J. L. Lean. "Thermospheric densities derived from spacecraft orbits: Accurate processing of two-line element sets." In: *Journal of Geophysical Research: Space Physics* 110.A3 (2005).

Picone, J. M., A. E. Hedin, D. P. Drob, and A. C. Aikin. "NRLMSISE-00 empirical model of the atmosphere: Statistical comparisons and scientific issues." In: *Journal of Geophysical Research: Space Physics* 107.A12 (2002), SIA–15. DOI: 10.1029/2002JA009430.

Picot, N., C. Marechal, A. Couhert, S. Desai, R. Scharroo, and A. Egido. "Jason-3 Products Handbook." In: 5.1 (2018).

Pilewskie, P., M. Hakuba, and G. Stephens. "The Future of Earth Radiation Budget Observations Beyond CERES: Libera and Continuity of the ERB Climate Data Record." In: EGU General Assembly 2023, Vienna, Austria. EGU23-17097. 2023. DOI: 10.5194/egusphere-egu23-17097.

Pilinski, M. D., B. M. Argrow, and S. E. Palo. "Semi-empirical model for satellite energy-accommodation coefficients." In: *Journal of Spacecraft and Rockets* 47.6 (2010), pp. 951–956. ISSN: 0022-4650, 1533-6794. DOI: 10.2514/1.49330.

Planck, M. *The theory of heat radiation*. Philadelphia: P. Blakiston's Son & Co., 1914.

Prölss, G. *Physics of the Earth's Space Environment: An Introduction*. Springer Science & Business Media, 2012. 522 pp. ISBN: 978-3-642-97123-5. Google Books: HvD9CAAAQBAJ.

Qian, L., A. G. Burns, B. A. Emery, B. Foster, G. Lu, A. Maute, A. D. Richmond, R. G. Roble, S. C. Solomon, and W. Wang. "The NCAR TIE-GCM: A community model of the coupled thermosphere/ionosphere system." In: *Modeling the Ionosphere-Thermosphere System* 201 (2014), pp. 73–83.

Qioptiq. *Optical Solar Reflectors. Designed and manufactured for thermal control*. 2023. URL: https://www.excelitas.com/de/file-download/download/public/58606?filename=Qioptiq_Space-Qualified_Solar_Reflectors_Datasheet.pdf (visited on 06/01/2023).

Qiu, H., L. Hu, Y. Zhang, D. Lu, and J. Qi. "Absolute Radiometric Calibration of Earth Radiation Measurement on FY-3B and Its Comparison With CERES/Aqua Data." In: *IEEE Transactions on Geoscience and Remote Sensing* 50.12 (2012), pp. 4965–4974. ISSN: 1558-0644. DOI: 10.1109/TGRS.2012.2202668.

Racca, G. D. "Moon surface thermal characteristics for moon orbiting spacecraft thermal analysis." In: *Planetary and Space Science*. Asteroids, Comets and Meteors 1993-V 43.6 (1995), pp. 835–842. ISSN: 0032-0633. DOI: 10.1016/0032-0633(95)00067-F.

Reddy, M. R. "Effect of low earth orbit atomic oxygen on spacecraft materials." In: *Journal of Materials Science* 30.2 (1995), pp. 281–307. ISSN: 0022-2461, 1573-4803. DOI: 10.1007/BF00354389.

Reigber, C., H. Lühr, and P. Schwintzer. *First CHAMP Mission Results for Gravity, Magnetic and Atmospheric Studies*. Springer Science  Business Media, 2003. ISBN: 3-540-00206-5.

Reigber, C., H. Lühr, and P. Schwintzer. "CHAMP mission status." In: *Advances in Space Research* 30.2 (2002), pp. 129–134. DOI: 10.1016/S0273-1177(02)00276-4.

Ren, X., P. Yang, D. Mei, H. Liu, G. Xu, and Y. Dong. "Global Ionospheric TEC Forecasting for Geomagnetic Storm Time Using a Deep Learning-Based Multi-Model Ensemble Method." In: *Space Weather* 21.3 (2023), e2022SW003231. ISSN: 1542-7390. DOI: 10.1029/2022SW003231.

Reubelt, T., G. Austen, and E. W. Grafarend. "Harmonic analysis of the Earth's gravitational field by means of semi-continuous ephemerides of a low Earth orbiting GPS-tracked satellite. Case study: CHAMP." In: *Journal of Geodesy* 77.5 (2003), pp. 257–278.

Richards, P. G., J. A. Fennelly, and D. G. Torr. "EUVAC: A solar EUV flux model for aeronomic calculations." In: *Journal of Geophysical Research: Space Physics* 99.A5 (1994), pp. 8981–8992. ISSN: 2156-2202. DOI: 10.1029/94JA00518.

Rietbroek, R. "Retrieval of Sea Level and Surface Loading Variations from Geodetic Observations and Model Simulations." PhD thesis. Universitäts- und Landesbibliothek Bonn, 2014.

Rietbroek, R., S.-E. Brunnabend, J. Kusche, J. Schröter, and C. Dahle. "Revisiting the contemporary sea-level budget on global and regional scales." In: *Proceedings of the National Academy of Sciences* 113.6 (2016), pp. 1504–1509. ISSN: 0027-8424, 1091-6490. DOI: 10.1073/pnas.1519132113.

Rievers, B. "High precision modelling of thermal perturbations with application to Pioneer 10 and Rosetta." PhD thesis. University of Bremen, 2012.

Riser, S. C. et al. "Fifteen years of ocean observations with the global Argo array." In: *Nature Climate Change* 6.2 (2016), pp. 145–153. ISSN: 1758-6798. DOI: 10.1038/nclimate2872.

Robertson, R., J. Flury, T. Bandikova, and M. Schilling. "Highly physical penumbra solar radiation pressure modeling with atmospheric effects." In: *Celestial Mechanics and Dynamical Astronomy* 123.2 (2015), pp. 169–202. ISSN: 0923-2958, 1572-9478. DOI: 10.1007/s10569-015-9637-0.

Robertson, R. V. "Highly physical solar radiation pressure modeling during penumbra transitions." PhD thesis. Blacksburg, Virginia: Department of Aerospace and Ocean Engineering at Virginia Polytechnic Institute and State University, 2015.

Roble, R. G. and R. E. Dickinson. "How will changes in carbon dioxide and methane modify the mean structure of the mesosphere and thermosphere?" In: *Geophysical Research Letters* 16.12 (1989), pp. 1441–1444. ISSN: 1944-8007. DOI: 10.1029/GL016i012p01441.

Rodriguez-Solano, C. J., U. Hugentobler, P. Steigenberger, M. Bloßfeld, and M. Fritsche. "Reducing the draconitic errors in GNSS geodetic products." In: *Journal of Geodesy* 88.6 (2014), pp. 559–574. ISSN: 1432-1394. DOI: 10.1007/s00190-014-0704-1.

Rodriguez-Solano, C., U. Hugentobler, and P. Steigenberger. "Adjustable box-wing model for solar radiation pressure impacting GPS satellites." In: *Advances in Space Research* 49.7 (2012), pp. 1113–1128. ISSN: 02731177. DOI: 10.1016/j.asr.2012.01.016.

Rodríguez-Solano, C. J. "Impact of albedo modelling on GPS orbits." MA thesis. TU München, 2009.

Rodríguez-Solano, C. J., U. Hugentobler, P. Steigenberger, and S. Lutz. "Impact of Earth radiation pressure on GPS position estimates." In: *Journal of Geodesy* 86.5 (2012), pp. 309–317. ISSN: 0949-7714, 1432-1394. DOI: 10.1007/s00190-011-0517-4.

Rubincam, D. P. "LAGEOS orbit decay due to infrared radiation from Earth." In: *Journal of Geophysical Research: Solid Earth* 92.B2 (1987), pp. 1287–1294.

Rubincam, D. P. "Yarkovsky Thermal Drag on LAGEOS." In: *Journal of Geophysical Research: Solid Earth* 93.B11 (1988), pp. 13805–13810. ISSN: 2156-2202. DOI: 10.1029/JB093iB11p13805.

Rubincam, D. P., D. G. Currie, and J. W. Robbins. "LAGEOS I once-per-revolution force due to solar heating." In: *Journal of Geophysical Research: Solid Earth* 102.B1 (1997), pp. 585–590. ISSN: 2156-2202. DOI: 10.1029/96JB02851.

Rubincam, D. P., P. C. Knocke, V. Taylor, and S. Blackwell. "Earth anisotropic reflection and the orbit of LAGEOS." In: *Journal of Geophysical Research: Solid Earth* 92.B11 (1987), pp. 11662–11668. ISSN: 2156-2202. DOI: 10.1029/JB092iB11p11662.

Rubincam, D. P. and N. R. Weiss. "Earth albedo and the orbit of LAGEOS." In: *Celestial Mechanics* 38.3 (1986), pp. 233–296. ISSN: 1572-9478. DOI: 10.1007/BF01231110.

Rudenko, S., D. Dettmering, J. Zeitlhöfler, R. Alkahal, D. Upadhyay, and M. Bloßfeld. "Radial Orbit Errors of Contemporary Altimetry Satellite Orbits." In: *Surveys in Geophysics* (2023). ISSN: 1573-0956. DOI: 10.1007/s10712-022-09758-5.

Russell, G. L., V. Gornitz, and J. R. Miller. "Regional sea level changes projected by the NASA/GISS Atmosphere-Ocean Model." In: *Climate Dynamics* 16.10 (2000), pp. 789–797. ISSN: 1432-0894. DOI: 10.1007/s003820000090.

Sarno-Smith, L. K., B. A. Larsen, R. M. Skoug, M. W. Liemohn, A. Breneman, J. R. Wygant, and M. F. Thomsen. "Spacecraft surface charging within geosynchronous orbit observed by the Van Allen Probes." In: *Space Weather* 14.2 (2016), pp. 151–164. ISSN: 1542-7390. DOI: 10.1002/2015SW001345.

Sarris, T. E. et al. "Daedalus: a low-flying spacecraft for in situ exploration of the lower thermosphere–ionosphere." In: *Geoscientific Instrumentation, Methods and Data Systems* 9.1 (2020), pp. 153–191. ISSN: 2193-0856. DOI: 10.5194/gi-9-153-2020.

Save, H. V., S. V. Bettadpur, and B. D. Tapley. "Single Accelerometer Gravity Solutions for GRACE." In: AGU Fall Meeting 2006. Abstract G13A-0026. Vol. 2006. 2006.

Scharroo, R., K. F. Wakker, B. A. C. Ambrosius, and R. Noomen. "On the along-track acceleration of the LAGEOS satellite." In: *Journal of Geophysical Research* 96.B1 (1991), p. 729. ISSN: 0148-0227. DOI: 10.1029/90JB02080.

Schlick, C. "An Inexpensive BRDF Model for Physically-based Rendering." In: *Computer Graphics Forum* 13.3 (1994), pp. 233–246.

Schunk, R. W., L. Gardner, L. Scherliess, and L. Zhu. "Problems associated with uncertain parameters and missing physics for long-term ionosphere-thermosphere forecasting." In: *Radio Science* 47.4 (2012). ISSN: 00486604. DOI: 10.1029/2011RS004911.

Seeber, G. *Satellite geodesy*. 2nd completely rev. and extended ed. Berlin; New York: Walter de Gruyter, 2003. 589 pp. ISBN: 978-3-11-017549-3.

Sehnal, L. "The motion of a charged satellite in the earth's magnetic field." In: *SAO Special Report* 271 (1969), pp. 1–15.

Sentman, L. H. *Free molecule flow theory and its application to the determination of aerodynamic forces*. Technical report. Lockheed Missiles & Space Company, Sunnyvale, California, 1961.

Serra, R., M. Vasile, K. Hoshi, and H. Yamakawa. "Study of the Lorentz force on debris with high area-to-mass ratios." In: *Journal of Guidance, Control, and Dynamics* 41.8 (2018), pp. 1675–1686. DOI: 10.2514/1.G003317.

Shirley, P. and C. Wang. "Distribution Ray Tracing: Theory and Practice." In: *Proceedings of the Third Eurographics Workshop on Rendering*. Proceedings of the third Eurographics workshop on rendering, 1992, pp. 33–44.

Siemes, C. *Swarm satellite thermo-optical properties and external geometry*. Memorandum ESA-EOPG-MOM-MO-15 2.1. European Space Agency, 2020.

Siemes, C., C. Borries, S. Bruinsma, I. Fernandez-Gomez, N. Hładczuk, J. van den IJssel, T. Kodikara, K. Vielberg, and P. Visser. "New Thermosphere Neutral Mass Density and Crosswind Datasets from CHAMP, GRACE, and GRACE-FO." In: *Journal of Space Weather and Space Climate* (2023). ISSN: 2115-7251. DOI: 10.1051/swsc/2023014.

Siemes, C., J. de Teixeira da Encarnação, E. Doornbos, J. van den IJssel, J. Kraus, R. Pereštý, L. Grunwaldt, G. Apelbaum, J. Flury, and P. E. Holmdahl Olsen. "Swarm accelerometer data processing from raw accelerations to thermospheric neutral densities." In: *Earth, Planets and Space* 68.1 (2016). ISSN: 1880-5981. DOI: 10.1186/s40623-016-0474-5.

Siemes, C., S. Maddox, O. Carraz, T. Cross, S. George, J. van den IJssel, M. Kiss-Toth, M. Pastena, I. Riou, M. Salter, H. Sweeney, M. Trigatzis, T. Valenzuela, and P. Visser. "CASPA-ADM: a mission concept for observing thermospheric mass density." In: *CEAS Space Journal* (2022). ISSN: 1868-2510. DOI: 10.1007/s12567-021-00412-1.

Silverman, E. M. *Space environmental effects on spacecraft: LEO materials selection guide, part 1*. Technical report NASA CR-4661, Part 1. Redondo Beach, CA: TRW Space & Electronics, One Space Park, 1995.

Silverman, E. M. *Space environmental effects on spacecraft: LEO materials selection guide, part 2*. Technical report NASA CR-4661, Part 2. Redondo Beach, CA: TRW Space & Electronics, One Space Park, 1995.

Smirnov, A., Y. Shprits, F. Prol, H. Lühr, M. Berrendorf, I. Zhelavskaya, and C. Xiong. "A novel neural network model of Earth's topside ionosphere." In: *Scientific Reports* 13.1 (2023), p. 1303. ISSN: 2045-2322. DOI: 10.1038/s41598-023-28034-z.

Smith, G., B. A. Wielicki, B. R. Barkstrom, R. B. Lee, K. J. Priestley, T. P. Charlock, P. Minnis, D. P. Kratz, N. Loeb, and D. F. Young. "Clouds and Earth radiant energy system: an overview." In: *Advances in Space Research* 33.7 (2004), pp. 1125–1131. ISSN: 02731177. DOI: 10.1016/S0273-1177(03)00739-7.

Solomon, S. C., T. N. Woods, L. V. Didkovsky, J. T. Emmert, and L. Qian. "Anomalously low solar extreme-ultraviolet irradiance and thermospheric density during solar minimum." In: *Geophysical Research Letters* 37.16 (2010). ISSN: 1944-8007. DOI: 10.1029/2010GL044468.

Sośnica, K., A. Jäggi, U. Meyer, D. Thaller, G. Beutler, D. Arnold, and R. Dach. "Time variable Earth's gravity field from SLR satellites." In: *Journal of Geodesy* 89.10 (2015), pp. 945–960. ISSN: 1432-1394. DOI: 10.1007/s00190-015-0825-1.

Sośnica, K., A. Jäggi, D. Thaller, G. Beutler, and R. Dach. "Contribution of Starlette, Stella, and AJISAI to the SLR-derived global reference frame." In: *Journal of Geodesy* 88.8 (2014), pp. 789–804. ISSN: 0949-7714, 1432-1394. DOI: 10.1007/s00190-014-0722-z.

Springer, T. A., G. Beutler, and M. Rothacher. "A New Solar Radiation Pressure Model for GPS Satellites." In: *GPS Solutions* 2.3 (1999), pp. 50–62. ISSN: 1080-5370, 1521-1886. DOI: 10.1007/PL00012757.

Srivastava, V. K., A. Ashutosh, M. Roopa, B. Ramakrishna, M. Pitchaimani, and B. Chandrasekhar. "Spherical and oblate Earth conical shadow models for LEO satellites: Applications and comparisons with real time data and STK to IRS satellites." In: *Aerospace Science and Technology* 33.1 (2014), pp. 135–144. ISSN: 12709638. DOI: 10.1016/j.ast.2014.01.010.

Steigenberger, P., O. Montenbruck, and U. Hugentobler. "GIOVE-B solar radiation pressure modeling for precise orbit determination." In: *Advances in Space Research* 55.5 (2015), pp. 1422–1431. ISSN: 02731177. DOI: 10.1016/j.asr.2014.12.009.

Steigenberger, P., S. Thoelert, and O. Montenbruck. "GNSS satellite transmit power and its impact on orbit determination." In: *Journal of Geodesy* 92.6 (2018), pp. 609–624. ISSN: 0949-7714, 1432-1394. DOI: 10.1007/s00190-017-1082-2.

Stephens, G. L., G. G. Campbell, and T. H. Haar. "Earth radiation budgets." In: *Journal of Geophysical Research: Oceans* 86.C10 (1981), pp. 9739–9760.

Stephens, G. L., D. O'Brien, P. J. Webster, P. Pilewski, S. Kato, and J.-l. Li. "The albedo of Earth." In: *Reviews of Geophysics* 53.1 (2015), pp. 141–163. ISSN: 1944-9208. DOI: 10.1002/2014RG000449.

Stolle, C., J. Matzka, J. Kervalishvili, J. Rauberg, S. Bruinsma, and Y. Yamazaki. "The High Cadence Planetary Geomagnetic Index Hp." Oral presentation (IUGG19-3327). 27th IUGG General Assembly (Montreal, Canada). 2019.

Stuckey, W. "Lessons Learned from the Long Duration Exposure Facility." In: *Journal of the IES* 36.5 (1993), pp. 38–42. DOI: 10.17764/jiet.2.36.5.5414335137225306.

Su, W., J. Corbett, Z. Eitzen, and L. Liang. "Next-generation angular distribution models for top-of-atmosphere radiative flux calculation from CERES instruments: Methodology." In: *Atmospheric Measurement Techniques* 8.2 (2015), pp. 611–632. ISSN: 1867-8548. DOI: 10.5194/amt-8-611-2015.

Su, W., J. Corbett, Z. Eitzen, and L. Liang. "Next-generation angular distribution models for top-of-atmosphere radiative flux calculation from CERES instruments: Validation." In: *Atmospheric Measurement Techniques* 8.8 (2015), pp. 3297–3313. ISSN: 1867-8548. DOI: 10.5194/amt-8-3297-2015.

Suesser-Rechberger, B., S. Krauss, S. Strasser, and T. Mayer-Guerr. "Improved precise kinematic LEO orbits based on the raw observation approach." In: *Advances in Space Research* 69.10 (2022), pp. 3559–3570. ISSN: 0273-1177. DOI: 10.1016/j.asr.2022.03.014.

Suttles, J. T., R. N. Green, P. Minnis, G. L. Smith, W. F. Staylor, B. A. Wielicki, I. J. Walker, D. F. Young, V. R. Taylor, and L. L. Stowe. *Angular radiation models for Earth-atmosphere system: Volume I - shortwave radiation*. Reference Publication NASA RP-1184. Hampton, VA: NASA Langley Research Center, 1988, p. 147.

Suttles, J. T., R. N. Green, P. Minnis, G. L. Smith, W. F. Staylor, B. A. Wielicki, I. J. Walker, D. F. Young, V. R. Taylor, and L. L. Stowe. *Angular radiation models for Earth-atmosphere system: Volume II - longwave radiation*. Reference Publication NASA RP-1184, Vol. II. Hampton, VA: NASA Langley Research Center, 1989, p. 87.

Sutton, E. K., J. M. Forbes, and R. S. Nerem. "Global thermospheric neutral density and wind response to the severe 2003 geomagnetic storms from CHAMP accelerometer data." In: *Journal of Geophysical Research: Space Physics* 110.A09S40 (2005). DOI: 10.1029/2004JA010985.

Sutton, E. K., J. M. Forbes, R. S. Nerem, and T. N. Woods. "Neutral density response to the solar flares of October and November, 2003." In: *Geophysical Research Letters* 33.22 (2006). ISSN: 1944-8007. DOI: 10.1029/2006GL027737.

Sutton, E. K. "Effects of solar disturbances on the thermosphere densities and winds from CHAMP and GRACE satellite accelerometer data." PhD thesis. University of Colorado at Boulder, 2008.

Sutton, E. K., R. S. Nerem, and J. M. Forbes. "Density and winds in the thermosphere deduced from accelerometer data." In: *Journal of Spacecraft and Rockets* 44.6 (2007), pp. 1210–1219.

Sutton, E. K. "Normalized Force Coefficients for Satellites with Elongated Shapes." In: *Journal of Spacecraft and Rockets* 46.1 (2009), pp. 112–116. ISSN: 0022-4650. DOI: 10.2514/1.40940.

Švehla, D. and M. Rothacher. "Kinematic and reduced-dynamic precise orbit determination of low earth orbiters." In: *Advances in Geosciences* 1 (2003), pp. 47–56.

Švehla, D. and M. Rothacher. "Kinematic precise orbit determination for gravity field determination." In: *A Window on the Future of Geodesy* (2005), pp. 181–188.

Švehla, D. and L. Földváry. "From Kinematic Orbit Determination to Derivation of Satellite Velocity and Gravity Field." In: *Observation of the Earth System from Space*. Ed. by J. Flury,

R. Rummel, C. Reigber, M. Rothacher, G. Boedecker, and U. Schreiber. Berlin/Heidelberg: Springer-Verlag, 2006, pp. 177–192. ISBN: 978-3-540-29520-4. DOI: 10.1007/3-540-29522-4_13.

Tapley, B. D. "Statistical orbit determination theory." In: *Recent Advances in Dynamical Astronomy*. Springer, 1973, pp. 396–425.

Tapley, B. D., S. Bettadpur, M. Watkins, and C. Reigber. "The gravity recovery and climate experiment: Mission overview and early results." In: *Geophysical Research Letters* 31.9 (2004). DOI: 10.1029/2004GL019920.

Tapley, B. D., J. C. Ries, S. Bettadpur, and M. Cheng. "Neutral density measurements from the gravity recovery and climate experiment accelerometers." In: *Journal of Spacecraft and Rockets* 44.6 (2007), pp. 1220–1225.

Tapley, B. D. et al. "Contributions of GRACE to understanding climate change." In: *Nature Climate Change* 9.5 (2019), pp. 358–369. ISSN: 1758-6798. DOI: 10.1038/s41558-019-0456-2.

Tapping, K. F. "The 10.7 cm solar radio flux (F10.7)." In: *Space Weather* 11.7 (2013), pp. 394–406. ISSN: 1542-7390. DOI: 10.1002/swe.20064.

Tasistro-Hart, A., A. Grayver, and A. Kuvshinov. "Probabilistic Geomagnetic Storm Forecasting via Deep Learning." In: *Journal of Geophysical Research: Space Physics* 126.1 (2021), e2020JA028228. ISSN: 2169-9380, 2169-9402. DOI: 10.1029/2020JA028228.

Taylor, F. W. *Elementary Climate Physics*. Oxford Univ. Press, 2005. ISBN: 0-19-856734-0.

Taylor, V. R. and L. L. Stowe. "Reflectance characteristics of uniform Earth and cloud surfaces derived from NIMBUS-7 ERB." In: *Journal of Geophysical Research: Atmospheres* 89.D4 (1984), pp. 4987–4996. ISSN: 2156-2202. DOI: 10.1029/JD089iD04p04987.

Touboul, P., E. Willemenot, B. Foulon, and V. Josselin. "Accelerometers for CHAMP, GRACE and GOCE space missions: synergy and evolution." In: *Boll. Geof. Teor. Appl* 40.3-4 (1999), pp. 321–327.

Trenberth, K. E. and J. T. Fasullo. "Atlantic meridional heat transports computed from balancing Earth's energy locally." In: *Geophysical Research Letters* 44.4 (2017), pp. 1919–1927. ISSN: 1944-8007. DOI: 10.1002/2016GL072475.

Trenberth, K. E., J. T. Fasullo, and J. Kiehl. "Earth's Global Energy Budget." In: *Bulletin of the American Meteorological Society* 90.3 (2009), pp. 311–324. ISSN: 0003-0007, 1520-0477. DOI: 10.1175/2008BAMS2634.1.

Trenberth, K. E., J. T. Fasullo, K. von Schuckmann, and L. Cheng. "Insights into Earth's Energy Imbalance from Multiple Sources." In: *Journal of Climate* 29.20 (2016), pp. 7495–7505. ISSN: 0894-8755, 1520-0442. DOI: 10.1175/JCLI-D-16-0339.1.

Uebbing, B. "Consistently closing global and regional sea level budgets." PhD thesis. Institut für Geodäsie und Geoinformation (IGG) der Rheinischen Friedrich-Wilhelms-Universität Bonn, 2022.

Vallado, D. A. and D. Finkleman. "A critical assessment of satellite drag and atmospheric density modeling." In: *Acta Astronautica* 95 (2014), pp. 141–165. ISSN: 0094-5765. DOI: 10.1016/j.actaastro.2013.10.005.

Van den IJssel, J. a. A. "GPS-based precise orbit determination and accelerometry for low flying satellites." PhD thesis. Delft University of Technology, 2014.

Van den IJssel, J., E. Doornbos, E. Iorfida, G. March, C. Siemes, and O. Montenbruck. "Thermosphere densities derived from Swarm GPS observations." In: *Advances in Space Research* 65.7 (2020), pp. 1758–1771. ISSN: 0273-1177. DOI: 10.1016/j.asr.2020.01.004.

Van Helleputte, T., E. Doornbos, and P. Visser. "CHAMP and GRACE accelerometer calibration by GPS-based orbit determination." In: *Advances in Space Research* 43.12 (2009), pp. 1890–1896. ISSN: 02731177. DOI: 10.1016/j.asr.2009.02.017.

Vielberg, K., E. Forootan, C. Lück, A. Löcher, J. Kusche, and K. Börger. "Comparison of accelerometer data calibration methods used in thermospheric neutral density estimation." In: *Annales Geophysicae* 36.3 (2018), pp. 761–779. ISSN: 1432-0576. DOI: 10.5194/angeo-36-761-2018.

Vielberg, K. and J. Kusche. "Extended forward and inverse modeling of radiation pressure accelerations for LEO satellites." In: *Journal of Geodesy* 94.4 (2020), p. 43. ISSN: 1432-1394. DOI: 10.1007/s00190-020-01368-6.

Vielberg, K., A. Löcher, and J. Kusche. "Validating radiation pressure force models for GRACE with SLR." In: EGU General Assembly 2023, Vienna, Austria. EGU23-6533. 2023.

Vielberg, K., C. Lück, A. Corbin, E. Forootan, A. Löcher, and J. Kusche. *TND-IGG RL01: Thermospheric neutral density from accelerometer measurements of GRACE, CHAMP and Swarm.* PANGAEA, 2021. DOI: 10.1594/PANGAEA.931347.

Visco, M. and D. M. Lucchesi. "Comprehensive model for the spin evolution of the LAGEOS and LARES satellites." In: *Physical Review D* 98.4 (2018), p. 044034. ISSN: 2470-0010, 2470-0029. DOI: 10.1103/PhysRevD.98.044034.

Visco, M. and D. M. Lucchesi. "The LArase Satellites Spin mOdel Solutions (LASSOS): a comprehensive model for the spin evolution of the LAGEOS and LARES satellites." In: *Physical Review D* 98.4 (2018), p. 044034. ISSN: 2470-0010, 2470-0029. DOI: 10.1103/PhysRevD.98.044034. arXiv: 1801.09098 [gr-qc].

Visser, P. and J. Van Den IJssel. "Aiming at a 1-cm orbit for low earth orbiters: reduced-dynamic and kinematic precise orbit determination." In: *Space Science RSeviews* 108 (2003), pp. 27–36.

Visser, P., E. Doornbos, J. van den IJssel, and J. T. Da Encarnação. "Thermospheric density and wind retrieval from Swarm observations." In: *Earth, Planets and Space* 65.11 (2013), p. 12. DOI: 10.5047/eps.2013.08.003.

Visser, P. M. and J. A. A. Van den IJssel. "Calibration and validation of individual GOCE accelerometers by precise orbit determination." In: *Journal of Geodesy* 90.1 (2016), pp. 1–13. DOI: 10.1007/s00190-015-0850-0.

Visser, T. "Cross-wind from linear and angular satellite dynamics: The GOCE perspective on horizontal and vertical wind in the thermosphere." PhD thesis. Delft University of Technology, 2019. 148 pp.

Visser, T., G. March, E. Doornbos, C. Visser, and P. Visser. "Horizontal and vertical thermospheric cross-wind from GOCE linear and angular accelerations." In: *Advances in Space Research* 63.10 (2019), pp. 3139–3153. ISSN: 0273-1177. DOI: 10.1016/j.asr.2019.01.030.

Visser, T., G. March, E. N. Doornbos, C. C. de Visser, and P. N. a. M. Visser. "Characterization of Thermospheric Vertical Wind Activity at 225- to 295-km Altitude Using GOCE Data and Validation Against Explorer Missions." In: *Journal of Geophysical Research: Space Physics* 124.6 (2019), pp. 4852–4869. ISSN: 2169-9402. DOI: 10.1029/2019JA026568.

Vokrouhlický, D., P. Farinella, and F. Mignard. "Solar radiation pressure perturbations for Earth satellites, I. A complete theory including penumbra transitions." In: *Astronomy and Astrophysics* 280 (1993), pp. 395–312.

Vokrouhlický, D. "The geomagnetic effects on the motion of an electrically charged artificial satellite." In: *Celestial Mechanics & Dynamical Astronomy* 46.1 (1989), pp. 85–104. ISSN: 0923-2958, 1572-9478. DOI: 10.1007/BF02426715.

Vokrouhlický, D. and W. F. Bottke. "Yarkovsky and YORP effects." In: *Scholarpedia* 7.5 (2012), p. 10599. ISSN: 1941-6016. DOI: 10.4249/scholarpedia.10599.

Vokrouhlický, D. and P. Farinella. "Specular reflection of sunlight from wavy ocean surfaces and the albedo effect on satellite orbits. I. A statistical model." In: *Astronomy and Astrophysics* 298 (1995), pp. 307–322.

Von Schuckmann, K., M. D. Palmer, K. E. Trenberth, A. Cazenave, D. Chambers, N. Champollion, J. Hansen, S. A. Josey, N. Loeb, P.-P. Mathieu, B. Meyssignac, and M. Wild. "An imperative to monitor Earth's energy imbalance." In: *Nature Climate Change* 6.2 (2016), pp. 138–144. ISSN: 1758-6798. DOI: 10.1038/nclimate2876.

Von Schuckmann, K. et al. "Heat stored in the Earth system 1960–2020: where does the energy go?" In: *Earth System Science Data* 15.4 (2023), pp. 1675–1709. ISSN: 1866-3508. DOI: 10.5194/essd-15-1675-2023.

Von Schuckmann, K. et al. "Heat stored in the Earth system: where does the energy go?" In: *Earth System Science Data* 12.3 (2020), pp. 2013–2041. ISSN: 1866-3508. DOI: 10.5194/essd-12-2013-2020.

Walker, A., P. Mehta, and J. Koller. "Drag coefficient model using the cercignani-lampis-lord gas-surface interaction model." In: *Journal of Spacecraft and Rockets* 51.5 (2014), pp. 1544–1563. DOI: 10.2514/1.A32677.

Wang, C., J. Guo, Q. Zhao, and J. Liu. "Empirically derived model of solar radiation pressure for BeiDou GEO satellites." In: *Journal of Geodesy* 93.6 (2019), pp. 791–807. ISSN: 0949-7714, 1432-1394. DOI: 10.1007/s00190-018-1199-y.

Wang, Y., M. Li, K. Jiang, W. Li, Q. Zhao, R. Fang, N. Wei, and R. Mu. "Improving Precise Orbit Determination of LEO Satellites Using Enhanced Solar Radiation Pressure Modeling." In: *Space Weather* 21.1 (2023), e2022SW003292. ISSN: 1542-7390. DOI: 10.1029/2022SW003292.

WCRP Global Sea Level Budget Group. "Global sea-level budget 1993–present." In: *Earth System Science Data* 10.3 (2018), pp. 1551–1590. ISSN: 1866-3508. DOI: 10.5194/essd-10-1551-2018.

Weinbach, U. and S. Schön. "Improved GRACE kinematic orbit determination using GPS receiver clock modeling." In: *GPS Solutions* 17.4 (2013), pp. 511–520. ISSN: 1521-1886. DOI: 10.1007/s10291-012-0297-1.

Wen, H. Y., G. Kruizinga, M. Paik, F. Landerer, W. Bertiger, C. Sakumura, T. Bandikova, and C. Mccullough. *Gravity Recovery and Climate Experiment Follow-On (GRACE-FO) Level-1 Data Product User Handbook*. JPL D-56935 (URS270772). NASA Jet Propulsion Laboratory California Institute of Technology, 2019, p. 60.

Wendisch, M. and P. Yang. *Theory of atmospheric radiative transfer*. John Wiley & Sons, 2012. ISBN: 978-3-527-40836-8.

Wetterer, C. J., R. Linares, J. L. Crassidis, T. M. Kelecy, M. K. Ziebart, M. K. Jah, and P. J. Cefola. "Refining space object radiation pressure modeling with bidirectional reflectance distribution functions." In: *Journal of Guidance, Control, and Dynamics* 37.1 (2014), pp. 185–196. ISSN: 0731-5090. DOI: 10.2514/1.60577.

Wielicki, B. A., B. R. Barkstrom, E. F. Harrison, R. B. Lee III, G. Louis Smith, and J. E. Cooper. "Clouds and the Earth's Radiant Energy System (CERES): An earth observing system experiment." In: *Bulletin of the American Meteorological Society* 77.5 (1996), pp. 853–868.

Wild, M. "The global energy balance as represented in CMIP6 climate models." In: *Climate dynamics* 55.3 (2020), pp. 553–577. ISSN: 1432-0894. DOI: 10.1007/s00382-020-05282-7.

Wild, M., D. Folini, M. Z. Hakuba, C. Schär, S. I. Seneviratne, S. Kato, D. Rutan, C. Ammann, E. F. Wood, and G. König-Langlo. "The energy balance over land and oceans: an assessment based on direct observations and CMIP5 climate models." In: *Climate Dynamics* 44.11-12 (2015), pp. 3393–3429. ISSN: 0930-7575, 1432-0894. DOI: 10.1007/s00382-014-2430-z.

Wild, M., D. Folini, C. Schär, N. Loeb, E. G. Dutton, and G. König-Langlo. "The global energy balance from a surface perspective." In: *Climate Dynamics* 40.11-12 (2013), pp. 3107–3134.

Williams, D. R. *Moon Fact Sheet*. NASA, 2021.

Wirnsberger, H., S. Krauss, and T. Mayer-Gürr. "First independent Graz Lunar Gravity Model derived from GRAIL | Elsevier Enhanced Reader." In: *Icarus* 317 (2018), pp. 324–336. ISSN: 0019-1035. DOI: 10.1016/j.icarus.2018.08.011.

Wöske, F. "Gravity Field Recovery from GRACE Satellite Data and Investigation of Sensor, Environment and Processing-Option Influences by Closed Loop Mission Simulation." PhD thesis. University of Bremen, 2020.

Wöske, F., T. Kato, B. Rievers, and M. List. "GRACE accelerometer calibration by high precision non-gravitational force modeling." In: *Advances in Space Research* 63.3 (2019), pp. 1318–1335. ISSN: 02731177. DOI: 10.1016/j.asr.2018.10.025.

Yuan, D.-N. *GRACE Follow-On Level-2 Gravity Field Product User Handbook*. JPL D-103922. JPL, California Institute of Technology, NASA, 2019.

Zehentner, N. "Kinematic orbit positioning applying the raw observation approach to observe time variable gravity." PhD thesis. Graz, Austria: Institute of Geodesy, Graz University of Technology (90000), 2017. 175 pp.

Zehentner, N. and T. Mayer-Gürr. "Precise orbit determination based on raw GPS measurements." In: *Journal of Geodesy* 90.3 (2016), pp. 275–286. DOI: 10.1007/s00190-015-0872-7.

Zeitler, L., A. Corbin, K. Vielberg, S. Rudenko, A. Löcher, M. Bloßfeld, M. Schmidt, and J. Kusche. "Scale Factors of the Thermospheric Density: A Comparison of Satellite Laser Ranging and Accelerometer Solutions." In: *Journal of Geophysical Research: Space Physics* 126.12 (2021), e2021JA029708. ISSN: 2169-9402. DOI: 10.1029/2021JA029708.

Zelensky, N. P., F. G. Lemoine, M. Ziebart, A. Sibthorpe, P. Willis, B. D. Beckley, S. M. Klosko, D. S. Chinn, D. D. Rowlands, S. B. Luthcke, D. E. Pavlis, and V. Luceri. "DORIS/SLR POD modeling improvements for Jason-1 and Jason-2." In: *Advances in Space Research* 46.12 (2010), pp. 1541–1558. ISSN: 02731177. DOI: 10.1016/j.asr.2010.05.008.

Zhang, R., R. Tu, P. Zhang, J. Liu, and X. Lu. "Study of satellite shadow function model considering the overlapping parts of Earth shadow and Moon shadow and its application to GPS satellite orbit determination." In: *Advances in Space Research* 63.9 (2019), pp. 2912–2929. ISSN: 02731177. DOI: 10.1016/j.asr.2018.02.002.

Ziebart, M., S. Adhya, A. Sibthorpe, S. Edwards, and P. Cross. "Combined radiation pressure and thermal modelling of complex satellites: Algorithms and on-orbit tests." In: *Advances in Space Research* 36.3 (2005), pp. 424–430. ISSN: 02731177. DOI: 10.1016/j.asr.2005.01.014.

Ziebart, M. "Generalized analytical solar radiation pressure modeling algorithm for spacecraft of complex shape." In: *Journal of Spacecraft and Rockets* 41.5 (2004), pp. 840–848. DOI: 10.2514/1.13097.

Ziebart, M., S. Edwards, S. Adhya, A. Sibthorpe, P. Arrowsmith, and P. Cross. "High precision GPS IIR orbit prediction using analytical non-conservative force models." In: *ION-GNSS- 2004*. 2004, pp. 1764–1770.

Ziebart, M., A. Sibthorpe, P. Cross, Y. Bar-Sever, and B. Haines. "Cracking the GPS-SLR orbit anomaly." In: Proceedings of the 20th International Technical Meeting of the Satellite Division of The Institute of Navigation (ION GNSS 2007). 2007, pp. 2033–2038.

Zuo, H., M. A. Balmaseda, and K. Mogensen. "The new eddy-permitting ORAP5 ocean reanalysis: description, evaluation and uncertainties in climate signals." In: *Climate Dynamics* 49.3 (2017), pp. 791–811. ISSN: 1432-0894. DOI: 10.1007/s00382-015-2675-1.

Zuo, H., M. A. Balmaseda, S. Tietsche, K. Mogensen, and M. Mayer. "The ECMWF operational ensemble reanalysis–analysis system for ocean and sea ice: a description of the system and assessment." In: *Ocean Science* 15.3 (2019), pp. 779–808. ISSN: 1812-0784. DOI: 10.5194/os-15-779-2019.